NIFS-PROC-92

Proceedings of A3 Foresight Program Seminar on Critical Physics Issues Specific to Steady State Sustainment of High-Performance Plasma, 22-25 January, 2013, Kushiro, Japan

Eds. S. Morita, L. Hu and Y.-K. Oh

June 24, 2013

A3 Foresight Program Seminar on Critical Physics Issues Specific to Steady State Sustainment of High-Performance Plasma
22-25 January, 2013, Kushiro, Japan

Proceedings of A3 Foresight Program Seminar on Critical Physics Issues Specific to Steady State Sustainment of High-Performance Plasmas

22-25 January, 2013, Kushiro, Japan

Edited by
Shigeru MORITA, Liqun HU and Yeong-Kook OH

Abstract

The A3 Foresight Program titled by "Critical Physics Issues Specific to Steady State Sustainment of High-Performance Plasmas", based on the scientific collaboration among China, Japan and Korea in the field of plasma physics, has been newly started from August 2012 under the auspice of the Japan Society for the Promotion of Science (JSPS, Japan), the National Research Foundation of Korea (NRF, Korea) and the National Natural Science Foundation of China (NSFC, China). A seminar on the A3 collaboration took place in Hotel Gozensui, Kushiro, Japan, 22-25 January 2013. This seminar was organized by National Institute for Fusion Science. One special talk and 36 oral talks were presented in the seminar including 13 Chinese, 14 Japanese and 9 Korean attendees.

Steady state sustainment of high-performance plasmas is a crucial issue for realizing a nuclear fusion reactor. This seminar was motivated along the issues. Results on fusion experiments and theory obtained through A3 foresight program during recent two years were discussed and summarized. Possible direction of future collaboration and further encouragement of scientific activity of younger scientists were also discussed in this seminar with future experimental plans in three countries.

Key words: magnetically confined devices, toroidal plasmas, high performance plasmas, steady state operation, edge plasma, divertor plasma and alpha particle.

Organization Committee

Shigeru MORITA (National Institute for Fusion Science, Japan)
Liqun HU (Institute of Plasma Physics, Chinese Academy of Sciences, China)
Yeong-KooK OH (National Fusion Research Institute, Korea)

Program Committee

Shigeru MORITA (National Institute for Fusion Science, Japan)
Liqun HU (Institute of Plasma Physics, Chinese Academy of Sciences, China)
Yeong-Kook OH (National Fusion Research Institute, Korea)
Mitsutaka ISOBE (National Institute for Fusion Science, Japan)
Satoshi OHDACHI (National Institute for Fusion Science, Japan)
Satoru SAKAKIBARA (National Institute for Fusion Science, Japan)
Yasushi TODO (National Institute for Fusion Science, Japan)

Conference Secretariats

Noriaki TONOUCHI (National Institute for Fusion Science, Japan)
Satsuki MATSUI (National Institute for Fusion Science, Japan)
Shaohua DONG (Institute of Plasma Physics, Chinese Academy of Sciences, China)
Jun-hie HAN (National Fusion Research Institute, Korea)

Preface

Seminar on The A3 Foresight Program, "Critical Physics Issues Specific to Steady State Sustainment of High-Performance Plasmas", newly started from August 2012 under the auspice of the Japan Society for the Promotion of Science (JSPS, Japan), the National Research Foundation of Korea (NRF, Korea) and the National Natural Science Foundation of China (NSFC, China), took place in Hotel Gozensui, Kushiro, Japan, 22-25 January 2013. This seminar was organized by National Institute for Fusion Science.

Steady state operation of high-performance plasmas is a crucial issue for realizing a nuclear fusion reactor. Education of younger scientists becomes also extremely important for future progress of the fusion research. Several A3 collaboration programs have been started along such an important issue. Scientific progresses in the field of fusion experiment obtained from A3 foresight program activities were discussed and summarized in this seminar in addition to related theoretical work. In the seminar one special talk and 36 oral talks were presented including 13 Chinese, 14 Japanese and 9 Korean attendees. The presentations were focused on the following topics which are the important issues in the present A3 foresight program, regardless of the difference in magnetic configurations such as tokamaks and helical devices.

I. Steady state sustainment of magnetic configurations
II. Edge and divertor plasma control
    IIa. Transport of edge and divertor plasmas
    IIb. Stability of edge plasma
III. Confinement of alpha particles

This seminar was closed with great success, clarifying remarkable progresses in researches related to these important topics obtained through A3 collaboration and contributing the fostering of younger scientists. The organizing and program committees are grateful to all participants for their supports and corporation to this seminar.

Shigeru MORITA, Liqun HU and Yeong-Kook OH
Chairpersons of the Organizing Committee

Contents

Preface i

Contents iv

Talks

1. Progress of the KSTAR experiments and perspective for ITER scientific researches
   Y.-K. Oh (NFRI) 1

2. Recent progress of MHD study in helical plasmas
   S. Sakakibara (NIFS) 5

3. Progress on high performance long-pulse operations in EAST
   H. Y. Guo (ASIPP) 9

4. Simulation of turbulence in toroidal plasmas
   —Concentrated on the study of multi-scale interaction using mainly gyro-fluid and gyro-kinetic code
   Y. Kishimoto (Kyoto U.) 15

5. Boundary conditions for ion speed in a two-ion-species plasma with finite ion temperature
   N. Xiang (ASIPP) 21

6. Diagnostics upgrade and capabilty available for physics study on EAST tokamak
   L. Q. Hu (ASIPP) 27

7. Status and plan of KSTAR heating systems for steady-state plasma achievement
   Y. S. Bae (NFRI) 34

8. Issues of high power/ long pulse ECRH experiments in LHD
   S. Kubo (NIFS) 38

9. Preliminary ICRF heating results on EAST
X. J. Zhang (ASIPP) 42

10. Recent progress of the ECE diagnostics on EAST
Y. Liu (ASIPP) 46

11. Plasma rotation behavior of RF-heated H-mode discharges on EAST
B. Lu (ASIPP) 51

12. R & D of PFMC at ASIPP
G.-N. Luo (ASIPP) 55

13. Research plan of plasma wall interactions in EAST and LHD
N. Ashikawa (NIFS) 60

14. Korean plasma-material interaction researches/facilities
K.-S. Chung (Hanyang U.) 64

15. Impurity spectroscopy in fusion plasmas and plan for A3 collaboration
S. Morita (NIFS) 69

16. Atomic and molecular processes in fusion plasmas
D. Kato (NIFS) 79

17. Validation of ELM dynamics via 2D electron cyclotron emission imaging in KSTAR
H. K. Park (POSTECH) 83

18. Detection of the magnetic field structure using imaging diagnostics.
S. Ohdachi (NIFS) 87

19. Comprehensive understanding and control of edge localized modes in 2D and 3D toroidal plasmas
K. Toi (NIFS) 93

20. Energetic-particle diagnostics and physics in toroidal fusion plasmas
M. Isobe (NIFS) 99

21. Current research efforts of EP study in Korea
C. M. Ryu (POSTECH) 105

22. Development of MHD spectroscopy using energetic-particle-driven global modes in 2D and 3D toroidal plasmas
K. Toi (NIFS) 110

23. Recent progress of hybrid simulation for energetic particles and MHD
Y. Todo (NIFS) 116

24. Study on TAE-Induced fast-ion loss process in LHD
K. Ogawa (NIFS) 120

25. Quantitative analysis of carbon radiation in edge plasmas of LHD
C. F. Dong (NIFS) 126

26. Numerical MHD analysis of JET edge localised modes with ITER-like wall
O. J. Kwon (Daegu U.) 130

27. The recent research progress on the J-TEXT tokamak
Z. J. Wang (HUST) 136

28. Physics of energetic electrons and positrons in tokamaks
J. Liu (USTC) 142

29. EAST ICRF system for long pulse operation
Y.P. Zhao (ASIPP) 148

Program 152

List of Participants 156

Progress of the KSTAR experiments and perspective for ITER scientific researches

Yeong-Kook Oh on be half of KSTAR team and collaborators

National Fusion Research Institute, Daejeon, Korea

Email : ykoh@nfri.re.kr

KSTAR is a superconducting tokamak aiming to explore the long-pulse high beta confinement. In the 2012 experimental campaign, the duration of the H-mode flattop has been extended up to 16 s at 0.6 MA and plasma current level in H-mode reached at 0.9 MA by adopting the real-time plasma shape control and 3.5 MW neutral beam injection. The equilibrium operating space could be extended surpassing the n=1 ideal no wall limit with betaN and betaN/li up to 2.9 and 4.1, respectively. The pedestal formation and characteristics were investigated according to L- and H-mode transition and during the edge localized mode (ELM). As one of the ITER high priority research topics, exploring the ELM mitigation or suppression by applying n=1 or n=2 resonance magnetic perturbation (RMP) field or by injecting the supersonic molecular beam. The toroidal rotation changes were inspected for the ohmic and H-mode plasma by applying the ECH or 3D magnetic field. Various experimental researches were conducted according to the proposals including the disruption mitigation by using massive gas injection, fast ion loss detection under the edge perturbation, plasma wall interaction and others.

1. Introduction

The Korea Superconducting Tokamak Advanced Research (KSTAR) device has a mission to explore the scientific and engineering research under the high performance and steady-state plasma confinement, which are essential for ITER and K-DEMO [1]. The key designed parameters of the KSTAR are compared recent achievement in the table 1. The basic designed parameters are toroidal field (TF) of 3.5 T, plasma current of 2 MA, and pulse length up to 300 s. The plasma shape is single null or double null with elongation up to 2.0. The achieved parameters are plasma current up to 1 MA, normalized beta up to 2.9, plasma discharge up to 21s. The KSTAR device in the experimental hall is shown in figure 1.

KSTAR Parameters	Designed	Achieved in 2012
Toroidal field, B_0 [T]	3.5	3.5
Plasma current [MA]	2.0	1.0
Pulse length [s]	300	21
Normalized beta	5.0	2.9
Plasma shape	DN, SN	DN, SN
Major radius, R0 [m]	1.8	1.8
Minor radius, a [m]	0.5	0.5
Elongation, κ	2.0	1.9
Triangularity, δ	0.8	0.8
Plasma volume [m^3]	17.8	17.8
Plasma fuel	H, D	H, D
Superconductor	Nb_3Sn, NbTi	Nb_3Sn, NbTi
Heating /CD [MW]	28	~5.5

Table 1. Designed KSTAR parameters compared with achieved values in 2012 campaign

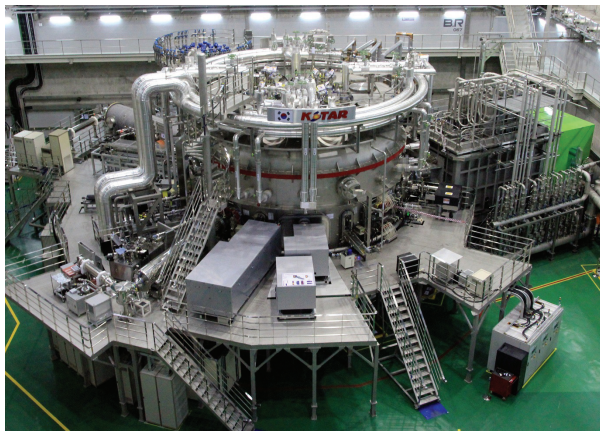

Fig. 1. The picture of the KSTAR device with installed heating and diagnostic systems in 2012

Key features of the KSTAR device for the high performance steady-state plasma researches are fully superconducting magnet system for the higher toroidal field and larger plasma current operation by using Nb_3Sn superconductor in TF and PF magnets as like as ITER magnets [2]. Other features for the high performance plasma control are passive stabilizer and in-vessel control coils (IVCCs) with 12 modules (4 arrays in toroidal and 3 arrays in poloidal) which have flexible controllability such as vertical and radial position controls, edge localized mode (ELM) control with resonant magnetic perturbation (RMP), field error correction (FEC), rotation control, or resistive wall mode (RWM) control. Figure 2 shows the in-vessel components including divertor and passive stabilizer and the IVCCs are shown in figure 3.

The KSTAR heating and current drive (H&CD) system contains the NBI, ICRF, ECH/ECCD, and LHCD systems [3]. The available beam power of NBI was 3.5 MW in 2012. The ICRF system with 2 MW source power at 30~60 MHz is under conditioning for the reliable power coupling into plasma. Three types of ECH/CD systems are in operation with various frequencies, 84 GHz, 110 GHz, and 170 GHz. Two ECH systems with 84 GHz and 110 GHz have a short pulse operation capability for about 2 s and were used for flux saving during the plasma startup. Another one is 170 GHz ECH/CD system with 0.7 MW and steady-state operation capability, which was developed for the ITER prototype. The diagnostic systems to supply the information of plasma for the analysis and control have been developed in collaboration with domestic and international collaborators. To study edge and pedestal physics, some diagnostics are dedicated for the profile measurements. Ion temperature and toroidal rotation profile variation according to the L- and H-modes were measured by X-ray imaging crystal spectrometers (XICS) and charge exchange spectroscopy (CES). To visualize and analyze the MHD instabilities, multi-chord fast frame detectors has been developed such as ECE imaging system (ECEI), beam emission spectroscopy (BES), and soft X-ray array (SXR). By the ECEI system the growth and burst of the edge localized filaments in H-mode could be visualized in two-dimension [2].

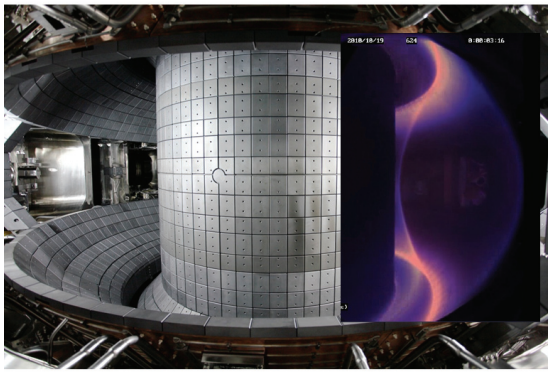

Fig. 2. The bird eye view of the in-vessel components including passive stabilizers and divertor.

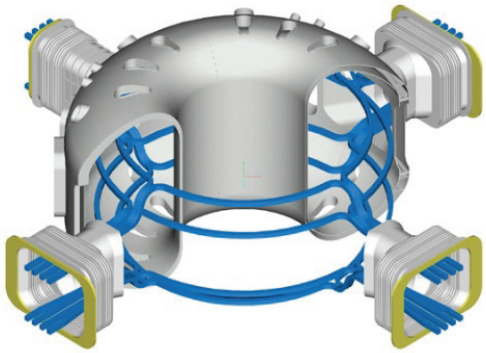

Fig. 3. The schematic view of the in-vessel control coils with 4 toroidal and 3 toroidal arrays.

2. Progress of the KSTAR experiments

Since the first plasma generation, the operation of KSTAR is dedicated to the development of operational capabilities for superconducting device with relatively short pulse. Brief history of the KSTAR experiments are; first plasma achievement in 2008 with plasma current at 108 kA, 1.5 T [3], first H-mode discharge in superconducting tokamak in 2010 at

0.6 MA [4], successful ELM suppression in 2011 by applying n=1 RMP [5], and extended H-mode at 0.6 MA up to 16 s in 2012.

In the 2012 experimental campain, real-time shape control task forth was launched to extend the H-mode plasma over 10 s to investigate various physics during the same plasma shot. To save the runtime, a magnetic control simulator, TOKSYS, was developed to find out the the target control logics. ISO-flux shaping could be achieved with accuracy within 2 cm. By properly controlled plasma shape and particle control, the pulse length of H-mode at the flattop was extended over 15s and 3.5s at 0.6MA and 0.9 MA, respectively as shown in figure 4. Typical ELMy H-mode discharges have been obtained in the KSTAR since 2010 [8]. Several H-mode characteristics have been investigated such as the L-H power threshold, characteristics of ELMs and confinement, and the inter-ELM pedestal profile evolution.

One of the urgent issues for ITER is to control the ELMs to meet the material requirements on diverter. KSTAR also showed three distinctive types of ELMy H-mode [6]: Several methods have been conducted such as resonant magnetic perturbations (RMPs), supersonic molecular beam injection (SMBI), plasma vertical jogging/kicking, and edge-localized current drive by ECCD [7]. Especially successful ELM suppression was achieved by applying the RMPs in n=1 as shown in figure 5 and n=2 types of non-axisymmetric magnetic perturbations. The ELM mitigation by SMBI was found with increased ELM frequency and loss energy per peak. The change in profile of density, temperature, and toroidal rotation according to ELM were observed from a CES and reflectometer. Detailed ELM dynamics were analyzed by visualization of the edge filaments from ECEI.

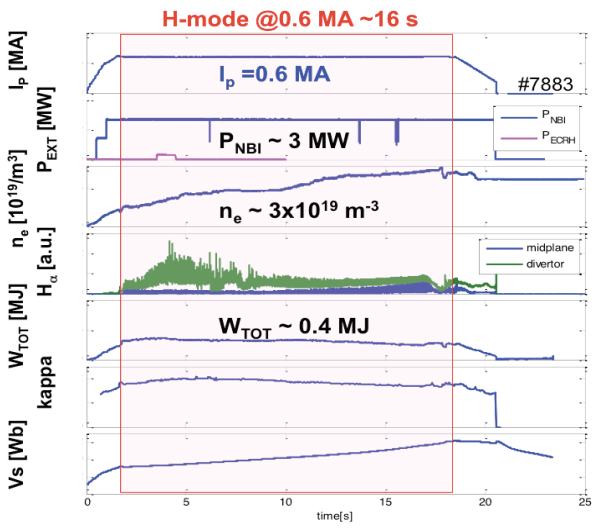

Fig. 4. Extended H mode plasma discharge up to 16 s at 0.6 MA

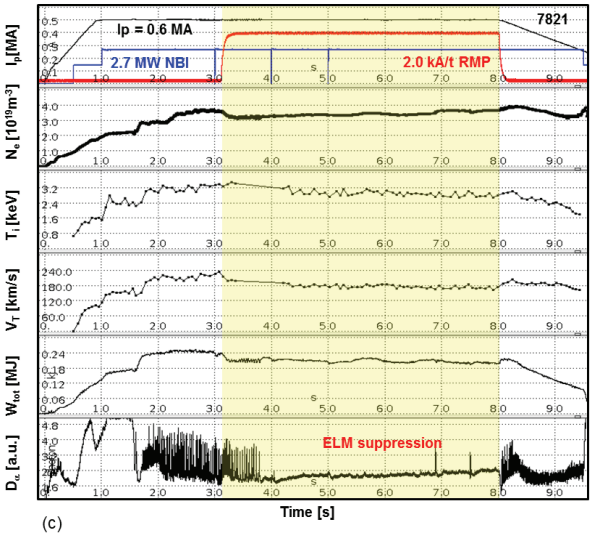

Fig. 5. Successful ELM suppression in KSTAR by applying n=1 RMP.

The operating regime expressed in stability relevant parameter space, normalized beta versus internal inductance (li, β_N) as shown in figure 6. The equlibria for the first H-mode achieved in 2010 are β_N = 1.3, li = 0.94. In 2012 the plasma β_N has reached 2.9 transiently, sustained β_N = 2.5 for programmed pulse lengths of 6 s. Plasma li were in the range of 0.65 to 0.8. The β_N/li exceeded 4 and surpassed the computed n = 1 ideal no-wall stability limit computed for H-mode pressure profiles, a key threshold defining advanced tokamak operation [8]. Other researches were conducted such as MHD instability analysis, plasma

wall interaction, disruption analysis, runaway electron, and other subject according to the experimental proposals.

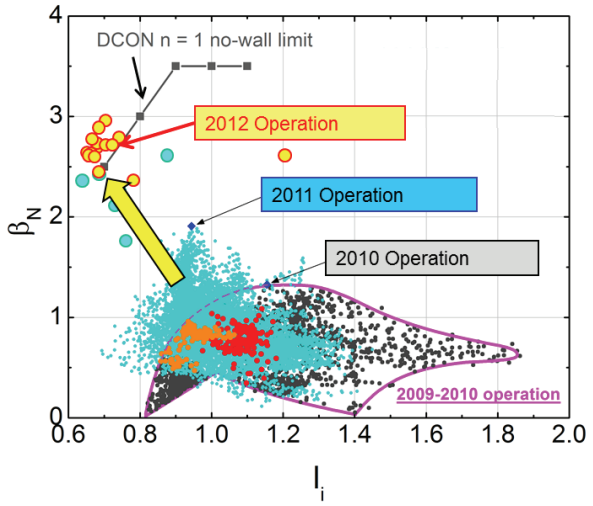

Fig. 6. KSTAR equilibrium and operating space surpassed the no wall limits. (Courtesy of Y.S Park and S. Sabbagh)

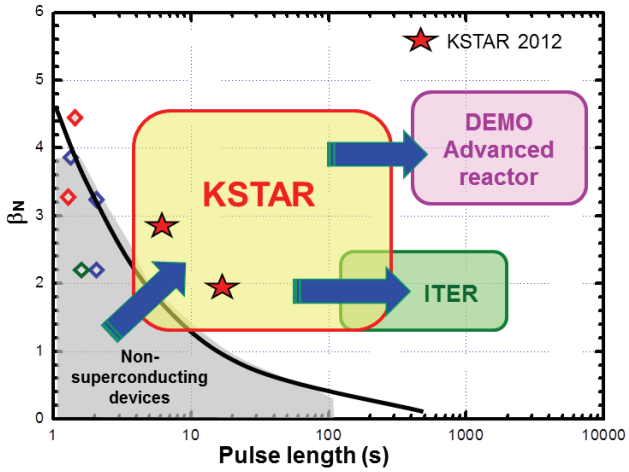

Fig. 7. The projection of the planned KSTAR operation space in normalized beta and pulse length.

3. Plan for next operation

The future researches will be concentrated on several topics, which are more urgent and relevant to ITER and DEMO due to the limited human resources. Expected key research topics are solving the ITER relevant and urgent physics issues such as ELM suppression by using the KSTAR intrinsic tools, 3-D physics, and disruption prediction, avoidance, and mitigation. And integrated operating scenarios will be developed in preparation for the advanced tokamak operation by utilizing the various type of heating systems.

In the next five year, plasma performance in KSTAR will be extended to H-mode operation at 2 MA for longer pulse about 50s. KSTAR will be an effective research device for exploring the scientific and technological breakthrough in preparing the era of ITER and DEMO as shown in figure 7.

Acknowledgement

This work was partly supported by the JSPS-NRF-NSFC A3 Foresight Program in the field of Plasma Physics (NSFC: No.11261140328).

References

[1] G.S. Lee, et al., *Nuclear Fusion,* **41** (2001) 1515
[2] G.S. Yun, et al., *Physics Review Letter,* **107** (2011) 045004
[3] Y.K. Oh, et al., *Fusion Engineering and Design*, **84** (2009) 344
[4] S.W. Yoon, et al., *Nuclear Fusion,* **51** (2011) 113009
[5] Y.M. Jeon, et al., *Physics Review Letter,* **109** (2012) 035004
[6] J-W. Ahn, et al., *Nuclear Fusion,* **52** (2012) 11400
[7] J. Kim, et al., *Nuclear Fusion,* **52** (2012) 114011
[8] Y.S. Park, et al., *submitted to Nuclear Fusion,* **53** (2013)

Recent Progress of MHD Study in Helical Plasmas

Satoru Sakakibara
National Institute for Fusion Science

1. Introduction

MHD instability is one of key issues for realization of economical fusion reactor because it limits an achieved beta value (ratio of plasma pressure of magnetic one) and terminates the plasma confinement. In tokamaks and RFPs, neoclassical tearing mode and resistive wall mode degrade the confinement of high-beta plasma, which sometimes leads to major disruption. Therefore, the development of the control techniques of their modes is ongoing. In helical plasmas, pressure driven modes such as interchange, ballooning modes and so on are key instabilities for maintaining steady state high-beta plasmas. Especially, in heliotron configuration such as Large Helical Device (LHD), since the interchange mode is easily destabilized even in low beta regime, the characteristics and the effect on confinement have been investigated for a long time. The linear MHD theory suggests that resistive interchange mode is always unstable in the periphery with magnetic hill, whereas ideal mode is destabilized in the configurations with weak magnetic shear and magnetic hill. Although the destabilization of ballooning mode is predicted in high-beta regime, there is no experimental evidence in the present beta range (~ 5%).

The recent progress of studies of resistive and ideal interchange modes is briefly summarized here. The final goal of this study is to find the common physics in helical devices and tokamaks through the comparison between observed instabilities in both devices. Obtained knowledge is expected to contribute the establishment of the stability control technique for the maintenance of steady-state plasmas.

2. Linear Stability Analysis

Figure 1 shows the unstable regions of ideal and resistive interchange modes in the configuration used for high beta experiments [1]. The D_I is the index of ideal interchange stability and the positive D_I means that the ideal mode is "unstable". The ideal mode excited in the core region is destabilized when the beta (and beta gradient) exceeds about 1 %, and stabilized by effects of magnetic well formation and the magnetic

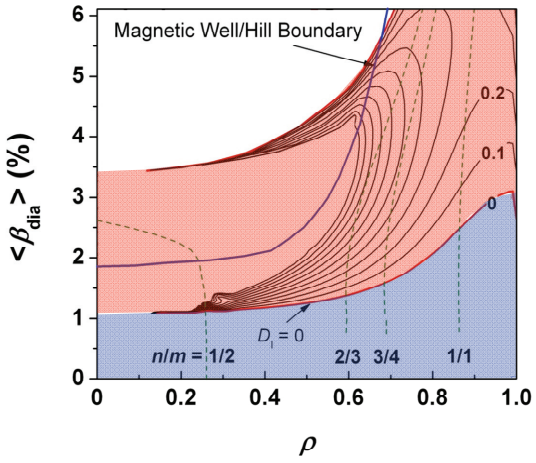

Fig.1 Unstable regions of resistive (blue) and ideal (red) interchange modes in the configuration selected for high beta experiments.

curvature. In the periphery, although the mode can be stabilized by strong magnetic shear in the low beta regime, it is destabilized by reduction of the shear as well as existence of the magnetic hill when the beta increases. The resistive interchange mode is predicted to be always unstable as far as the magnetic hill is formed, which suggests that the peripheral MHD activity is one of key subjects to get the high-beta state.

The changes of the growth rate and the radial structure of the m/n = 1/1 mode as a function of magnetic Reynolds number, S, are shown in Fig.2, which was calculated by FAR3D code [2]. When the ideal mode is stable ($D_I < 0$), the growth rate and the radial structure of the interchange mode are proportional to $S^{-1/3}$. However, when the ideal mode is unstable ($D_I > 0$) and D_I increases, the S dependence on the growth rate and the radial structure becomes weak with increasing S and are decided by the ideal condition with $S = \infty$. The growth rate in ideal unstable plasma is always higher than the ideal stable (resistive unstable) case and this tendency is enhanced in the high S regime. Here we define the modes observed in ideal stable (unstable) regime as the *resistive (ideal) interchange modes* for convenience. The actual experiments show that the mode grows and is nonlinearly saturated in many cases. However, verifying the validity of the prediction of linear theory is still important for design of the fusion reactor.

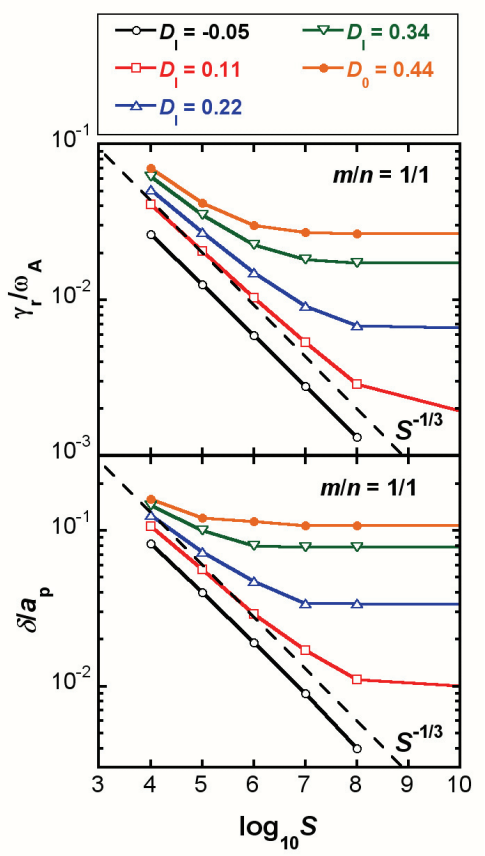

Fig.2 Changes of growth rate (upper) and radial structure (lower) of the interchange mode as a function of magnetic Reynolds number in different D_I conditions [2].

3. Characteristics of MHD modes observed in resistive unstable regime

Previous experiments clarify characteristics of the modes observed in resistive unstable regime. To clarify the parameter dependence of the onset of modes and to confirm that observed modes resonate with corresponding rational surfaces, the pressure gradient was controlled by using movable limiter [3]. Consequently, we found that the mode onset depends on D_R and S, which is qualitatively consistent with the theoretical model, where D_R is the stability parameter of the resistive interchange mode. Also, each mode is stabilized by reduction of the pressure gradient on the resonance due to insertion of the limiter. The high

beta experiments in the range of $<\beta> \leq 5$ % show that the amplitude of the mode is increased with the reduction of S and/or the increment of $<\beta>$ [2]. Especially, it was found that the mode amplitude is proportional to $S^{-0.355}$, which is almost the same as that of the linear growth rate of the resistive mode as shown in Fig.3. When the mode grows significant level in the low S regime, it causes profile flattening around the resonance and degrades the plasma confinement by about 10 % [4].

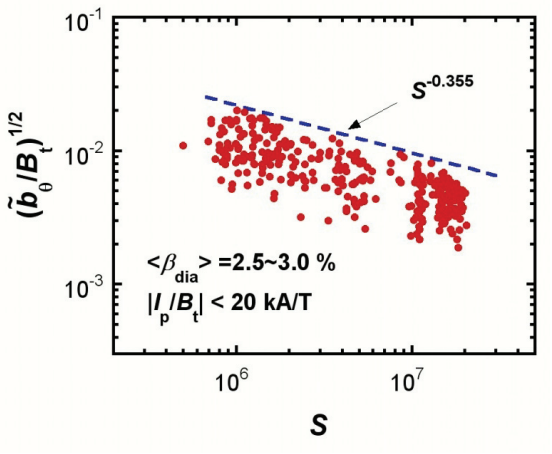

Fig.3 Change of amplitude of the m/n = 1/1 mode as a function of S. [2]

4. Characteristics of MHD modes observed in ideal unstable regime

In LHD, the ideal unstable plasma can be produced by shifting the magnetic axis, R_{ax}, to the inward and/or by reducing the magnetic shear. The inward shift of R_{ax} leads to an enhancement of the magnetic hill, whereas the magnetic shear can be decreased by the plasma current increasing the rotational transform and/or by controlling central position of helical coils. A lot of experiments were done in order to investigate the effect of ideal mode. The relationship between the prediction of low-n ideal MHD mode and actual operation regime was investigated in wide beta range [5], which shows that the operation regime was independent of Mercier criteria shown in Fig.1, it seems to be limited when the growth rate of the low-n ideal mode exceeded a certain value. In the inward shifted plasma, m/n = 2/1 mode in the core region appeared at the beginning of a discharge and affected the serious damage of the core pressure [6]. When the magnetic shear is reduced, the strong m/n = 1/1 mode was destabilized and led to the beta degradation by more than 50 % [7]. Figure 4 shows the amplitude of the radial component of m/n = 1/1 magnetic field on the $<\beta_{dia}>$ and magnetic shear diagram. The magnetic shear is defined as $(\iota_a-\iota_0)/\iota_a$, where ι_a and ι_0 are edge and central rotational transforms. The $\iota_a/2\pi$ is about 1.6 in the configurations selected in Fig.4, and ι_0 was changed by the helical coils and the plasma current. The m/n = 1/1 mode appeared in the weak magnetic shear regime, and the operation limit seems to be decided by the beta and the magnetic shear. This limit is qualitatively consistent with the ideal stability

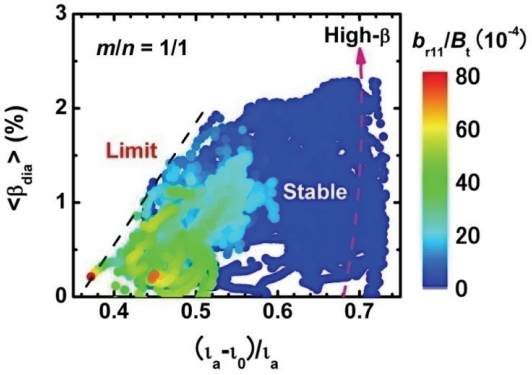

Fig.4 Amplitude of radial component of m/n = 1/1 mode on the beta and magnetic shear diagram.

boundary. Recent experiments show that the growth of the mode is sometimes observed with the mode locking [8]. The locking phenomena seem to be similar to tearing locked mode in tokamaks, whereas the mode has interchange type structure, at least, before the locking.

5. Future Plan

The LHD experiments clarify a lot of characteristics of the resistive and ideal interchange modes, and the details are reviewed in Ref.9. The quantitative estimation of stability parameters for the actual operation limit is one of remaining subjects and still ongoing. Although stellarators and heliotrons can avoid the risk of major disruption, the minor collapse in ideal unstable regime gives significant loss of core pressure. Therefore, the control of MHD activities in such unstable regime contributes the extension of operational capability and the increase of the degree of the reactor design. In the framework of A3 collaboration, we propose the comparative studies of the following subjects to deeply understand essential differences between current and pressure driven instabilities:

(1) Basic characteristics of interchange and tearing modes (onset, growth rate etc.)
(2) Mode locking phenomena (effect of the error field, mode structure etc.)
(3) Termination of MHD equilibrium due to major (minor) disruption

And also, the development of the stability control system for avoiding major (minor) disruption is one of key tasks to be established. We expect that the experimental knowledge obtained in the collaboration work contribute the maintenance of the stable plasma for a long time.

6. Acknowledgements

This work was partly supported by the JSPS-NRF-NSFC A3 Foresight Program in the field of Plasma Physics (NSFC: No.11261140328).

References

[1] M. Sato *et al.*, Proc. 22nd IAEA Fusion Energy Conference (13-18 Oct.2008, Geneva) TH/P9-18.
[2] S. Sakakibara *et al*., *Plasma Phys. Control. Fusion* **50**, 124014 (2008).
[3] S. Sakakibara *et al*., *Plasma Fusion Res.* **1**, 049 (2006).
[4] K.Y. Watanabe *et al*., *Phys. Plasmas* **18**, 056119 (2011)
[5] K.Y. Watanabe *et al*., *Nucl. Fusion* **45**, 1247 (2005).
[6] S. Sakakibara *et al*., *Plasma Fusion Res.* **1**, 003 (2006).
[7] S. Sakakibara *et al*., *Fusion Sci. Technol*. **50**, 177 (2006).
[8] Y. Takemura *et al*., *Nucl. Fusion* **52**, 102001 (2012).
[9] S. Sakakibara *et al*., *Fusion Sci. Technol*. **58**,176 (2010).

Progress on High Performance Long-Pulse Operations in EAST

H. Y. Guo[1*], J. Li[1], B. N. Wan[1], X. Z. Gong[1], Y.F. Liang[2], G.S. Xu[1], and the EAST Team[1]

[1] Institute of Plasma Physics, Chinese Academy of Sciences, Hefei 230031, P. R. China
[2] Forschungszentrum Jülich GmbH, Association EURATOM-FZ Jülich, Institut für Energie- und Klimaforschung - Plasmaphysik, Trilateral Euregio Cluster, D-52425 Jülich, Germany
* *E-mail contact of main author*: hyguo@ipp.ac.cn

ABSTRACT

Significant progress has been made in the Experimental Advanced Superconducting Tokamak (EAST) on both technology and physics fronts, achieving long pulse L-mode discharges over 400 s, entirely driven by Lower Hybrid Current Drive (LHCD), with improved plasma facing components, active Li gettering, cryopuming and flexible divertor configurations. High confinement plasmas, *i.e.*, H-modes, have been extended over 30 s with combined operation of LHCD and Ion Cyclotron Resonant Heating (ICRH). Various means for mitigating ELMs have also been explored to facilitate high power, long pulse operation in EAST, such as supersonic molecular beam injection, D_2 pellet injection, as well as innovative solid Li granule injection.

1. INTRODUCTION

The Experimental Advanced Superconducting Tokamak (EAST) was built to demonstrate high power, long pulse operations under fusion relevant conditions, with major radius R = 1.9 m and minor radius a = 0.5 m. Plasma current is presently limited to I_p = 1 MA and toroidal field B_T = 3.5 T with envisioned pulse length of 1000 s [1, 2]. EAST has ITER-like magnetic configurations and heating schemes, *i.e.*, dominated by electron heating from Lower Hybrid Current Drive (LHCD) and Ion Cyclotron Resonant Heating (ICRH), thus providing a unique platform to address plasma physics and technology issues for ITER and DEMO under steady-state operation conditions. EAST carried out an extensive upgrade during the last shutdown in 2011, from Plasma Facing Components (PFC), plasma control system, to auxiliary heating. In addition, a new pellet injection system and a Supersonic Molecule Beam Injection (SMBI) system have been newly implemented for ELM mitigation and fast density feedback control. With these augmented capabilities and control tools, EAST has recently demonstrated long pulse divertor operation over 400s, fully driven by LHCD with active-cooled PFC and divertor cryopumping in the 2012 spring campaign. Furthermore, high confinement plasmas, *i.e.*, H-modes, have been extended over 30 s [3]. This paper presents some highlights of these advances.

2. PROGRESS ON TECHNOLOGY FRONT

To ensure high power, long pulse operations, EAST has newly upgraded its first wall & in-vessel components. The machine was fully covered with graphite tiles in 2010. During the last

shutdown in 2011, the graphite tiles on the main chamber wall were replaced with molybdenum (Mo), but the divertor target plates remain covered with graphite, as shown in Fig. 1. All the PFCs are actively water cooled, which allows steady state operation with a maximum heat flux of 2 MW/m^2. In addition, an internal cryopump is located underneath the outer divertor target at the bottom of the machine with a pumping speed of ~76 m^3/s for D_2 and over 100 m^3/s for hydrogen to facilitate particle exhaust.

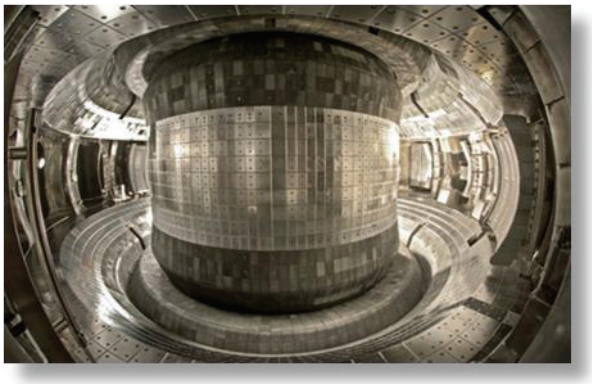

FIG. 1. In-vessel view of EAST with molybdenum PFCs on the main chamber wall and divertor target plates covered with graphite tiles.

Current drive and heating are predominantly provided by LHCD in EAST. The present LHCD system is operating at 2.45 GHz, with total power of 4 MW. In addition, EAST is equipped with an ICRH heating system with tunable frequency in the range of 20 to 70 MHz. The system consists of two double-strap antennas, each delivering 3 MW of power, total 6 MW. ESAT has a flexible plasma control system to enable various magnetic configurations and plasma shapes ranging from upper single null (USN), double null (DN) and lower single null (LSN) configurations with stable control of strike point locations on the divertor target plates, using the real time EFIT (RTEFIT) and Iso-flux control techniques. The poloidal field power supply and plasma control system have also been upgraded during the last shutdown to increase flexibilities and safety margins, thus significantly extend plasma operation regimes.

There are presently over 40 diagnostics on EAST. Many key diagnostics, such as Thomson scattering, interferometry, electron cyclotron emission and reflectometer have been completely refurbished and upgraded during the last shutdown, significantly improving diagnostic capability for the key profile measurements. In addition, two X-ray Crystal Spectrometers (XCS), polarimetry, and CO_2 Laser Collective Thomson Scattering (LCTS) have been developed to provide new information on ion and electron temperature profiles, toroidal and poloidal plasma rotation, current profiles, as well as turbulence structures in the core plasma. A large effort has also been devoted to the development of edge plasma diagnostics.

Recently, supersonic molecular beam injection (SMBI), and D_2 pellet injection at both low field side (LFS) and high field side (HFS) have been developed and applied in EAST for deeper fuelling and fast density feedback control. SMBI produces a rapid travelling gas jet with a speed exceeding 1 km/s and pulse length ranging from 2 to 20 ms. This leads to a much shorter density response time (2 – 4 ms), than the conventional gas puffing (16 ms and 77 ms for LHS and HFS, respectively). SMBI has been successfully employed as a fast density feedback tool to maintain plasma density for steady-state operations during the recent EAST experimental campaign. The pellet injection system produces frozen D_2 pellets of ~ 1 mm, which can be injected into the plasma from both outboard and inboard sides at midplane with a speed up to ~300 m/s at frequency up to ~10 Hz. The present pellet injection system is mainly used for core plasma fuelling. A second pellet injection system will be implemented in EAST in the near future with a higher frequency, up to 100 Hz, and faster speed, up to 500 m/s for effective ELM pacing. As

expected, pellet injection from HFS exhibits a higher fuelling efficiency with deeper penetration into the core plasma than from LFS, *i.e.*, 18-30% for LFS and 30-60% for HFS. The pellets from HFS appear to penetrate well inside the separatrix, viewing from a CCD camera. Pellet injection, especially from HFS, offers a stronger gas fuelling efficiency than SMBI and gas puffing, which have similar fuelling efficiency ~ 20%. Both SMBI and pellet injection have also been employed for active control of ELMs. Furthermore, an innovative Li pellet injection system with controllable speeds has also been implemented in EAST for ELM pacing.

To facilitate density control and reduce recycling for long pulse operation, a large effort has been devoted to the development of wall conditioning techniques suitable for superconducting tokamak operation, such as ICR conditioning and high frequency glow discharge cleaning (GDC) [4]. In particular, we have also explored various lithium (Li) coating techniques. In addition to conventional Li evaporation, we have applied ICR technique to Li GDC conditioning to improve the uniformity of Li coverage on the wall in the presence of toroidal magnetic fields. Furthermore, we have carried out real-time Li gettering with Li droplets. Li coating also provides a useful tool for controlling hydrogen concentration. The H to D ratio is typically about 50%, reducing to below 10% with Li coating, which is essential for effective ICRF heating and promotes H-mode access.

3. SCIENTIFIC ACHIEVEMENTS

3.1. 3D Magnetic Topology Induced by LHCD

LHCD appears to induce a profound change in the magnetic topology by driving currents in the edge plasma [5], as evidenced by the non-rotating Helical Current Filaments (HCFs) flowing along the magnetic field lines in the SOL, as shown in Fig. 2. HCFs induce a 3D distortion of the edge magnetic fields, as identified by Mirnov probe measurements. This leads to the splitting of divertor strike points (SP) with similar effects to the resonance magnetic perturbations (RMPs), which is clearly manifested by the striated heat deposition footprints on the divertor target plates. With LHCD, the heat flux spreads over a large area on the divertor target plate, up to 20 cm away from the separatrix, exhibiting a multi-peak structure. The change in edge magnetic topology has been qualitatively modelled by including HCFs in a field line tracing code with actually measured filament currents (~100's A), as shown in Fig. 2 as an insert. The code predicts that the magnetic parturitions induced by HCFs can extend

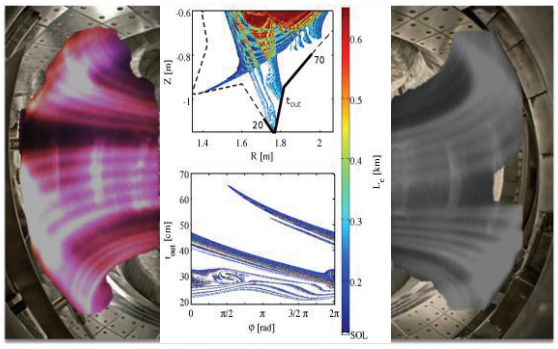

FIG. 2. Non-rotating helical radiating belts induced by LHCD in the plasma edge, seen by two visible cameras viewing different sides of the EAST torus (left and right); Contour of connection length of the expanded view of the bottom divertor region at toroidal angle, φ, equals zero degree (middle-upper) and calculated footprint on the outer divertor plate as a function of toroidal angle (middle-lower) for shot #29100 at 3.5 s with modeled HCFs.

inside the separatrix with some flux tubes near the X-point directly terminating on the outer divertor target plate, thus generating striated heat flux (SHF) footprints, in agreement with experimental observations.

The 3D edge topology induced by LHCD can be actively controlled by SMBI [6]. The application of SMBI reduces the peak heat flux near the strike point, while further enhances SHF, thus shifting power deposition from the primary strike point to the far SOL region. The amount of heat transferred from OSP to SHF increases with the SMBI pulse length.

3.2. ELM Control

LHCD tends to generate small ELMs, compared to the H-modes with similar ICRH power. This has been verified by modulating LHCD power; fast switching-on of LHCD (at 10 Hz with 50% duty cycle) appears to trigger small amplitude, high frequency ELMs, or even completely suppress ELMs.

Furthermore, we have explored various techniques for the active control of ELMs in EAST, including innovative solid Li pellet injection newly developed at PPPL [7], SMBI, D_2 pellet injection from both high field and low field sides, modulation of LHCD power, as well as conventional gas puffing.

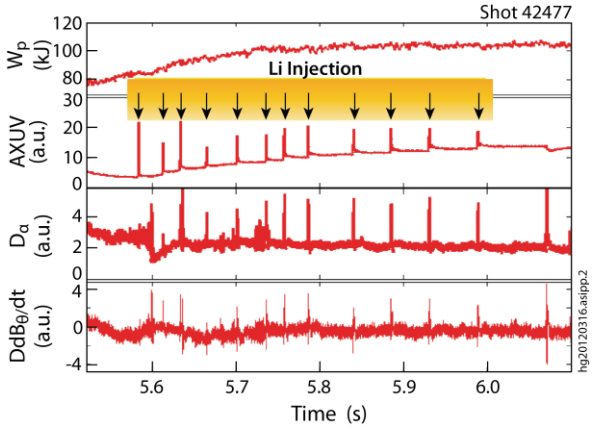

FIG. 3. ELM pacing in EAST using the new Li-injection technique with pellet size of 0.7 mm at 45 m/s. Each pellet triggers an ELM during ELM free phase after the L-H transition.

EAST has demonstrated, for the first time, ELM pacing using the innovative solid Li-pellet injection technique in H-mode plasmas. Small Li granules, ~ 0.7 mm, are injected from the outer midplane into the edge plasma using a rotary motor with a tunable velocity to actively control the depth of penetration. Figure 3 shows the time evolution of an H-mode discharge with the injection of Li granules during the ELM free phase, right after the L-H transition. The Li granules are injected into the plasma at a speed of ~45 m/s with a repetition rate of ~ 25 Hz. It appears that Li pellet injection is highly efficient at triggering ELMs, at nearly 100% efficiency. ELM mitigation with SMBI has also been demonstrated recently in EAST, achieving a quasi-steady state small ELM regime with a slight increase in density and little degradation in confinement [6]. SMBI appears to prevent the formation of large, low frequency ELMs, while triggering small, more frequent ELMs with a strong decrease in amplitude by a factor of ~3, and increase in frequency over a factor of 5 − 10.

3.3. Demonstration of Long Pulse Operations

Long pulse L-mode discharges over 400 s have been achieved in EAST, entirely driven by LHCD by carefully controlling heat exhaust and neutral recycling. Since the present steady-state power handling capability is limited to 2 MW/m^2, plasma configuration was varied from USN

via DN to LSN during the discharge with strike point sweeping to further improve power handling at the divertor target plates, thus minimizing divertor heat load, impurity influxes and plasma wall interactions under the steady-state condition. Real-time plasma control was also applied to maintain plasma shape to ensure effective coupling for LHCD.

The first high confinement plasma, *i.e.*, H-mode, was achieved in 2010 at marginal input power with Li coating. The H-mode has now been further extended with enhanced heating capacities during the recent EAST experimental campaign in the spring of 2012, achieving reproducible, long pule H-modes over 30 s, with combined LHCD with ICRH. Figure 4 shows a typical long pulse H-mode plasma discharge obtained under the double null (DN) divertor configuration in EAST. This particular discharge is dominated by small ELMs, as manifested by small amplitude oscillations on D_α emissions, with $H_{98,y2} \sim 0.9$, due to marginal auxiliary heating, with total injection power of ~ 2.5 MW from LHCD and ICRH. The H-mode duration is only limited by presently attainable discharge durations. Stationary type-I like ELMy H-modes with higher confinement quality have also been achieved in EAST by further increasing RF heating.

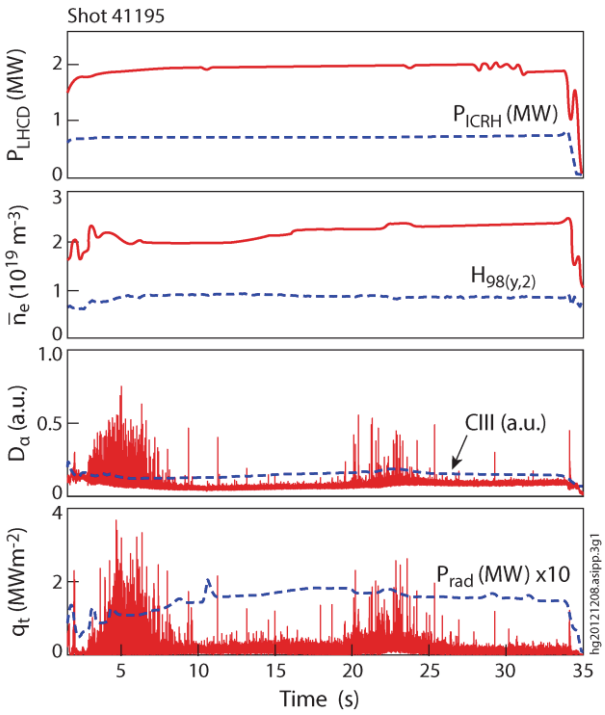

FIG. 4. Demonstration of a high confinement H-mode discharge over 30 s, driven by LHCD with additional ICRH. Data shown are the injected heating power from LHCD and ICRH, P_{LHCD} and P_{ICRH}, line average density, $\bar{n}_e$, H-mode confinement factor, $H_{98(y,2)}$, deuterium line emission, D_α, and carbon ion C^{2+} line emission, CIII, divertor target heat flux, q_t, derived from Langmuir probes, and radiated power, P_{rad}.

4. SUMMARY

EAST has started to demonstrate high performance, long pulse operation capability with improved PFCs, active Li gettering and cryopuming, together with new control tools such as SMBI, low/high field side pellet injection, and Li-pellet injection, achieving long pulse operation over 400 s, entirely driven by LHCD, and H-modes over 30 s with combined operation of LHCD and ICRH. EAST will be upgraded to more than 20MW CW H&CD and ITER-like W mono-block divertor, which will further broaden high power, long pulse operation space.

ACKNOWLEDGEMENT

The authors want to acknowledge support from the rest of EAST Team. This work is supported in part by National Magnetic Confinement Fusion Program under contract Nos. 2010GB104001 and 2010GB104002, as well as the JSPS-NRF-NSFC A3 Foresight Program in the field of Plasma Physics (NSFC No.11261140328).

REFERENCES

[1] Wan, Y.X., *et al*., *Nucl. Fusion* **40**, 1057 (2000).
[2] Wan, Baonian, *Nucl. Fusion* **49**, 104011 (2009).
[3] Li J. *et al* "RECENT PROGRESS ON EAST", *Fusion Sci. Technol*. (in press).
[4] G. Z. Zuo *et al*., *Plasma Phys. Control. Fusion* **54**, 015014 (2012).
[5] Y. Liang *et al*., "Magnetic Topology Changes Induced by LHW and Its Profound Effects on ELMs in EAST", *Phys. Rev. Lett*. (submitted, January 2013).
[6] X. L. Zou *et al*., "Divertor Power Deposition Control and ELM Mitigation with Supersonic Molecular Beam Injection in the EAST Tokamak", Presented at the 24th IAEA Fusion Energy Conference, San Diego, 8-13 October 2012.
[7] D. K. Mansfield *et al*., "First Observations of ELM Triggering by Injected Lithium Granules in EAST", Presented at the 24th IAEA Fusion Energy Conference, San Diego, 8-13 October 2012.

Simulation of turbulence in toroidal plasmas

—Concentrated on the study of multi-scale interaction using mainly gyro-fluid and gyro-kinetic code

Y. Kishimoto (岸本泰明)
Graduate School of Energy Science, Kyoto Universuty

I Introduction and motivation

An important aspect in ITER physics is the understanding of complex turbulence property in burning plasma to reduce the turbulent transport, which is always a central topic in the field. This is because fusion plasma is generally subject to various instabilities at differing spatio-temporal scales due to varied magnetic configurations and plasma profiles. The modern gyrokinetic theory is generally employed to develop first principle particle code using particle-in-cell method or continuum (Vlasov) code with advanced computational fluid dynamics (CFD) schemes. Such large-scale simulations are promoted by the high-per-formance parallelization. An amount of gyrokinetic codes have been applying in present tokamak and stellarator to-wards the ITER. On the other hand, the fluid (or gyrofluid) approach in 3D configuration is still helpful and has advantages to clarify the dominant physical processes and to scan the parametric dependence in a long time simulation, particularly for macro-scale MHD fluctua-tions. Hence, this work proposes both gyrofluid and gyrokinetic approaches to explore the cross-scale problem involving the MHD island dynamics and micro-turbulence. The attention is focused on the nonlinear interaction mechanism between different modes with different scales and EM features.

II Numerical simulation on complex nonlinear interaction of plasma turbulence

Multi-scale turbulence problem in fusion plasma is extremely complicated due to various instabilities distributed in wide spatio-temporal spectra, as schematically shown in Fig.1 [1]. It seems to be unfeasible at Multi-scale turbulence problem in fusion plasma is extremely complicated due to various instabilities distributed in wide spatio-temporal spectra, as schematically shown in Fig.1. It seems to be unfeasible at present to perform a full scale turbulence simulation covering all MHD activities, ion- and electron-scale micro-fluctuations as well as

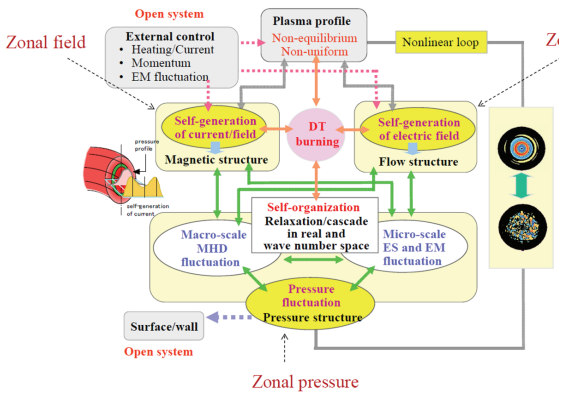

Fig.1 Schematic diagram of complex nonlinear

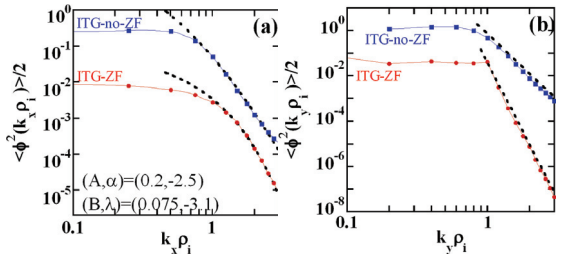

Fig.2 k_x (a) and k_y (b) spectra of both the ITG-no-ZF and the ITG-ZF turbulence. The dashed curves in (a) plot corresponding fitting functions $\langle\phi^2/2\rangle_P = Ak_x^{-\alpha}/(1+k_x^2)^2$ and $\langle\phi^2/2\rangle_E = Be^{-\lambda k_x}$. The dot straight lines in (b) are for reference.

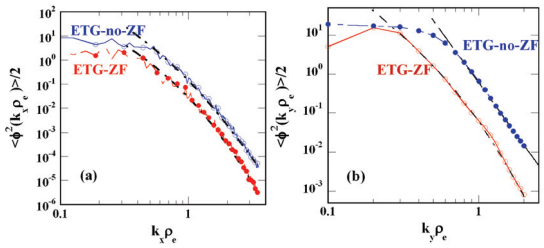

Fig.3 k_x (a) and k_y (b) spectra of both the ETG-ZF and the ETG-no-ZF turbulence. The dot-dashed curves matching with the spectra in ETG-ZF turbulence in both (a) and (b) plot corresponding best fitting functions $\langle\phi^2/2\rangle_P = Ae^{-\lambda k_{x,y}}k_{x,y}^{-\alpha}/(1+k_{x,y}^2)^2$ and the one to the ETG-no-ZF case in (a) corresponds to the best fitting function $\langle\phi^2/2\rangle_P = Ak_x^{-\alpha}/(1+k_x^2)^2$. The dashed straight line in (b) represents the power-law function $\langle\phi^2/2\rangle_P \propto k_y^{-\alpha}$ for reference.

the transport dynamics. While many efforts are being made to consistently involve non-adiabatic ion and electron responses over a transport time scale in a first principle gyrokinetic simulation, various simplified models that emphasize important physics processes in a relatively narrow spectral regime are also being proposed as a practical step. In this work, we perform simulations with individual scales like the MHD, ITG or ETG turbulence and the multi-scale combination with resistive MHD (RMHD) and ion-scale micro-fluctuation, namely RMHD+ITG, which aims at exploring the nonlinear interaction between magnetic island dynamics and ion-scale turbulence with zonal flows (ZFs).

II Gyro-fluid simulation of plasma turbulence

II(a) Turbulent spectra in the presence of zonal flows [2]

Experimental measurement of plasma flows and turbulence is of essential importance in transport and confinement study. Recently the diagnoses of the edge fluctuations and flows, including the zonal flows (ZFs) and geodesic acoustic mode (GAM) have been extensively carried out to characterize the formation of structures and to understand the suppression mechanism of the turbulent transport by sheared mean flows and ZFs. The spectral analysis is extensively applied to the investigation of nonlinear interaction processes through the basic three-wave coupling. Furthermore, the turbulence spectra are among the measurable quantities in experiments, which are generally diagnosed and analyzed to characterize the fluctuation and the coherent structures. We have analyzed the wave-number spectral properties of ITG and also ETG turbulence with a focus on the feedback reaction of large-scale structures (LSSs) including zonal flows and Kelvin-Holmheltz (KH) mode to the

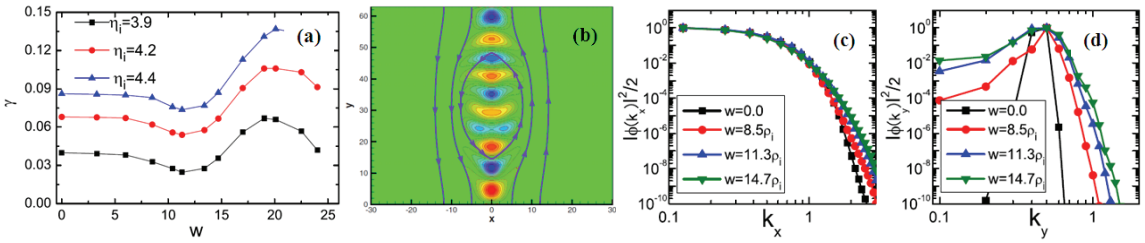

Fig.4 (a)Dependence of the linear growth rate γ of the system composed of all k_y harmonics on island width w for different η_i. (b) Typical contours of linear potential perturbations in the presence of the magnetic island with w=19 when $\eta_i = 4.2$. The thick streamlines with arrows represent the magnetic field lines. (c) and (d) Normalized spectra in the linear ITG/MITG mode in the cases with different island width w when $\eta_i = 4.2$.

ambient turbulence based on 3D gyrofluid simulations in a slab geometry. The comparison of the spectral scaling laws between ion/electron temperature gradient (ITG/ETG) driven turbulence is carried out. It is shown that the spectral scaling of the ITG turbulence with robust ZFs are fitted well by an exponential-law function $\langle \phi^2/2 \rangle_E \propto e^{-\lambda k_x}$ in k_x and a power-law one $\langle \phi^2/2 \rangle_P \propto k_y^{-\beta}$ in k_y, as shown in Fig.2. However, the ETG turbulence is characterized by a mixing Kolmogorov-like power-law and exponential-law $\langle \phi^2/2 \rangle \propto e^{-\lambda k_{x,y}} k_{x,y}^{-3} / (1+k_{x,y}^2)^2$ scaling for both k_x and k_y spectra due to the ZFs and KH mode dynamics as shown in Fig.3. Here λ and β are the slope index factors. The underlying physical mechanism is understood as the spectral scattering caused by the back-reaction of the LSSs on the ambient turbulence. These findings may provide helpful guideline to diagnose the plasma fluctuations and flow structures in experiments.

II(b) MHD island interaction with micro-turbulence: linear analysis[3-5]

MHD dynamics is generally a slow process on the Alfven time scale for the fluctuations with low mode number in low β plasmas, which is much longer than the time scale typical of ion's and electron's dynamics. Hence it is hard to numerically incorporate full kinetic electron response in multi- scale turbulence simulation with MHD fluctuation due to light electron mass. To investigate the MHD influence on micro-turbulence and transport, a simplified model mainly including essential MHD dynamics and ion-scale turbulence is principally feasible. As the first step of the study of the multi-scale turbulence, we numerically examine the new characteristics of ITG mode in the presence of a magnetic island. It is found that when the magnetic island is wide enough to produce a broad distribution of rational surfaces near the O-point region, the ITG perturbations at these rational surfaces form a radially global-type eigenmode with a fast growth rate, which is referred to as the magnetic-island-induced ITG (MITG) mode, as shown in Fig.4(a) and (b).

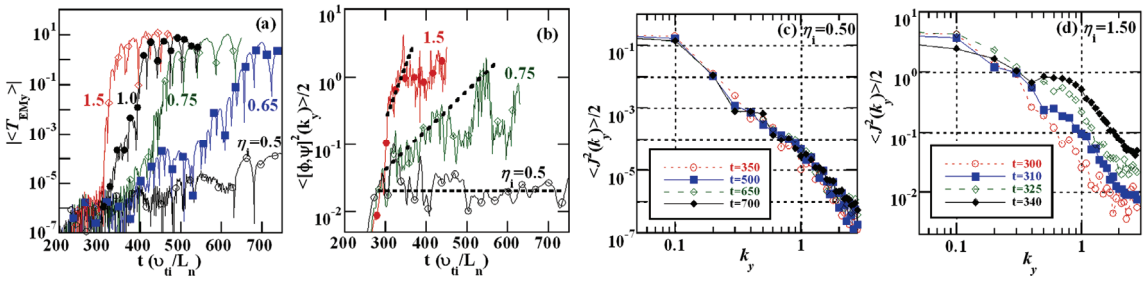

Fig.5 Evolution of the cross-scale dynamo action versus ITG turbulence intensity. (a)-(d) corresponds to the averaged EM torque amplitude $|T_{EMy}|$; dynamo driving intensity $<[\phi,\psi]^2(k_y)>/2$ for a representative of $k_y = 0.7$; and the k_y spectra of fluctuating current for different ITG driving force.

Moreover, the magnetic island also causes both radial and poloidal mode couplings, which play a stabilizing role, as shown in Fig.4(c) and (d).

II(c) MHD island interaction with micro-turbulence: Cross-Scale Dynamo Action [6]

To investigate the MHD influence on micro-turbulence and transport, a simplified model mainly including essential MHD dynamics and ion-scale turbulence is employed. Taking the resistive tearing mode and the ion temperature gradient (ITG) driven drift wave instability as the example of the EM MHD and ES micro-turbulence, respectively, the multi-scale multi-mode nonlinear simulation is performed based on a 5-field gyrofluid model to study the energy exchange mechanism between ES and EM turbulence in a tokamak plasma. The simulation is performed using an initial value code with a focus mainly on the island dynamics. A prominent magnetic island oscillation is commonly observed in the final nonlinear stage with a fully reconnected island (namely, with larger tearing instability parameter Δ'), showing a dynamic quasi-steady state. The island oscillation is visualized by a movie of island evolution, and much more clearly, by snapshots of the dominant flux component $m = 1$. The oscillation occurs as pivoting along the singular surface like a seesaw (referred to hereafter as an *island seesaw*). This proposes a new concept of *cross-scale dynamo action* induced by micro-turbulence, which is shown to be responsible for an island seesaw oscillation pivoting around the singular surface in multi-scale ES and EM turbulence. A turbulent cross-scale dynamo action is excited due to the micro-scale ES turbulence in a nonlinearly interacting MHD and ITG turbulence, as shown in Fig.5. The turbulent dynamos are evidenced by an oscillatory magnetic island dynamics, which is referred to as the island seesaw. It is found that the threshold of the dynamo action depends on the intensity of micro-turbulence. This mechanism offers a new energy exchange channel between multi-scale MHD and ES micro-fluctuations in an EM plasma environment.

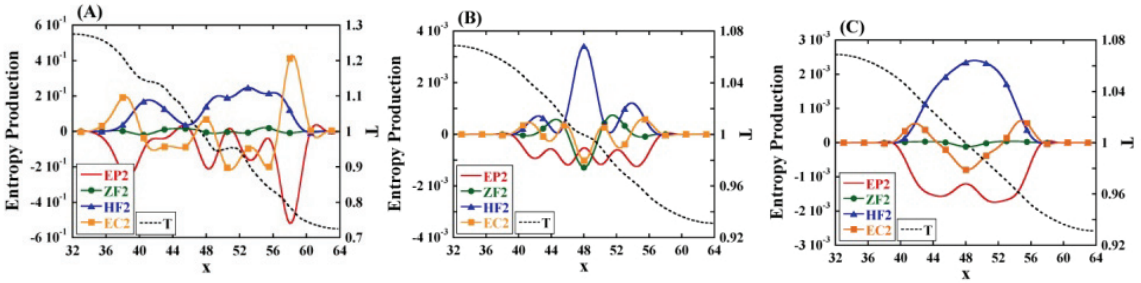

Fig.6 Spatial profile of each term of Eq. (1) in the cases with (a) $L_T(x)=37$ and (b) $L_T(x)=148$ in ITG turbulence and (c) $L_T(x)=148$ in ETG turbulence. The temperature profile is also illustrated.

III Gyro-kinetic simulation of multi-scale turbulence: turbulent transport and structure formation [7,8]

Turbulent transport in magnetically confined fusion plasmas exhibits various prominent features characterized by different time and spatial scales. Zonal modes, such as zonal flow and pressure, which are poloidally and toroidally symmetric macro-scale structures nonlinearly generated from micro-scale turbulence, are found to play an important role, regulating turbulent transport and structure. In order to investigate such dynamics, we extend the entropy balance equation by keeping the dynamics in radial direction as $\frac{\partial}{\partial t}\int s^{(2)}dZ^3+\frac{\partial}{\partial x}\int\left(-\frac{\partial\Phi}{\partial y}\right)s^{(2)}d^3Z+\frac{\delta U_{(0,0)}}{2L_T}-\frac{\delta Q_{(0,0)}}{2TL_T}=0$. We have investigated the entropy dynamics in ion temperature gradient (ITG) and electron temperature gradient (ETG) driven turbulence by using the global gyrokinetic Vlasov simulation in slab geometry. The spatial profiles of the first (EP2), second (EC2), third (DF2) and fourth (HF2) terms in the right hand of Eq. (1) in the cases with (a) $L_T=37$ and (b) $L_T=148$ in ITG turbulence and (c) $L_T=148$ in ETG turbulence and the temperature profile are shown in Fig.6, respectively. It is found that the relaxation is dominated by avalanche-like front propagation in the ITG turbulence with steep temperature gradient (Fig. 6(A)). The perturbed entropy convection, which corresponds to turbulent spreading, plays an important role. On the other hand, in the ITG case with gentle gradient, the second order heat flux shows a strong correlation with the zonal flow production and then a self-organized relaxed state is established, which is characterized by a spatially corrugated short wavelength zonal pressure (Fig. 6(B)). We found that the wave number and phase of the zonal pressure are regulated by the zonal flow shear. The contribution of the zonal flow becomes weak in the ETG case, as can be seen from Fig. 6(C), and the global profile relaxation can take place. Thus, the zonal flow plays an important role to regulate the turbulent transport in the ITG turbulence, depending on the temperature scale length. The global scale length may be determined by source and sink terms, which needs to be further investigation in future.

IV Future plan

The gyrokinetic Vlasov code is being advanced to simulate full kinetic ion and electron dynamics on equal foot in the slab geometry and also to approach to a realistic tokamak toroidal configuration. The multi-scale turbulence covering the MHD scale and micro-scale and associated turbulent transport will be investigated. The code verification and simulation validation again the experiments will be performed through the collaboration under the A3 program.

Acknowledgements

This work was partly supported by the JSPS-NRF-NSFC A3 Foresight Program in the field of Plasma Physics (NSFC: No.11261140328).

References

[1] E.J. Doyle, et al., Y. Kishimoto, et al., Nucl. Fusion 47(6), S18 (2007)

[2] Jiquan Li and Y. Kishimoto,]Wave-number spectral characteristics of drift wave micro-turbulence with large-scale structures, Plasma Science & Tech., 13(3), 297-301 (2011)

[3] Z. X. Wang, J. Q. Li, J. Q. Dong, and Y. Kishimoto, Phys. Rev. Lett. 103, 015004 (2009)

[4] Z. X. Wang, J. Q. Li, J. Q. Dong, and Y. Kishimoto, Phys. Plasmas 18, 012110(2011)

[5] Z. X. Wang, J. Q. Li, Y. Kishimoto, and J. Q. Dong, Phys. Plasmas 16, 060703 (2009)

[6] Jiquan Li and Yasuaki Kishimoto , Small-scale dynamo action in multi-scale magnetohydrodynamic and micro-turbulence, Physics of Plasmas 19, 030705 (2012)

[7] Kenji Imadera, Yasuaki Kishimoto, Daisuke Saito, Jiquan Li, Takayuki Utsumi, A numerical method for solving the Vlasov－Poisson equation based on the conservative IDO scheme, Journal of Computational Physics228, 8919－8943 accepted (2009)

[8] Kenji Imadera, Y. Kishimoto and Jiquan Li, Global Profile Relaxation and Entropy Dynamics in Turbulent Transport, Plasma and Fusion Research: Rapid Communications 5, 019 (2010)

Boundary conditions for ion speed in a two-ion-species plasma with finite ion temperature

Nong Xiang

Institute of Plasma Physics, Chinese Academy of science, Hefei, Anhui 230031, P.R.China

Abstract:

It is well known that the ion flow velocities at the sheath edge in a plasma with two warm ion species should satisfy
the Bohm criterion. To determine the ion flow velocity of each ion species at the sheath edge, one more condition is required. In this work
the second constraint for the ion flow velocities at the sheath edge is obtained analytically provided the collisions and ionization
can be neglected in the presheath. The ion flow velocity at the sheath
edge for each ion species can thus be determined. It is shown that the deviations of the flow speeds of two ion species from each
individual sound speed mainly come from the differences in the ion temperatures and the flow speeds at which the two ion species
enter the presheath.

I.Introduction

Determining the ion velocity at the presheath-sheath interface is not only of interest inunderstanding the physics of plasma-sheath transition, but for practical needs such as providing the boundary conditions to solve the fluid equations which have been found many applications in the fields of plasma physics. For instance, in fusion devices, it is often needed to find out the particle and heat flux transferred from the plasma interior to the wall. In the collisionless limit, for a plasma with one single ion species, it is well known that ions enter the sheath-plasma interface at the Bohm velocity. For a multiple-ion-species plasma, the situation becomes much more complicated. It has been shown that the Bohm criterion for the ion flow velocities at the sheath edge can be expressed as a hyperbolic function of the squares of the ion flow speeds [1]

$$\sum_j \frac{Z_j N_j}{m_j V_j^2 - \nu T_{j,0}} \le \frac{1}{T_e}$$

Here the index j represents ion species, Z_j and N_j are the charge number and density ratio for each ion species, respectively.
Vj is the flow velocities of each ion species at the sheath edge. T_e and $T_{j,0}$ are the electron and ion temperatures, respectively.
γ is the "polytropic coefficient" which depends on the flow conditions. In such a plasma, the system acoustic wave speed.

The ion flow velocity for each ion species at the sheath edge cannot be determined by the Bohm criterion alone. We need to find out other condition to determine the flow velocity for each ion species. The boundary conditions for ion flow velocity at the sheath edge in a two ion species plasma have been intensively studied in recent years [2-[10]. If the temperatures of two ion species are much smaller than the electron temperature, the conclusion has been drawn from fluid as well as kinetic treatments that each ion species enters the sheath-plasma interface at each individual sound speed if the ion-ion two stream instability is absent [2,8,10]. In this case, as argued in ref.[8], the non-dimensional Vlasov equations with the velocity normalized to each individual sound speed for both ion species become the same provided the ionization and collisions are neglected. So are theresulting ion momentum equations. The experimental measurements, however, suggest the existence of the case where the two ion species enter the sheath-plasma interface at the common sound speed [3,4,7] The theoretical model is then proposed which attributes the same ion flow velocity at the sheath edge to the enhanced ion-ion collisions due to the two stream instability [5,6,9]. The recent experimental result seems to support the theory[7]. However, both the fluid modeling [8] and the kinetic modeling [10] present cases where ion-ion two stream instability does not play a role and each ion species enters the sheath at each individual sound speed.

II. Governing equations

The plasma considered consists of the electrons and two species of positive ion. We assume that the ion temperature of each ion species is uniform. The fluid equations for ions in the steady state are:

$$\frac{\partial}{\partial x}(n_j V_j) = R_j \qquad (1)$$

$$V_j \frac{\partial V_j}{\partial x} = -\frac{Z_j e}{m_j}\frac{\partial \phi}{\partial x} - \frac{\nu T_{j,0}}{m_j}\frac{\partial n_j}{\partial x} - \gamma_j V_j \qquad (2)$$

The standard notation is used in the above equations. The index j= 1,2, corresponds to the two ion species. φ is the electric potential. Rj is the source term of ions. The last term on the RHS of eq.(2) represents the collisions between each ion species with neutral particles. The electrons are assumed to be in the Boltzmann distribution.

The normalized ion momentum equation is written as

$$u_j \frac{\partial u_j}{\partial z} = -\frac{\partial \Phi}{\partial z} - \frac{T_j}{N_j}\frac{\partial N_j}{\partial z} - \bar{\gamma}_j u_j \qquad (3)$$

In the plasma region, the ionization and collisions are important. They can be neglected in the sheath. The transition region connecting the plasma and sheath is referred as the presheath region. For a plasma with one ion species, it is well known that the sheath region can be disconnected from the bulk plasma region by providing an appropriate boundary condition for the sheath. However,

as shown in the paper, this is not necessarily true in a plasma containing two warm, positive ion species. Apparently, the flow speeds are different in the bulk plasma region if the ion temperatures and frictions are different. We can show that if the difference is significant, the ion flow speeds at the sheath edge are affected. Now let us consider the solution in the presheath. In the presheath, we assume that both the ionization and collisions can be neglected. By eq.(3) one obtains,

$$(u_j - \frac{T_j}{u_j})\frac{\partial u_j}{\partial z} = -\frac{\partial \Phi}{\partial z} \quad (4)$$

Integrating eq.(4), we obtain

$$\frac{u_2^2}{2} - \frac{u_1^2}{2} - T_2 \log(u_2) + T_1 \log(u_1) = S_0 \quad (5)$$

Where $S_0 = \frac{u_{2,0}^2}{2} - \frac{u_{1,0}^2}{2} - T_{2,0} \log(u_{2,0}) + T_1 \log(u_{1,0})$

Hence the value of S_0 depends on the ion flow velocities at the presheath edge. As demonstrated, S_0 is not necessarily negligible. To find out the value of S_0 the fluid equations in the plasma region should be solved which usually needs a numerical approach. However, it is possible that S_0 can be measured experimentally. The plasma-presheath interface is practically hard to define. Since S_0 is a constant in the presheath, we can choose any place in the presheath to evaluate S_0 by finding out its maximum and minimum values for given ion temperatures. In a collisionless presheath, the ion velocity should be greater than its thermal velocity in the presheath. Meanwhile, it should be smaller than the ion sound speed . The maximum and minimum values of S_0 for a given T1 are plotted in fig.1. One can see that S_0 decreases with the difference of the ion temperatures and is much smaller than unity as the ion temperatures are comparable to the electron temperature.

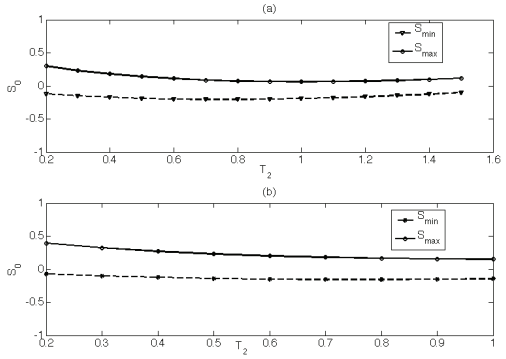

Fig.1. Maximum and minimum values of S_0 as a function of T2 for a given T1.

The Bohn criterion is written as

$$\frac{N_1}{u_1^2 - T_1} + \frac{N_2}{u_2^2 - T_2} = 1 \quad (6)$$

The ion flow velocity of each ion species is thus determined by eqs.(5) and (6). Apparently, the solution depends on the ion flow velocities at the presheath-plasma boundary. The smaller the difference between u_1 and u_2 is, the smaller S_0 is. A special case is that $u_{1,0} = u_{2,0}$ and $T_1=T_2$. It is evident that the normalized ion momentum equations for the two ion species are the same, and so are the boundary conditions. Thus, $u_1=u_2$. This is true not only at the sheath edge, but through the whole sheath. At the sheath edge, $V_1=V_{1B}$. $V_2=V_{2B}$ This indicates that the each ion species enters the sheath at each individual Bohm velocity.

To find the analytical solution, we assume that the ion flow velocities at the sheath edge do not deviate significantly from each individual sound speed, i.e, setting $u_1= C_{s1}+ X_1$ and $u_2= C_{s2}+ X_2$ with $|X_1| <<1$ and $|X_2| << 1$. By linearizing eqs.(5) and (6), we have

$$u_1 = C_{s1} - \frac{N_2}{2C_{s1}P_0 + C_{s1}/C_{s2}N_1 + C_{s2}/C_{s1}N_2} P_0 \qquad (7)$$

$$u_2 = C_{s2} - \frac{N_2 P_0}{2C_{s1}^2/C_{s2}P_0 + C_{s1}^2/C_{s2}^2 N_1 + N_2} + P_0 \qquad (8)$$

P_0 depends on ion temperatures and S_0. Clearly, the deviations of the flow speeds of two ion species from each individual sound speed mainly come from the differences in the ion temperatures and the flow speeds at which the two ion species enter the presheath. If the differences vanish, each ion species enters the sheath at each individual sound speed.

To illustrate the parameter dependence of the ion flow velocities, we neglect the first term containing P_0 in the denominators of eqs.(7) and (8) ,

$$u_1 = C_{s1} - \frac{\sqrt{(1+T_1)/(1+T_2)}N_2}{(1+T_1)/(1+T_2)N_1 + N_2}(Q_0 + S_0) \qquad (9)$$

$$u_2 = C_{s2} + \frac{N_1}{N_1 + (1+T_2)/(1+T_1)N_2}(Q_0 + S_0) \qquad (10)$$

Comparison of the analytical solutions given by eqs.(9) and (10) and the numerical solutions of eqs(5),(6) is shown in fig.2 and good agreement is obtained.
By eqs. (9) and (10), the deviation of the ion velocities depends linearly on
$Q_0 = 0.5\sqrt{1+T_2}[(T_1 - T_2) + T_2 \log(1+T_2) - T_1 \log(1+T_1)]$
which is a constant for given T1 and $T2, and on S0 which depends on the boundary condition at presheath-plasma interface.

As an example of application, now we discuss the effects of non-zero S0.
For cold ions, S0 = $0.5(u^2_{2,0} - u^2_{1,0})$ and it is usually ignored in the theoretical literature. We consider an Ar+ Xe+ plasma as discussed in refs.[7] and [9],

The electron and ion temperatures are Te = 0.7ev and $T_1 = T_2 = 0.04$ev. In this cae, $C_1 = C_2 \sim 1$. Note that $u_{1,0}$ and $u_{2,0}$ are not necessarily equal, which can be observed in fig.4 of ref.[7]. In this case, the Argon ion concentration N1 = 0.48 in

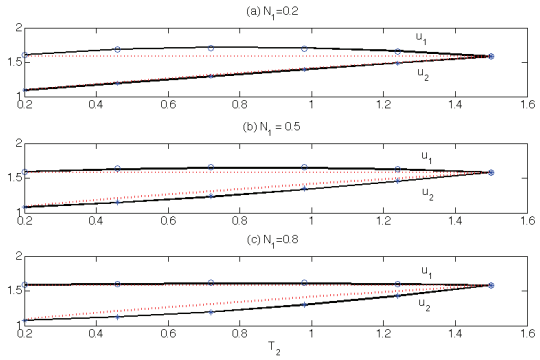

Fig.2. Comparison of u1 and u2 as a function of T2 by taking T1 = 1.5 for different ion concentrations (a) N1 = 0.2, (b) N1 = 0.5 and (c) N1 = 0.8. Analytical solutions are shown as the two solid lines while the numerical solutions are indicated by circles and stars. Each individual ion spund speed is marked by the red dotted line.

the bulk plasma, and the sheath edge is roughly located near z = 0.27cm. S0 at different locations can be calculated by reading the ion flow speeds of Ar+ and Xe+ in the figure are approximately equal to 0.49,0.45,0.42,0.42,0.36 at z = 0.27cm,0.3cm,0.4cm,0.5cm and 0.7cm, respectively.
Considering the measurement accuracy, S0 is nearly a constant in the region from z = 0.5cm to the sheath edge. This indicates the conservation of the ion kinetic energy in the region. Taking S0 = 0.42 and N1 = 0.48,
Eqs.(5) and (6) can be solved numerically. We obtain V1 = 1136 m/s and V2 = 920 m/s. For S0 = 0.5, we obtain V1 = 1159 m/s and V2 = 958 m/s. The measured ion flow speeds of Ar+ and Xe+ ions at the sheath edge are V1 ~ 1100 m/s and V2 ~940 m/s, respectively (ref.[7]) . Therefore, very good agreement is obtained between the theoretical and experimental results.

III. Summary

The ion flow velocities at the sheath edge in a plasma with two warm ion species are studied. If the ionization and collisions can be neglected in the presheath, the modified energy conservation equations for ions are derived from which the flow velocities of two ion species are related to each other. Combining this condition with the Bohm criterion, the ion flow velocity for each ion species can be determined and the analytical expression is derived. It is shown that ion flow velocities at the sheath depend on the relative ion concentrations, electron and ion temperatures. and in addition, on the ion flow velocity at which each ion species enter the presheath. The deviations of the flow speeds of two ion species from each individual sound speed mainly come from the differences in the ion temperatures and the flow speeds at which the two ion specie enter the presheath. If the differences vanish, each ion species enters the sheath at each individual sound speed. This is in the agreement with the PIC simulation result.

For a plasma containing two cold ion species, it is shown that the flow speed of each ion species at the sheath edge is determined by the flow speeds at the presheath edge. Even in the absence of the ion-ion two stream stability, the obtained deviations of the ion flow speeds from each individual sound speed in an Ar-Xe plasma are consistent with the experimental measurements.

Acknowledgment : This work is supported partially under the JSPS-NRF-NSFC A3 Foresight Program in the field of Plasma Physics (NSFC : No.11261140328).

References

[1] K.-U. Riemann, IEEE Trans. Plasma Sci. 23, 709 (1995).
[2] R. N.Franklin,{ J.Phys.D}, { 33}, 3186 (2000), {34}, 1959 (2001), {36}, R309 (2003).
[3]Wang X and Hershkowitz N., Phys.Plasma, 13, 053503 (2006)
[4]D. Lee, N. Hershkowitz, and G. D. Severn, Appl. Phys. Lett. 91, 041505 (2007).
[5]S. D.Baalrud, C. C Hegna, and J.D. Callen, Phys.Rev.Lett., 103, 205002 (2009).
[6]S. D.Baalrud , J.D. Callen, and C. C Hegna, Phys.Plasma, 17, 055704 (2010).
[7]Chi-Shung Yip, N. Hershkowitz, { Phys.Rev.Lett.},{ 104},225003 (2010).
[8] Xiang Nong, Hu Yemin, and Ou Jin, Plasma Sci. Technol. 13, 385(2011).
[9]S. D.Baalrud and C. C Hegna, Phys.Plasma, 18, 023505 (2011).
[10] J. T. Gudmundsson and M. A. Lieberman, Phys.Rev.Lett., 107, 045002(2011).
[11] S. Azuma, A. Fukuyama, and T. Takizuka, Contrib. Plasma Phys. 52, 512(2012).

Diagnostics upgrade and capabilty available for physics study on EAST tokamak

*Liqun Hu, on behalf of EAST diagnostic team and collabrators**
Institute of Plasma Physics, Chinese Academy of Science, P.O. Box 1126, 230031, China
Email of the responsible person: lqhu@ipp.ac.cn

Abstract: as a consequence of employment of many new techniques and upgrade of EAST superconducting tokamak to enhance divertor plasma performance, significant achievement has been realized in 2012, including 400s long pulse plasma, stationary 35s H-mode and 3.45s H-mode with only ion cyclotron resonant heating (ICRH) etc. To approach steady-state (SS) operation of high-performance plasmas and address key physics on fusion reactor-relavent subjects, recently, capabilty of the plasma heating and current drive of EAST machine are doubled with total auxiliary injection power over 20MW, including new methodology of neutral beam injection (NBI) and electron cyclotron resonant heating (ECRH). Most diagnostics have been upgraded to be more compact and integrated due to limited port window and space available, and new advanced neutral-beam related diagnostics have been developed as well, to provide profile of all key parameters for study and understanding critcal issues specific to SS high performance plasma.

Keywords: plasma diagnostics, plasma physics, tokamak

PACS: 52.70.–m, 52.25.-b, 52.55.Fa

1. Introduction

EAST (Experimental Advanced Superconducting Tokamak) device is aimed to achieve steady-state (SS) high-performance plasma sustained by intensive use of radio frequency heating and current drive, and to study relevant physics and technology. The initial three campaigns (2006-2008) addressed the feasibility of the full superconducting magnets and control algorithm with new features to explore some critical issues relating to steady-state operation with shaped plasma configurations [1-3]. From the third to the fifth campaign (2008-2010), modification of in-vessel structures and plasma facing components (PFCs), such as employment of full graphite wall with active water cooling and internal cryo-pump, utilization of new facilities like low hybrid current drive (LHCD) and ICRF, optimized configuration real-time feedback control, optimum wall conditioning techniques etc., had made the EAST machine into routine step-way of the physics experiment, repeatable long divertor plasma discharges with 0.25MA/60s, 0.25MA/8s fully non-inductive current driven by 1MW LHW had been obtained [3-6]. In the 6^{th} campaign 2010, 1MA/10s plasma sustained by 1MW LHW, repeatable long divertor plasma discharges with 0.25MA/100s and 0.7MA plasma with 2.5MW injected RF power (0.8MW LHW plus 1.7MW ICRF) were acquired [5-6]. Moreover, after successful use of lithium wall conditioning to control impurity concentration and ratio of hydrogen to deutrium, H-mode with mixed types of ELMs and longest type-III ELMy H-mode with a duration up to 6.4s were demonstrated [7]. In the latest 7^{th} campaign 2012, benefited from recent years' advanced technification and accumulated experiemence both on physics and technology, including flexible iso-flux real-time feedback control, upgrade of ICRF antenna structure

and tremendously increased capability of both LHCD and ICRF with injected power feedback control, 400s long pulse plasma discharge (0.28MA, ne~1.2, Te~1.8keV, P_{LHCD}~1.2MW, Bt~2.5T), stationary H-modes with durations of 35s (0.28MA, ne~2.2, P_{LHCD}~1.8MW, P_{RF}~1.2MW, Bt~1.9T, H98(y,2)~0.8) and 32s (0.4MA, LSN, P_{LH} ~1.2MW, P_{RF}~1.6MW, f=27MHz, Bt~1.9T), ICRF Heating (0.5MA, ne~2.0, Bt~1.9T, ΔW~30KJ) and H-mode heated only by ICRH with a duration of 3.45s have been achieved [7]. Being a very important tache of EAST project, in the meantime, diagnostics have been developed in various ways to keep step with requiremnt and progress of the EAST machine [8]. Untill the 7th campaign 2012, tens of diagnostics providing most of key profiles of plasma parameters were equipped for machine operation and protection, plasma equilibrium control, physics analysis and performance improvement et al [7].

2. Setup and upgrade of EAST diagnostics

Diagnostic requirements of the EAST are determined by demands of measurement and physics study to characterize the plasma behavior over the full range of conventional plasma parameters, which are varied in different operation scenarios and evolved gradually. In the initial two EAST campaigns with full stainless-steel first wall and hydrogen operation gas, about 15 diagnostics were used, except in-vessel diagnostics of magnetic diagnostic, divertor probe and thermocouple, external diagnostics were those used on HT-7 tokamak with some modification of connecting flange and cables due to short of budget. Since the 3rd campaign in 2008, specific diagnostics became setup to accommodate EAST features of DN/SN configuration, LHW and ICRF plasma, long pulse discharge, and to cover whole region of conventional plasma operation. Until the 5th campaign 2010, 25 basic diagnostics were utilized routinely with extensive function for divertor plasma performance study. From 6th campaign, development of advanced diagnostics focusing on profile of key parameters were on the way, such as a Nd:YAG Thomson scattering system (TS), a x-ray imaging crystal spectrometer (XCS) and a metal bolometer array with newly developed Pt resistor intending for intension of evaluation and optimization of the plasma performance, and physics understanding [8]. In the latest 7th camapign, profile of electron density and electron temperature came from TS, Electron Cyclotron Emission (ECE), soft-X-ray pulse height analyser (SX-PHA), far-infrared (FIR) HCN laser interferometer and Microwave reflectometry, profile of ion temperature and plasma rotation speed relied on two 2D-XCS both in poloidal and toroidal direction, the radiated power distribution and impurity species got from Pt metal bolometry, AXUV, OSMA (Optical Spectroscopy Multi-Channel Analysis), UV-VIS monochrometer. The core and edge fluctuation, MHD instabilty, energetic particles dynamics, neutron yield and spectrum etc., had been diagnosed and studied as well. It has demonstrated that those diagnostics can play an very important role on physics analysis and interpretation based on integrated modeling, and enhancement of plasma performance.

To approach steady-state (SS) operation of high-performance plasmas and address key physics on fusion reactor-relavent subjects in coming 8th campaign 2013, recently, capabilty of the heating and current drive of the EAST plasma are doubled with total injection power over 20MW, including new methodology of the neutral beam injection (NBI) and electron

cyclotron resonant heating (ECRH). Most diagnostics are being in upgrade to become more compact and integrated due to limited port window and space available, and some advanced neutral-beam related diagnostics are developed as well with emphasis of distinguishable ability to provide all parameters' profile including the current density profile and characteristics of the pedestal region in H-mode plasma, to study and understand critcal issues specific to SS high performance plasma.

3. Coming physics capability from the diagnostics upgrade

Expectable diagnostics for the coming 8th camapign on EAST tokamak is listed in the table 1, in which their function, measurement and purpose are presented. YAG TS system with expanding capability of better spatial and temporal resolution up to 50-100Hz and 50 points in core and 20 points in the edge will play a key role on fine profile of electron temperature and density, additionally two 2D-XCS both in poloidal and toroidal using new crystal mornitoring He-like and Fe line emission, new ECE radiometer and SX PHA can compensate core missing information, and edge Te profile can be reinforced from Multi-energy SXR (ME SXR), Hot helium beam, Li-CXRS. As usual, FIR HCN interfemeter is used for density feedback control, microwave reflectometer will provide global density profile, and Faraday Rotation system (Polarimetry-Interferometry) is expected to be ready for density profile as well. 2D XCS with solid detector together with new NBI-related CXRS will provide profiles of ion temperature and plasma rotation speed, reliable assistance can be got from neutron camera and TOF (time of flight spectrometer), and edge Ti can be gained from RFA (retarding field analyzer). ITER-like Pt metal Bolometer and AXUV apply to study radiated power behaviors, local and global radiation energy balance in fast and slow time scale, optical filterscope system together with OSMA and UV-VIS monchrometer give nearly all types of light impurity species and distribution. Medium and heavy impurity species and distribution will be provided by EXUV spectrometer, SX PHA and ME-SXR. Plasma rotation profile variation during the discharge can rely on XCS and CXRS for the core, hot-helium beam, ERD and reciprocating probe for the edge. Fusion product and spectrum, and lost ions will be measured and analyzed by ^{3}He and BF3 proportional countertube, fission chamber, liquid scintillator BC501 monitor, sLIP, SS-NPA and FIDA. Fluctuation study can be carried out based on CO2 laser scattering, doppler reflectometer, ECEI, poloidal and radial correlation reflectometer for the core, and Li-BES, GPI and Hot-helium beam, fast CCD and reciprocating probe for the edge.

It is believed that upgraded diagnostics will provide more comprehensive, reliable and precise data to accommodate EAST athirst requirements of physics study on various advanced issues in coming campaign. Diagnostics available in the coming campaign will be ready for deep study of following physics issues: (1) stable and flexible plasma equilibrium and control, such as plasma initiation at low Vp, flexible shaping with iso-flux feedback control for more effective RF power coupling to plasma, advanced divertor operation scenario especially at ADSSO; (2) understanding and optimization of the high plasma performance plasma, such as SS H-mode, High Ti/β_N; (3) RF wave physics, NBI physics and Synergic effect among RF and NBI; (4) Energetic particle instablilty and MHD-ELM control; (5) Divertor and edge fluctuation and transport; (6) PSI issues at SS high performance

operation, et al.

4. Summary

In the coming 8th campaign 2013, as the tremendous increase of EAST machine capabilty on auxillary heaitng and current drive up to 20-25MW (LHCD, 4MW@2.45GHz, 6MW@4.6GHz; ICRF 12MW@25-75MHz; NBI 4MW; ECRH, 2MW@140GHz) and upgrade of reliable mockup structure and ITER-like in-vessel components (W, C, IC Coils, enhanced active cooling), optimized wall conditioning technique (Li oven/drop/pellet) and flexible fuelling method (GP, SMBI, Pellet), and upgraded diagnostics with more advanced precise and specific diagnostics for plasma physics understanding will find ways to extend EAST operation regimes, achieve higher physical targets, and seek for answers of existing observations which do not be fully understood at the moment, and new physics. It is believed that diagnostics avaliable will play a key role in studying and understanding critcal issues specific to steady-state high performance plasma, including current drive and profile control, transport of edge and divertor plasmas, stability of edge plasma, and interaction between energetic particle and bulk plasma.

Acknowledgments

The author would like to thanks all members of EAST diagnostic team, and all attendee from domestic and international facilities for their contributions to EAST project. This work is undertaken partially under the support of the JSPS-NRF-NSFC A3 Foresight Program in the field of Plasma Physics (National Nature Science Foundation of China, NSFC, No.11261140328). This work was also supported partially by the CAS Key International S&T Cooperation Project collaboration with grant number GJHZ1123, and by National Magnetic Confinement Fusion Science Program with No. 2011GB101000.

References:

[1] Baonian Wan for the EAST team and international collaborators, “The first plasma of EAST”, 21th Interational Atomic Energy Agency (IAEA) Fusion Energy Conference, Chendu, China, Oct. 16-21, 2006

[2] Baonian Wan, The EAST team and Interational Collaborators, “Physical engineering test and first divertor plasma configuration in EAST”, Plasma Science and Technology, Vol.9, No.2, 2007

[3] Baonian Wan for the EAST and HT-7 teams and collaborator, “Recent experiments in the EAST and HT-7 superconducting tokamaks” (Overview talk), 22nd IAEA Fusion Energy Conference, OV3-4, October 13-18, 2008, Switzerland; Nuclear Fusion, Volume 49, Number 10, 2009

[4] J G Li, Y P Zhao, J S Hu, X Z Gong, Review, R-3, 19th PSI Conference, San Diego, May 24-28, 2010

[5] H.Y. Guo, X. Gao, J. Li, G.-N. Luo, S. Zhu, J.F.Chang, Y.P.Zhao, W.Gao, X.Z.Gong, Q.S.Hu, Q.Li, S.C.Liu,T.F.Ming,J.Qu, Y.J.Shi, B.N.Wan, D.S.Wang, H.Q.Wang,J.Wang, Z.W.Wu, B.J.Xiao, Q.Xu, L.Zhang, W.Zhang, “Recent progress on divertor operations in EAST”, Journal of Nuclear Material, Vol.415, 2011: p.369-374

[6] Jiangang Li and Baonian Wan for the EAST Team and International Collaborators,

"Recent progress in RF heating and long-pulse experiments on EAST", Nuclear Fusion, Volume 51, Number 9, 2011
[7] B. N. Wan, et al., "Progress of Long Pulse and H-mode Experiments on EAST" (OV/2-5), 24th IAEA Fusion Energy Conference, October 8-13, 2012, San Diego, USA
[8] Liqun Hu, on behalf of EAST diagnostic team and collaborators, "Present Status of the EAST Diagnostics", Plasma Science Technology, Vol.13, No.1, 2011, p.125-128

*Domestic and international collaborators for the EAST: USTC, South West Institute of Physics, Peking Univ.; Tsinghua Univ., Donghua Univ., General Atomic, FRC Austin, PPPL, UCLA, UC Davis, Tri Alpha Energy in USA; NIFS and JAEA in Japan; Association Euratom-CEA in France, NFRI and KBSI in Korea, etc.

Table 1 Diagnostics available on the EAST machine

Function	Diagnostics in 8th campaign (2013-2014)
Te profile	P: Core, TS (50 points); Edge, TS (20 points) B: Global, 2D-XCS (solid detector) Core, ECE radiometer (32ch, 2.5-2.8T; 16ch, 2T) Michelson interferometer (Grating polychromator) Edge, ME-SXR; Li-CXRS; Hot He beam (pedestal) S: Core, SX PHA (down half volume, 10ch) Edge, divertor probe, reciprocating probe
Ne profile	P: HCN interfemeter (5ch), Faraday Rotation System B: TS (core 50points+edge 20points), Li-BES (edge); MW reflectometer (global Q, W, V) S: Edge, divertor probe, HFS probe, reciprocating probe
Ti profile	P: 2D-XCS (solid D), CXRS; SOL: RFA (Retarding Field Analyzers) B: Neutron monitor; S: TOF
Radiation power (local and global loss and balance)	P: Pt Metal Bolometer, H (core 48ch +edge 8ch), V(12ch) B: AXUV photodiode, H (global, 4×16ch), V(16ch), T(16ch)
Profile of Radiation	Photodiode array, H (3×35ch), V(35ch), T(35ch) ; 2D SXS camera (T) HX (CdTe, 16ch, Z>0), 2D γ-ray camera (T, LYSO, H8500) Visible bremmsstrahlung (11ch, 2.5cm), CIII and Ha array Div. Filterscope (U&D), Filterscope (Tang.)
Light impurity species	Optical Filterscope (Udiv, Ddiv, Tangen.; Da/b/g, CII, C III,

and distribution	CH, Li I, O II, B II, Ar II and He II) OSMA (SP750, 15ch+15ch; SP300, 8ch+8ch); VB, 10ch; Fibre spectrometer; Top Dα/CIII Array UV-VIS Monochrometer (CIII, CII, BIV, BII, OII, OV, LI, LII);
Medium and heavy impurity (species and distribution)	SX PHA (down half volume, 10ch), CXRS EXUV spectrometer (USTC, LHD), ME-SXR
Plasma rotation profile	Core: XCS (solid D), CXRS Edge: Hot-He beam (5mm, 50kHz, Ti>20eV, >1km/s); ERD(P&T), reciprocating probe
q profile	P: Faraday Rotation, BES (NBI, Li-beam), MSE (2014) B: SXR+EFIT reconstruction
Fusion product Neutron flux & spectrum Lost ions	3He + BF3, Fission chamber, BC501 array (3ch) sFLIP, H-NPA, FIDA (active and passive, 4cm)
Fluctuation	Core: CO2 laser scattering (CTS), ECEI (18ch×16ch, 2.5-2.8T), Doppler reflectormeter, Poloidal and radial correlation reflectometers Edge: Li-BES (Ne,r2cm,p1cm); GPI (Ne, 2mm,400k); Fast CCD; Hot Helium beam (100K); Ne/Te (slow, ME-SXR); Reciprocating probe+HFS probe
Plasma-wall interact.	Endscope visible CCD camera (two slow, one fast) Endscope IR camera (two)
MHD instability Lock mode (MHD)	ECEI (16ch×16ch, 2.5-2.8T), 2D T-SXR camera SXR camera, Mirnov coil,10%, Tang. SXR, Saddle coil
Runaway behaviors	Midplane: BGO + NaI (Forward+backward) NaI array (5ch) + CdTe + BGO array (4ch)
Edge plasma parameters RF sheath behavior	Reciprocating probe, Bolometer, Tri-probe, Mach probe, Ha/Da, GPI Katusmata probe
Species, pres. & distrib.	Divertor fast pressure gauge, penning spectrometer

P: primary
B: sackup
S: supplementary

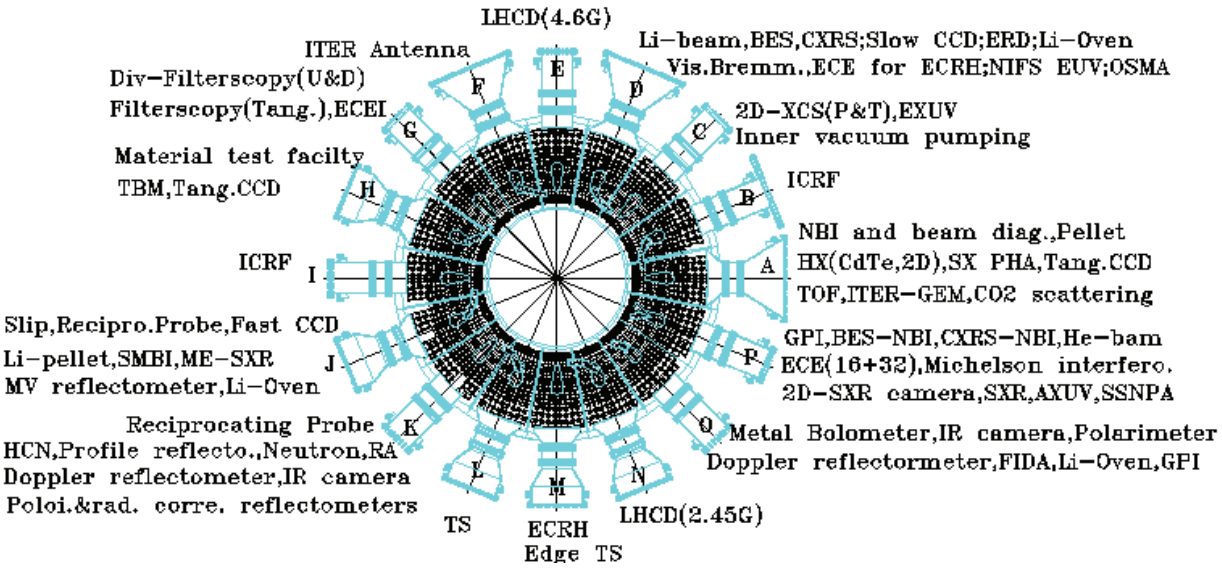

Fig.1 Down view of the EAST diagnostics arrangement

Status and Plan of KSTAR Heating Systems for Steady-State Plasma Achievement

Y.S. Bae
National Fusion Research Institute, Daejeon, Korea

The KSTAR heating and current drive (H&CD) system contains the NBI, ICRF, LHCD, and ECH systems. The combination of multiple heating and current drive technologies is aimed at providing flexible control functions for current density and pressure profile in the KSTAR operation scenarios; a D0 neutral beam power of 12 MW at the beam energy of 100 keV with two beam lines and three ion sources in each beam line, an ICRF coupled heating power of 6 MW at 30~60 MHz, an LH heating power of 4 MW at 5 GHz tube, an EC heating power of 0.7 MW at 84 GHz and 110 GHz for start-up, and an EC heating power of 4 MW at 170 GHz tube for current drive and MHD mode stabilization, respectively. Among the various H&CD systems described above, there were significant upgrades in the NBI system and ICRF system in 2012. Furthermore, an initial 5 GHz, 0.5 MW, LHCD system was installed for non-inductive current drive experiments in 2012 campaign. This paper describes the progress of the KSTAR heating and current drive system development and steady-state technology issues for steady-state fully non-inductive current drive in KSTAR.

1. Introduction

The main mission of Korea Superconducting Tokamak Advanced Research (KSTAR) is the demonstration of advanced tokamak (AT) steady-state operation with high performance of high-β, which is defined as the ratio of the plasma energy to the external magnetic energy, and of high confinement time [1, 2]. This mission requires various heating and current drive schemes using neutral beam heating and radio frequency (RF) heating and current drive system. KSTAR is a superconducting tokamak device for 16 toroidal coils and 7 pairs of poloidal coils. KSTAR has also the normal conducting in-vessel control coils (IVCC) inside vacuum vessel. The IVCC design and installation in KSTAR is considered to play a very important role to study and understand the hot issues of MHD modes such as edge localized control mode (ELM) and resistive wall mode (RWM) and the issue of 3D field effect [2]. Figure 1 shows the perspective view of present KSTAR heating and current drive system. The first neutral beam line is upgraded with installation of full triple set of beam line components and the second ion source.

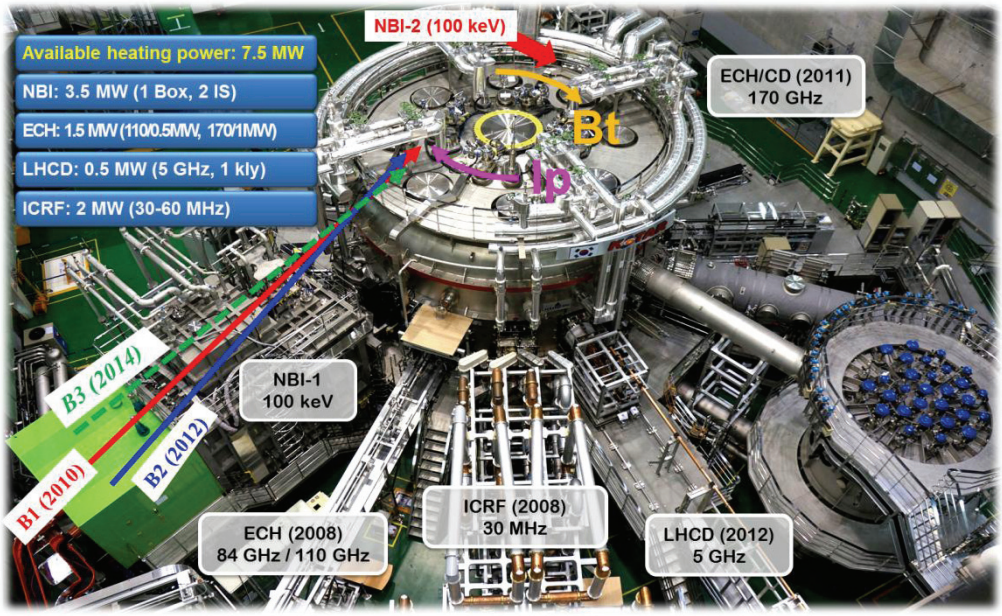

Fig. 1. Present status of KSTAR heating and current drive system.

2. First NBI System (NBI-1)

2.1 Characteristics and key technologies of the NBI-1

The KSTAR first neutral beam injection (NBI-1) system is designed with three co-tangential neutral beams. Figure 2 shows the NBI-1 beam line containing three beams from each ion source. All three beams are extracted with straight forward fashion, and side two beams are injected with 4-deg steering angle from the centered beam so that beams cross at the middle of beam duct as shown in fig. 2. The shine-through armor is currently just graphite tile. It could resist the maximum 5 MW with pulse duration of 50 s every 15 min without water cooling. For higher power injection with longer pulse duration in near future, the shine-through armor will be replaced by water-cooled CFC. The second NBI beam line design is under discussion between two options; movable co/counter beam line and off-axis co-beam or counter beam depending the physics requirements of KSTAR future advanced tokamak operation and ITER-relevant experiments. Since

details of system description of NBI-1 is reported in previous PAC report, here we describe the main characteristics and key technologies of NBI-1.

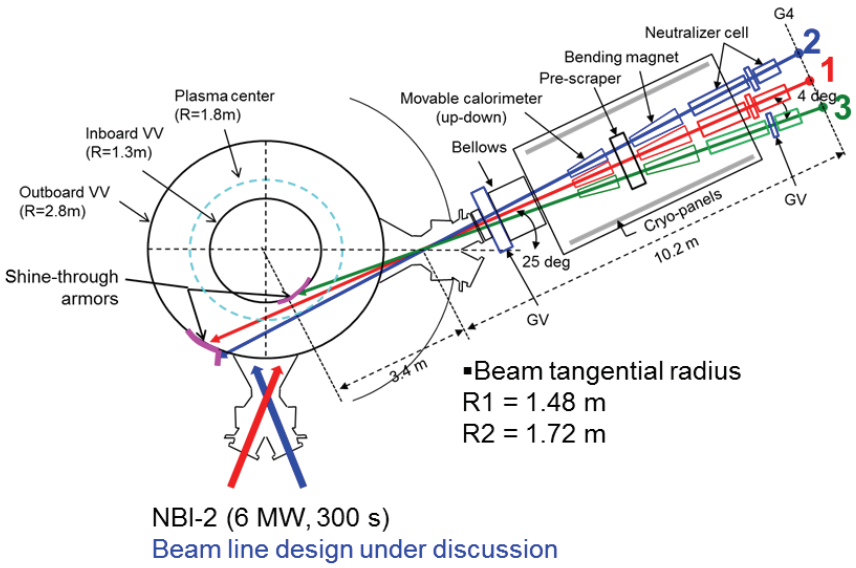

Fig. 2. Design of KSTAR first co-tangential neutral beam injection system with three ion sources.

2.2. Beam operation results

In 2012 KSTAR campaign, two ion sources were conditioned simultaneously with two independent power supply and control system. The old first ion source is conditioned from the perveance of K = 1.2 microP to maximum K ~ 1.4 microP up to 100 keV. The new second ion source is also conditioned successfully from the perveance of K = 1.5 microP to K = 1.7 microP. For 100-keV beam energy, the two ion sources were conditioned with pulse duration of 4 ~5 s. The D0 beam power of two ion sources is measured with 1.66 MW and 1.8 MW, respectively.

NBI-1 was also essential for the KSTAR physics experiments also in 2012 campaign. We able to perform many interesting experiments in 2012 KSTAR campaign using two independently controlled beams. The upgraded beam power, typically 2.7 MW D0 beam power, supported the 20.5-s (total pulse length) long pulse H-mode discharge (Ip = 0.6 MA, Bt = 2 T, Pnbi = 2.7 MW). Also, we achieved the highest beam power injection of 3.5 MW with pulse duration of 4.5 s at 100 keV to KSTAR plasma (Ip = 0.6 MA, Bt = 3 T) using two ion sources. For the highest beam power injection at the higher toroidal magnetic field (3 T), the L-H transition was not obtained unfortunately due to the issue of divertor shaping control.

We had the excess heat load at the electron back plate dump of the new second ion source during the conditioning. It is suspected by high gas pressure in the accelerator grids due to the increased gas flowing in large hole-aperture or non-uniformity of plasma density in the plasma generator. Due to this reason, we limited the beam power of second ion source by 1.2 MW for the long pulse operation.

3. ECH System

KSTAR has two different ECRH systems of different frequencies, 84/110 GHz and 170 GHz. The first ECRH system consists of 84 GHz and 110 GHz gyrotron and about 40-m long evacuated corrugated waveguide of 31.75-mm inner diameter for the transmission line. The 110 GHz gyrotron was loaned from General Atomics, and its installation and conditioning was supported by General Atomics. Operation of 84 GHz gyrotron and 110 GHz gyrotron is shared with the same transmission line and high voltage power supply. The second one consists of 170 GHz gyrotron and about 70-m long evacuated corrugated waveguide of 63.5-mm inner diameter for the transmission line. The 170 GHz gyrotron is an ITER pre-prototype model and was loaned from Japan Atomic Energy Agency. The 1 MW output power at the output window with pulse duration of 20 s is recently achieved with support of JAEA's group.

The present launcher is two-mirror front steering launcher installed at the equatorial port. It is designed to be capable of power rating of 1 MW with pulse duration of 5 s every 15 min. The launcher mirrors are passively cooled. Figure 3 shows the launcher with two passively cooled mirrors installed at KSTAR equatorial port. Two passively cooled mirrors are a fixed mirror made of solid Glidcop in front and steering mirror made of copper-plated stainless steel with inlaid copper blocks to maximize the radiation cooling and reduce eddy currents. During 2012 KSTAR campaign, 180 kW 84 GHz O1 EC power is injected for the non-inductive startup by ECH, and 350 kW 110 GHz X2 EC power and maximum 800 kW 170 GHz X2 EC power is injected for the startup during the ramp-up phase and MHD physics experiments. Also, the EC wall cleaning (ECWC) discharge is performed using 110 GHz ECH system as like in 2011 campaign. In the initial phase of the 2012 KSTAR campaign, we had difficulty in successful startup due to the impurity in the vacuum vessel. Because of troubles in ICRF system, we tried EC wall cleaning discharge using 170 GHz X2 power injection to the vacuum with the toroidal magnetic field of 3 T. We injected EC

power of 1 MW at source with pulse duration of 1 s every 10 sec for 10 shots. After second trial of 170 GHz ECWC, the temperature on the back side of fixed and steering mirror increased to 85 C and 120 C, respectively after two ECWC shots. The temperature is measured by thermocouple sensors installed on the back side of mirrors before the 2012 campaign. Ansys thermal analysis to estimate the front surface temperature showed the maximum temperature of 540 C at the front surface of the steering mirror. This temperature should not be a problem, the poloidal steering fork axis is jammed. After this incident until the end of the campaign, the steering mirror is not moved in poloidal direction, but is moved in toroidal direction. When the vacuum vessel is opened, we found the steering mirror is melted down and poloidal fork busing is also melted to the link axis. We suspect some arcs on the surface of steering mirror during ECWC caused the evaporation of copper plating and excess power deposition on the stainless steel metal surface leading to eventually melt-down.

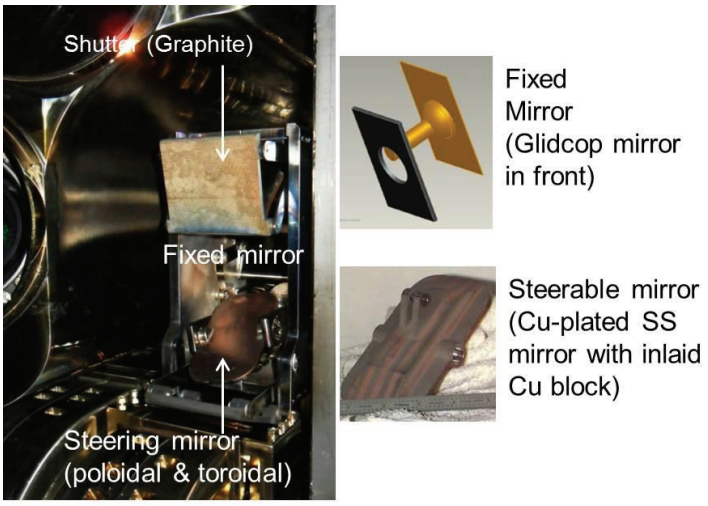

Fig. 3. KSTAR ECH launcher installed in the equatorial port.

4. LHCD System

The initial LHCD system with capacity of 0.5 MW for 2-s is installed for 2012 campaign using the prototype of 5 GHz, 500 kW CW klystron and un-cooled fully active waveguide grill launcher. The prototype klystron, which was designed by POSTECH and fabricated by Toshiba in Japan, was successfully tested at KSTAR site in early start of 2010. In 2011, the maximum pulse length of 3 s at the output power of 514 kW was achieved with the matched load condition of VSWR ~ 1.2, and this achievement is beyond the contract criteria of 0.5 s for prototype klystron. Moreover, the klystron is successfully tested with longer pulse duration of 800 s at 300 kW and 20 s at 460 kW. Since the klystron is placed far away from the KSTAR tokamak, the transmission line is an oversized rectangular waveguide to reduce the Ohmic loss. The transmission line is WR284 oversized waveguide with the total length of ~ 80 m. The special curvature of the radius of WR284 oversized H/E-bends are found for 5 GHz TE01 operating mode to suppress the high order mode generation during the bends. The measured total transmission line efficiency is about 60% according to 34% loss in the transmission line and 6% loss in the power dividing network. The launcher is a conventional grill launcher with 8 columns by 4 rows (total 32 waveguide grills). The unit of the waveguide grill launcher is a 4-way splitter with one input and 4-splitted outputs. The vacuum window is alumina ceramic metal brazed in the standard WR187 input waveguide of 4-way splitter.

We attempted the longer pulse operation of the klystron at 500 kW RF output. The klystron is successfully demonstrated with the pulse duration of 600 s at the output power of 500 kW. For 300-s pulse, the output RF power decreased slowly due to the beam current decrease caused by cathode emission cooling effect. In order to keep the constant output power, the anode voltage is controlled to compensate the beam current drop. So, the RF output power of 500 kW is sustained for 600-s pulse duration. The window temperature is saturated at around 200 s after the pulse, and the vacuum pressure inside the klystron increased up to very low level, 0.02 μA. The vacuum current was still increasing very slowly. But, the body temperature was not still saturated even at the 600 s pulse. That is why we limited the pulse duration by 600 s just in case. But, we expect that longer pulse than 600 s will be possible because there is still enough margin in the body power loss. The measured body power loss was 8.7 kW less than the design value of 10 kW. The body power loss and temperature will be saturated after additional 10 min with $\Delta T \sim 45$ C (< 52 C, safety level).

5. ICRF System

In 2012 campaign, a de-coupler between resonant loop A and B (loop A is connected to right two straps among 4 straps looking from outside of tokamak, and loop B to other two straps) were installed to avoid the mutual coupling between two loops keeping the power balance between straps. The mutual coupling causes the power unbalance leading to excess voltage in one side among resonant loops. Also, a coaxial 3-dB

hybrid splitter at 30.8 MHz was designed and manufactured to prevent the reflected wave back to the transmitter. The 3-dB hybrid splitter was installed at the end of main transmission line in tokamak hall. The two outputs of the 3-dB hybrid splitter are connected to the inputs of resonant loop A and B. The matched output of the 3-dB hybrid splitter is connected to the dummy load located in heating room through 9-inch long coaxial transmission line so that the reflected wave is absorbed in the dummy load. Figure 4 shows the schematic drawing of improved resonant loop systems with a de-coupler and a 3-dB hybrid splitter.

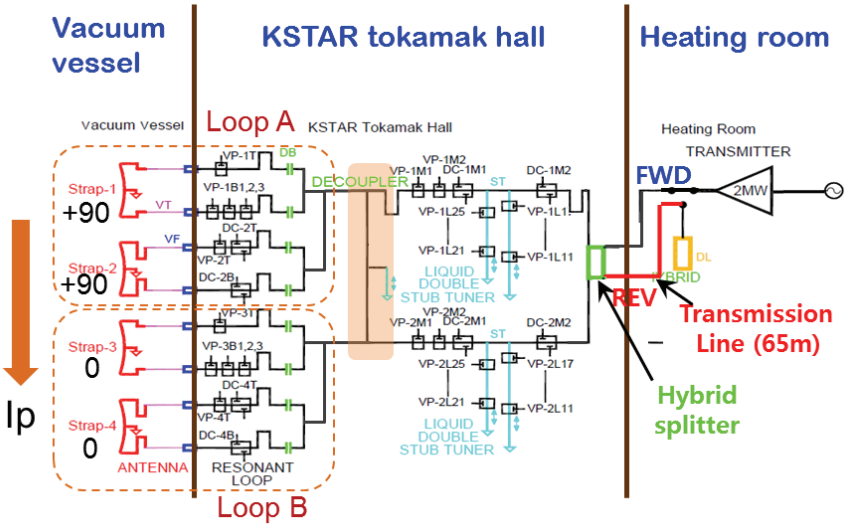

Fig. 4. The schematic layout of new improved resonant loop system in KSTAR ICRF.

The de-coupler worked well in 2012 campaign and solved the power unbalance problem that we had in 2011 campaign. Also, the reflected power is reduced by 15% (VWSR ~ 2) in 2012 campaign in the case of total forward power of ~400 kW with pulse duration of 3 s. In 2011 campaign, the high reflection from H-mode plasma caused the unstable oscillation of the transmitter. In 2012 campaign, there were no unstable phenomena in the operation of the transmitter even in the high reflection because the most of the reflected wave were absorbed to the dummy load not going to the transmitter. We obtained reliable load resilient operation of the transmitter regardless of the H-mode discharge and high reflection.

Main 2012 ICRF experiment is an minority ion heating with single arbitrary n// with the toroidal magnetic field, 1.5 T < B0 < 2.5 T and the current drive with B0 < 1.5 T or B0 > 2.5 T. For the current drive, the antenna strap phase difference is set to (0,0,pi/2,pi/2) from the left side to the right side of antenna straps looking from the tokamak outside. In order to change the phase difference of antenna straps during the campaign, a phase shifter was installed at one output branch of the hybrid splitter. However, high minority contents (more than 50%) in 2012 KSTAR campaign, the electron heating and ion heating was never seen.

6. Upgrade Plan of KSTAR Heating and Current Drive Systems

KSTAR heating system will be upgraded to total 12.5 MW in 5 years. First NBI system will be upgraded to 6 MW with addition of final third ion source in 2014. We are planning the design of the second NBI system from 2014 and the construction in 2015 aiming at first 2 MW beam operation in 2016. The 170 GHz ECH system upgrade plan is the installation of an additional 1 MW system in 2015. The 5 GHz LHCD system will be also upgraded at the same time with 170 GHz ECH system. ICRF system will not be upgraded with additional power, but the present system will be improved to deliver maximum the full power rating of 1.5 MW with longer pulse duration. But, note that this upgrade plan is still under evaluation in terms of consistency with KSTAR upcoming 5-year operation plan.

Acknowledgements

This work was partly supported by the JSPS-NRF-NSFC A3 Foresight Program in the field of Plasma Physics (NSFC: No.11261140328).

References

[1] G.S. Lee, M. Kwon, C. J. Doh, and et. al., “Design and construction of the KSTAR tokamak”, *Nucl. Fusion,* **41**, 1515 (2001).

[2] H.L. Yang, Y.M. Park, Y.S. Bae, H.K. Kim, and et. al., “Development of KSTAR in-vessel components and heating systems”, *Fusion Eng. Des.,* **86**, 588 (2011).

Issues of High Power/Long Pulse ECRH Experiments in LHD

Shin KUBO[1,2)], Takashi SHIMOZUMA[1)], Yasuo YOSHIMURA[1)], Masaki NISHIURA[1)], Hiroe IGAMI[1)], Hiromi TAKAHASHI[1)], Takashi MUTOH[1)], Shinya OGASAWARA[2)], Ryohei MAKINO[2)], LHD experiment group[1)]

[1)] *National Institute for Fusion Science, Toki 509-5292, Japan*

[2)] *Department of Energy Engineering and Science, Nagoya University, Nagoya 464-8463, Japan*

ECRH system in LHD has been upgraded to perform high power, long pulse ECRH experiments. Recent upgrades includes the introduction and the operation of three 77 GHz and one 154 GHz 1 MW/10s, 0.3MW/CW gyrotrons. This powerful ECRH system enabled to explore electron heating effects in the wide range of plasma parameters of LHD. These includes the highest electron temperature of more than 20 keV at the center in the low density region of below 2×10^{18} m^{-3} or highest electron density of 1.4×10^{20} m^{-3} which is far over the cut-off density for the 77 GHz fundamental ordinary mode ECRH. In the CW operation regime, the plasma of $n_e = 0.5 \times 10^{19}$ m^{-3} and $T_{e,0} = 3$ keV is maintained for 30 minutes by injecting more than 200 kW CW ECRH.

This upgraded ECRH system is also applied to heat electrons in high ion temperature NB heated plasma and also collective Thomson scattering to measure ion velocity distribution function.

1 Introduction

Owing to the recent development of high power of more than 1 MW stable gyrotrons at the frequency range of 60 to 170 GHz, 77 GHz and 154 GHz in replace of old 168 GHz gyrotrons that originally been introduced in the mid 1990's for second harmonic heating in LHD which turned out to be hardly operable at the magnetic field strength of 3 T to perform 2 nd harmonic electron cyclotron resonance heating at the center of the confinement region. These three gyrotron at 77 GHz and one at 154 GHz demonstrated to be effective enough to achieve highest electron temperature of more than 20 keV at the density of 2×10^{18} m^{-3} and more than 0.1 billion degree Kelvin a the density of 1×10^{19} m^{-3}. Those powerful gyrotrons are also appleied for various transport or wave physics study and also diagnostics utilizing its highly localized and fast modulation capability.

Here, the upgraded ECRH system, high power gyrotorons and associated upgrade of the transmission system are described in section 2 Several experimental topics using this upgraded system are described in section 3 including extensions in plasma parameters, effete of central electron heating of high T i plasmas, and long pulse trial. On the other hand, several issues associated with high power density operation became apparent and discussed in section 3.3.

2 ECRH System Upgrade

ECRH system in LHD has been upgraded to perform high power, long pulse ECRH experiments. Recent upgrades includes the operation of three 77 GHz and one 154 GHz 1 MW/10s, 0.3MW/CW associated with relevant improvement of the corrugated transmission line and antenna systems.

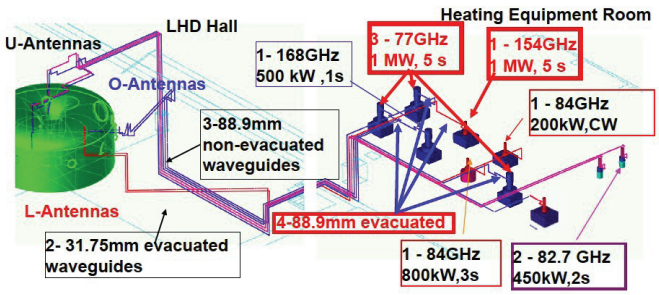

Fig. 1 ECRH system installed on LHD, Three 77 GHz and one 154 GHz gyrotrons are in operation in 2012. Evacuated

2.1 Gyrotron Upgrade

In table 1 are listed the specification and achieved operation parameters of 1MW gyrotrons. It should be noted the maximum power achieved in 77 GHz is enabled by adopting two step anode voltage start-up[1]. These gyrotrons are routinely operated for the plasma production and electron heating experiments during LHD experimental campaigns. In Fig. 2 is shown the set-up of the 154 GHz gyrotrons in the gyrotron hall. All of these gyrotrons are operated with cryo-free magnets. Matching optics unit (MOU) is placed between gyrotron output window and the corrugated waveguide to couple the gyrotron output efficiently and in high purity HE_{11} mode. Waveguide switch (WG SW) switches the direction of the waveguide to LHD or to the dummy load.

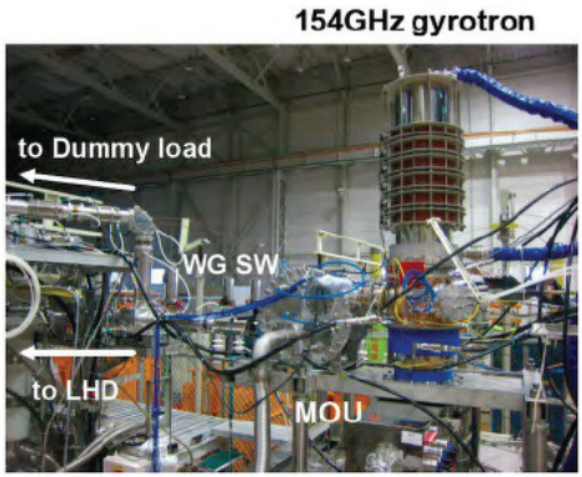

Fig. 2 154 GHz Gyrotron system installed on LHD

2.2 Transmission System Upgrade

The transmission system is upgraded so as to transmit the 1 MW level power reliably and efficiently. Improved components are shown in Fig. 3. Each transmission line have a diamond window at the end. The diamond window protection is assured by both sensitive arc detector and a small IR temperature monitor looking at the center of the diamond window. Originally the 3.5 inch inner diameter corrugated waveguide system had been adopted for 1MW transmission at the air, but It turned out that the microwave breakdown often occurs at the power level of more than 500 kW. To keep the high reliability at more than 1 MW, all the 3.5 inch corrugated waveguide system attached to the 1 MW gyrotrons are now evacuated and kept the pressure below 1.0×10^{-2} Pa. The connecting flanges of corrugated waveguide are totally modified. For the CW operation, waveguide cooling is enforced by attaching copper plates with cooling water channels.

3 Recent Experimental Topics

Utilizing these upgraded ECRH system, the central electron temperature of more than 20 keV with the density

Item	77GHz #1	77 GHz #2	77 GHz #3	154 GHz#1
spec.	1.0 MW/5 s 0.3/CW	1.2 MW/ 5 s 0.3/CW	1.5 MW/ 2 s 0.3/CW	1.0 MW / 5 s 0.5/CW
achieved	1.01/ 5 s	1.02/ 5 s	1.30/ 0.45 s	1.16/ 1 s
(two step V_a)	1.41/0.2 s	1.30 / 0.45 s	1.78/ 1 s	
(CW mode)	0.29/ 60 s 0.13/ 935 s	0.24/ 1800 s 0.3/ 165 s	0.3/ 2400 s 0.22/ 4500 s	

Table 1 List of 1MW class gyrotron operated up to 2012 in LHD

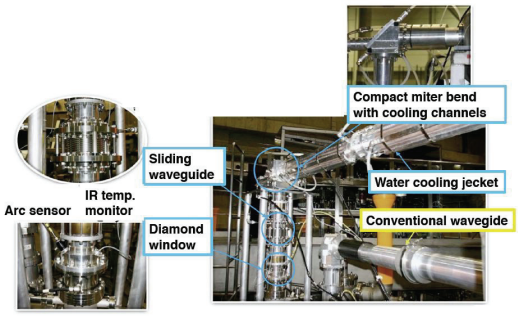

Fig. 3 Improved 88.9 mm id corrugated waveguide transmission system.

of 2.0×10^{18} m^{-3} or more than 8.6 keV with the density of 1.0×10^{19} m^{-3} are achieved. The 154 GHz power injection demonstrated an clear electron heating effect at 1.4×10^{20} m^{-3} which is far over the cut-off density for the 77 GHz fundamental ordinary mode ECRH. This high power ECRH is also applied to high T_i plasma in LHD. This ECRH system is operated routinely and applied for the heating and transport physics study. Several topics are discussed In the following subsections.

3.1 High density electron heating

One of the advantages of introducing second harmonic electron cyclotron frequency (154 GHz) is the accessibility to higher density regime where the fundamental frequency wave can not penetrate while the absorption rate is comparable. In Fig. 4 are shown the clear modulated heating effects for second harmonic heating (154 GHz), but not for fundamental heating (77 GHz) on the stored energy at the density of 1.3-1.4 $\times$ 10^{20} m^{-3} which is far over the cutoff for the 77 GHz fundamental O mode, but less than 154 GHz second harmonic X mode. Strong neutral beam injection (NBI) is used to keep such high density and the fluctuation in the stored energy that is not correlated with ECRH modulation is due to the NBI power fluctuation and other instabilities.

3.2 Electron heating of High Ti discharge

The original idea to reach high energy confinement regime in LHD is to inject ECRH power to put the plasma into the electron root in the neoclassical transport theory. So far, high T_i regime has been explored by increasing direct ion heating utilizing strong NBI and carbon pellet injection or strong gas puffing. The first trial to superpose ECRH to high T_i plasma was executed in 2012. Fig. 5 are shown the time evolution of electron and ion temperature at several radial position measured by YAG-Thomson scattering and charge exchange recombination spectroscopy (CXRS). Although the central electron temperature increased from 3.2 keV to 5.0 keV and an electron thermal barrier seems to be formed, the decrease in the central ion temperature,

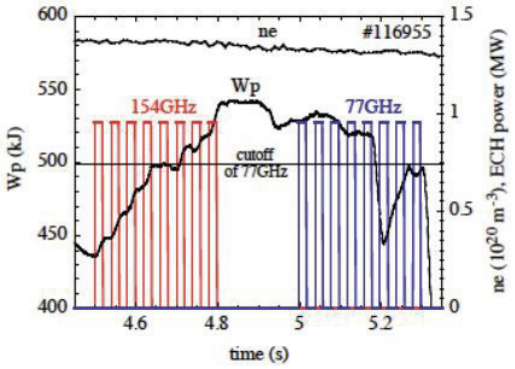

Fig. 4 Effects of power modulated second harmonic X mode heating (154 GHz) and fundamental O mode heating (77 GHz) on the stored energy at electron density of 1.3-1.4 × 10^{20} m^{-3} (¿ 0.735 × 10^{20} m^{-3} (cut off density for 77 GHz O mode))

but a small increase in the peripheral ion temperature were observed. In the present parameter regime, it might be possible that the ion confinement is dominated by an anomalous transport and the T_e/T_i ratio might have enhanced the anomalous transport.

3.3 High power density issue

Issues of the high power density injection gradually become apparent, in particular at the opposite side wall started arcing. Due to the nature of Gaussian beam, strongly focused beam tends to expand. Upper port antenna focus the beam strongly from the need to confine the beam size within narrow region due to high magnetic field gradient near the resonance layer at the magnetic axis. That means the weakly focused beam reaches the wall with high power density if it is not absorbed at the plasma sufficiently. That actually happened several times when the beam missed to pass through the resonance layer or injected with improper polarization. An example of such event is shown in Fig. 6. The hot spots produced by the arc discharge just in front of the wall have melted the wall material and remained hot even after 3 s of the ECRH turned off. To avoid such dangerous events, interlock system to detect such arcing and turn off the relevant ECRH power is installed as well as precise polarization setting software.

3.4 Long pulse discharge

In the last experimental campaign, available CW source for ECRH was one 84 GHz 100 kW and two 77 GHz 140 kW gyrotrons. Since the both 77 GHz gyrotrons could operate 150 kW and 130 kW for 2 min, these two gyrotrons are exchanged turned on and off every 2 min. Fig. 7 a) shows a time evolution of the density and injected power. The injection power were kept about 240 kW in average. The electron density was adjusted to be 0.7 × 10^{19} m^{-3}. Fig. 7 b) show typical electron temperature and density profiles.

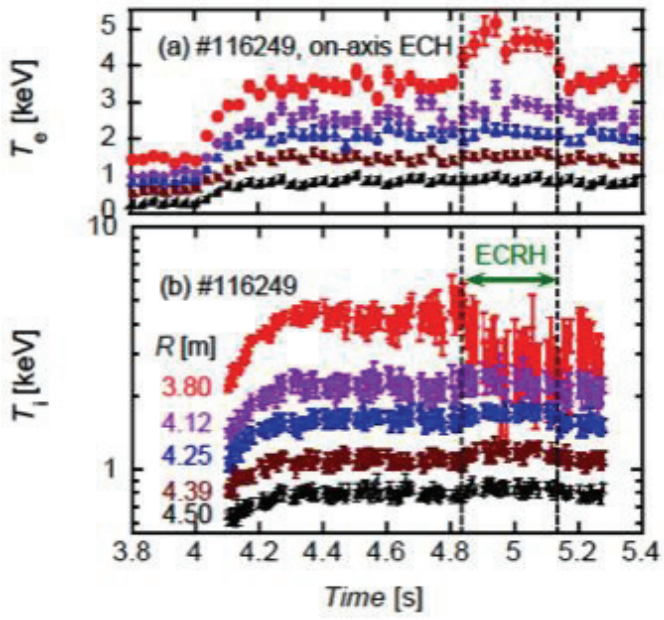

Fig. 5 Time evolution of a) electron and b) ion temperature at several radial positions. ECRH is injected from 4.82 to 5.12 s

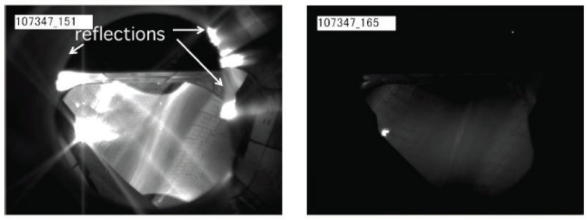

Fig. 6 a) Arcing observed at the opposite wall of the injection antenna. b) Hot spot remaining 3 s after the ECHR turned off.

This discharge was terminated by a sudden radiation collapse. These seems to indicate that some large flakes attached to the wall or diverter contaminated into the plasma and caused a small increase of the radiation at t=1788.3 s.

That caused the peripheral electron temperature decrease down below critical temperature (typically 100 eV which corresponds to the radiation barrier) and triggered a main radiation collapse. It should be necessary to prevent such events by injecting more power or to develop some methods to get rid of such flakes accumulated at the wall or diverter.

3.5 Collective Thomson Scattering

The availability of high power gyrotron is also beneficial from the view point of diagnostics. Since the cross-section of the collective Thomson scattering (CTS) is small, high power probe beam and sensitive detector are required. In LHD ECRH system, two sets of injection antenna are installed in 4 ports. Utilizing this system, it is rather easy to

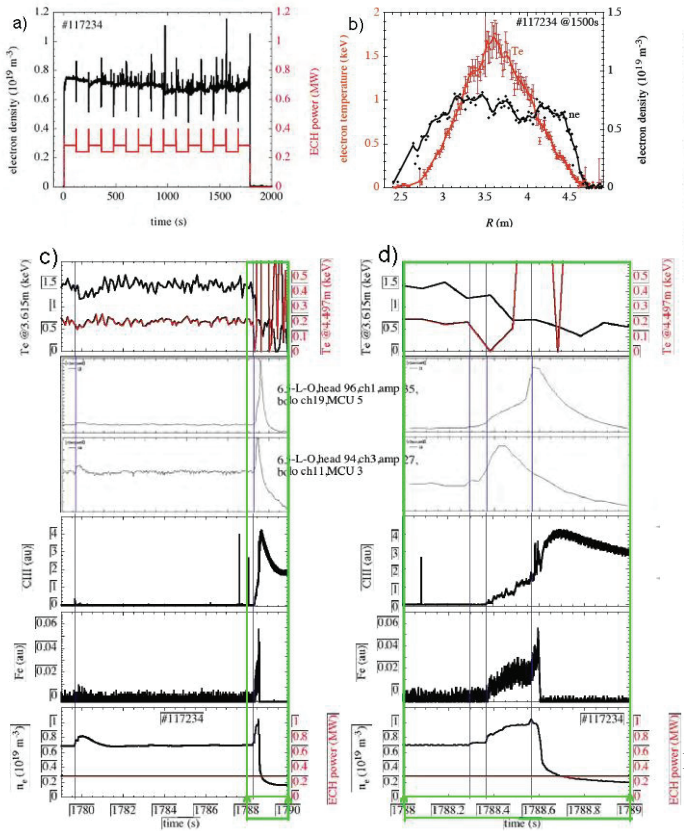

Fig. 7 Discharge waveforms of the LHD shot #117234 where the discharge was maintained about 30 minutes by ECRH power only with averaged injection power of 240 kW. a) Time evolution of the electron density and injected power. b) electron density profile and temperature profile measured by YAG-Thomson scattering. c) Time evolutions of central and peripheral electron temperature, central bolometer, peripheral bolometer, CIII line intensity, and ion impurity line intensity and density at the last 11 s of the 30 min discharge. d) same as c) but expanded time span from 1788 s to 1789 s at the plasma collapse.

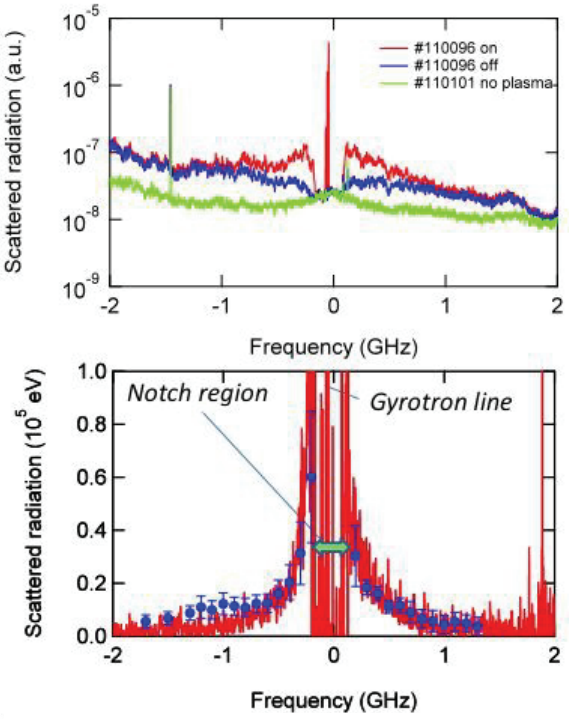

Fig. 8 FFT spectra of the IF signal after CTS heterodyne mixer. a) raw spectra when the probe beam is on (red) and off (blue) and without plasma (green) b) CTS spectra background ECE subtracted. Corresponding spectra obtained by the conventional filter bank are over plotted with blue dots with error bar.

set-up CTS system in LHD. By installing the CTS receiver on the gyrotron side of the ECRH transmission line, one can use ECRH injection system as a CTS receiving system. Such receiving system started with conventional heterodyne receiver with strong notch filter to suppress stray radiation and succeeded in deriving the CTS spectrum in NBI heated plasma[3]. Recently, this receiver system is upgraded to install fast digitizer with the maximum sampling of 12.5 G samples/s directly at the heterodyne mixer. Fig. 8 a) show the FFT spectra when probe beam turned on (red, background ECE plus scattering) , off (blue, background ECE) and without plasma (green, system noise). It is noted that the spectra have a dip within ± 200 MHz which is the characteristic of notch filter. Fig. 8 b) shows the subtracted CTS spectra (red - blue in Fig. 8 a)). It is also shown that the conventional 32 channel filter bank signal gives quite similar spectra for the same shot. These spectra demonstrate that the FFT spectra obtained from the fast digitizer give fine structure of the spectra with good signal to noise ratio. Another recent modification is that the steering mechanism of the receiving antenna. The steering driver is exchanged from super-sonic motor to a normal servo motor so as to scan the scattering volume with in a single shot. That also gave a good confidence as receiving a CTS. The conventional filter bank system and fast digitizer system are used in parallel and collecting data for various scattering configuration and plasma parameters.

4 Summary

The high power ECRH system with four 1 MW class gyrotron are successfully operated to attain total ECRH injection power of more than 4.6 MW at short pulse. This system is used for various plasma heating and transport study in LHD and clarified many physics. This system is also demonstrated to be powerful to observe collective Thomson scattering spectra.

[1] H. Takahashi, T. Shimozuma *et al.*, Plasma and Fusion Research **7**, 1205154 (2012).
[2] T. Shimozuma, S. Kubo *et al.*, Journal of Microwave Power and Electromagnetic Energy, Vol. **43** (2009) 60.
[3] S. Kubo, M. Nishiura *et al.*, Review of Scientific Instruments, Vol. **81** (2010) 10D535.

Acknowledgements
This work was partly supported by the JSPS-NRF-NSFC A3 Foresight Program in the field of Plasma Physics (NSFC: No.11261140328).

Preliminary ICRF Heating Results on EAST

X.J.Zhang[1],Y.P. Zhao[1], J.G. Li[1], B.N. Wan[1],L. Hu[1], X.Z. Gong[1], C.M.Qin[1],B.Lu[1], Y.T. Song[1],Y. Lin[2], G.Taylor[3], J.M. Noterdaeme[4,5],F.Braun[4], S. Wukitch[2], R. Magne[6], X. Litaudon[6],R. Kumazawa[7], H. Kasahara[7] and EAST Team

[1]Institute of Plasma Physics, Chinese Academy of Sciences, Hefei 230031, China

[2]MIT Plasma Science and Fusion Center, Cambridge, MA 02139, USA

[3]Princeton Plasma Physics Laboratory, USA

[4]Max-Planck Institute for Plasma Physics, D-85748, Garching, Germany

[5]University of Gent, Belgium

[6]CEA, IRFM, F-13108 Saint-Paul Lez Durance, France

[7]National Institute for Fusion Science, Toki, Japan

Significant progress has been made with Ion Cyclotron Range of Frequencies (ICRF) heating in EAST. This is mainly because lithium wall conditioning was routinely used to reduce both impurity and Hydrogen (H) recycling and to improve the ICRF power absorption. During the last two experimental campaigns in EAST, ICRF Heating experiments were carried out at the fixed frequency of 27MHz. Effective ions and electrons heating were observed with the H Minority Heating (H-MH) mode. Using the H-MH mode gave the best performance, and the increase of the stored energy reached 30 kJ in L-mode plasma by using the ICRF power of 1.0 MW alone when the H cyclotron resonance layer was at plasma center. On the 2012 experimental campaign, the first ICRF heated H-mode plasmas and the first successful application of the ICRF Heating in the D (He3) plasma were achieved.

1. Introduction of ICRF heating system in EAST

Experimental Advanced Superconducting Tokomak (EAST) is a full superconducting device [1-3]. EAST has a major radius R = 1.85m and a minor radius a=0.48 m, with an elongation of 1.2–2 for Single-Null (SN) and Double Null (DN) divertor operations. ICRF heating is one of the primary auxiliary heating methods for the EAST device. EAST is equipped with an ICRF system consisting of 4 generators, totaling 6.0 MW and two low field side antennas at two dedicated horizontal ports, B-port and I-port. All the ICRF systems are operated with a frequency range of 25 – 70MHz for long pulse length up to 1000 s [4]. Two of them power the I-port antenna and the other two of them power the B-port antenna. Each transmitter is connected by a nine inch transmission line, through a three stub matching system, and vacuum insulated transmission lines to an antenna. A new folded 4-strap antenna at I port instead of O-port 2-strap antenna is grounded at both ends and fed in the center. The 2×2 loop antenna at B-port is fed at end and grounded at the other end. Both the current straps and Faraday shield of the two antennas are made of stainless steel. The faraday screen of the B-port antenna coated with B4C and cooled by water aimed for reducing the impurity production and long pulse operation.

2. ICRF Heating In D (H) and D (^{3}He) Plasma

By the baking of plasma-facing components and extensive Li wall conditioning, effective ICRF heating [5] was successfully performed in EAST after the hydrogen concentration was decreased less than 10%.

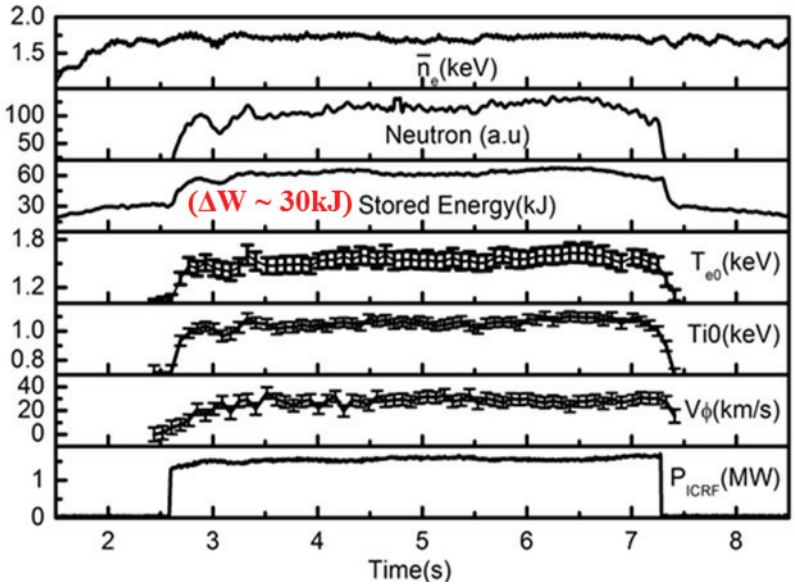

Figure 1. An example of ICRF Heating in EAST from the 2012 campaign with 1.7MW of ICRF power injected from the B- and I- port antennas

Both ions and electrons heating were observed in the H-minority heating scheme in a deuterium majority plasma. An example of ICRF heated discharge at Bt=2.0T and Ip=500kA and hydrogen concentration is about 5%. is shown in Fig.1 where the B and I port antennas are operated in (0,pi) phasing and 27MHz. The neutron rate and stored energy are increased when ICRF switched on. A significant rise of central ions and electrons temperature measured by X-ray crystal spectrometer [6] are seen. The sawtooth stabilization is also obtained during the ICRF pulse. This could be illustrated that the high-energy populations of H produced by MH is contributed to the sawtooth stabilization.

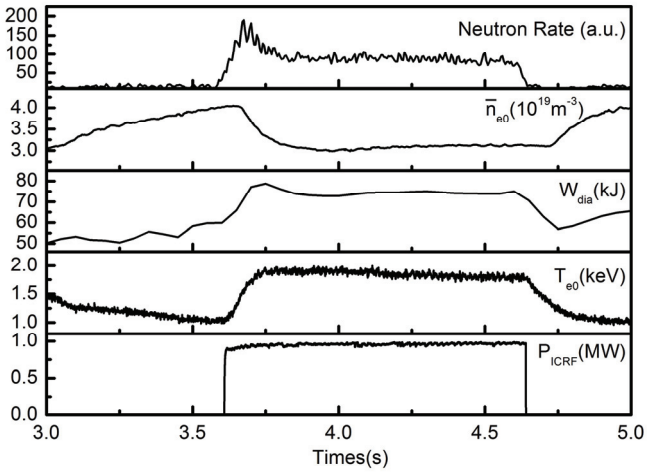

Figure 2. An example of ICRF Heating in EAST from an earlier campaign with 1.0 MW ICRF power at 27MHz injected from the O- and I- port antennas

The second example of this heating[7] from an earlier campaign is shown in Fig.2 where 1.0MW of ICRF power at 27MHz was injected from O and I port two strap antennas into a discharge at 2.0T and 500kA and hydrogen concentration is about 7%. One can clearly see that electron density drops by about 20% after the ICRF power is applied. Heating by ICRF waves may affect the underlying transport of particles in tokamak plasmas. Enhanced transport of particles may thus lead to reduced electron density. The increase in the electron temperature was above 1.0 keV. The stored energy has an increase of 30kJ.

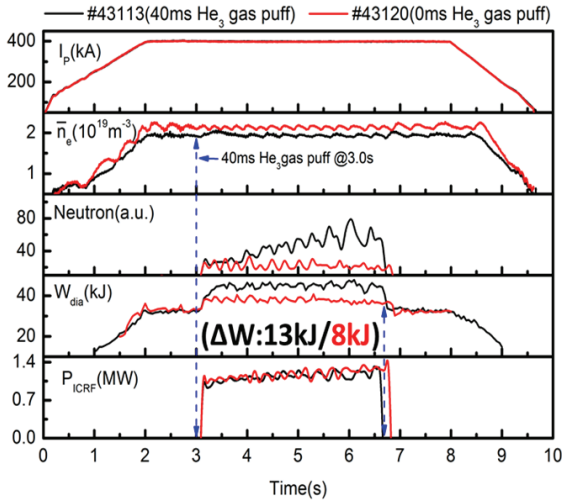

Figure 3. An example of ICRF Heating in D (He3) plasma from the 2012 campaign with 1.0MW of ICRF power injected from the B- and I- port antennas

The first effective heating in D (3He) plasma was observed. This is confirmed by the stored energy and neutron measurements. An example is shown in Fig.3. Traces of two discharges at different Helium 3 gas puff time are compared, where Bt=3.0T and Ip=400kA and hydrogen concentration is about 5%. The fusion neutron rate on both plasma decreases immediately after ICRF power is turned off. Greatly different neutron rates and the stored energy have been observed. This observations show that single pass absorption is weak for the discharge without Helium 3 gas puff. This is also confirmed by a big difference in the stored energy in these two shots.

3. First ICRF-generated H-mode plasma

With D(H) plasma heating, for the first time, the ICRF heated H mode[8] has been reproducibly achieved with injected RF power of ~1.7MW launched by B- and I- port antennas. The H-mode plasma is sustained up to 3.45 s, as shown in Fig.4. H-modes started with a short ELM-free period, lasting ~ 500 ms, followed by type III ELMs (figure 4 (a)) with frequencies from 200Hz to 500Hz (figure 4 (b)). Confinement times for the H-mode discharges are in the range of 110ms to 150ms for 1.7 MW of total heating power at 500 kA. The H factor, $H_{IPB98}(y, 2)$, for the L mode plasma just before the transitions is about 0.5 and then up to 0.7±0.1.

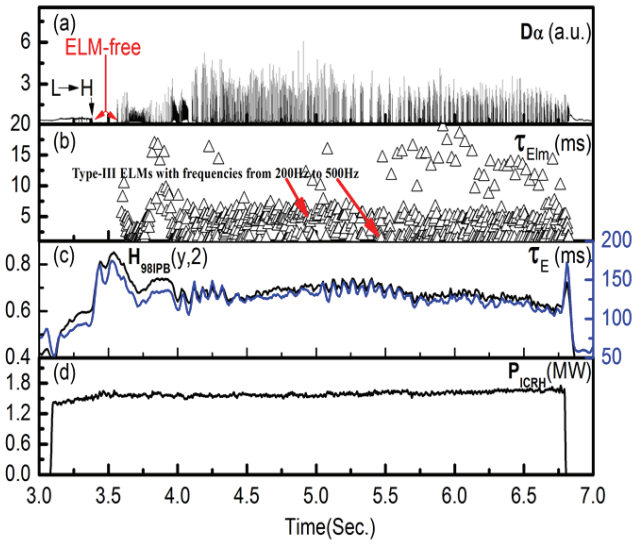

Figure 4. An example of ICRF heated H mode from the 2012 campaign with 1.7MW of ICRF power injected from the B- and I- port antennas

3. Summary

An ICRF system with power level up to 6.0 MW (1000 s) has been built for the EAST at ASIPP. Effective ions and electrons heating due to ICRF were successfully achieved in EAST. The H-minority heating scheme was shown to provide the best performance, and the increase of the stored energy reached 30 kJ using ICRF alone. Using this heating, first ICRF heated H-mode plasma up to 3.45s was obtained. ICRF heating in D (He3) plasmas was demonstrated for the first time in EAST.

Acknowledgments

The authors would like to acknowledge the support of the EAST operation and diagnostics group. This work was supported partly by National Magnetic confinement Fusion Science Programme (grant no. 2010GB110000). This work was also supported partly by the National Natural Science Foundation of China under grant no.11105179, and 11175208. This work was supported partly by JSPS-NRF-NSFC A3 Foresight Program in the field of Plasma Physics (NSFC no. 11261140328).

Reference

[1] Wan B.N. et al., Fusion Eng. Des. 85(2010) 1048.
[2] Wan B.N. and International Collaborators Nucl. Fusion 49(2009) 104011.
[3] Jiangang Li et al., Nucl. Fusion 51 (2011) 094007
[4] X.J.Zhang, et al. Physics and Engineering Aspects of the ICRF Heating System on EAST，23rd IAEA，2010
[5] X.J. Zhang et al., Plasma Sci. Technol. 13 (2011) 172
[6] Y.J. Shi et al., Plasma Phys. Control. Fusion 52 (2010) 085014
[7] X.J. Zhang et al., Nucl. Fusion 52 (2012) 032002
[8] X.J Zhang et al., Nucl. Fusion 53 (2013) 023004

Recent progress of the ECE diagnostics on EAST

Y. Liu[1], B.L. Ling[1], X. Han[1], C.W. Domier[2], X. Kong[2], N.C. Luhmann, Jr.[2], J. Fessey[3], P. Trimble[3], J.L. Bu[1], A. Ti [1], L.Q. Hu[1], B.N. Wan[1], J.G. Li[1]

(1)Institute of plasma physics, Chinese Academy of Sciences, Hefei 230031, China

(2)Department of Applied Science, University of California at Davis, Davis, California 95616

(3)Euratom/CCFE Fusion Association, Culham Science Centre, Abingdon, Oxon. OX14 3DB, United Kingdom

Abstract

On EAST, a 32-channel radiometer system with wider frequency range and better spatial resolution has been commissioned in 2012, and a Michelson interferometer system from JET was relocated very recently. These systems together with the systems we already have, satisfy the requirement of the electron cyclotron emission measurements on EAST for a wide range of toroidal magnetic field.

I. Introduction

Electron cyclotron emission (ECE) measurements have been widely used in magnetically confined plasmas since the 1960s, to provide the temporal evolution of local electron temperature [1,2] and information on the electron velocity distribution [3,4] with fairly good spatial and temporal resolution. Comprehensive ECE diagnostics have been established on EAST [5]. TABLE 1: ECE diagnostics on EAST lists the ECE diagnostics on EAST, including what we already have and those will be installed soon. The 16-channel radiometer [6,7] has been working since the first pulse of EAST, and it could cover half plasma for an optimum toroidal magnetic field. To make the ECE measurement on EAST more flexible, a 32-channel radiometer was commissioned in 2012. A 20-channel grating polychromator [8,9], which was transferred from PPPL in 2008, has been re-built and tested. Very recently, one of JET's Michelson interferometer systems was relocated to EAST, and will be utilized for the ECE measurement in a very wide frequency range. The cooperation of these systems meets the requirement of ECE measurement on EAST for the toroidal magnetic field up to 3.5 T, and these systems play different role regarding their own specifications. Generally, the Michelson interferometer serves as full spectrum measurement with absolute intensity calibration. The radiometers are ideal for physics study with better spatial and temporal resolution.

TABLE 1: ECE diagnostics on EAST

Name	Frequency range	Resolution	
		Spectral	Temporal
16-channel radiometer	98.5-126 GHz	1 GHz	10 us
32-channel radiometer	104-168 GHz	0.5 GHz	2.5 us
Michelson interferometer	60-1800 GHz	3 GHz	15 ms
Grating polychromator	90-250 GHz	0.5-5 GHz	10 us

This proceeding will focus on the 32-channel radiometer and the Michelson interferometer, and they will be introduced in the following sections. Also introduced in this proceeding is the in-situ absolute intensity calibration system which is being

built now.

II. 32-channel radiometer

The 32-channel radiometer system utilizes an unique receiving optics to minimize the Doppler broadening of the emission layer. Shown in Figure 1, ECE radiation from the plasma is firstly focused by the main lens, and then optically separated into four beams using a set of 3 beamsplitters. The beamsplitters are made of low loss dielectric sheets which have been stretched tight to ensure that the optical qualities of the beams are retained upon reflection from the beamsplitters. The position of each lens is adjusted to form a beam waist in the vicinity of the ECE radiation layer for that receiver. Then each of the 4 beams is downconverted, and divided into 8 channels.

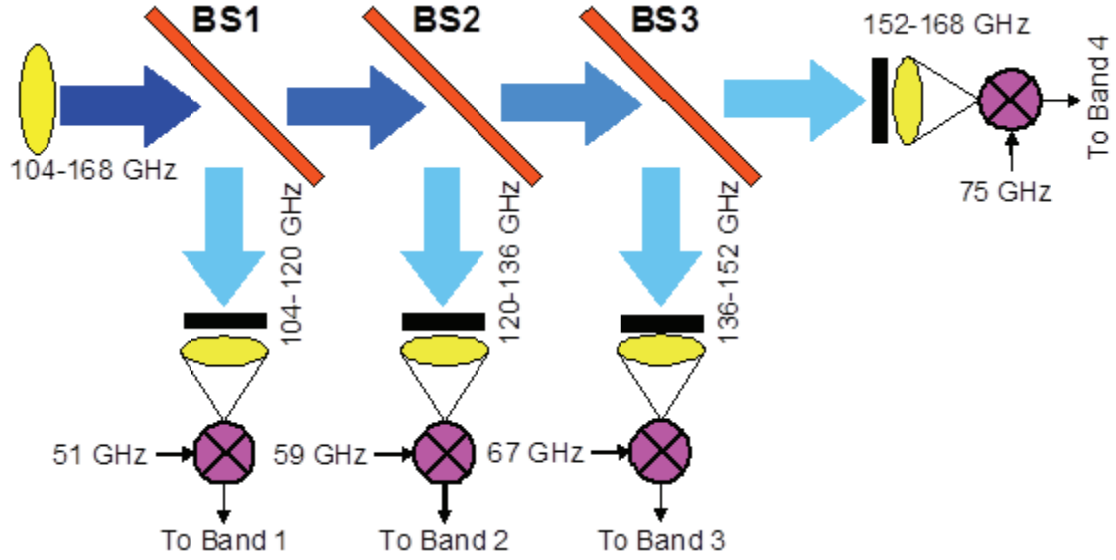

Figure 1: Schematic layout of the 32 channel ECE radiometer

The system has been characterized in laboratory in following steps: (i) to check the linearity and the frequency response of the IF part, (ii) to align the optics and measure the spot size of each receiver, (iii) to measure the noise temperature and sensitivity of each channel. Figure 2 (a) and (b) are separately the measured spot size and linearity characterization for one of the 4 receivers.

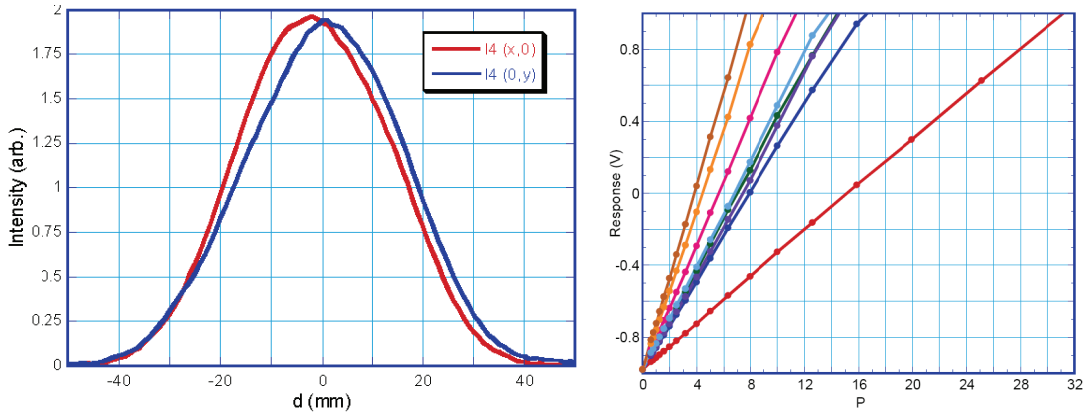

Figure 2: (a) Spot size (b) Linearity

In 2012 experimental campaign, this system has been commissioned, and provided the Te evolution and profiles. Whereas the Te profiles from cross-calibration with other electron temperature diagnostic, indicate that the sensitivity is smaller than

expected values from an in-lab calibration by a factor of around 2. Figure 3 illustrates the cross-calibrated and expected Te profiles for a typical ohmic discharge. The investigation of the cause is still under way and the system will be modified.

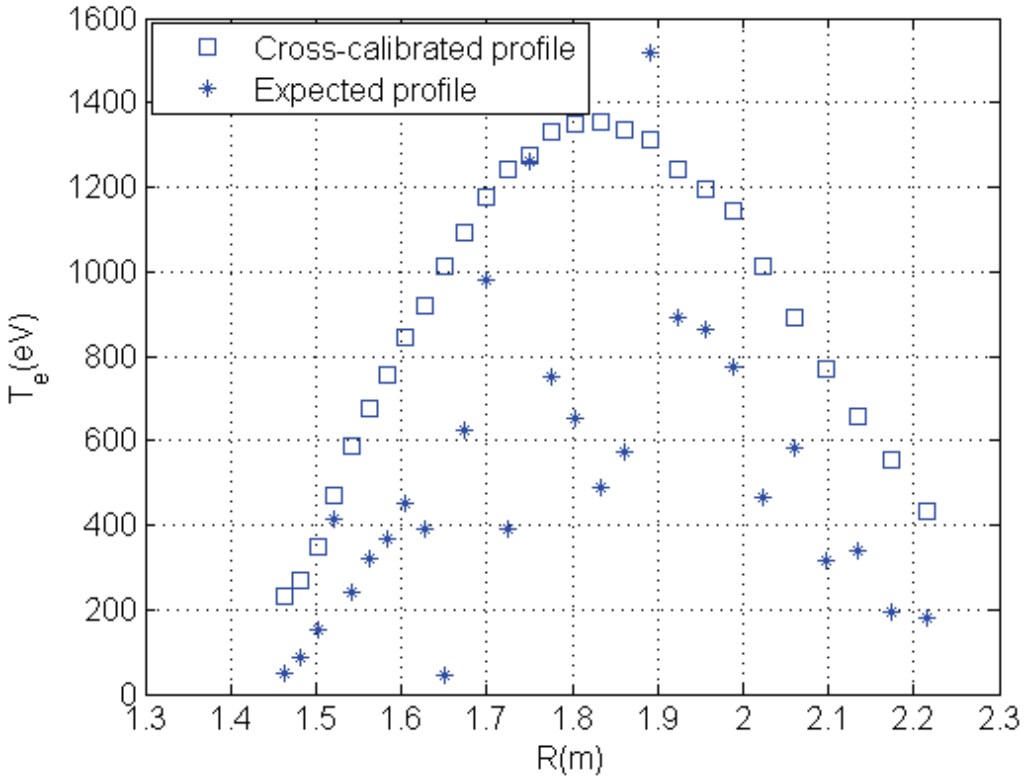

Figure 3: Cross-calibrated and expected Te profiles for a typical ohmic discharge.

III. Michelson interferometer

The Michelson interferometer was originally designed for ECE measurement in JET, and was relocated to EAST recently. The specification of the system is summarized in TABLE 2. It is a high resolution interferometer for infrared Fourier transform spectroscopy over the spectral range 60-1800 GHz with a spectral resolution capability of 3 GHz. The spectral range is limited by the spectral response of the detector, the sampling interval of the moving mirror position, and the spectrum of the calibration source. The spectral resolution is determined by the maximum optical path difference (the scan length). Detailed information concerning about this kind of system can be found in reference [10].

TABLE 2: Specification of the Michelson interferometer

Aperture	Scan length	Active scan length	Scan rate	Sampling interval
70 mm	49.5 mm	46 mm	35 Hz	20 um

Refurbishment and in-lab measurements have been done in JET last year. Figure 4 (a) is the linearity performance of the detector and electronics, and Figure 4 (b) illustrates the measured spectral resolution (of ~2.7 GHz FWHM) using a monochromatic source as input. The system was also tested with hot/cold sources. The in-lab measurements demonstrate that the system is still in a good shape.

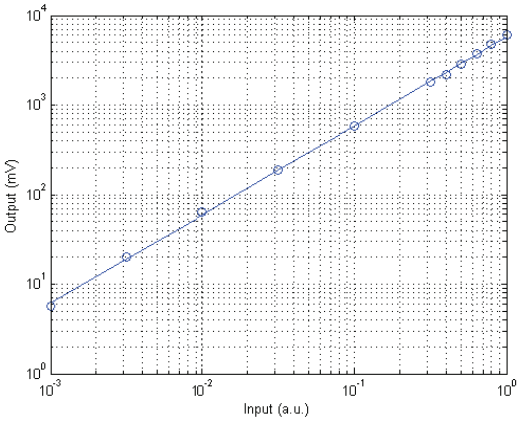

Figure 4: (a) Linearity

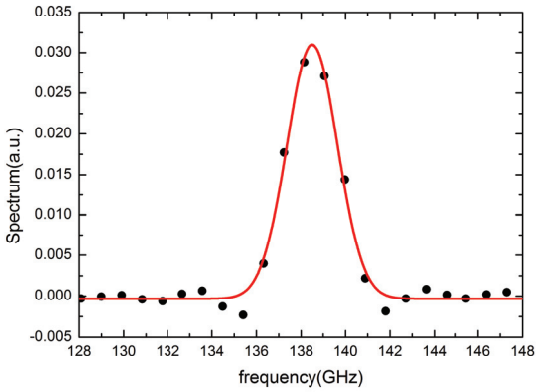

(b) Spectral resolution

IV. Calibration

The ECE measurement systems on EAST were relatively calibrated using two discharges with different toroidal magnetic field in the past [11]. This method is tricky and it is difficult to obtain the accuracy of the calibration. To provide reliable and independent Te information, an in-situ absolute intensity calibration system is being built now. The schematic of the system is shown in Figure 5. The rotatable ellipsoidal mirror can be directed to either the plasma or the calibration source. Microwave absorber immersing in LN_2 is used as cold source, and heated silicon carbide in Pyramid shape acts as the hot source. The chopper and lock-in amplifier are employed to pick-up the ultra-weak intensity from the radiometers or the polychromator, and they are absent for the calibration of the Michelson interferometer benefitting from its high light throughput.

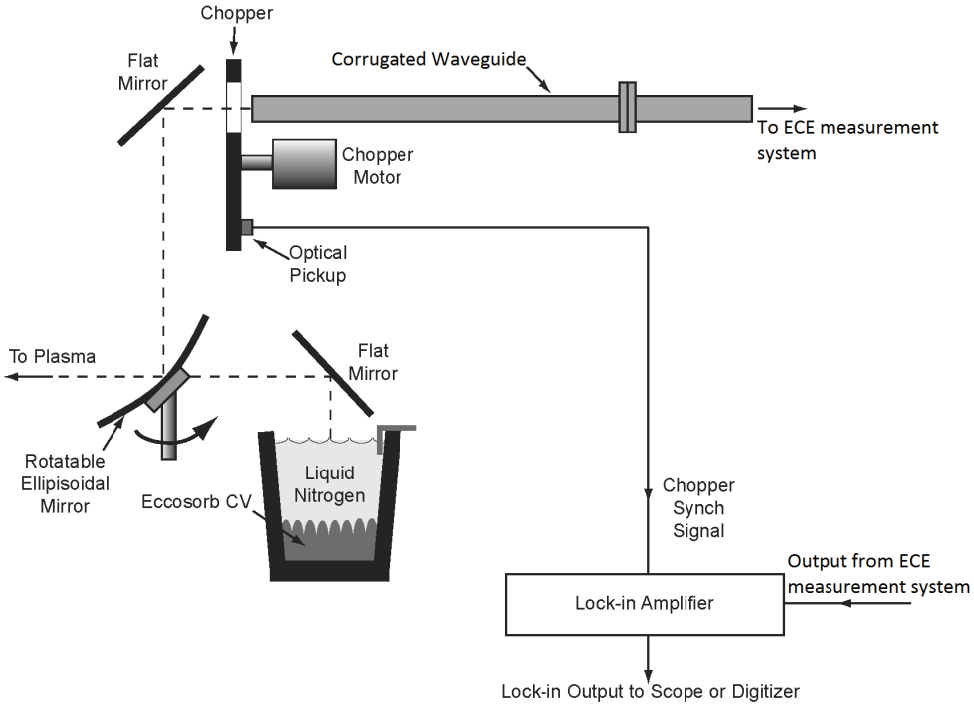

Figure 5: Schematic layout of the in-situ calibration system

V. Summary

A 32-channel radiometer system with better resolution and wider frequency range has been fabricated and tested in 2012 experimental campaign. One of JET's Michelson interferometer systems was relocated to EAST, to meet the requirement of ECE measurement in a very wide frequency range. The refurbishment and in-lab measurements of the Michelson interferometer have been done.

Acknowledgements

This work is supported by the JSPS-NRF-NSFC A3 Foresight Program in the field of Plasma Physics (NSFC No.11261140328), and the National Magnetic Confinement Fusion Science Program of China under Contracts No. 2011GB107000.

References

[1] Lichtenberg A J et al 1964 Phys. Rev. Lett. 13 387
[2] Hutchinson I H and Komm D S 1977 Nucl. Fusion 17 1077
[3] Kato K and Hutchinson I H 1986 Phys. Rev. Lett. 56 340
[4] Kato K and Hutchinson I H 1987 Phys. Fluids 30 3809
[5] Wu S and the EAST Team 2007 Fusion Engineering and Design 82 463
[6] Ling B L et al 2005 Journal of Microwaves 21 66
[7] Ti A et al 2007 Int. J. Infrared Milli. Waves 28 243
[8] Cavallo A et al 1988 Rev. Sci. Instrum. 59 889
[9] Liu Y et al 2011 Fusion Sci. and Technol. 59 657
[10] Schmuck S et al 2012 Rev. Sci. Instrum. 83 125101
[11] Sajjad S et al 2008 Meas. Sci. Technol. 19 075701

Plasma Rotation Behavior of RF-Heated H-mode Discharges on EAST

Bo Lu[1*)], Fudi Wang[1)], Yuejiang Shi[1, 2, 3)], Manfred Bitter[4)], Kenneth W. Hill[4)], Sanggon Lee[5)], Yingying Li[1)], Jia Fu[1)], Yongcai Shen[1)], Hongming Zhang[1)], Yanwei Xiong[1)], Baonian Wan[1)] and the EAST team

[1)]*Institute of Plasma Physics, Chinese Academy of Sciences, Hefei, 230031, China*
[2)]*WCI Center for Fusion Theory, National Fusion Research Institute, Daejeon 305-806, Korea*
[3)]*University of Science and Technology of China, Hefei 230026, China*
[4)]*Princeton Plasma Physics Laboratory, Princeton, New Jersey, USA*
[5)]*National Fusion Research Institute, 52 Eoeun-Dong, Yusung-Gu, Daejeon, Korea*

Plasma rotation driven by RF waves such as lower hybrid current driven (LHCD) and ion cyclotron range of frequencies (ICRF) heating is considered to be able to provide the sufficient rotation for suppressing RWM instability on ITER. Substantial rotation has been recorded on major MCF devices without external momentum input. Recent experimental rotation observations of H-mode plasmas on EAST under LHCD and ICRF were presented in this paper. It was found that co-current core rotation increase was induced for H-mode discharges. For stationary type-III H-mode, core plasma rotation was constant. Type-I ELM decreases the rotation over each burst while ion temperatures remain unchanged. Rotation increase in H-mode plasmas scales proportionally to the increase in plasma stored energy normalized by the plasma current.

1. Introduction

The origin of spontaneous plasma rotation and its characteristics are currently being widely investigated on many tokamaks, since it is considered to be capable of providing the sufficient rotation required for steady-state operations of ITER and future fusion devices, on which neutral beam may not provide enough torque input due to high density and large machine size [1]. This was based on the extrapolation from the scaling derived from the current experiment data of H-mode discharges on several major devices with varying sizes and operating conditions. Currently, LHCD and ICRF are the only auxiliary heating schemes on EAST, which can deliver a maximum power of 4MW and 6MW, respectively. Steady-state long pulse H-mode plasmas have been obtained in the recent campaigns [2]. EAST provides the unique capability of studying spontaneous rotation behaviour under auxiliary heating and current drive without perturbations from external momentum source. During the latest EAST campaigns, plasma rotation profiles were measured for a wide range of plasma conditions and related physics experiments were carried out on EAST.

EAST is a fully superconducting tokomak (R~1.85m, a~0.45m, B_t<3.5T, I_p~1MA) with flexible magnetic configuration and wall conditioning techniques, which is aimed at long-pulse steady-state high performance plasma operations [4]. Since the 2010 campaign, several major upgrades have been carried out, including the replacement of first wall material with molybdenum tiles and upgrade of ICRF and LHW system with a total power of 6MW and 4MW, respectively. Lithium wall conditioning techniques were also improved and several new fueling techniques (pellet injection, supersonic molecular beam injection) were added. These upgrades have greatly extended the EAST's operation regimes. Long-pulse steady-state H-mode plasmas have been readily achieved in the recent EAST campaign [2]. Ion temperature and plasma rotation were reliably measured with two imaging X-ray crystal spectrometers for the core plasma [3]. Recently, the spectrometer was upgraded to improve the time and spatial resolution (~10ms and ~1cm) using new X-ray detecting technology [3]. This passive spectrometer is capable of providing measurements for nearly all kinds of discharges with auxiliary heating schemes. The rotation measurements presented in this paper were entirely from the tangential X-ray crystal spectrometer on EAST.

2. Rotation characteristics of steady-state ELMy H-mode discharges

Figure 1 plots the time histories of plasma parameters for a stationary LSN H-mode discharge with H-mode duration of ~5.9s. Lower hybrid wave (f=2.45GHz, $n_{//}$=2.1) and ICRF wave (f=27MHz) are applied at 1.5 and 1.2 MW, respectively.. On-axis ICRF heating occurs for the toroidal field of ~2.0T. Lower hybrid wave was injected at as early as 0.75s during the current ramp-up phase to suppress the runaway generation at the beginning of the discharge. L-H at 3.1s shortly after the application of ICRF wave, as could been seen in the density increase, the sudden drop in the divertor Dα signal, and the abrupt increase in central electron density, central plasma temperatures and stored energy, and the co-current increase in the central toroidal rotation. The plasma exited H-mode following the withdrawal of ICRF wave at ~9.0s, after which the stored energy, electron density and rotation velocity, plasma temperatures all returned to their previous L-mode values.

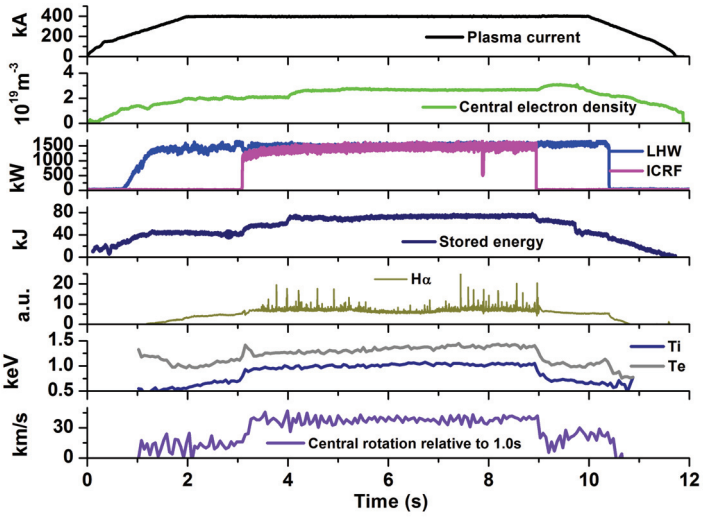

Figure 1 Time histories of plasma parameters for a LHW/ICRF steady-state H-mode discharge (#43251)

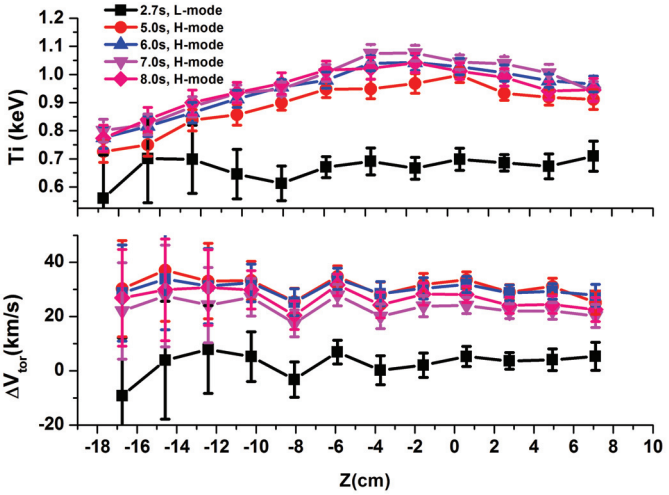

Figure 2 Profile of ion temperature and plasma rotation (#43251)

After L-H transition, central electron density increases from 2.0×10^{19} to 3.0×10^{19}m^{-3}. Plasma stored energy increased from 40kJ to 70kJ. Ion temperature increases from 0.6keV before L-H transition to about 1.0keV in the H-mode phase, while electron temperature increases from 1.2keV to 1.4keV in the H-mode phase. Central rotation increase of 40km/s relative to the L-mode phase was induced due to L-H transition, which takes about ~300ms to reach steady-state. All these parameters remain nearly unchanged during the H-mode phase.

Profiles of ion temperature and plasma rotation were also measured. Figure 2 plots the profile of ion temperature and plasma rotation of the core plasma relative to the L-mode phase at 1.0s for five different moments. It can be seen that ion temperatures are centrally peaked on the magnetic axis. Ion temperature increases over L-H transition and the profiles remain nearly unchanged during the H-mode period. The rotation profiles were also elevated following L-H transition during the entire H-mode phase. For the region covered by the tangential XCS, the rotation profile is very flat. Different from the C-Mod results, the increase in the central rotation is already in the co-current direction before the injection of ICRF, which was induced by LHCD [7]. Although the rotation velocity remains very stable, it could be seen that rotation does change slightly when ELMs burst.

Since other parameters were kept constant, ELM bursts might be the source of the change in rotation, which is more prominent in type-I ELMy discharges.

3. Rotation characteristics of steady-state type-I ELMy H-mode discharges

Type-I ELMy H-mode was also obtained with high-power auxiliary heating. Figure 3 plotted time histories of plasma parameters for a discharge with type-I ELMs. The current was lowered to 0.3MA to reduce the power threshold. LHCD (f=2.45GHz, $n_{//}$=2.1) and ICRF (f=27MHz) are injected at 1.2 and 1.8 MW, respectively. L-H transition occurs at 2.77s, first followed by a period of ELM-free phase and then type-I phase before back transition to the L-mode again. The frequency of ELM ranges from 6Hz to 25Hz.

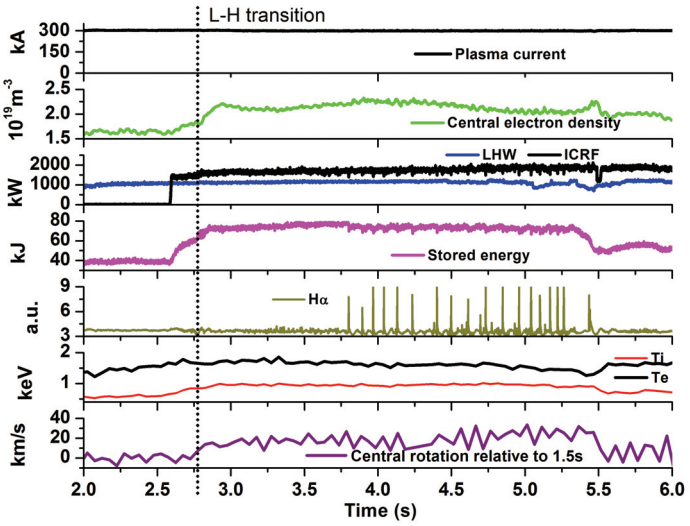

Figure 3 Time histories of plasma parameters for a LHW/ICRF type-I ELMy H-mode discharge (#42556).

For each type-I ELM burst, there is simultaneous drop in the stored energy (3-6 kJ per burst). Between two consecutive bursts, the stored energy tends to recover. ELM also changes the central rotation velocity. On JET, the effect on rotation for type-I ELM of NBI H-mode plasmas was only seen for the outer region up to $r/a \sim 0.65$, with no effect on the core region [8]. The difference may be due to the different heating mechanism between NBI and RF. Figure 4 plots the profiles of ion temperature and rotation velocity at three different times with t=3.77s close to and before the first ELM burst, t=3.85s between the first and second bursts, and t=3.93s between the second and third bursts. For T_i, there was nearly no noticeable change caused by the ELM burst; while the rotation profile was different at pre- and post- ELM burst, with different magnitude of change for each burst. For example, for the first two bursts presented here, the maximum change in rotation velocity is about 9.0 and 13.0 km/s, respectively.

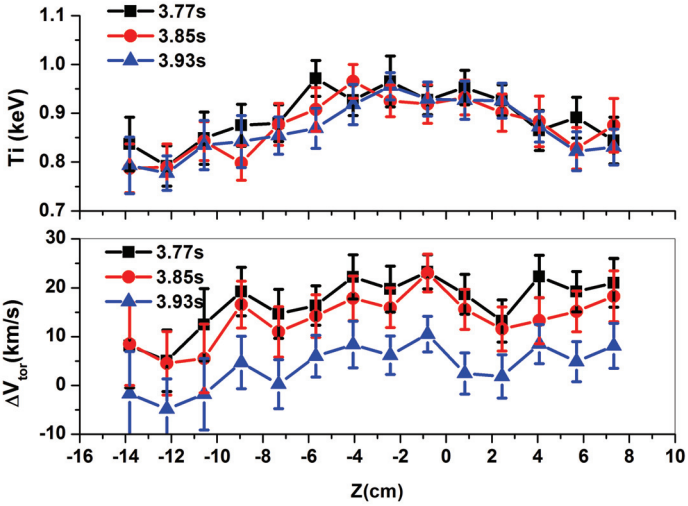

Figure 4 Profile of ion temperature and plasma rotation (#42556)

4. Global scaling of rotation

The effort to unify the rotation measurement on various devices has led to global Rice scaling law for H-mode plasmas, i.e. the core rotation change is proportional to the change in the stored energy divided by the plasma current [1]. The scaling works on various devices for Ohmic H-mode plasmas or plasmas with different auxiliary heating methods Experimental observations for

LHCD/ICRF H-mode plasmas on EAST were also collected. Figure 5 showed the rotation increase over L-H transition as a function of the change in plasma stored energy normalized by plasma current. Two groups of data were included: one for LHW/ICRF H-mode with I_p=0.4MA and the other for ICRF H-mode discharges with I_p=0.5MA. It can been that there is a clear linear trend between the rotation change and plasma stored energy change normalized by the plasma current.

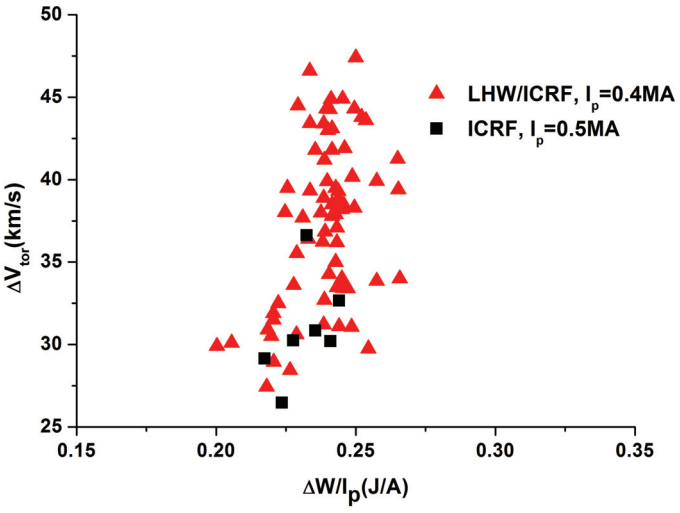

Figure 5 The change in central rotation as a function of the change in stored energy

5. Conclusions

Profiles of H-mode plasma rotation and ion temperature under LHCD and ICRF heating were measured using high-resolution X-ray crystal spectrometer on the EAST tokamak. Strong co-current rotation increase over L-H transition was effectively driven by the two waves. For steady-state ELMy H-mode discharges, plasma rotation is also very stable and the profiles remain nearly constant during the H-mode phase. Type-I ELM H-modes were also obtained with lowered plasma current. Rotation was found to be reduced by the ELM burst. H-mode rotation change on EAST also follows consistently the Rice scaling.

Acknowledgement

The authors are thankful to the diagnostic group, vacuum group, LHCD and ICRF group and the operation team of EAST. The work is supported by National Magnetic Confinement Fusion Science Program of China (No. 2011GB101000, 2011GB107000, 2012GB101000 and 2013GB112004), National Science Foundation of China (No. 10975155, 10990212 and 11175208) and JSPS-NRF-NSFC A3 Foresight Program in the field of Plasma Physics(NFSC,No.11261140328)

References

[1] Rice, J.E, et al.,Nucl. Fusion **47** (2007) 1618.

[2] Wan, B.N., et al., Proceeding of 24th IAEA FEC (2012).

[3] Lu, B., et al., Rev. Sci. Instrum. **83** (2012) 10E130.

[4] Wan, B.N., et al., Nucl. Fusion **49** (2009) 104011.

[5] Shi, Y.J., et al, Plasma Phys., Control. Fusion **52** (2010) 085014.

[6] Wang, F.D., et al., J. Korean Phys. Soc. **59** (2011) 2734.

[7] Shi, Y.J., et al., Phys. Rev. Lett. **106** (2011) 235001.

[8] Versloot, T.W., et al., in JET", Plasma Phys. Control. Fusion **52** (2010) 045014.

R & D of PFMC at ASIPP

G. -N. Luo

Institute of Plasma Physics, Chinese Academy of Sciences, Hefei, 230031China

Abstract

A project to realize a W/Cu divertor on Experimental Advanced Superconducting Tokamak (EAST) with ITER-like Plasma Facing Component (PFC) configuration before 2015 has been launched in order to withstand rapid increase in particle and power impact onto divertor and demonstrate the feasibility of the ITER design under practical long pulse tokamak plasmas. The EAST W/Cu divertor consists of ITER-like monoblock targets and flat type or coating dome. Both mono-block and flat type W/Cu PFCs are under development using different technologies. Once this project completed, together with the expected long pulse high performance plasma EAST will be the best testing device for the ITER divertor physics, design and engineering issues.

Key words: Plasma Facing Component, mono-block, flat type

1. Introduction

EAST W/Cu divertor project with ITER-like PFC configuration and the expected heat removal capability of 10MW/m^2 has been launched and will be completed before 2015. The EAST W/Cu divertor consists of ITER-like mono-block targets and flat type or coating dome. Three kinds of actively-cooled W/Cu-PFCs with direct connection of W as Plasma Facing Material (PFM) to CuCrZr heat sink are under development currently at ASIPP. The first is mono-block type similar to that to be used for the ITER divertor targets [1]. The second is flat type with many flat W tiles brazed directly onto the heat sink, and the third is vacuum plasma spraying (VPS) and chemical vapor deposition (CVD) W coatings on the Cu heat sink [2].

2. The PFC development strategy for EAST

The EAST has been designed to operate under long pulse/steady state conditions. Such operation conditions impose severe criteria for the PFMC. Application of the PFMC in EAST machine has been divided into several phases [3]. The first is the initial phase (2006-2007), employing SS-316L plates directly bolted to the supporting structure. In the first phase (2008-2010), the PFMC is the GBST1308 graphite tiles bolted to Cu alloy heat sink. In the transition phase (2011-2012), PFMC for first wall was changed into TZM and kept carbon on divertor. In the second phase (2013-2014), PFMC for upper divertor will be changed into ITER-like actively-cooled W/Cu-PFC, and then lower divertor will be upgraded to W/Cu-PFC in third phase (2015-) .

3. Structure design of EAST divertor

The structure design of EAST divertor has been finished and R & D started for the key issues. The upper divertor consists of 80 cassette bodies that support the components of mono-block vertical targets and flat type domes and baffles, as shown in fig.1. The tolerance of all PFCs in toroidal direction is 1mm and the step of neighboring blocks is 0.5mm.

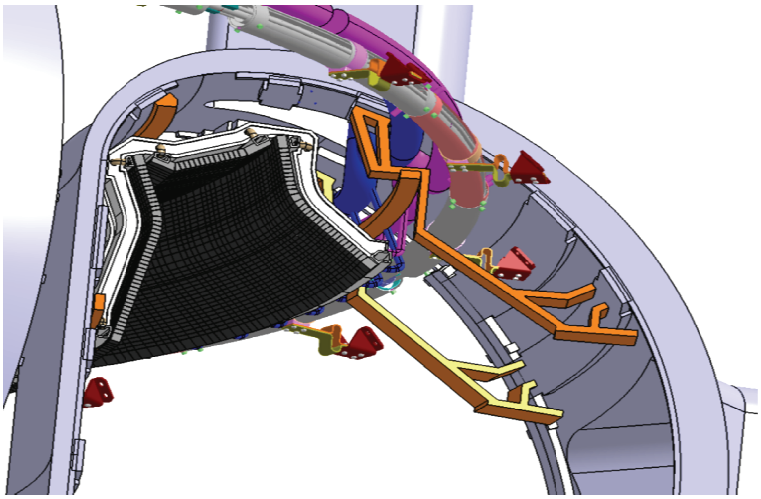

Fig.1 structure design of EAST divertor

4. Mono-block W/Cu PFCs

ITER grade W and ITER-like W/Cu mono-blocks have been manufactured recently in collaboration with domestic institutions at batch scale. The joining of W mono-blocks and pure copper interlayer were achieved by means of HIP technology. Fig.2a shows a W block manufactured by the HIP process. The good quality of bonding between W and Cu was achieved and the bonding strength was about 150MPa. Fig.2b shows a SEM picture of the bonding interface of W and Cu.

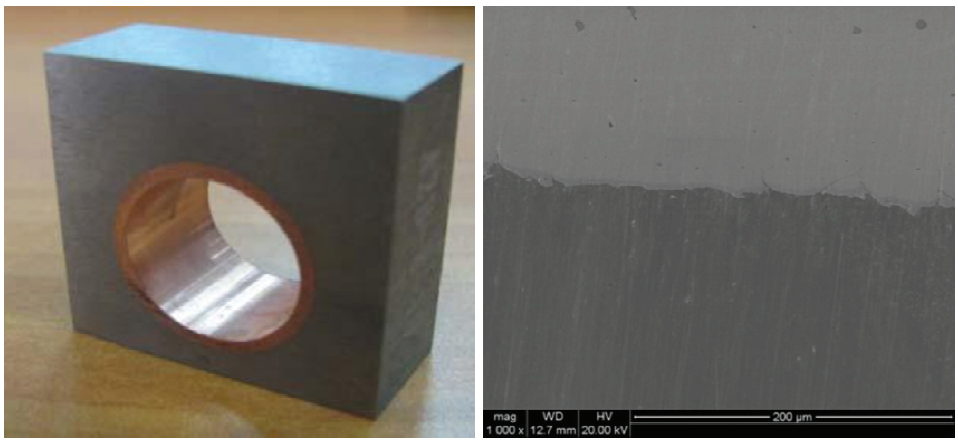

Fig.2. a) A tungsten block manufactured by HIP process; b) A SEM picture of the bonding interface of W and Cu.

The joining of W mono-blocks with pure copper interlayer and CuCrZr tubes were obtained by hot radial pressing (HRP) or hot isostatic pressing (HIP) technologies. Some small cacle W/Cu mock-ups were manufactured by HRP and HIP method, as shown in Fig.3 and 4, and Ultrasonic NDT shows that the bonding of tube and copper was excellent.

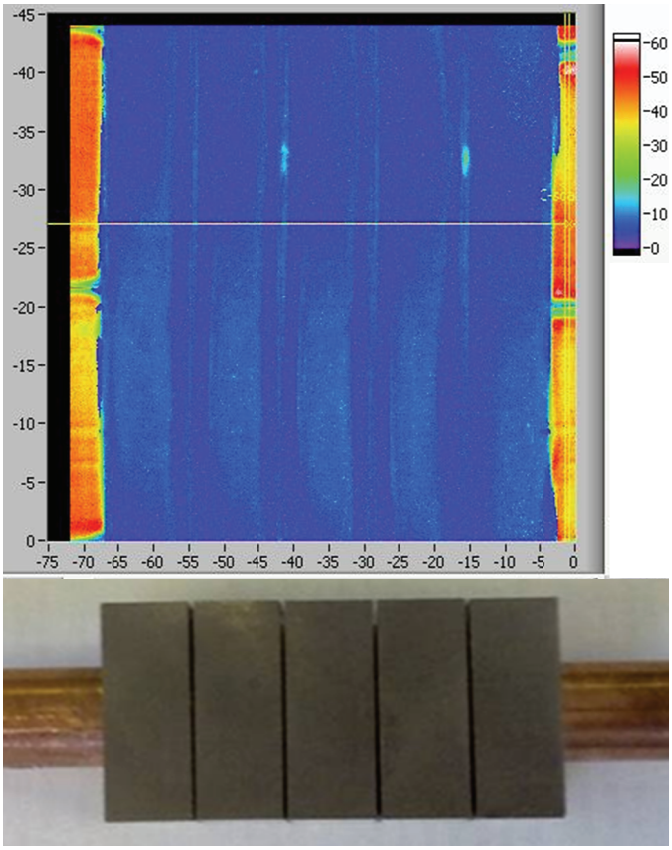

Fig.3. Results of Ultrasonic NDT of the W/Cu mock up with five W tiles manufactured by HRP method.

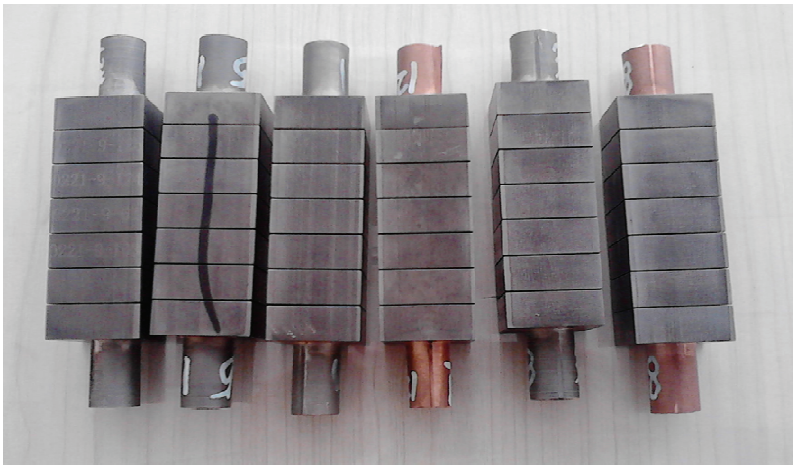

Fig.4. A picture of mono-block W/Cu mock-ups

5. Flat type W/Cu PFCs

Flat-type W/Cu PFC which may be applied on dome and first wall region has also been being explored by means of HIP or VHP technologies. The interface of W/Cu was joined by HIP or casting at higher temperature and then the interface of Cu/CuCrZr was bonded by VHP or HIP at lower temperature of 500-600℃. Good quality of the W/Cu interface tested by ultrasonic inspection NDT was also obtained. Fig.5 shows a picture of Flat-type W/Cu mock-up with six W tiles. VPS and CVD W coatings on castellated CuCrZr heat sink with a pure copper interlayer joined previously to it by HIP or VHP methods were also developed.

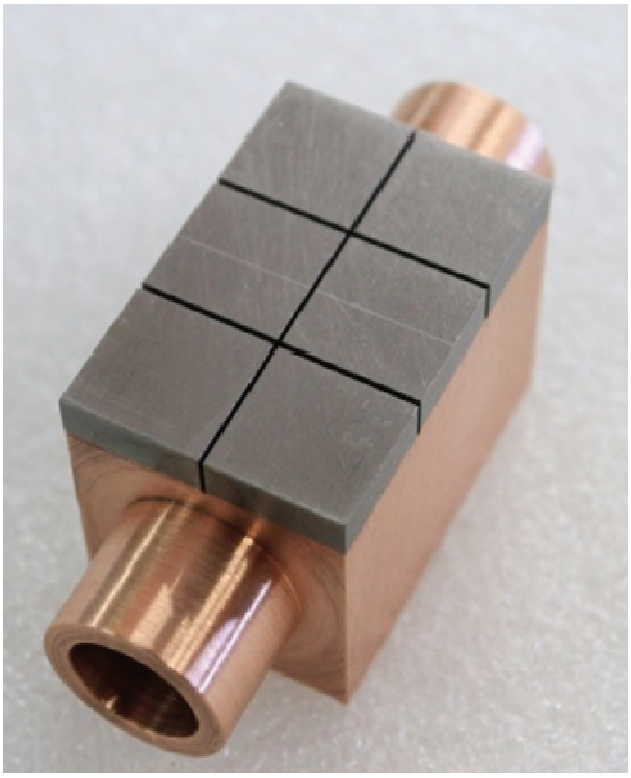

Fig.5. A picture of flat type W/Cu mock-up

6. High heat flux testing

In order to evaluate the thermo-mechanical performance of the mock-up manufactured by "HIP+HRP" technology under cyclic thermal loads, thermal fatigue testing has been performed by means of an e-beam device at SWIP. Because of limitation of the cooling condition, the mock-up was cooled with the cooling water parameters of 2m/s, 20℃, 0.2MPa. To perform thermal fatigue testing, 1000 cycles at absorbed heat load of 8.4MW/m^2 were loaded on the mock-up with the acceleration voltage of 140 kV and the current of 190 mA. The cycle times were 15s on and 15s off. The mock-up survived 1000 cycles heat loads with no significant changes in its temperature response. Fig.6 shows the developments of the surface temperature distributions of the mock-up during the 1st (up) and 1000th (down) cycles. It was observed that the temperature of the surface reached stable at 10s after loading on. No change of the surface temperature response of the mock-up was observed during 1000

cycles of heat loads. Ultrasonic NDT was performed after the thermal fatigue testing and no obvious defects were detected.

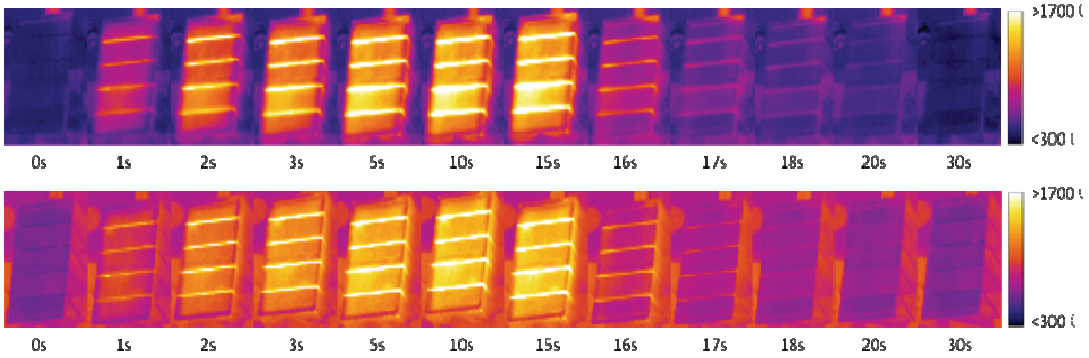

Fig.6. The developments of the surface temperature distributions of the mock-up during the 1st (up) and 1000th (down) cycles.

7. Conclusions

With rapid increase in H&CD powers, EAST will upgrade its divertor to ITER-like structure before 2015. The structure design of EAST divertor has been finished and R & D started for the key issues. Both mono-block and flat type W/Cu PFCs are under development using different technologies. For W/Cu mono-block PFCs, two innovative technologies of "HIP+HRP" and "HIP+HIP", i.e., W mono-block joining with a pure copper interlayer by means of HIP technology and then the W mono-blocks with the pure copper interlayer welding to a CuCrZr tube by means of HRP or HIP technologies, were developed. The manufacturing process of the W/Cu flat type PFCs is that pure copper was casted firstly onto the W tiles and then the W tiles with copper interlayer were joined to CuCrZr heat sinks by means of HIP or VHP technologies. VPS and CVD W coatings were also developed for EAST. The thermal cycle fatigue testing of the mock-up manufactured by "HIP+HRP" has been carried out by means of an e-beam device in Southwest Institute of Physics, Chengdu (SWIP) and the mock-up withstood 1000 cycles of heat loads up to 8.4MW/m^2 with the cooling water of 2m/s, 20℃. Till now, R & D for W/Cu-PFCs was almost finished and batch production contract starts soon.

Acknowledgement

This work is undertaken partially under the support of the JSPS-NRF-NSFC A3 Foresight Program in the field of Plasma Physics (National Nature Science Foundation of China, NSFC, No.11261140328).

References

[1] G. -N. Luo, et al., Development of W/Cu Divertor Components for EAST, 13th International Workshop on Plasma Facing Materials and Components for Fusion Applications, Rosenheim, May 9-13, 2011.

[2] G. -N. Luo, et al., Coating Materials for Fusion Application in China, Journal of Nuclear Materials, **417**(1-3) (2011) 1257.

Research plan of plasma wall interactions in EAST and LHD

Naoko Ashikawa
National Institute for Fusion Science, 509-5292, Toki, Japan

1. Purpose of study

Mechanisms of hydrogen retention and hydrogen isotope-exchange reactions in deposition layer and bulk target in plasma facing wall are important issues investigated in fusion devices. These plasma wall interactions relate to wall recycling, a dilution of fueling gasses and tritium inventories in vessel are important issues in EAST, LHD, ITER and DEMO.

In this study, two kinds of experimental plans were set in EAST and LHD. One is samples exposed to EAST plasmas during two days to investigate mechanisms of deuterium retention and deposition layer. The other is samples exposed to LHD plasmas during one experimental campaign to investigate characterization of deposition layer and their hydrogen trappings.

2. Instrumentation method

A. Sample setup

Two molybdenum sample holders (our group made holders) are set on cupper cooling plate of MAPES in EAST. 6 samples of 10 mm x 10 mm x 1 mm are installed in a holder as shown in Fig.1. One holder is used for each experimental topic, such as tungsten experiment and an isotope exchange experiment. Details are as followings,

1) Bulk tungsten prepared for manufacturing of mono-block tungsten/cupper target for EAST for tungsten retention experiment.

Target samples cut from the bulk tungsten prepared for manufacturing of mono-block tungsten/cupper target for EAST are exposed to the EAST first wall plasmas using MAPES.

2) Bulk tungsten (polished) tungsten deposition on bulk tungsten, silicon for hydrogen isotopes exchange reaction experiment.

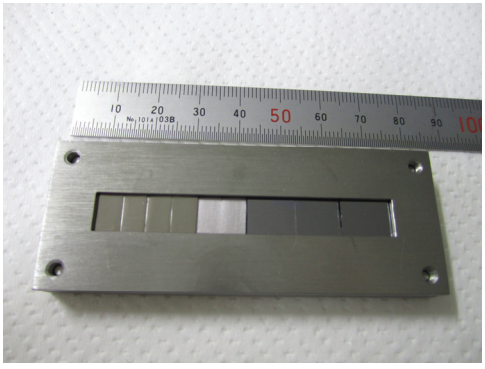

Fig.1 Mo sample holder

Tungsten deposited layer will be produced on tungsten substrate (W bulk) in hydrogen plasma by using the capacitively coupled RF plasma sputtering in Kyushu Univ.. The sputtering device is a parallel plate type generally used. A tungsten plate (99.95% in purity) was mounted on a cathode electrode as sputtering target material. Tungsten substrates were mounted on an anode electrode. When an RF power of

13.56MHz is supplied to the cathode electrode, plasma discharge begins between the cathode electrode and the anode electrode. The tungsten plate on the cathode electrode is sputtered by ion incidents from plasma and emitted tungsten atoms are deposited on the substrates. The thickness of the deposited layer will be about 1 μm.

B. Plasma experiment

Samples expose to deuterium plasma by MAPES in EAST. In the same plasma experiments, Dr. A. Litnovsky (Juelich, Germany) sets his tungsten targets on Cu cooling plate of MAPES, and then pulse lengths per a shot, total number of discharges, position of MAPES and plasma parameters (ne, Te, Wp, et al.,) are determined by Dr. A. Litnovsky. Our samples are not attached plasma and this control is done by a difference of thickness between our sample holders and Dr. A. Litnovsky's holders and Dr.F.Ding organizes this positioning control.

C. Diagnostics

For target samples and holders, thermocouples are needed with their time evaluation. Langmuir probes are set on Cu cooling plate to measure parameters of edge plasma. Standard diagnostics in EAST are also needed.

D. Analysis

1) Postmortem surface analysis is carried out for the tungsten samples at Japan Atomic Energy Agency. Depth profiles of deuterium and some impurities such as carbon are measured by secondary ion mass spectroscope (SIMS).Chemical state of the impurity in the tungsten samples are analyzed by X-ray photoelectron spectroscope (XPS). Deuterium retention and desorption characteristics are measured by thermal desorption spectroscopy (TDS). Trap energies for deuterium in the tungsten samples are analyzed by simulation of thermal desorption based on the results of post mortem surface analysis. In order to investigate the detailed mechanisms of deuterium retention in the tungsten samples exposed to EAST tokamak plasmas, same surface analysis following plasma irradiation experiments using similar tungsten samples is planned.

2) It has been found from our previous studies that the deposited layer has large porosity (0.3-0.7) and a large amount of hydrogen is retained during sputter-deposition process(H/W:0.01-0.25).However, the behavior of hydrogen isotopes in the deposited layers has not been understood sufficiently so far. In this experiment, we focus on an isotope exchange in the deposited layer. After the deposition layers are exposed to deuterium plasma discharges, TDS analysis will be carried out. From the change of the amount of hydrogen isotopes (H and D) in the deposited layer, we can evaluate an effect of charge exchange particles produced by main plasma discharges. Further, we can discuss the mechanism of hydrogen-isotope exchange in porous tungsten materials. SEM-EDX observation will be done before TDS analysis in order to investigate crack,

flaking, deposition of sample targets. Impurities/lithium depositions and chemical state on samples are analyzed by X-ray photoelectron spectroscope (XPS).

3. Experimental result

The first experiment using MAPES in EAST was done in 2012. Deposition layer at exposure position using MAPES is very thin and this thickness is about 10-20 nm during two days as shown in Fig.2. Main concentrations of deposition layer are oxygen and carbon. Small amounts of iron molybdenum also observed. Lithium used by wall conditionings is not observed and then influence of Li re-deposition is negligible.

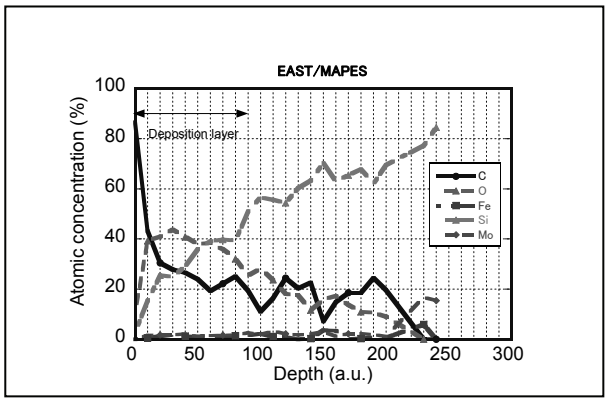

Fig.2 atomic concentration of deposition layer

Tungsten deposition layer on bulk tungsten were exposed to deuterium plasma in EAST. Retained hydrogen and deuterium were measured by thermal desorption spectrometry (TDS). Initial amounts of hydrogen were implanted by working gassed during sputtering to make deposition layer and this ratio between tungsten and hydrogen, H/W, is 0.032. This amount of W/H to compare with before and after plasma exposures are the same. Retained deuterium after plasma exposure was implanted by deuterium plasma in EAST and the ratio between tungsten and deuterium, D/W, is 0.002. A deuterium trapping depth on targets is mainly deposition layer and amount of initial hydrogen did not change after plasma exposure.

From X-day photoelectron spectroscopy (XPS) measurement, W and Li signals are negligible on deposition layer. Li was not injected and only a night it was operated during experiments. But MAPES escaped from main chamber to outside of gate-valve at night. Small amounts of Fe and Mo were observed. An estimated thickness is about 10-20nm, and it is needed calibrations of this thickness in future plan.

Deposition layers in LHD, hydrocarbon bindings are measured by ellipsometry in NFRI. TDS, scanning electron microscope (SEM), XPS, Raman spectroscopy were done as previous analysis in Japan and then amounts of retained hydrogen and ratio between carbon and hydrogen were shown. Characteristics of carbon bindings seem like amorphous carbon measured by Raman and XPS and a difference for different types of carbon bindings and compositions in this experiment were not clear. Two kinds of parameters, refractive index and extinction coefficient, are measured by ellipsometry and

a comparison with results of reference target for C2H2-DLC, C2H4-polimar like, CH4-DLC and CH4-polimer like were done. From refractive index, deposition layers in LHD are similar to C2H4-polimar like and CH4-DLC.

4. Study results

Two kinds of experiments and analysis for plasma wall interactions were done in EAST and LHD. MAPES in EAST is useful tool for experiment of plasma wall interactions and we have a plan to apply in the next experimental campaign in 2013-2014. During this seminar, we have a discussion to improve of our experimental plan toward next campaign.

STAR is one of useful devices. We started new researching frameworks of plasma wall interactions with previous research for deposition layer in LHD. New results for hydrocarbon bindings of carbon deposition layer measured by ellipsometry in NFRI are shown. It is important result related a removal of hydrogen-isotopes, such as tritium.

5. Future subject

In J-C collaborations, improvements of experimental setup at next campaign in MAPES/EAST were discussed. Motivations in next EAST experiment are deuterium retention of tungsten target and hydrogen isotope-exchange reactions by wall conditionings In J-K collaboration, more discussions about hydrocarbon bind of carbon deposition layer in LHD are planned.

6. Acknowledgements

This work was partly supported by the JSPS-NRF-NSFC A3 Foresight Program in the field of Plasma Physics (NSFC: No.11261140328).

Korean Plasma-Material Interaction Researches/Facilities

K.-S. Chung[1,2,*], H.-J. Woo[1,2], S.-G. Cho[1,2], Y.-S. Choi[3], S.-H. Han[7],
B.-G. Hong[4], S.-H. Hong[6], H.-S. Kim[5], S.-J. Noh[5], T. Lho[3], S.-J. Park[1,2], and H.-J. You[3]

[1]*Dept. of Electrical Engineering, Hanyang University, Seoul 133-791, Republic of Korea*
[2] *Center for Edge Plasma Science (cEps), Hanyang University, Seoul 133-791, Republic of Korea*
[3]*Plasma Technology Research Center, National Fusion Research Institute, Daejeon 305-333, Republic of Korea*
[4]*High Enthalpy Plasma Research Center, Chonbuk National University, Jeonju, Jeollabuk 561-756, Republic of Korea*
[5]*Dept. of Applied Physics, Dankook University, Yongin, Gyeonggi 448-701, Republic of Korea*
[6]*KSTAR Team, National Fusion Research Institute, Daejeon 305-333, Republic of Korea*
[7]*Korea Institute of Science and Technology, Seoul, Republic of Korea*
*kschung@hanyang.ac.kr

I. INTRODUCTION

Plasma-material interaction in fusion devices is one of the key issues for the success of ITER and DEMO, which is complex and coherent[1], one needs to understand the edge plasma state, material damage, and their mutual interactions. Generally, the plasma-material interactions should be analyzed by studying the plasma properties in the scape-off layer and divertor (limiter) regions[2], material erosion and deposition[3], impurity transport[4], fuel retention[5], dust production and detection[6]. This indicates that the laboratory simulations of PMI are necessary to quantify the long-term results of plasma-beam illuminations on the plasma facing components, and to repeat a tedious and multiple procedures. For these, various PMI facilities have been developed recently in Korea, such as DiPS, MP2, ECR plasma, a segmented plasma torch system, e-beam accelerator, and the TReD (Transport & Removal experiment of Dust) device. In this paper, these devices are briefly to be explained in terms of objective and specifications along with initial experimental results.

II. PMI FACILITIES

II.A. DiPS-2 Linear Plasma Facility

DiPS (Divertor Plasma Simulator)-2 has been modified from the DiPS-1 [7] to focus the edge plasma simulation and plasma-material interaction research with diagnostics developments, while the latter had wide range of applications : fusion, space and processing plasma simulations. DiPS-2 generates the plasma a LaB_6 cathode like DiPS-1. The main objective of DiPS-2 is the development of plasma diagnostics for the fusion edge plasmas, edge plasma simulations such as the effect of atomic processes in the scrape-off layer (SOL) and divertor regions, and material test of the plasma facing components (PFCs).

Four-inch LaB_6 disk is heated by a graphite heater cooled by water, and it has a central hole for the passage of LIF(laser induced fluorescence) system. Figure 1 shows the schematic diagram of DiPS-2. DiPS-2 is separated by 5 regions, such as source region (A), 1st differential pumping (DP) stage (B), 2nd DP stage (C), magnetic nozzle (D), and test region (E) by adapting highly differential pumping to control the test region plasma strongly independent from the source plasma. Typical magnetic field shape is shown in Figure 2, which varies 0 – 3.5 kG.

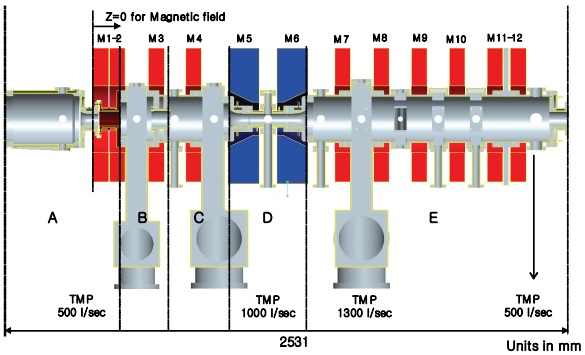

Figure 1. *Schematic diagram of DiPS-2: Labels of A, B, C, D, E, and M1-12 are source region, 1st differential pumping stage, 2nd differential pumping stage, magnetic nozzle, test region, and electromagnets.(Hanyang University)*

DiPS-2 is generally operated with the following conditions: discharge voltage (V_d) = 0 - 200 V, discharge current (I_d) = 0 - 150 A, operating pressure (P_n) = 20 mTorr (source region), 3 mTorr (2^{nd} differential pumping (DP) stage) and 1-100 mTorr (test region) within less than variations of 20% of 2^{nd} DP pressure and 5% of source region, plasma density (n_p) = upto 5 ± 10^{13} cm^{-3} at test region, electron temperature (T_e) = 2-3 eV for Ar plasma and 5-7 eV for He plasma, and ion temperature (T_i) ~ 0.1 eV for Ar ions.

DiPS-2 has the four main plasma diagnostics, such as probe systems (four fast scanning probes and one fixed probes) [7], two laser-induced fluorescence systems for Ar ion diagnostics [8], optical emission spectroscopy [9] and one laser Thomson scattering (LTS) system which is recently installed while others are already developed for DiPS-1.

Initial LTS diagnostics is shown in Figure 2, comparing with those by a single electric probe. The electron temperatures and plasma density measured by LTS agree well to those of electric probe deduced by ion saturation currents, while the plasma density by electron saturation current is not matched to those by LTS due to reduction factor by the magnetic field, which is related cross- and parallel diffusions and sheath impedance.

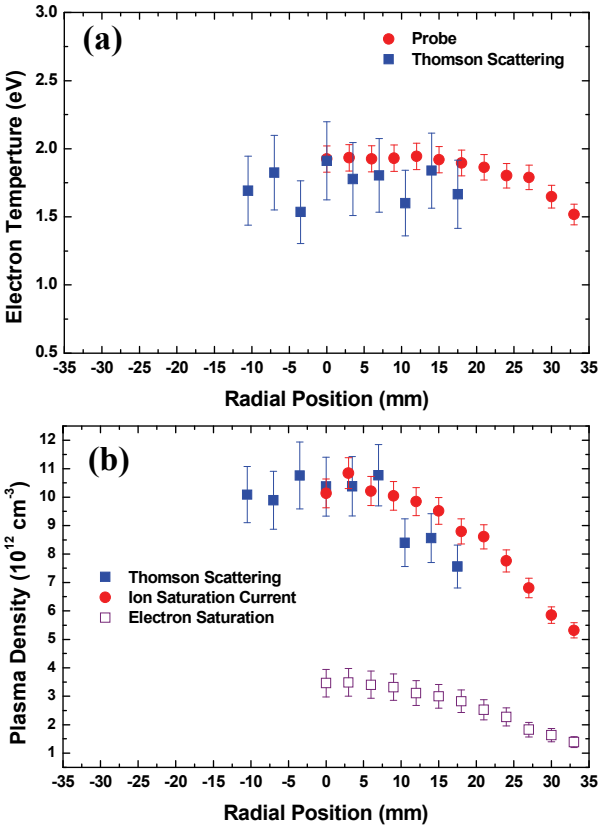

Figure 2: *Initial LTS diagnostics comparing with probes – electron temperature (a) and plasma density (b).*

II B. MP^2 Linear Plasma Facility [10]

MP^2 plasma facility was developed from former Hanbit mirror device at NFRI with similar concept of DiPS-1, but with a larger plasma source and a higher particle flux plasmas. For larger plasma generation, MP^2 has adapted honeycomlike large area LaB6 cathode (HLA-LaB6) with 4 inch diameter (center, one disk) and 2 inch diameter (outer, 6 disks) LaB_6 plates along the peripheral side, which becomes about 8 inch of total source diameter. The plasma shape or density controls can be possible by separately heating center and outer cathode in MP^2. The MP^2 is now idling since it will be moved to a separated branch institution in Kunsan site of the NFRI (at Daejeon), but it will be resumed soon.

II C. ECR Plasma Facility [11]

During resting phase of MP^2, a complimentary machine has been developed with small size ECR plasma for the test liquid PFCs materials, especially molten salts (FLiNaK). This is to be incorporated with MP^2 after resuming at Kunsan site. Figure 3 shows the schematic diagram of ECR device and its diagnostics systems. The plasma is produced by 2.45 GHz Magnetron upto 2 kW of Power. Typical plasma density and electron temperatures are 5 ± 10^{10} cm^{-3} and 10 eV from probe measurements, respectively. The magnetic field at molten salt surface is about 200 G. The typical heating temperature is about 540 ºC for liquid FLiNaK.

As for the H_2 retention in FLiNaK versus plasma irradiation time, one uses the outgassing rate of H_2 without plasma irradiation as the reference value. The integrated amount of the difference between measured one with plasma and the reference with the time gives the total about of the retention of H_2 molecules in FLiNaK at a given pressure. The main mechanism of H_2 retention would be caused by the ion bombardment on material surface accelerated by the sheath potential, and it will be discussed more detail in a separated report.

II D. E-beam Test Facility

High energy electron beam facility was developed for thermal heat load experiments at Dankook University. The electron beam energy and beam current are 70 keV (maximum) and 100 mA (maximum) within 40 x 40 mm^2 of target size. This means that the maximum heat load over 4-5 MW/m^2, which is acceptable for fusion material tests of KSTAR and even parts of ITER.

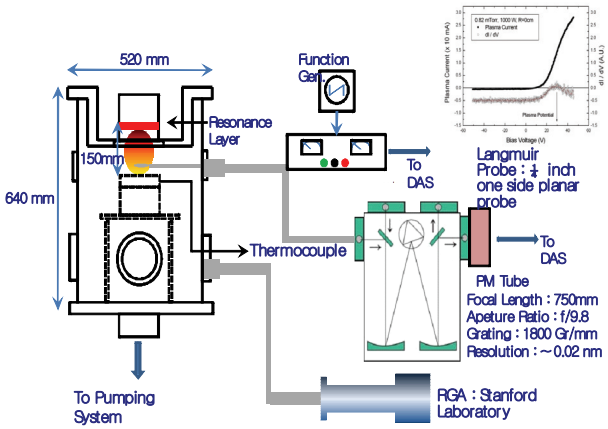

Figure 3. *ECR plasma facility with diagnostics systems for liquid PFCs tests.(NFRI)*

II E. Torch Plasma Facility

The high power plasma torch has been developed in Chonbuk National University for the material tests at the extreme environments, such as material erosions by aerodynamic heating, thermal protection at extremely high temperature condition, heat load tests for fusion and space plasmas.

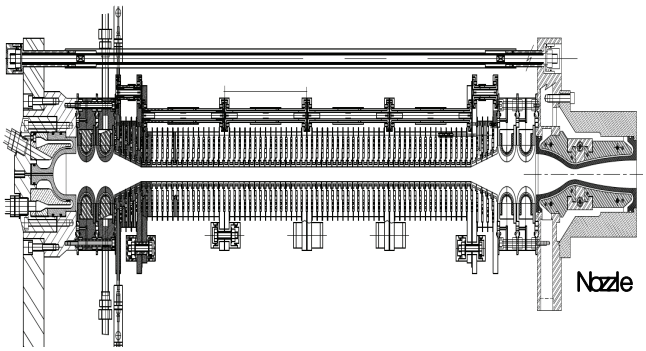

Figure 4. *Drawing view of segmented plasma torches.* (Chonbuk National University)

Figure 4 shows the cross-sectional view of a segmented plasma torch, which will be operated with the following conditions: arc heating power = 400 kW, voltage = 800 – 2200 V (normal 1000 V), maximum current per cathode = 250 A (total 500 A, double cathode), pressure = 0.2 – 1 Torr, plasma velocity at nozzle = 1-4 Mach numbers. Diagnostic systems include enthalpy probe with mass spectrometer for measurement

of enthalpy, plasma composition and plasma temperatures, and heat flux probe for measurement of heat flux. Visualization systems such as a pyrometer, a fast camera and an emission spectroscopy are installed to monitor the surface temperature of the substrate, plasma density, flow pattern etc. Measured performance data of the segmented arc plasma torch is shown in Table 1. This torch can produce the high heat flux above 10 MW/m^2 to target area of ~ 100 cm^2.

II. F. PIIID Plasma Facility

The plasma immersion ion implantation and deposition (PIIID) device was developed at KIST for the test of various material and surface modifications with high energy ions. Figure 5 shows the schematic diagram of PIIID system equipped with high-power pulsed magnetron sputtering system along with plasma immersion ion implantation capability. The intense pulse power to the magnetron can increase the ionization rate of sputtered atoms and can be implanted with the use of negative high-voltage pulse bias to the sample. The specifications of PIIID system are as follows; implantation energy = up to 70 keV, peak current = up to 10 A, peak power density = 100 MW/m^2, averaged power density = 0.5 MW/m^2, and maximum sample size = 50 x 50 mm^2.

II. G. TReD Facility [12]

TReD (Transport & Removal experiment of Dust) device has been developed for the tests of dust particle transport, removal and its diagnostics. As shown in Fig. 6, TReD is adapted the method of electrostatic curtain with tripolar grid and three phase alternative current (AC) operation. For versatile experiments, the chamber is designed as a rectangular shape with dimension of 0.5 (W) x 1.2 (L) x 0.5 (H) m^3 and equipped large rectangular view ports for dust monitoring. The total 100 traveling electrode was located bottom of the chamber with dimensions of 9 (W) x 450 (L) mm^2 and gap spacing is of 1 mm. The plasma is generated by inductively coupled plasma (ICP) source with the frequency of 13.56 MHz and 3 kW of maximum RF power (typically, < 50 W operation). One uses four linear antennas with ladder shape for uniform plasma generation from the upper region of the rectangular chamber.

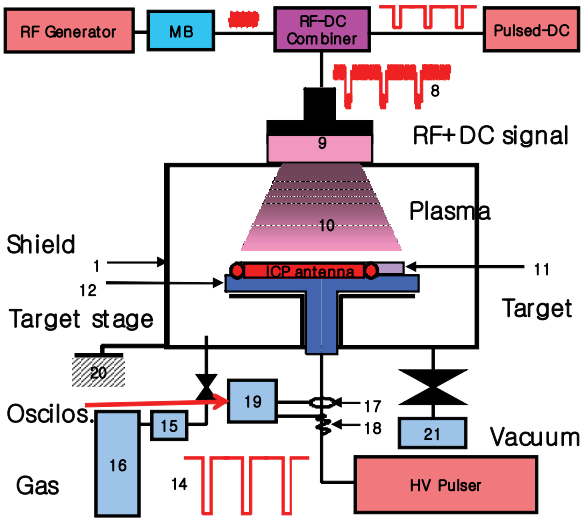

Figure 5. *Schematic diagram of plasma immersion ion implantation and deposition (PIIID) system, which is equipped with high-power pulsed magnetron sputtering along with plasma immersion ion implantation capability.* (KIST)

In the first phase, one tries to test the dust particle detector based upon capacitive diaphragm gauge (CDG), which will be used KSTAR and ITER. One uses the dust tray with aluminum ball(2.1 g) for centering the weight position since the response of CDG is dependent on the position. The CDG gauge will be checked at KSTAR during the 2012 campaign.

II. CONCLUSIONS

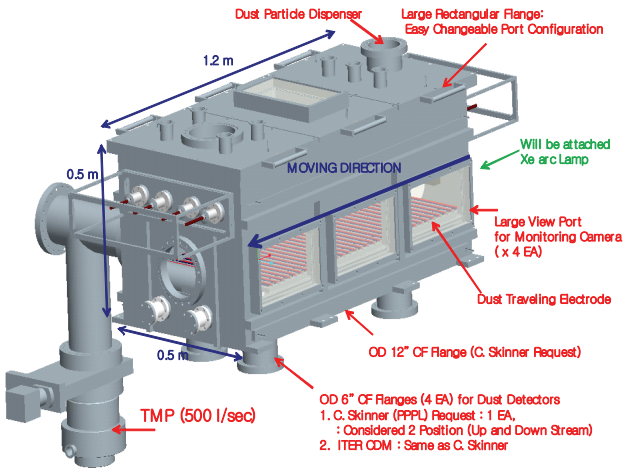

Figure 6. Drawing view of TReD device.

Recently, the various plasma devices have been developed in Korea for the plasma-material interaction (PMI) researches. These can be categorized by the followings; (1) edge plasma simulator - DiPS-2 (HYU), MP2 (NFRI) (2) plasma diagnostics developments - DiPS-2 (HYU) and MP2 (NFRI), (3) material test by plasma - DiPS-2 (HYU), MP2 (NFRI), ECR plasma facility (NFRI), by ion beam – PIIID (KIST), (4) thermal heat load test by electron beam (e-beam facility: DKU), by high heat flux plasma (segmented plasma torch: CBNU) and (5) dust particle transport and removal (TReD: HYU).

ACKNOWLEDGMENTS

This work is supported by the A3 Meeting Program via National Fusion Research Institute(NFRI) of Korea. This research was also supported by National R&D Program through the National Research Foundation of Korea (NRF) funded by the Ministry of Education, Science and Technology (20100020044, 20110018734, and 20120005927). This work is partially supported by the Basic Research Program of the National Fusion Research Institute (NFRI) of Korea.
This work is partly supported by the JSPS-NRF-NSFC A3 Foresight Program in the field of Plasma Physics(NSFC: No.11261140328).

REFERENCES

1. 1. G. Federici, C. H. Skinner, J. N. Brooks, J. P. Coad, C. Grisolia, A. A. Haasz, A. Hassanein, V. Philipps, C. S. Pitcher, J. Roth, W. R. Wampler, D. G. Whyte, *Nucl. Fusion*, **41**, 1967 (2001).
2. N. Asakura, H. Takenaga, S. Sakurai, G. D. Porter, T. D. Rognlien, M. E. Rensink, K. Shimizu, S. Higashijima, and H. Kubo, *Nucl. Fusion*, **44**, 503 (2004).
3. J. P. Coad, N. Bekris, J. D. Elder, S. K. Erents, D. E. Hole, K. D. Lawson, G. F. Matthews, R. D. Penzhorn, and P. C. Stangeby, J. Nucl. Mater., 290-293, 224 (2001).
4. B. Lipschultz, D. A. Pappas, B. LaBombard, J. E. Rice, D. Smith, and S. J. Wukitch, Nucl. Fusion, 41, 585 (2001).
5. R. A. Causey, J. Nucl. Mater., **300**, 91 (2002).
6. J. Winter, Plasma Phys. Control. Fusion, **46**, B583 (2004)
7. K.-S. Chung, H.-J. Woo, G.-S. Choi, J.-J. Do, Y.-J. Seo, and H.-J. You, *Contrib. Plasma Phys.*, **46**, 354 (2006).
8. H.-J. Woo, K.-S. Chung, T. Lho, and R. McWilliams, *J. Korean Phys. Soc.*, **48**, 260 (2006).
9. Y. H. Jung, J.-S. Yoon, S. J. Yoo, Y.-W. Kim, T. Lho, B. Lee, J.-J. Do, H.-J. Woo, and K.-S. Chung, *Contrib. Plasma Phys.*, **46**, 451 (2006).
10. H.-J. Woo, K.-S. Chung, H.-J. You, M.-J. Lee, T. Lho, K. K. Choh, J.-S. Yoon, B. Lee, Y. H. Jung, S. J. Yoo, and M. Kwon, *Rev. Sci. Instrum.*, **78**, 103505 (2007).
11. H. Park, Y.-S. Choi, and T. Lho, 53rd Annual Meeting of the APS Division of Plasma Physics, Nov. 14-18, Vol. 56, No. 16, PP9.171, Bulletin of the American Physical Society (2011).
12. H.-J. Woo, S.-G. Cho, K.-S. Chung, E.-K. Park, S.-J. Park, and S.-H. Hong, 53rd Annual Meeting of the APS Division of Plasma Physics, Nov. 14-18, Vol. 56, No. 16, PP9.55, Bulletin of the American Physical Society (2011).

Impurity spectroscopy in fusion plasmas and plan for A3 collaboration

Category IIa

S.Morita, M.Kobayashi, C.F.Dong, T.Oishi, M.Goto, E.H.Wang* and X.L.Huang*
National Institute for Fusion Science, Toki 509-5292, Gifu, Japan
*Graduate University for Advanced Studies, Toki 509-5292, Gifu, Japan

L.Zhang, Z.W.Wu, L.Q.Hu and B.Lu
Institute of Plasma Physics Chinese Academy of Sciences, Hefei 230031, China

Z.Y.Cui and H.Y.Zhou
Southwestern Institute of Physics, Chengdu 610041, China

1. Introduction

In order to mitigate the heat load over divertor in the steady state discharge, several methods based on different physics backgrounds have been considered. Main subjects on these issues in category IIa are;

1. Plasma detachment in tokamaks and in LHD with three-dimensional divertor
2. Divertor plasma control with high-Z material
3. Wall conditioning and edge plasma control

In relation to such subjects, recently, the comparative study between tokamaks and helical devices has been strongly motivated to obtain deeper understanding on the plasma physics. A comparative study of the edge impurity transport is attempted between different edge magnetic field geometries by comparing the stochastic layer of Large Helical Device (LHD) and the scrape-off layer of Huan Liuqi-2A (HL-2A) tokamak [1-5]. For the purpose carbon emission profiles are measured in LHD and HL-2A using extreme ultraviolet (EUV) and vacuum ultraviolet (VUV) spectrometers. In LHD two EUV spectrometers are working in 10-100 and 50-650 wavelength ranges [6,7]. The radial profiles [8] and two-dimensional profiles [9] are also measured with excellent absolute calibration of the spectrometer system [10]. In HL-2A 1m VUV spectrometer is working to measure the radial profile [11] and recently EUV spectrometer is also start to work [12]. The analysis is based on the 3D edge fluid

transport code simulation, EMC3 - EIRENE, which is implemented in the both devices.

2. Edge magnetic field structures in LHD and tokamak

LHD has poloidal and toroidal field periods of l=2 and n=10, respectively. The major radius and the averaged minor radius are 3.75m and 0.704 m , respectively. The divertor plates on the first wall are made of carbon and the first wall is made of stainless steel. Figures 1 (a) and (b) show the magnetic field structure with last closed flux surface (LCFS) and the poloidal plasma cross section with divertor configuration in major radius and vertical (R-Z) coordinates, respectively. The magnetic field connection length (L_C) is shown with color bar. High-temperature plasmas are basically confined without net toroidal current by two helical coils wound around the torus shown in Fig.1 (a). The two helical coils create two X-points at inboard and outboard sides outside the confinement region (see Fig.1(b)), and these X-points turn poloidally together with the helical coils when they move toroidally. The four divertor legs created beyond these X-points are connected to the divertor plates. This coil system also creates the stochastic magnetic field structure in the edge region due to the overlapping of magnetic island chains. Some of the flux tubes are stretched out from the X-point and reach the divertor plates, resulting in open field lines. The open field lines near the separatrix of each remnant island constitute magnetic field lines with connection lengths longer than 1 km. On the other hand, the open field lines near the O-point of the remnant islands become short flux tubes with lengths shorter than a few tens of meters, as shown with blue and black colors in Fig.1 (b). Thus, the long and short flux tubes co-exist in the outermost region of LHD.

Figure 2 (a) shows a schematic of vacuum vessel and divertor chamber/baffles in tokamak (HL-2A). The tokamak has an axi-symmetric X-point poloidal divertor configuration, which is created by three multi-pole coils as shown in Fig.2 (a). The major radius and the minor radius of plasma is 1.65m and ~ 0.4 m, respectively. The divertor plates are made of copper while the baffle and the first wall are made of carbon and stainless steel, respectively. The L_C distribution in the poloidal cross section is shown in Fig.2 (b). The confinement region with infinite L_C has a circular shape cross section, surrounded by the scrape-off layer with flux tubes of L_C~50 m in brown colour. Strictly speaking on the LCFS (or separatrix), the L_C is infinity due to the singularity of the X-point where the poloidal field (B_θ) is zero. Then, the L_C rapidly decreases in several millimetres down to the value estimated with $\sim 2\pi R q_{edge}$. Here, q_{edge} is the safety factor and ranges at q_{edge}=2.8 ~ 4.6 in the present case. The L_C then slightly increases outward due to the increase in the safety factor. However, such behaviour of

the L_C is not visible in the Fig.2 due to the size of figure and also due to the color bar scale set to the same level as that of LHD for comparison. In addition, it seems that the clear separatrix does not exist in reality due to the error field and instead is stochastized to a certain extent.

The divertor has a closed structure with a deep throat in the divertor chamber. The 5m long divertor legs are clearly formed below the X-point. The private region is connected to the inner and outer divertor plates with several meters long flux tubes. Parallel distance along the flux tube (those at ~0.01 m from separatrix at midplane) starting from the outer divertor plate is also denoted with numerals in Fig.2 (b).

Different magnetic field structure between the two devices predicts entirely different edge transport. In the stochastic layer of LHD, the open field lines make a large number of poloidal turns while gradually moving outward due to the radial component of magnetic field, $B_r / B_\phi = 10^{-5} \sim 10^{-3}$. The strong parallel transport distributes the energy in poloidal direction, producing an outward radial flux by replacing the transport into the cross-field direction. Therefore, plasma parameters in the stochastic layer of LHD are almost uniform in the poloidal direction with certain modulation due to the mode structure. A substantial parallel temperature gradient appears in the outside of stochastic layer where the flux tubes are clustered to form the divertor legs. In the SOL of HL-2A, on the other hand, outer and inner divertor plates are directly connected by the flux tubes in one poloidal turn. The parallel transport then becomes dominant to deliver the energy and particles towards divertor plates, and necessarily creates parallel gradient of plasma parameters along the flux tubes. Thus, there appears a strong poloidal asymmetry of plasma parameters in HL-2A.

3. Impurity transport modeling

In the fluid model, the impurity transport along the magnetic field line is expressed by the following classical force balance as

$$m_z \frac{\partial V_{z//}}{\partial t} = -\frac{1}{n_z}\frac{\partial T_z n_z}{\partial s} + ZeE_{//} + m_z \frac{V_{i//} - V_{Z//}^{imp}}{\tau_s} + 0.71Z^2 \frac{\partial T_e}{\partial s} + 2.6Z^2 \frac{\partial T_i}{\partial s}, \qquad (1)$$

where s is the coordinate along magnetic field, and the first and second terms on the right hand side express the pressure gradient of impurity and the electrostatic force working on the impurity, respectively. The last three terms originate in the collision with background plasma. The third term is the friction force exerted by the background

ion moving with the fluid velocity, $V_{i//}$, where τ_s is the collision time between impurity and background plasma. The fourth and the fifth terms express the temperature gradient force of electron and ion, respectively, which appears with the parallel temperature gradients and has its origin in the temperature dependence of Coulomb collision, $\nu \propto T^{-1.5}$. These terms are also called thermal force and directing from low to high temperature region.

It is readily found in the present modeling, that the dominant terms on the right hand side of eq.(1) are the friction and the ion thermal forces. The parallel impurity velocity is then given by

$$V_{Z//}^{imp} = V_{i//} + \frac{2.6Z^2 \tau_s}{m_z} \frac{\partial T_i}{\partial s}. \qquad (2)$$

Since the background plasma flow, $V_{i//}$, is usually directed toward the divertor plates, at least near the divertor plates, the flow pushes the impurity downstream through the friction. On the other hand, the parallel temperature gradient is directed upstream. The second term (thermal force) therefore drives the impurity upstream. The resulting impurity velocity is a consequence of the competition between the two terms. Since the term of $\frac{\partial T_i}{\partial s}$ indicates upstream flow, the condition of $|V_{i//}| < \left|\frac{2.6Z^2 \tau_s}{m_z} \frac{\partial T_i}{\partial s}\right|$ also leads to upstream flow for the impurity, suggesting impurity build up at upstream region. Therefore, a necessary condition for avoiding such an impurity build up is given by $|V_{i//}| > \left|\frac{2.6Z^2 \tau_s}{m_z} \frac{\partial T_i}{\partial s}\right|$.

4. Scrape-off layer of tokamak and stochastic layer of LHD

The reference dataset of HL-2A tokamak for transport simulation are taken from Ohmic discharges with B_t = 1.42 T, where the operational parameters range in n_e=0.75 ~ 4.5 x 10^{19} m^{-3}, Ip = 150~250 kA and V_L = 1.2 ~ 1.5V for line-averaged electron density, plasma current and loop voltage, respectively. In these discharges the ohmic heating power ranges from 100 to 400kW. In the present impurity transport analysis, the value of 200kW is selected as a typical SOL input power. The power is equally split into electron and ion energies at the upstream boundary, i.e., LCFS. The resulting 2D distributions of impurity density are plotted in Fig.3 (a) for low and high density cases, together with the force balance of $|V_{//}^{fric}|$-$|V_{//}^{thi}|$ in Fig.3 (b). In the figures yellow (or

bright) color and blue (or dark) color mean the friction and thermal force dominant regions, respectively. It is seen that most of the scrape-off layer is in the thermal force dominant regime at low density (Fig.3 (b) upper), leading to the significant impurity build up above the X-point (Fig.3 (a) upper). The screening effect near the divertor plates becomes strong and the impurity released from the divertor plates are retained in the divertor when the density increases, as shown in Fig.3 (a) (lower). There remains, however, an upward impurity velocity near the X-point as indicated with the blue color in Fig.3 (b) (lower) even at the high density. This implies less screening effect against the impurity released from the first wall.

In LHD the discharge in R_{ax}=3.75m with B_t=2.64T is maintained by neutral beam injection (NBI) with input power of 4 to 8MW. The electron density at LCFS, n_{LCFS}, is varied from 1.5 to 6.0 x 10^{19} m^{-3}. The perpendicular transport coefficients for particle and energy are fixed to $D_{\perp}$=0.50 and $\chi_{\perp e,i}$=1.50 m^2/s, respectively. The simulated 2D distribution of impurity density is plotted in Fig.4, indicating the force balance of $|V_{//}^{fric}|$-$|V_{//}^{thi}|$ between friction and thermal forces. In the figure the friction force dominant region with high impurity density and the thermal force dominant region with low impurity density are expressed with bright colours like yellow and dark colours like blue, respectively. In the low density range (n_{LCFS}=2.0x10^{19} m^{-3}), the impurity build up is appeared near the LCFS (see Fig.4 (a)). This is caused by appearance of a strong thermal force, as shown in upper plot of Fig.4 (b) with blue color. With increasing the density , on the other hand, the strong thermal force appeared in the stochastic region begins to be suppressed and replaced by the friction force at high density range (n_{LCFS}=5.0x10^{19} m^{-3}), as shown in lower plot of Fig.4 (b). The impurity can be then effectively screened at the edge surface layers. It should be noted that the friction dominant region indicated with yellow and white colors in Fig.4(b) is expanded to all poloidal locations in the periphery region. This implies that the screening is effectively independent of the impurity source location.

5. Experimental results from LHD and tokamak

The density dependence of the carbon emission observed in the experiment is plotted in Fig. 5, where the intensity is normalized by the electron density. Due to the different ionization potential of carbon ions, i.e., CIII (48eV), CIV(65eV) and CV(392eV), the intensities of CIII and CIV are interpreted as a proxy for the carbon source and CV as a proxy for the impurity located at deeper radial position. CIII and CIV intensities indicate a constant carbon influx against the line-averaged density. The reduction of CV intensity indicates the impurity screening. The modeling is

studied to explain the experimental result in details. The summation of these different sources is plotted in Fig. 6, where the CIII and CIV tend to increase with density while the CV decreases with density until it saturates at $n_{LCFS}=4.0x10^{19}$ m^{-3}. It is found that the physical sputtering contributes to the emission only at the low density, where it has a comparable flux with the chemical sputtering. A deeper penetration of physically sputtered impurity provides larger radiation due to the high plasma density at the inner radius. With increasing density, the contribution of the physical sputtering is replaced by the chemical one, which starts to dominate in the amount of carbon influx. Thus, the density dependence at the high density range roughly follows the result of chemical sputtering. When the experimental result in Fig.5 is compared with the modeling result in Fig.6, we notice that the contribution from the chemical sputtering is considerably overestimated in the modeling. In LHD, the emission from hydrocarbon molecule is usually weak except for extremely high density discharges with strong hydrogen gas puffing at $n_e>10^{20}m^{-3}$. This experimental result, which is different from general feature appeared in tokamaks, may be caused by low operational density range (order of $10^{18}m^{-3}$) in open divertor system of LHD. Since the ion temperature in divertor region is higher than tokamak due to the low divertor density, the self physical sputtering by carbon can be possibly enlarged.

The density dependence is also studied by measuring carbon emissions in different ionization stages. The result is plotted in Fig. 7. Although the data are a little scattered reflecting a small difference among discharges of HL-2A, the CIII and CIV emissions seem to be nearly constant against the line averaged density, while the CV emission clearly shows a gradual reduction against the density. The density dependence of these emissions is analyzed with the modeling. The density dependence of these emissions is plotted in Fig. 8. It shows that the CIII and CIV intensities in low charge states slightly decrease in higher densities, while the CV intensity in high charge state continuously decreases with density. The roughly constant CIII and CIV intensities against the density scan observed in the experiment indicate a little difference from the modeling in higher density range. It simply tells us the importance of the chemical sputtering at the first wall because the wall chemical sputtering predominantly determines the CIII and CIV intensities at the high density range. The decrease in measured CV intensity has a similar tendency to the modeling, but it is quantitatively different. The reduction of CV in the modeling is roughly two orders of magnitude, while the reduction in the modeling is only a factor of 3. The CV intensity in the modeling is entirely underestimated by the limited computational domain as mentioned above.

6. Summary

The edge impurity is studied in comparison between LHD and tokamak as an example of HL-2A. In A3 collaboration the study is planned to extend to EAST and KSTAR including tungsten transport study. The detailed discussion with EAST and KSTAR will be soon accelerated.

Acknowledgements

This work was partly supported by the JSPS-NRF-NSFC A3 Foresight Program in the field of Plasma Physics (NSFC: No.11261140328).

References

[1] M.Kobayashi, S.Morita, C.F.Dong, Z.Y.Cui et al., to be published in Nucl. Fusion.

[2] M.B.Chowdhuri, S.Morita, M.Kobayshi, et al. Physics of Plasmas **16** (2009) 062502.

[3] C.F.Dong, S.Morita, M.Kobayashi, et al., Phys. Plasmas **18** (2011) 082511

[4] S.Morita, C.F.Dong, M.Kobayashi, et al., submitted to in Nucl. Fusion.

[5] Z.Y.Cui, S.Morita, H.Y.Zhou, et al., submitted to in Nucl. Fusion.

[6] M.B.Chowdhuri, S.Morita, M.Goto et al., Rev. Sci. Instrum. **78** (2007) 023501.

[7] M.B.Chowdhuri, S.Morita and M.Goto, Appl. Optics **47** (2008) 135.

[8] C.F.Dong, S.Morita, M.Goto and H.Y.Zhou, Rev. Sci. Instrum. **81** (2010) 033107.

[9] E.H.Wang, S.Morita, M.Goto and C.F.Dong, et al., Rev. Sci. Instrum. **83** (2012) 043503.

[10] C.F.Dong, S.Morita, M.Goto and E.H.Wang, Rev. Sci. Instrum. **82** (2011) 113102.

[11] Z.Y.Cui, S.Morita, B.Z.Fu, et al., Rev. Sci. Instrum. **81** (2010) 043503.

[12] H.Y.Zhou, Z.Y.Cui, S.Morita, et al., Rev. Sci. Instrum. **83** (2012) 10D507.

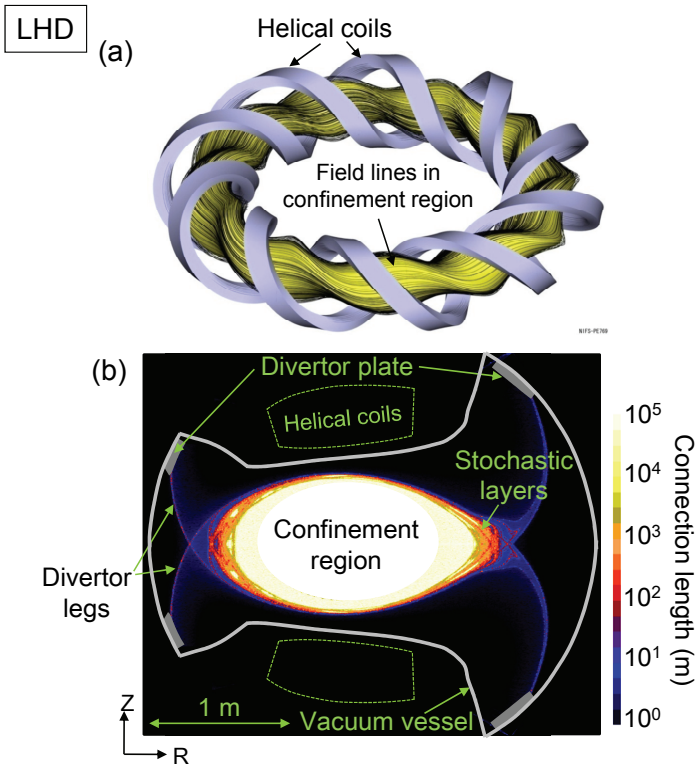

Fig.1 (a) Magnetic field structure in confinement region of LHD and configuration of helical coils and (b) poloidal cross section of LHD with divertor plates and divertor legs. Color represents the connection length (L_C).

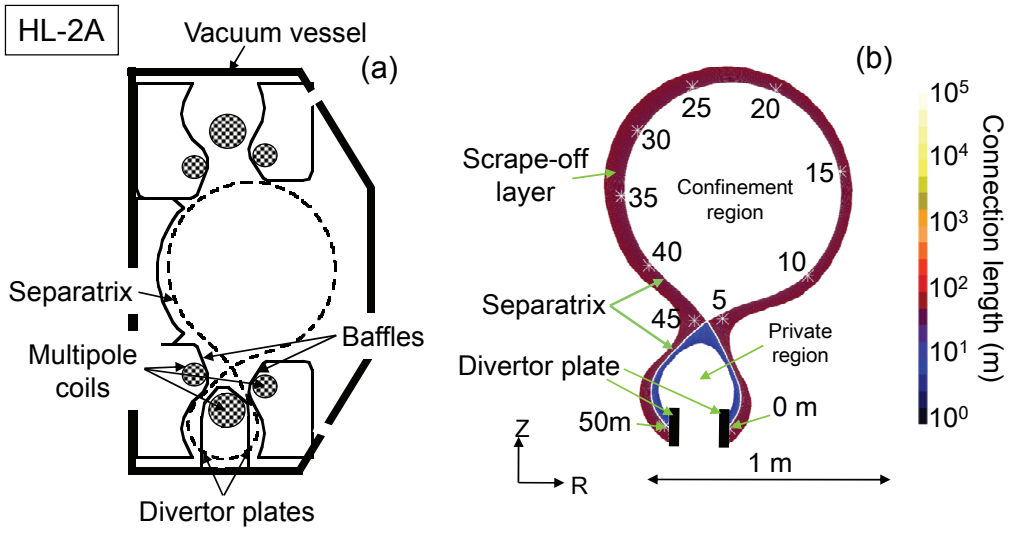

Fig.2 (a) Schematic of HL-2A tokamak in poloidal cross section with vacuum vessel and divertor chamber/baffle. Three multi-pole coils create divertor configuration and (b) L_C distribution in poloidal cross section. The numerals of 0 to 50 in (b) denote parallel distance, s, in meter along flux tubes with $L_C = 50 \pm 0.5\,m$, mapped to poloidal cross section.

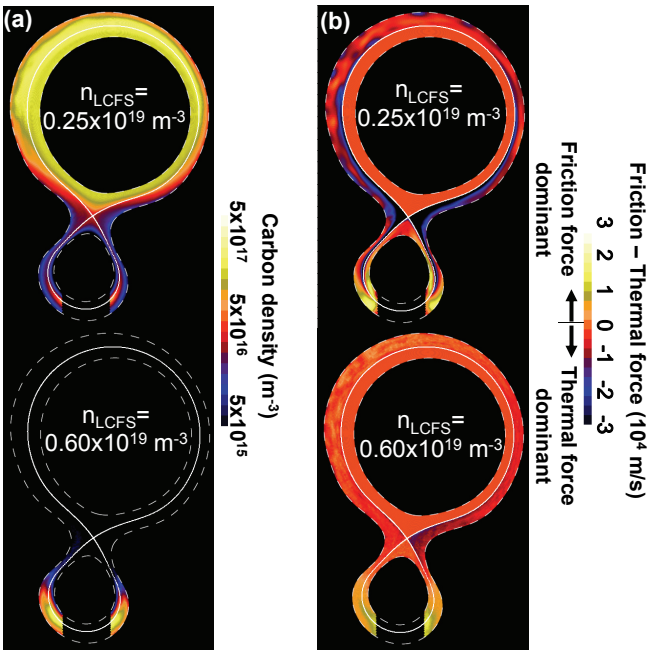

Fig.3 (a) Two dimensional distribution of carbon density summed over all charge states and (b) force balance of $|V_{//}^{fric}|-|V_{//}^{thi}|$ in HL-2A, for n_{LCFS}=0.25 x10^{19} m^{-3} (upper) and 0.60 x10^{19} m^{-3} (lower). Bright (yellow) and dark (blue) colors indicate friction and thermal force dominant region, respectively.

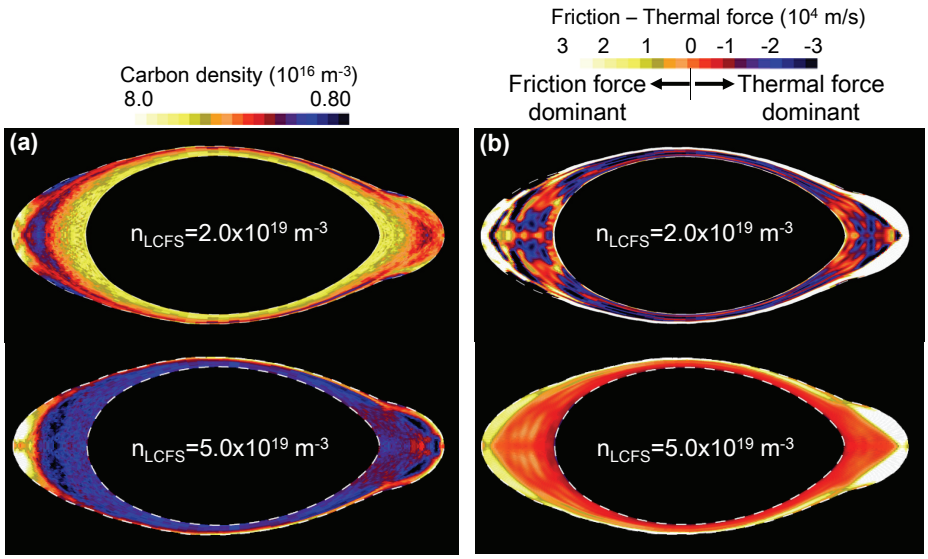

Fig.4 (a) Two dimensional distribution of carbon density summed over all charge states and (b) force balance of $|V_{//}^{fric}|-|V_{//}^{thi}|$ in LHD, for n_{LCFS}=2.0 x10^{19} m^{-3} (upper) and 5.0 x10^{19} m^{-3} (lower). Bright (yellow) and dark (blue) colors indicate friction and thermal force dominant regions, respectively.

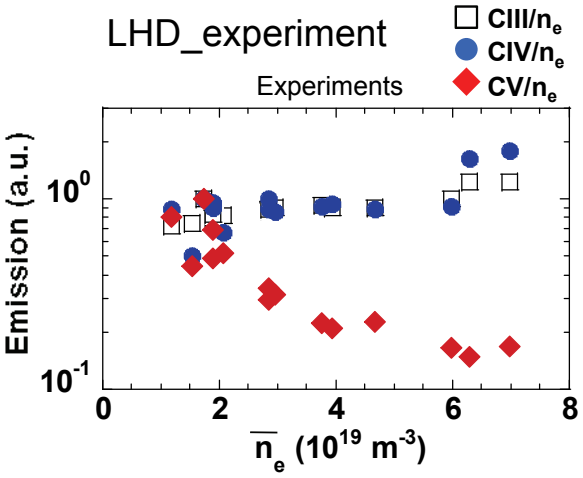

Fig.5 Carbon emission from LHD normalized by electron density as a function of line averaged density n_e (open squares: CIII/n_e, closed circles: CIV/n_e, closed diamonds: CV/n_e).

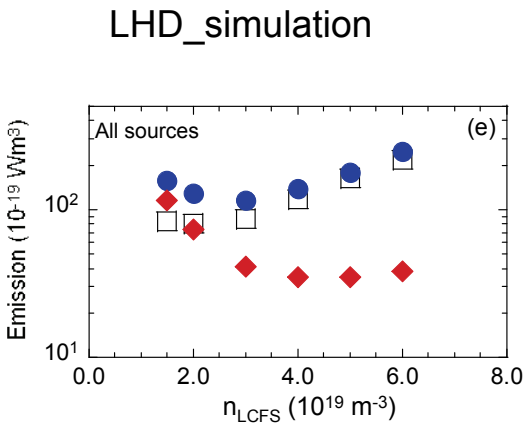

Fig.6 Carbon emission normalized by electron density as a function of n_{LCFS}, simulated by 3D transport code EMC3-EIRENE with the viewing area (open squares: CIII/n_e, closed circles: CIV/n_e, closed diamonds: CV/n_e).

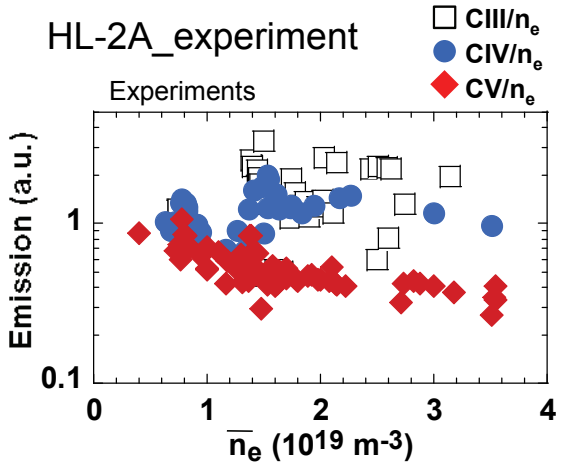

Fig.7 Carbon emission from HL-2A normalized by electron density as a function of the line averaged density (open squares: CIII/n_e, closed circles: CIV/n_e, closed diamonds: CV/n_e).

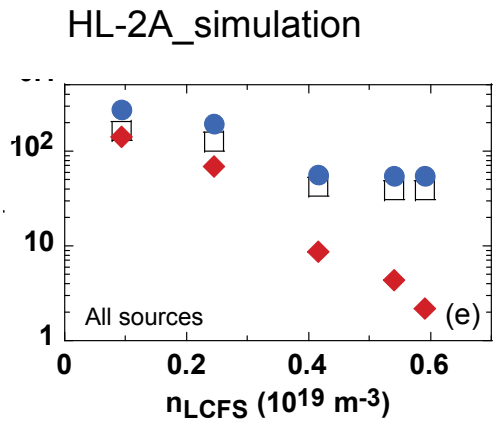

Fig.8 Carbon emission normalized by electron density as a function of n_{LCFS}, simulated by 3D transport code EMC3-EIRENE with the viewing area (open squares: CIII/n_e, closed circles: CIV/n_e, closed diamonds: CV/n_e).

Atomic and Molecular Processes in Fusion Plasmas

Daiji Kato
National Institute for Fusion Science
Nobuyuki Nakamura
Inst. Laser Science, Univ. Electro-Communications

1. Introduction

One of important issues concerning steady state sustainment of magnetically confined plasmas (MCPs) is distribution of impurity ions in the MCPs and radiation powers by the ions. Since tungsten divertors will be used in ITER, the primary element of heavy impurity ions would be tungsten. Tungsten cannot be fully ionized even in core plasmas of ITER. Line radiations by bound electrons of the tungsten ions following electron impact excitations decrease temperatures of the core plasmas. Thus, it is required to keep tungsten concentration in the core plasmas as small as possible; some theoretical simulations predict that the concentration should be limited below $5\text{x}10^{-5}$.

In ITER, electron temperatures span from < 100 eV at peripheral regions up to about 30 keV at a plasma center. Many ionization stages (up to W^{65+}) contribute to the line radiation. In scrape-off and divertor regions, open 4f sub-shell (W^{14+} ~ W^{27+}) and open 5s/5p sub-shell (W^{6+} ~ W^{13+}) ions may be dominant emitters. Peak temperature at a plasma center of the Large Helical Device (LHD) is about 4 keV or lower using neutron beam injection heating. We can investigate tungsten emission lines anticipated in the ITER edge plasmas through scrape-off and divertor regions by using LHD.

Measurements of line spectra of the ions give useful knowledge about ion distribution in MCP, provided that we can assign the line (or group of the lines) to a specific charge state of the ion.

In LHD, we have identified several charge states of tungsten ions by spectroscopy. A strong neutral tungsten line in visible region is observed near a tungsten plate installed in the vacuum vessel. In contrast, Cu- and Zn- like tungsten lines are observed in 6 nm region after a tungsten pellet is injected. Similarly, in 5nm region, 27, 28, and 29+ charge state lines are observed. Since electronic configurations of these ionization stages are away from the closed shell, energy level structures are very complex. As a result, these emission lines exhibit a quasi-continuum feature, i.e. so-called unresolved

transition array (UTA).

2. Tungsten EUV line spectra measurements with EBITs and spectral synthesis

A compact electron beam ion trap (CoBIT) has been developed to measure spectral data of highly charged ions relating to fusion and solar plasma researches. Electron-beam energy from 100 eV upto 2 keV is used to produce tungsten ions of about 10+ through 30+ charge states relevant to LHD plasmas. Extreme-Ultra-Violet (EUV) emission lines from the tungsten ions inside the CoBIT were measured using a flat-field grating EUV spectrometer equipped with a CCD detevtor. Tungsten was injected as a vapor of $W(CO)_6$ compound into the CoBIT. Charge states associated with emission lines are clearly identified in the CoBIT spectra. Detailed spectral synthesis was performed by a collisonal-radiative model (CR-model) using tungsten atomic data obtained from HULLAC code calculations. Very good agreement with CoBIT spectra has been obtained. The validated CR-model will be applied to investigate tungsten spectra in LHD plasmas.

3. Visible forbidden transition of highly charged tungsten ions

Visible line emission from highly charged tungsten ions has been observed at the LHD using a Tracer Encapsulated Solid Pellet (TESPEL). A Czerny-Turner-type visible-UV spectrometer (1800 grooves/mm grating and an entrance slit width of 50 μm) equipped with a CCD detector was used for the present observation. One of the measured lines is assigned to a magnetic-dipole (M1) line of the ground-term fine-structure transition of W^{26+}. The other line is unidentified but probably due to a highly charged tungsten ion. Photon emission was observed at 40 lines of sight divided along the vertical direction of a horizontally elongated poloidal cross section of the LHD plasma. The line-integrated intensity of the M1 line along each line of sight indicates a peaked profile at the plasma center where the electron temperatures are high enough so that tungsten ions are highly ionized. However, the ion distribution cannot be reconciled with a transport-less model using available ionization/recombination rate coefficients of tungsten ions (e.g. JATOM code by Sasaki).

4. X-ray spectra of heavy highly charged ions

In the core plasma of ITER, Ne-like W ions will be most abundant. Precise spectral data for the Ne-like ions, therefore, become important for diagnostics of plasma parameters and plasma rotation. High-resolution X-ray spectroscopy of highly charged ions using a crystal spectrometer has been performed at Tokyo electron-beam-ion-trap (Tokyo-EBIT). Hard X-ray spectra (a few Å in wavelength) from Ne-like ions were measured for high-Z elements. Measured wavelengths of strongest electric dipole lines are significantly different from predictions of state-of-the-art theories for heavier elements of $Z > 60$. As for tungsten, some measurements with calorimeters and Bragg-crystal spectrometers have been performed. However spectral resolutions of these measurements are rather low.

5. China-Japan joint seminar (AMPP2012)

As one of the activities of JSPS-NRF-NSFC A3 Foresight Program in the field of Plasma Physics (NSFC: No.11261140328), Japan-China Joint Seminar on Atomic and Molecular Processes in Plasma was held on July 30 – August 4, 2012, in Lanzhou, China, organized by Profs. Chenzhong Dong (NWNU, China) and Fumihiro Koike (Kitasoto Univ., Japan). The proposal of the present joint seminar has placed its intention not only on the presentations of the collaborative studies, but also on offering an opportunity for the wide range of researchers from both countries to be acquainted with each other, who would have made an extensive exchange of information about the recent progress of the research activities, and also would have made an extensive discussion about the plan of the future collaborations.

In the present seminar, the total number of 31 oral talks was presented by experts from Japan, China, Germany and Ireland. The total number of the officially registered participants was 37, in which 14 from Japan, 21 from China, 1 from Germany, and 1 from Ireland. Topics cover spectroscopic properties of atoms and ions in the plasma, the collisions of electrons or ions with atoms or ions in the plasma, the analysis and diagnostics of the confinement fusion plasma especially for the properties of tungsten atoms and ions, and, further, topics from wide area of atomic physics related to plasma. Proceedings will be published in a coming issue of NIFS-PROC

series.

This work is performed with the support and under the auspices of the NIFS Collaboration Research program (NIFS10KLPF009) and JSPS-NRF-NSFC A3 Foresight Program in the field of Plasma Physics (NSFC: No.11261140328). DK is grateful for a financial support by KAKENHI (23246165).

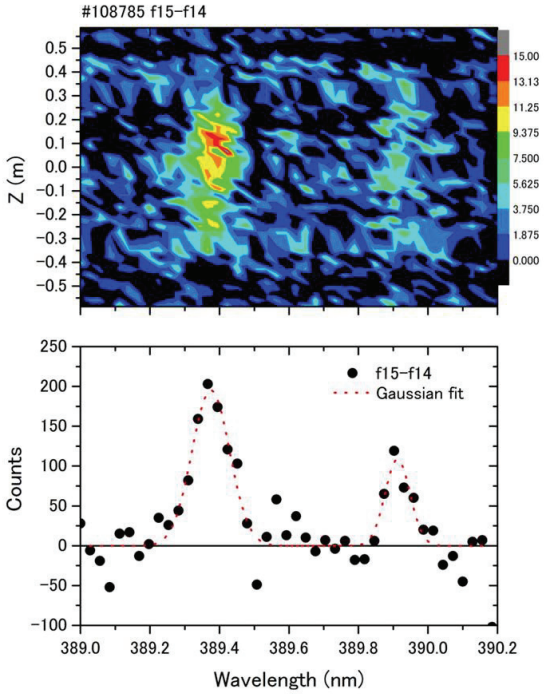

Fig. 1 A spectrum of emission lines from highly charged tungsten ions observed at LHD (shot No.108785). The scale on the right hand side of the top panel shows photon counts per pixel of the CCD detector.

Fig.2 Group photo of AMPP2012.

Validation of ELM dynamics via 2D Electron Cyclotron Emission Imaging in KSTAR

Hyeon.K. Park

POSTECH, Pohang, Korea
e-mail: hyeonpark@postech.ac.kr

Abstract. Enhanced physical understanding of the nature of the Edge Localized Mode (ELM) instability in the H-mode regime of toroidal plasmas requires advanced diagnostic tools to visualize their dynamics. A high spatial and temporal resolution 2-D Electron Cyclotron Emission Imaging (ECEI) system [1] was utilized successfully characterize the real time dynamics of ELMs [2] including the growth, saturation and bursting process of this instability during two campaigns (2010 and 2011) of the Korean Superconducting Tokamak Advanced Research (KSTAR) device. The measured ELMs are validated with the synthetic images based on numerical simulations.

Introduction

Edge-localized modes (ELMs) are ubiquitous in the high confinement mode (H-mode) of a tokamak plasma, where the edge pressure gradient is large over a short physical distance near the separatrix, and have been extensively studied in many tokamak devices[3-10] for the last three decades since their first observation in ASDEX [11]. The H-mode was adopted as a standard mode of operation in ITER, yet large ELMs can severely limit the life time of the divertor; thus, understanding and control of this instability became an essential research subject for all diverted tokamaks. A control system that requires actively cooled current carrying in-vessel structures are difficult to engineer for not only for ITER but also for future devices, such as a DEMO facility. Therefore, it is desirable to develop a control technique that is both effective and relatively simple to engineer. The nonlinear behavior of an ELM including the bursting of the mode, which appears to be localized in toroidal plane, is still under investigation. Following the first real time visualization of the core *m=1* physics with the Electron Cyclotron Emission Imaging system on TEXTOR [12], the technique has been successfully translated to the ELM physics study in AUG [13, 14] and KSTAR [2]. During the KSTAR campaigns of 2010 and 2011, both stationary images as well as dynamic images such as the ELM growth from the initiation phase to burst were successfully documented. The 2D image in the saturated regime is compared with the numerical simulation results from the BOUT++ code [15, 16] and the observation will be compared with theoretical models. Future plans for 3D imaging which will resolve outstanding is also discussed.

1. Visualization using the High Resolution 2D ECEI System

The electron cyclotron emission imaging (ECEI) technique is based on established heterodyne radiometry for the measurement of the electron cyclotron emission (ECE) intensity from the magnetically confined optically thick plasmas, in which the emission intensity (I_{rad}) is proportional to the local electron temperature (T_e); $I_{rad}(R) = \alpha T_e(R)$, where α is a calibration factor. Utilizing a vertical detector array and large optics which collects the emission to form an image on the detector plane, the first real time 2D ECEI system was successfully tested on TEXTOR. Following this work, a number of tokamaks have successively implemented more advanced ECEI systems that have contributed to the physics understanding of sawteeth, tearing modes, and Alfvén eigenmodes through direct comparative studies with the predicted images from theoretical models. However, application of the ECE measurement to edge plasmas in the medium performance plasmas in which the optical thickness is marginal requires careful attention in the analysis of the measured emission. Under such edge plasma conditions, the measured emission intensity may not represent the

local T_e; however, localization of the measurement is still valid with a slightly broadened spatial resolution. If the optical thickness falls further, then the measurement is no longer localized. The ECEI system on KSTAR consists of two independent receiver arrays and large aperture optics with zooming capability as illustrated in Fig. 1, providing a simultaneous measurement of two independent regions along the field of view as shown in this figure. The two viewing areas, which correspond to the individual receiver arrays as denoted by HFS (high-field side) and LFS (low-field side) in the figure, can be placed anywhere in the poloidal cross-section with a variable vertical coverage from ~30 to ~90 cm owing to the wide-band (85–145 GHz) microwave heterodyne detection technologies and the optimized zooming and focusing capabilities of the optics. This flexibility has allowed various combinations of HFS and LFS view positions, providing excellent opportunities to study a variety of plasma instabilities and turbulence phenomena in 2D such as sawteeth, tearing modes, ELMs, and turbulent fluctuations during the H-mode transition. Each detector array provides 24 (vertical) x 8 (radial) = 192 local emission measurements with a spatial resolution ~1–2 cm and a time resolution down to ~1 μs. The detector arrays are optimized for the extraordinary (X) mode 2nd harmonic ECE at B_o~2T (corresponding to the magnetic field at the major radius R_o = 1.8 m).

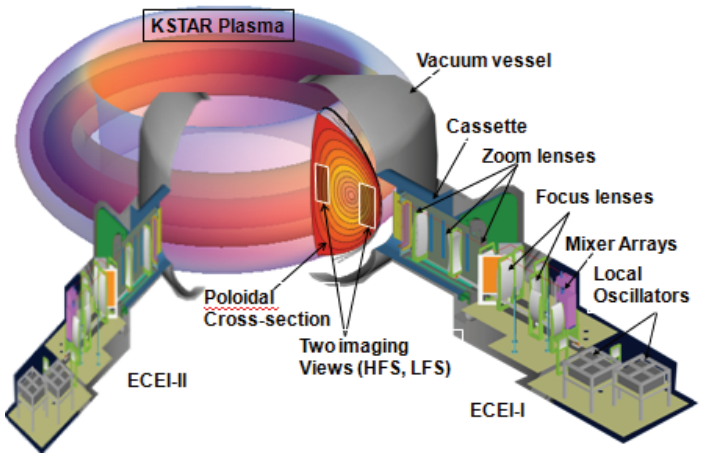

Fig.1. 3D schematic of the two ECEI systems on KSTAR. The ECEI-I system has been successfully operated for the 2010 and 2011 campaigns. The second system (ECEI-II) will be commissioned during the 2012 campaign to directly measure toroidal uniformity of the mode structure, magnetic shear of the ELMs and rotation speeds (toroidal, poloidal and flow).

In KSTAR H-mode operation, the detailed dynamics of ELMs were studied via a 2-D ECEI system that is capable of simultaneously visualizing both the core and edge MHD instabilites. 3D nature of these instabilities will be one of the challenges in the 2012 KSTAR campaign with the aid of the second ECEI-II system which is located at an adjacent port (22.5^0 apart) as illustrated in Fig.1. The 3D data will be used not only for clarifying the rotation speed of the ELMs (mixture of toroidal, poloidal and flow) but also to assess the toroidal uniformity of the mode due to possible mode competition and magnetic shear.

2. Comparison of the measured 2D image with BOUT++ simulations

The measured 2D image of the ELM for n~5 has a radial size of ~3cm and a poloidal mode spacing of ~22cm (peak to peak) as shown in Fig.2a. In the BOUT++ simulation [15,16], the toroidal mode number (*n~5*) determined by magnetic probe is used to obtain the largest growth rate for various pressure profiles based on the measured T_e profile and the line average density. The narrow radial extent of the ELM mode structure (~1cm) is maximized

with the relaxed pressure profile that allows a solution with a finite growth rate. Here the radial width of the mode was increased from ~1cm to ~1.5 cm. Then the poloidal mode spacing of the calculated mode was adjusted with various edge q profiles until the poloidal mode spacing is close to that of the measured image (~13cm, peak to peak). In the course of this exercise, it was found that the poloidal mode spacing driven by the same toroidal mode number (n~5 for this case) is extremely sensitive to the local q-value. The local q value at R=222 cm (ρ~0.85) was varied from ~5 to ~8 while the poloidal mode spacing was changed from ~25 cm to ~13 cm. Note that there are other possible solutions that agree with the measurement for adjacent n numbers with different q profiles. Considering that the radial extent of the simulated ELM mode is comparable to the instrumental resolution of the system as shown in Fig. 2b, one would expect that the measured image will be broadened. In fact, there are two broadening effects that should be superposed in order to compare the calculated image with the measured one. The first one is the emission broadening that occurs when the optical depth is marginal. The other is instrumental broadening that occurs when the target size is comparable to the instrumental width (i.e. the antenna pattern of each detector). The synthetic image deduced from the simulation result with tightly constrained pressure and q profiles is in a good agreement with the measurement as shown in Fig. 2a. simulation results for n=5 case is shown for KSTAR in Fig.2c.

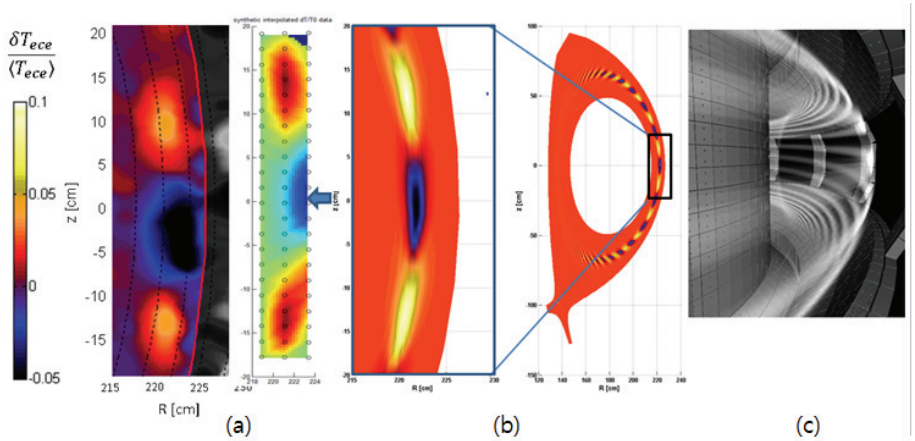

Fig.2. (a) Synthetic image is directly compared with the experimentally measured 2D images. (b) The simulated 2D image from the BOUT++ code (in the middle) is further processed considering the emissivity and instrumental broadening. (c) Simulation result for the ELM with n~5 is plotted against the KSTAR in-vessel structure

Acknowledgement

This work is supported by NRF of Korea contract No. 20090082507 and BK21. This work was partly supported by the JSPS-NRF-NSFC A3 Foresight Program in the field of Plasma Physics (NSFC: No.11261140328).

References

[1] Yun, G.S., et al., "Development of KSTAR ECE Imaging System for Measurement of Temperature Fluctuations and Edge Density Fluctuations", Rev. Sci. Instrum. **81**, 10D930 (2010).

[2] Yun, G.S., et al., "Two-Dimensional Visualization of Growth and Burst of the Edge-Localized Filaments in KSTAR H-mode Plasmas", Phys. Rev. Lett. **107**, 045004 (2011).

[3] Kirk, A., et al., "Spatial and Temporal Structure of Edge-Localized Modes", Phys. Rev. Lett. **92**, 245002 (2004).

[4] Kirk, A., et al., “Evolution of Filament Structures during Edge-Localized Modes in the MAST Tokamak”, Phys. Rev. Lett. **96**, 185001 (2006).
[5] Josheph, I, “Edge-Localized Mode Control and Trnasport gEnerated by Externally Applied Magnetic Perturbations”, Contrib. Plasma Phys., **52**, 326-347 (2012)
[6] Schmid, A., et al., “Experimental Observation of the Radial Propagation of ELM Induced Filaments on ASDEX Upgrade”, Plasma Phys. Controlled Fusion **50**, 045007 (2008).
[7] Silva, C., et al., “Reciprocating Probe Measurements of ELM Filaments on JET”, Plasma Phys. Controlled Fusion **51**,105001 (2009).
[8] Osborne, T.H., et al., “Edge stability of stationary ELM-suppressed regimes on DIII-D”, J. Phys. Conf. Series, **123** 012014 (2008)
[9] Maqueda, R.J., Maingi, R., and NSTX Team, “Primary Edge Localized Mode Filament Structure in the National Spherical Torus Experiment”, Phys. Plasmas **16**, 056117 (2009).
[10] Terry, J.L., et al., “The Dynamics and Structure of Edge-Localized-Modes in Alcator C-Mod”, J. Nucl. Mater. **363–365**, 994 (2007).
[11] Wagner, F., et al., “Regime of Improved Confinement and High Beta in Neutral-Beam-Heated Divertor Discharges of the ASDEX Tokamak”, Phys. Rev. Lett. **49**, 1408, (1982).
[12] Park, H.K., et al., “Observation of High-Field-Side Crash and Heat Transfer during Sawtooth Oscillation in Magnetically Confined Plasmas”, Phys. Rev. Lett. **96**, 195003, (2006).
[13] BOOM, J.E., et al., “2D ECE measurements of type-I edge localized modes at ASDEX Upgrade”, Nucl. Fusion, **51** 103039, (2011)
[14] Classsen, I.G.J., et al., “Characterization of temperature fluctuations during type-I and type –II edge localized modes at ASDEX Ugrade”, EX/P4-07, ibid, (2012)
[15] Xu, X.Q., et al., “Nonlinear ELM simulations based on a nonideal peeling–ballooning model using the BOUT++ code” , Nucl. Fusion, **51,** 103040 (2011) .
[16] Dudson, B.D., et al., **“**A framework for parallel plasma fluid simulations”, Computer Physics Communications, **180**, 1467 (2009)

Detection of the magnetic field structure using imaging diagnostics.

S. Ohdachi
Natural Institute for Fusion Science

1. Introduction

The interaction between externally applied magnetic field and the plasma attracts wide interests. For example, the mitigation of the edge localized mode with the resonant magnetic field perturbation (RMP) becomes the standard procedure for the present and future large tokamak experiments. However, the detailed process, e.g., how the magnetic field penetrate to / is shielded by the plasma has not fully been understood so far. Development of the diagnostics to detect the magnetic field structure in the plasma confined region is urgently required. The magnetic field structure is closely related with the transport phenomena; the transport parallel to the magnetic field is much larger to that perpendicular to the magnetic field, the heat pulses propagate rapidly when the magnetic field line becomes more stochastic and the closed magnetic surfaces is lost.

Two types of the measurement using this property of the transport have been proposed. One is the modification of the plasma profile. Generation of the magnetic island can be detected by the flattening of the electron temperature profile measured by Thomson scattering. Shafer et.al. [1] measured the 2-dimentional soft X-ray emission profile and compare with the model emission profile assuming the modification of the magnetic configuration by the RMP field. The other way is to measure the propagation profile of the heat pulse. Ida. et. al. [2] has studied the heat pulse propagation measured by the electron cyclotron emission (ECE) measurements, and show that there is the stochastic magnetic field region in the core of the Large Helical Device (LHD). Only one dimensional (radial) information of the magnetic field structure can be estimated by this method since the heat pulse is detected on a line located on the equatorial plane. If the heat pulse can be detected 2 or 3 dimensionally, the spatial structure of the magnetic field can be precisely determined. Thereby the physical process between the externally applied field and the plasma would be understood further.

In this report, the possibility whether the 2D/3D heat pulse propagation profile can be measured by the 2D line emission measurement, which is sensitive to the electron temperature. Especially the case of the tangentially viewing VUV camera measuring C^{5+} emission on LHD device is discussed.

2. VUV camera system

The spatial structure of the MHD instabilities is important information in understanding the MHD instabilities. However, since the LHD plasma is surrounded by two superconducting helical coils, there are restrictions on the port arrangement; it is not easy to develop a standard computed tomography based soft x-ray (SX) measurement.
Two-dimensional tangentially viewing camera system has been therefore developed in LHD [3]. In addition to the SX camera system for the core plasma, a tangential viewing vacuum ultraviolet (VUV) telescope system which is suitable for the edge plasma is being developed [4, 5].
An inverse Schwarzschild type optical configuration, consisting of two multi-layer mirrors, is used to form the image. The mirrors are made of layers of molybdenum and silicon (typical thickness: 6.66 nm, δMo:δSi=4:6); VUV light with a wavelength of 13.5 nm (Δλ~1nm) is reflected. Images are detected by a two-stage micro-channel plate (MCP) and finally measured by a fast-framing visible camera.
Line emission from CVI impurities (~13.5 nm) can be selectively measured by this imaging diagnostic with a framing rate up to 2 kHz.

3. Interpretation of the data

The emission from the impurity can be written as

$$N \propto n_e n_I \varepsilon$$

, where, n_e / n_I is the local electron / impurity density and ε is the photo emissivity coefficient. Since the coefficient ε is almost constant from 10eV to 10keV [6], CVI emission intensity mainly reflects the electron and/or impurity density and not the electron temperature. However, if the ionization / recombination process are considered, the local fraction of the certain ionization level is a function of the local electron temperature. Fig. 1 shows the ionic fraction of the carbon impurity assuming the coronal equilibrium. Fraction of the C^{5+} (which emits CVI) would decrease where the electron temperature (Te) increases when Te exceed 70eV. This means that the CVI emission decreases with Te in the most of the plasma confined region. Fig. 2(A) shows a typical time evolution of the CVI intensity measured by the VUV camera system. The emission decreases where the modulated ECH heating system is on. This observation is consistent with this simple model. The profile of the emission intensity and the amplitude of the modulation are shown in Fig. 2(B). The bright area of two parameters is different. While the emission profile is rather broad, the profile modulated component

is localized in the edge region (lower area). Since the CVI emission is sensitive around the Te = 70eV (Fig. 1), the perturbation can be sensitively detected in the edge region. The time constant of the ionization of C^{5+} is less than 1ms. Perturbation slower than 1ms can be studied with this method.

In order to confirm whether propagation of the heat pulse can be studied with this kind diagnostic, a simple model calculation is made; synthetic image assuming a 1D heat pulse propagation is calculated using geometry of the LHD [7]. Profiles of the assumption are shown in Fig. 3. The electron temperature profile (A), fluctuation level (B) and the phase (D) of the electron temperature perturbation and expected change of the CVI emission by the local electron temperature (C) are shown together. The triangles are experimentally measured values in a heat pulse propagation experiments. Fig. 4 shows a synthetic image of the CVI emission. Emission intensity (A) and fluctuation amplitude (B) are shown. The fluctuation amplitude is large in the very edge region which consistent with the experimental observation. Fig. 4(C) shows the phase of the perturbation along the white dashed-line shown in Fig. 4(B). Solid / Dashed lines are correspond to those in Fig. 3(D). The change of the phase shift due to the change of the propagation can be detected assuming this simple model with realistic geometrical condition. Though the phase shift can be nicely detected, detailed spatial structure of the phase cannot be reconstructed so far. It is mainly due to the complexity of the shape of the LHD.

4. Summary and future prospect

A new type of diagnostics for measuring the phase of the electron temperature perturbation using a 2D imaging diagnostics measuring impurity emission is discussed. Comparison of the model and the experimental has just begun and further improvements are required. When this tangential imaging method is applied to the tokamaks, having simpler shapes, two dimensional structure of the heat pulse propagation might be resolved. Detailed structure of the magnetic field will by thereby studied with this method.

5.Acknowledgments

This work was supported partly by JSPS-NRF-NSFC A3 Foresight Program in the field of Plasma Physics (NSFC no. 11261140328).

References

[1] M. Shafer et. al Nucl. Fusion **52** (2012) 122001

[2] K. Ida, et. al., ``Evidence of Stochastic Region near a Rational Surface in Core Plasmas of LHD", in Proc. of 24th Fusion Energy Conference, EXS/5-2.

[3] S. Ohdachi et al., Fusion Sci. Technol.**58**, 418 (2010)

[4] M. Takeuchi and S. Ohdachi, Fusion Plasma Research **6**, S1037 (2010).

[5] T. F. Ming, Rev. Sci. Instrum, **83**, 10E513 (2012).

[6] F. Fang. et. al., Atomic Data and Nuclear Tables, **61**, 91 (1995)

[7] S. Ohdachi, et. al., ``Retrieval of information of perturbed displacement of MHD instabilities from the tangentially viewing imaging data", in Proc of 39th European Physical Society Conference on Plasma Physics 16th International Congress on Plasma Physics Stockholm, Sweden, 2012, P5.001.

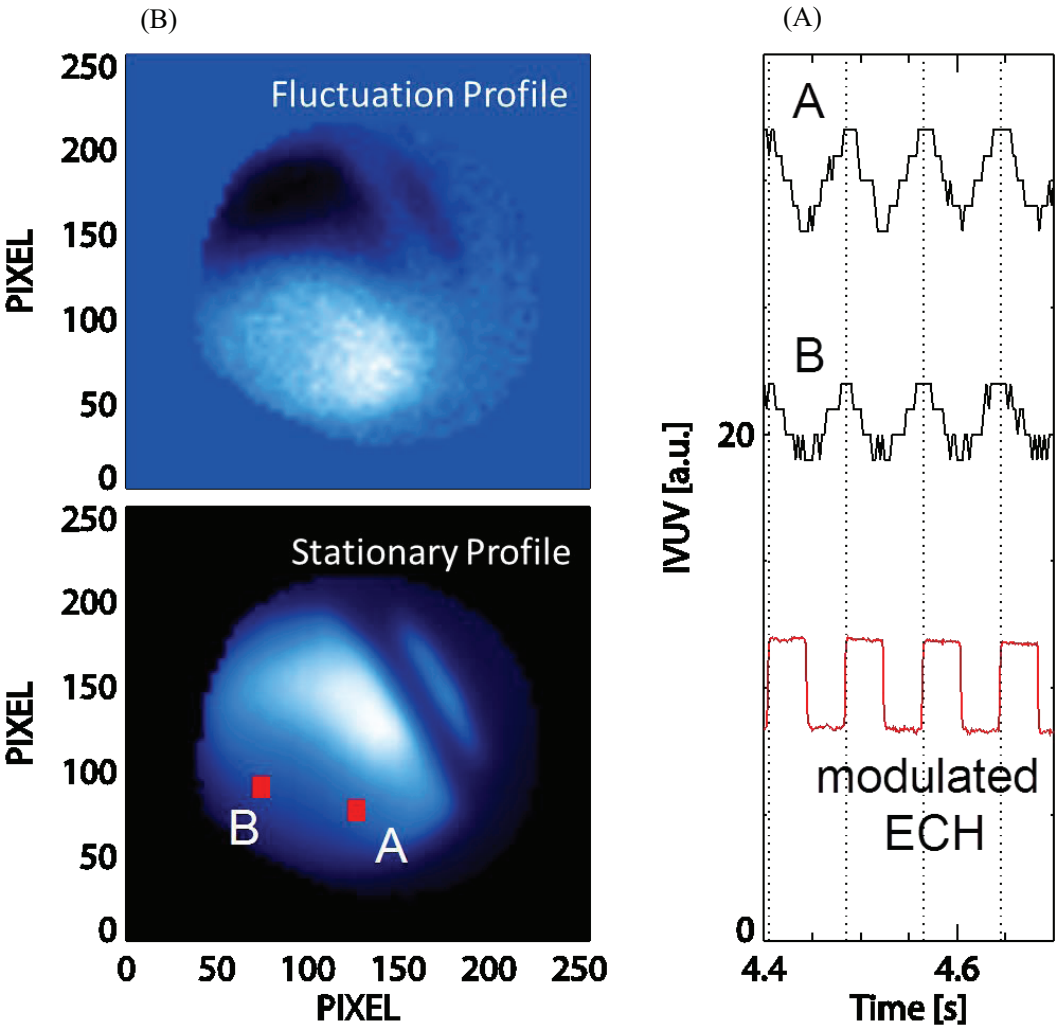

Fig 1. Typical time evolution of the CVI intensity with modulated ECH experiments.

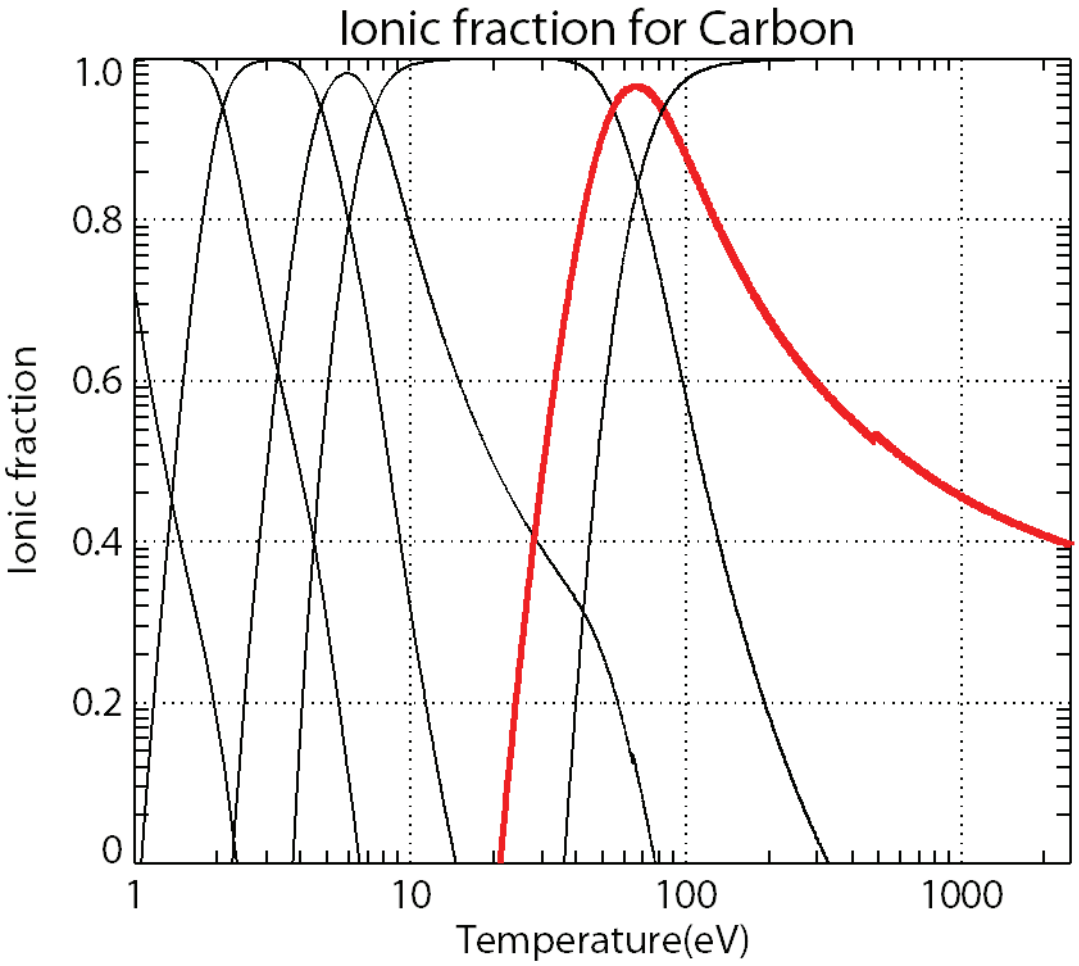

Fig. 2 Ionic fraction for carbon impurity assuming coronal equilibrium

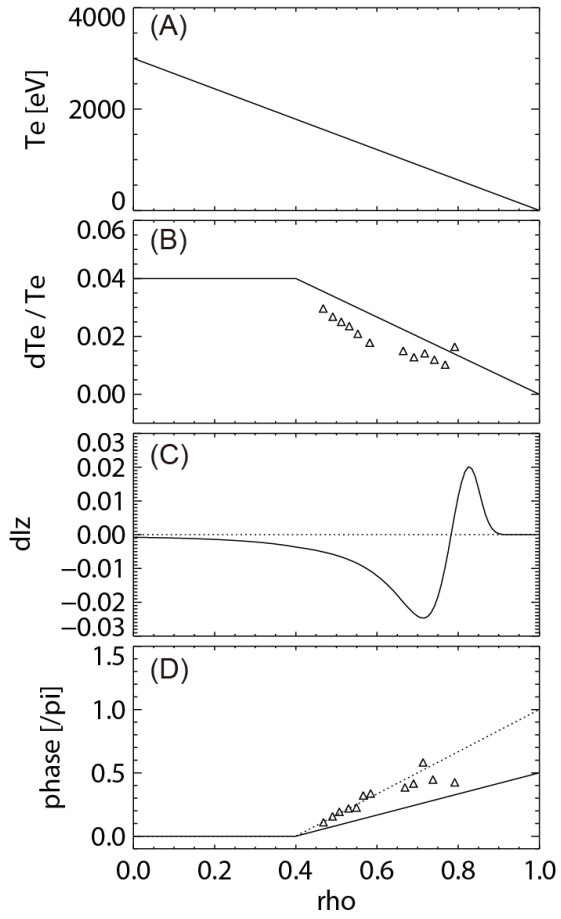

Fig. 3 Assumption of the parameters for the calculation of the synthetic image shown in Fig. 4. Two type of phase profile shown in (D) are used.

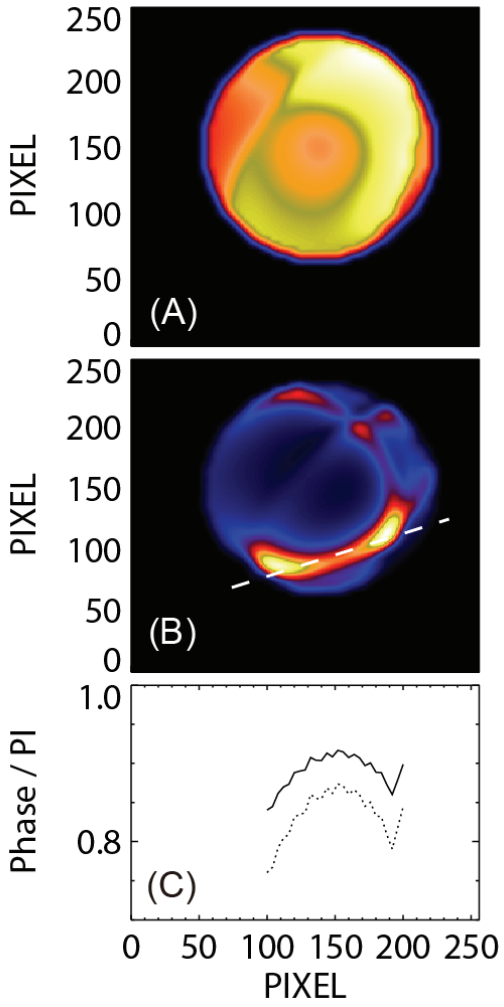

Fig. 4 Synthetic image of the emission (A) and fluctuation amplitude (B) and phase in the peak location are shown.

Category IIb-1

Comprehensive Understanding and Control of Edge Localized Modes in 2D and 3D Toroidal Plasmas

K. Toi
National Institute for Fusion Science, Japan

Abstract

The characteristics of edge localized modes (ELMs) in the Large Helical Device (LHD) are briefly summarized. The triggering MHD instabilities are thought to be ideal/resistive interchange modes, and are different from peeling/ballooning modes which are thought to be the cause of ELMs in tokamaks. Interchange mode in an LHD plasma and ballooning mode in a tokamak plasma can be destabilized by the pressure gradient at the edge transport barrier (ETB) or pedestal, while peeling mode can be destabilized in a tokamak plasma by the toroidal current density at the pedestal. ELMs in LHD were also mitigated by resonant magnetic perturbations (RMPs) as similar to tokamaks. The ELM amplitude was reduced by a factor of two or more and the repetition frequency was enhanced by a factor of more than five. This result is similar to that observed in tokamaks. In the *JSPS A3 foresight program*, the ELMs observed in LHD are compared to those observed in EAST and KSTAR tokamaks for comprehensive understanding of global stability of ETB /pedestal region, focused on the roles of interchange, ballooning and peeling modes in the edge. The final goal is to develop effective ELM control scenarios, without deterioration of other MHD stability and confinement performance.

1. Introduction

Control of edge localized modes (ELMs) is one of critical issues to sustain high performance plasmas in a steady state, and is attempted using various techniques in many tokamaks [1]. The JSPS A3 foresight program aims at clarifying and solving critical physics issues specific to steady state sustainment of high-performance plasmas

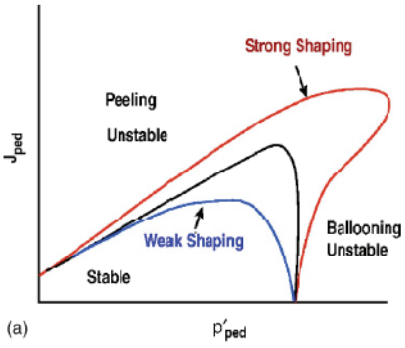

Fig.1 Calculated stability boundary of ELMs in a tokamak plasma[2].

through trilateral collaborations using three super conducting toroidal devices EAST, KSTAR and LHD. In the Category IIb-1 of the A3 foresight program, ELM control in H-mode plasmas is one of important target topics. ELMs in tokamak plasmas are induced by peeling and/or ballooning modes. This is shown in Fig.1 which is cited from [2]. Triggering of large amplitude ELMs by peeling-ballooning mode is widely accepted for interpretation of ELMs in tokamaks. Studies of characteristics of ELMs are conducted in RF-heated H-modes of EAST [3] and in NBI-heated H-modes of KSTAR [4]. In parallel to these studies, mitigation of large amplitude ELMs are attempted by RMPs, super-sonic gas injection, vertical jogging of a plasma, and so on [5]. In particular, mitigation, suppression and even excitation of ELMs are observed by application of RMPs.

In the following sections, characteristics of ELMs in LHD and the mitigation by RMPs are presented. An initial experiment of plasma current modulation in EAST to study edge current density effect on ELMs is briefly discussed.

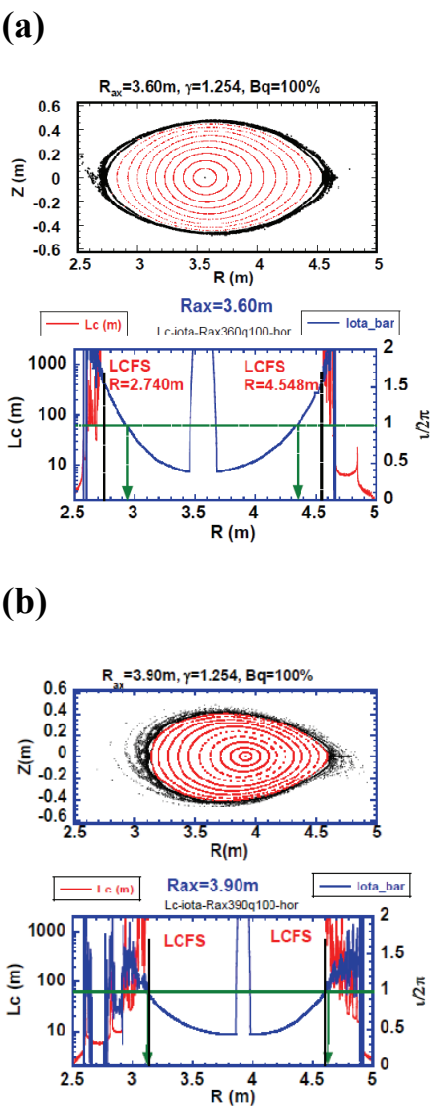

Fig.2 Poincare plot of the vacuum field line and the radial profiles of $\iota/2\pi$ and the connection length of the field line in the configurations of R_{ax}=3.6m (a) and 3.9m (b).

2. Study of H-modes and ELM characteristics on LHD

The LHD is a stellarator/helical device. The confined plasmas are three-dimensional (3D) and the nested magnetic surfaces are surrounded by stochastic field region in the vacuum field. An MHD equilibrium calculation without assumption of the existence of nested magnetic surfaces shows that the edge stochastic region survives and further expands from the last closed flux surface (LCFS) to more interior in H-mode plasmas with finite beta. Moreover, the edge region of LHD is always in the magnetic hill even

in high toroidal beta regime. Interchange modes can be destabilized by the pressure gradient at the ETB. Another important difference for the tokamak configuration is that the lowest order rational surface $\iota/2\pi$=1 (or q=1) locates near the edge, not near the center. The location moves outward with the increase of the magnetic axis position of the vacuum field (R_{ax}), that is, the $\iota/2\pi$=1 locations are the normalized minor radius r/a~0.85 and 1.02 in the configurations of R_{ax}=3.6m and 3.9m, respectively (Fig.2). The ETB in H-modes of LHD is formed in the magnetic hill region [6]. Typical ELMs excited in both magnetic configurations of R_{ax}=3.6m and 3.9m are shown in Fig.3. The ELMs in the former configuration exhibit high frequency and small amplitude character and the reduction rate of the plasma stored energy by an ELM $\Delta W_p/W_p$ is small (= 1-2 %)(Fig.3(a)). The ELMs in the latter configuration have low frequency and large amplitude character, and $\Delta W_p/W_p$ is large (= 4 – 6 %)(Fig.3(b)). These ELMs in LHD are thought to be interchange modes, in particular, resistive interchange modes are most likely instabilities in ETB [6,7]. That is, free energy to excite the MHD modes is the pressure gradient at the ETB, while toroidal current density as well as pressure gradient at the ETB or pedestal are free energy of ELMs in tokamak plasmas, as mentioned above.

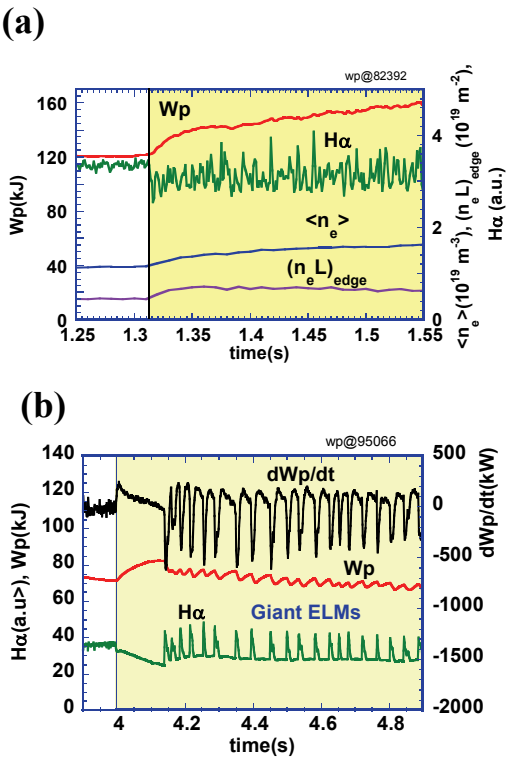

Fig.3 Typical ELMs in the configurations of Rax=3.6m (a) and 3.9m (b).

3. ELM Mitigation by RMPs on LHD

In LHD, large amplitude ELMs in the R_{ax}=3.9m configuration were successfully mitigated by RMPs for the first time in a stellarator/ helical device [8]. The RMPs were produced by a set of external coils called "LID coil" which is placed outside the vacuum vessel and is shown in

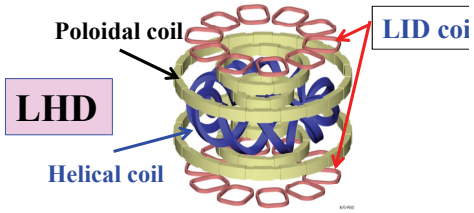

Fig.4 Coil assembly in LHD. The LID coil consists of 20 coils placed above and below the vacuum vessel.

Fig.4. The dominant Fourier component of RMPs is m=1/n=1 where m and n are the poloidal and toroidal mode numbers, respectively. The generated maximum radial field is about several mT at the magnetic axis of the vacuum field. For the ELM mitigation, stationary RMPs were applied. When the coil current was increased up to 0.6 kA which corresponds to ~ 5G at the magnetic axis of the vacuum field, the large amplitude ELMs were mitigated clearly, where the toroidal field strength is B_t=0.9T. At this condition, the vacuum field calculation shows that a narrow annular region of 0.9<r/a<1 becomes stochastic by RMPs. An m=1/n=1 remnant magnetic island is formed by the m=/n=1 RMPs, since the $\iota/2\pi$=1 (or q=1) resonance layer resides in stochastic region of r/a>1. In Fig.5, the characteristics of ELMs are compared for two cases without RMPs and with RMPs. In the H-mode obtained without RMPs, large amplitude ELMs modulate W_p significantly, i.e., up to ~ 20 %. In this H-mode, the electron density increases linearly until an ELM. The ELM repetition frequency is low, i.e., 5-30 Hz. When the RMPs having the magnitude were applied to the H-mode with large amplitude ELMs, the amplitude is reduced by a factor of two or more, and the repetition frequency increased by a factor of more than 5, i.e., 50-150 Hz. In the phase of 4.1-4.7s where both shots are in H-phase, RMPs clearly reduced electron density, although the gas puff rate feedback controlled increased to compensate the density

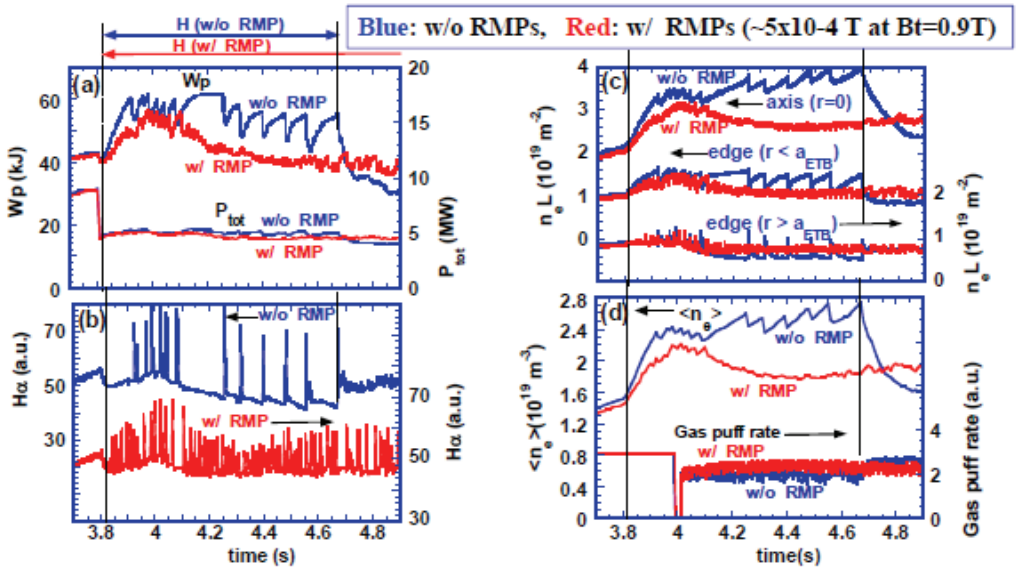

Fig.5 Characteristics of the H-modes without (blue curves) and with (red curves) RMPs. The applied stationary RMP is ~ 5G at the magnetic axis in the vacuum, where B_t=0.9T. (a) Stored energy and absorbed NBI power, (b) Hα emission, (c) line integrated electron densities at the center, just inside the last closed flux surface (LCFS) and just outside LCFS, and (d) line averaged electron density and gas puff rate.

decrease. In H-phase, RMPs enhanced particle transport in the ETB region. This is similar to DIII-D and JET results [9,10]. The radial profile of the changes in electron density and electron temperature indicates that the ELMs mitigated by RMPs affect the narrower region of the ETB in the electron density. The time evolution of 10 electron pressure profiles for 0.3s indicates that the pressure gradient at the ETB is slightly reduced for those in the H-mode without RMPs. Nevertheless, the ELM repletion frequency is enhanced by a factor 5. This fact suggests that a certain stabilization factor of magnetic configuration for ELMs may be resuced by the application of RMPs. The ELM mitigation on LHD will be different from that with RMPs in tokamaks, because the enhanced ELM frequency in tokamak plasmas is thought to be caused by peeling modes [11]. Detailed mechanism of ELM mitigation on LHD is under investigation.

4. Proposal for the study of peeling modes in EAST and KSTAR

In order to investigate a role of peeling modes in ELMs, an initial experiment was done on the EAST tokamak in the fiscal year 2012. A rapid current ramp-down and ramp-up altered the characteristics of ELMs slightly, where type III ELMs were excited in the experiment. Although the experiment was preliminary, the current waveform modulation is expected to alter ELM behaviors in the next EAST experiment campaign, where upgraded ICRF heating will be applied to produce H-modes having type I ELMs. This current waveform modulation may also affect type I ELMs observed in NBI heated H-modes on KSTAR. In the former half of the next fiscal year 2013, possible modulation amplitude and frequency of the plasma current should be investigated for these super conducting tokamaks EAST and KSTAR.

Acknowledgements

We acknowledge the EAST team for their support in the initial experiment of plasma current modulation. We are also grateful to Liqun Hu for his support in the EAST experiment. This research is supported in part by the *Japan-China Collaboration Program* succeeded from *the JSPS-CAS Core University Program*, and the *JSPS A3 Foresight Program on Critical Physics Issues Specific to Steady State Sustainment of High-Performance Plasmas*. This work was partly supported by the JSPS-NRF-NSFC A3 Foresight Program in the field of Plasma Physics (NSFC: No.11261140328).

References

[1] E.J. Doyle et al., Nucl. Fusion **47** (2007) S18–S127.

[2] P.B. Snyder et al., Phys. Plasmas **12**, 056115 (2005).

[3] G.S. Xu et al., Nucl. Fusion **51,** 072001(2011).

[4] G.S. Yun et al., Phys. Rev. Lett. **107**, 045004 (2011).

[5] J.G. Kwak et al., "Overview of KSTAR Results", 24th IAEA FEC 2012, San Diego, paper No. OV/2-4.

[6] K. Toi et al., Fusion Sci. Technol. **58**, 61 (2010).

[7] F. Watanabe et al., Contrib. Plasma Phys. **50**, 651(2010).

[8] K. Toi et al., "Mitigation of Large Amplitude ELMs by Resonant Magnetic Perturbations on LHD", 24th IAEA FEC 2012, San Diego, paper No. EX/P4-10.

[9] T.E. Evans et al., Phys. Rev. Lett. 92, 235003(2004).

[10] Y. Liang et al., Phys. Rev. Lett. 98, 265004 (2007).

[11] C. G. Gimblett et al., Phys. Rev. Lett. 96, 035006 (2006).

Energetic-particle diagnostics and physics in toroidal fusion plasmas

Mitsutaka Isobe[1,2], Kunihiro Ogawa[1]
[1] *National Institute for Fusion Science, Toki, Japan*
[2] *The Graduate University for Advanced Studies, Toki, Japan*

Hideki Tomita[3], Yosuke Yamamoto[3], and Fumitaka Yamashita[3]
[3] *Nagoya University, Nagoya, Japan.*

MunSeong Cheon[4], Jun-Young Kim[5], Junghee Kim[4], and Siwoo Yoon[4]
[4] *National Fusion Research Institute, Daejeon, Korea.*
[5] *University of Science and Technology (UST), Daejeon, Korea.*

Jiafeng Chang[6], Guoqiang Zhong[6], and Liqun Hu[6]
[6] *Institute for Plasma Physics, Chinese Academy of Sciences, Hefei, China.*

Yipo Zhang[7], Guoliang Yuan[7], and Yi Liu[7]
[7] *Southwestern Institute of Physics, Chengdu, China*

Yiqin Liu[8] and Xiaobing Luo[8]
[8] *Institute for Nuclear Science and Technology, Sichuan University, Chengdu, China*

1. Introduction

Good confinement of energetic ions in magnetically confined fusion plasmas is required in order to realize a fusion reactor, since fusion-born energetic α particles play an essential role as a primary heating source in future burning plasmas. With a burning plasma stage imminent, the physics of the interplay between energetic ions and energetic-ion-driven MHD instabilities such as toroidicity-induced Alfvén eigenmodes and energetic-particle continuum modes have become more important in recent years because those MHD instabilities can potentially lead to the anomalous loss of energetic αs, resulting in the loss of a self-ignited condition. Actually, Alfvénic modes have been regularly observed in tokamak and helical/stellarator plasmas with strong super-Alfvénic ion tails [1,2]. Although the transport of energetic particle (EP) due to

axisymmetry breaking of the system is one of the oldest issues, it is also becoming the object of attention again since the non-axisymmetric perturbed field produced by resonant magnetic perturbation (RMP) coils is often superposed on tokamak equilibrium to mitigate ELMs in recent experiments, giving unfavorable effects on EP orbit and/or confinement. For reasons mentioned above, EP physics experiments have been intensively conducted in Asian fusion machines. In this proceeding, EP diagnostics and physics in LHD, KSTAR, EAST, and HL-2A are briefly overviewed and subsequently ongoing collaborative works on EP in the framework of A3 foresight program are described.

2. Energetic-particle diagnostics and physics

LHD, KSTAR, EAST and HL-2A have been equipped with a comprehensive set of EP diagnostics to study behavior of EPs caused by axisymmetry breaking and/or EP-driven MHD instabilities. EP and neutron diagnostics in four large-scale machines in Asia are listed in Table 1. In addition, EP-related physics issues are listed in Table 2. A scintillator-based fast-ion loss detector (FILD) is a powerful and effective tool to investigate anomalous transport of EP due to EP-driven MHD instabilities. FILD has been installed onto LHD, KSTAR, and HL-2A and is going to be installed on EAST in the collaboration between ASIPP and NIFS. A satisfactory whole to make a comparison of effects of EP-driven MHD instabilities on EP transport and/or loss between tokamaks and LHD is almost ready. Deuterium experiments are being performed in KSTAR, EAST and HL-2A expect LHD, producing fusion neutrons. Note that in neutral beam (NB)-heated plasmas, neutron diagnostics play an important role not only in measuring fusion output but also in assessing global confinement property of beam ions because most of neutrons are produced by beam-plasma reactions in existing experiments.

Table 1. Energetic particle and neutron diagnostics in four large-scale machines in Asia

Devices	Existing		Future
	Escaping	Confined	
LHD	FILDs [3]	NPAs, FICXS, CTS, PCX, and HX-rays [4]	NFM, NAS, NC, NES and γ-rays [5]
KSTAR	FILD [6]	NFM, NAS [7], γ(HX)-rays [8], NES, and NPA	FIDA
EAST		NFM [9], NC, γ(HX)-rays	FILD, FIDA, and NPA
HL-2A	FILD	NFM, γ(HX)-rays, and NPA	FIDA

Table 2. Energetic particle-related physics issues in four large-scale machines in Asia

Devices	Orbit issues	MHD effects on energetic particles	
		EP-driven	Non-resonant
LHD	Ripple transport due to 3D-ness[10], RMP effect	TAE, RSAE, EPM, eEPM, HAE, EGAM •• [2]	Resistive interchange mode [11], ELM
KSTAR	RMP effect, TF ripple	TAE, EPM	ELM, Tearing mode, Sawtooth
EAST	TF ripple		Sawtooth
HL-2A	TF ripple	FB, eFB, eBAE, BAAE [12,13]	Tearing mode [14]

3. Ongoing collaborative works on energetic particle

3.1 Setup of Lorentz orbit code for tokamaks

NIFS Lorentz orbit code, called "LORBIT" was originally developed for CHS escaping beam ion diagnostics [15] and is now used for LHD. Recently, it has been modified for ITER in search of position suitable for escaping a-particle diagnostics [16]. Subsequently, the LORBIT code has been applied to KSTAR, EAST and HL-2A. The Lorentz orbit calculation is essentially required to find a position suitable for detection of escaping energetic ions. It is also necessary to design the probe head section. Moreover, it is helpful to understand orbit topology of escaping beam ions reaching the FILD. In the LORBIT code, energetic-ion orbits are calculated in a cylindrical coordinates system (R,Z,ϕ). The local magnetic field is reconstructed from the rectangular grid of the value of the poloidal flux function $\Psi(R,Z)$ provided by EFIT. Energetic-ion orbits with finite Larmor radii are tracked in the tokamak equilibrium mentioned above by numerically solving the Lorentz force equation $(m \bullet dv/dt = q \bullet (v \times B))$. Figure 1 shows typical collisionless beam-ion orbits in KSTAR, EAST and HL-2A.

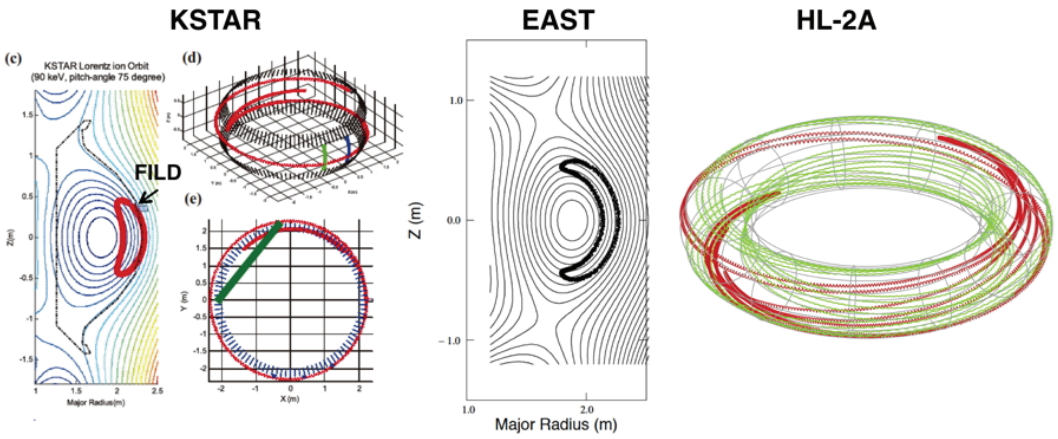

Fig. 1 Beam-ion orbits in KSTAR, EAST and HL-2A calculated by LORBIT.

3.2. Fast-ion loss detector collaboration in KSTAR and HL-2A

FILD is based on a magnetic spectrometer concept [11, 15], providing information of both gyroradius and pitch angle of escaping energetic ions as a function of time. Start of operation of KSTAR FILD was in 2011. The scintillation light due to impact of escaping beam ions was measured with camera only in 2011. In 2012, the measurement section was largely enhanced to follow rapid MHD events. In addition to the camera, 16 channel photomultiplier tube (PMT) array was intalled. In 8, Nov. 2012, we performed calibration of PMT's viewing position and made an effort to obtain good focus. As a result of collaborative work, fluctuation of beam-ion loss correlated with non-resonant MHD activities was obtained. Spectrograms of PMT (ch#11) and Mirnov coil signals while tearing mode and sawtooth coexisted are shown in Fig. 2 as an example.

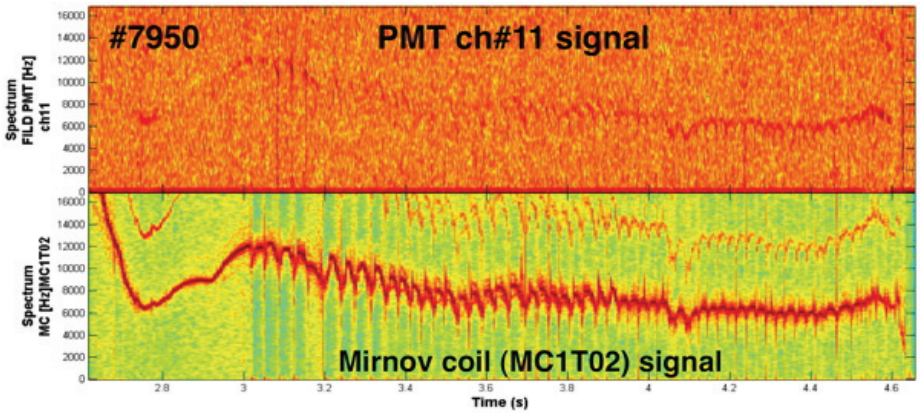

Fig. 2 Spectrogram of FILD and Mirnov coil signals while tearing mode and sawthooth coexisted.

Collaborative efforts between SWIP, Sichuan University and NIFS have been made for the design and construction of FILD on HL-2A. In 2010, the FILD position suitable of escaping beam ion detection was carefully investigated for HL-2A by the LORBIT code. The detailed design of the probe head section was also carried out. FILD was constructed in Sichuan University in 2011 and fundamental check of the system was performed. In 2012, FILD was installed onto HL-2A as shown in Fig.3. The HL-2A FILD is now ready for measurement.

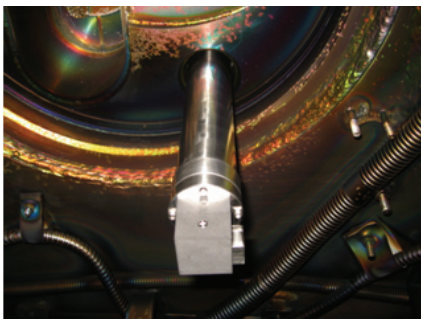

Fig. 3 Fast-ion loss detector installed on HL-2A.

3.3. Neutron energy spectrometer collaboration in KSTAR

Neutron energy spectrometry was originally proposed for measurement of fuel-ion temperature [17]. In NB(D^0)-heated plasmas, neutron spectrometry is no longer applicable to ion-temperature diagnostic. It provides slowing-down distribution and/or confinement of beam ions. DD neutron energy spectrometer (NES) developed by Nagoya University (NU)–NIFS collaboration was exported to KSTAR in 2012. Fundamental function of NU-NIFS NES consisting of thee detectors, i.e. scintillator as a recoil proton radiator, recoil proton detector (RPD) and scattered neutron detector is described in Ref. 18 in detail. Proof of principle experiment was performed at fusion neutron source facility at JAEA before exportation to KSTAR, indicating energy resolution of ~6 % for 2.5 MeV neutrons. After we performed neutronics design on NES for KSTAR [19], the spectrometer was installed at J-port, having perpendicular line of sight. Fig. 4 shows time evolutions of RPD signals of the NU-NIFS NES and neutron flux monitors (NFMs) of KSTAR. As can be seen in Fig.4, the time trend of RPD signal agrees with that of NFMs. It should be noted that coincident three signal pulses were not dominant in the 2012 operation. Further efforts will be made to improve this situation toward 2013 campaign.

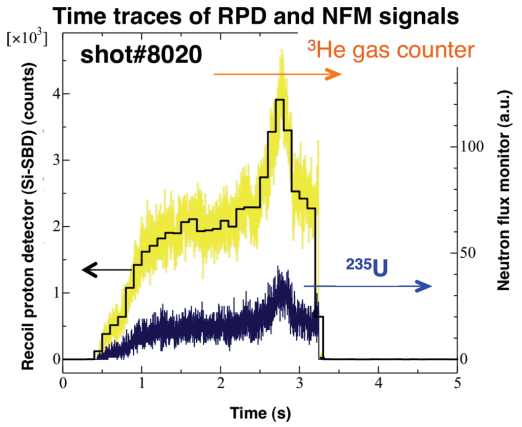

Fig. 4 Time traces of recoil proton detector signal of NU-NIFS NES and neutron flux monitor of KSTAR in NB-heated plasma.

4. Summary and future

Energetic-particle and neutron diagnostics have been steadily enhanced in LHD, KSTAR, EAST and HL-2A to investigate physics related to energetic ions. FILD has been installed in LHD, KSTAR and HL-2A. It is also going to be installed on EAST. A satisfactory circumstance to make a comparison of interplay between energetic ions and EP-driven MHD instabilities between tokamaks and LHD is being ready.

Lately, effect of non-axisymmetric perturbed field produced by RMP coils on energetic ions is of great concern in tokamaks. Transport of energetic ions due to non-axisymmetric helical field components has been one of key physics issues in LHD because helical or stellarator plasma is intrinsically three-dimensional. In addition to

EP-driven MHD instabilities, effect of three-dimensional field on orbit and/or confinement energetic ions is going to be investigated.

Acknowledgements

This work was partly supported by the JSPS-NRF-NSFC A3 Foresight Program in the field of Plasma Physics (NSFC: No.11261140328).

References

[1] B.N. Breizman and S.E. Sharapov, Plasma Phys. Control. Fusion **53** (2011) 054001.

[2] K. Toi, K. Ogawa, M. Isobe *et al*., Plasma Phys. Control. Fusion **53** (2011) 024008.

[3] K. Ogawa, M. Isobe, and K. Toi, J. Plasma Fusion Res. SERIES **8** (2009) 655.

[4] M. Isobe, M. Osakabe *et al*., Fus. Sci. Technol. **58** (2010) 426.

[5] M. Isobe, H. Yamanishi *et al*., Rev. Sci. Instrum. **81** (2010) 10D310.

[6] Junghee Kim, Jun-Young Kim, S.W. Yoon, M. García-Muñoz, M. Isobe and W.C. Kim, Rev. Sci. Instrum. **83** (2012) 10D305.

[7] M.S. Cheon, Y.S. Lee *et al*., Journal of Instrumentation **7** (2012) C05009.

[8] J.W. Yoo, Y.S. Lee *et al*., Tran. Fus. Sci. Technol. **60** (2011) 90.

[9] Guoqiang Zhong, Liqun Hu *et al*., Plasma Science and Technology **13** (2011) 162.

[10] S. Murakami, H. Yamada *et al*., Fus. Sci. Technol. **46** (2004) 241.

[11] K. Ogawa, M. Isobe *et al*., Plasma and Fusion Research **4** (2009) 033.

[12] W. Chen, X.T. Ding *et al*., Nucl. Fusion **50** (2010) 084008.

[13] Yi Liu, M. Isobe *et al*., Nucl. Fusion **52** (2012) 074008.

[14] M. Isobe, Yi Liu *et al*., Chin. Phys. Lett. **26** (2009) 105201.

[15] M. Isobe, D.S. Darrow *et al*., Rev. Sci. Instrum. **70** (1999) 827.

[16] M. Isobe, D. Funaki, and M. Sasao, J. Plasma Fusion Res. SERIES **8** (2009) 330.

[17] H. Brysk, Plasma Physics **15** (1973) 611.

[18] H. Tomita, H. Iwai, T. Iguchi, M. Isobe *et al*., Rev. Sci. Instrum. **81** (2010) 10D309.

[19] Y. Yamamoto, H. Tomita, M. Isobe, MunSeong Cheon *et al*., accepted for publication in Progress in Nuclear Science and Technology.

Current research efforts of EP study in Korea

C. M. Ryu,
POSTECH/NFRI

1. Introduction

The physics of energetic particle-driven modes destabilized by resonant fast ions or electrons is one of the key issues in the controlled thermonuclear fusion research.[1-8] Unstable wave modes with global eigenfunctions, such as AE(Alfven Eigenmode)s, can scatter energetic ions out of the plasma core before these ions have been thermalized.[4] This causes deleterious effects on alpha particle confinement, making self-sustaining ignition more difficult and also imposing a great wall loading problems. Destabilization of AEs by NBI ICRH ions, and ECRH electrons has been observed in TFTR, DIII-D, W7-AS, HL-2A, JT-60U, JET, and other tokamaks.[9-18] After the successful demonstration of H mode on KSTAR, the problem of fast-ion driven MHD modes such as Alfven eigenmodes (AEs) and the reverse effects on fast ions of MHD modes is under study in KSTAR. In this paper, I will briefly describe some recent efforts of KSTAR on energetic particle physics study.

2. Current KSTAR research efforts

Current heating source equipped by KSTAR are as follows:

ECH	110GHz, 400kW, 2s 84GHz, 300kW, 2s 170GHz, 800kW, 10s
LHCD	5GHz, 300kW, ss
ICRH	30MHz, ~1.0MW, 10s
NBI	1.6MW @ 100keV, D_0, >10s

NBI is a powerful tool for the investigation of fast ion driven MHD modes such as TAE modes and fishbone modes. The fast electron driven mode is a critical and important issue in tokamaks. ECH at different frequencies can be used to excite electron fishbone modes or to control the fast ion driven modes by ICRH. The physics objectives of 2012 campaign are

1) Investigation of the energetic ion driven Alfvenic modes (TAE or BAAE)

2) Investigation of the energetic ion driven modes (fishbone or LLM)
3) Investigation of the energetic electron driven modes (e-fishbone or BAE),
and we found evidence of some of these modes.

For the diagnostics of EP physics several basic diagnostics such as MC (Mirnov coil) and ECE are employed. Frontier diagnostics such as FILD for the fast ion loss are under development . Runaway electrons have interesting physics and are an important subject for particularly for the wall issues.[19-22] For the study of runaway electrons, 2D synchrotron imaging system is developed, and theory of its whistler wave suppression is studied.

In Fig. 1-2, we show the evidence of the TAE modes together with EPM modes. With early injection of the NBI during the ramp-up phase, we could find that Alfvenic activities are excited. The experimental scenario is as shown in the figure.

Figs.3-4 show the FILD and the 2D synchrotron imaging system

3. Conclusions

After the H mode is well established in a long pulse more than 10sec, KSTAR provides a good environment for energetic particle study. Diagnostics for this study are currently mainly MC, ECE, but new diagnostics are rapidly added. Basic energetic particle driven modes such as TAE, EPM , LLM start to be seen. Our FILD and synchrotron imaging systems start showing interesting data, which will be further improved via the collaboration with other country A3 member teams.

4. Acknowledgement

This work has been supported by the A3 program and also by NRF-2008-0062-209 and NRF- 2011-0026107. This work was partly supported by the JSPS-NRF-NSFC A3 Foresight Program in the field of Plasma Physics (NSFC: No.11261140328).

References

[1] Chen L. *et al* 1984 *Phys. Rev. Lett.* **52** 1122
[2] Chen L. and Zonca F. 2007 *Nucl. Fusion* **47** S727
[3] Wong K.L. *et al* 2000 *Phys. Rev. Lett.* **85** 996
[4] Heidbrink W.W. *et al* 2006 *Plasma Phys. Control. Fusion* **48** 1347
[5] Nazikian R. *et al* 2008 *Phys. Rev. Lett.* **101** 185001
[6] McGuire K. *et al* 1983 *Phys. Rev. Lett.* **50** 891
[7] Zonca F. *et al* 2007 *Nucl. Fusion* **47** 1588
[8] Wong K.L. *et al* 2000 *Phys. Rev. Lett.* **85** 996
[9] Ding X.T. *et al* 2002 *Nucl. Fusion* **42** 491
[10] Chen W. *et al* 2009 *Nucl. Fusion* **49** 075022
[11] Lazaros A. 2001 *Phys. Plasmas* **8** 1263

[12] Berk H.L. *et al* 1997 *Phys. Lett.* A **234** 213
[13] Heidbrink W.W. and Sadler G.J. 1994 *Nucl. Fusion* **34** 535
[14] Fasoli A. *et al* 2007 *Nucl. Fusion* **47** S264
[15] Sun Y. *et al* 2005 *Phys. Plasmas* **12** 092507
[16] Wang Z.T. *et al* 2006 *Chin. Phys. Lett.* **23** 158
[17] Wang Z.T. *et al* 2007 *Nucl. Fusion* **47** 1307
[18] Zonca F. *et al* 2007 *Nucl. Fusion* **47** 1588
[19] Porcelli F. et al 1996 Plasma Phys. Control. Fusion **38** 2163
[20]Dreicer, H., Electron and ion runaway in a fully ionized gas, 1960, Phys. Rev. **117**, 329.
[21]Rosenbluth, M.N. and Putvinski, S.V., Nucl. Fusion 1997, **37** 1355.
[22]Connor, J.W. and Hastie, R.J., 1975 Nucl. Fusion **15** 415.

Figures

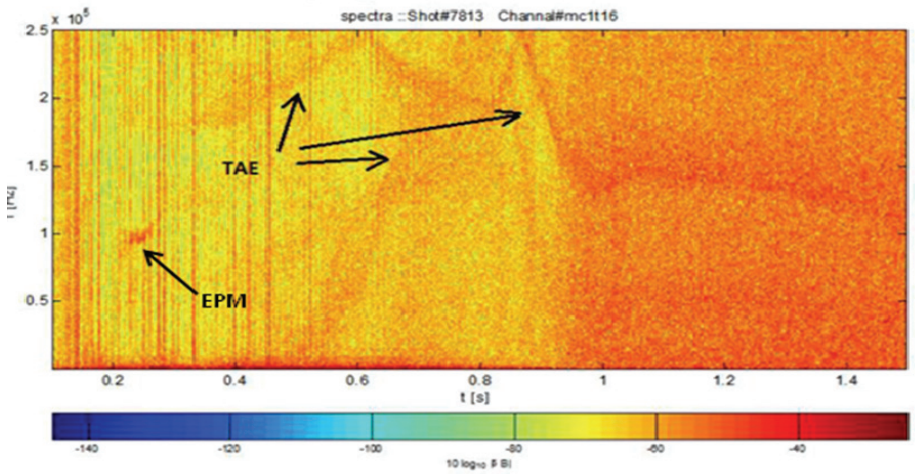

spectogram of MC data(shot 7813) showing Alfvenic activity

Fig1. Evidence of TAE and EPM modes.

(Shot #7813 Bt= 3,0 T Deuterium plasma, Ip = 600 kA, Ip flattop = 4.5 s, Two D-NBI beams: E=90keV(0.2s,1.46MW),80keV(0.9s ,1.2MW))

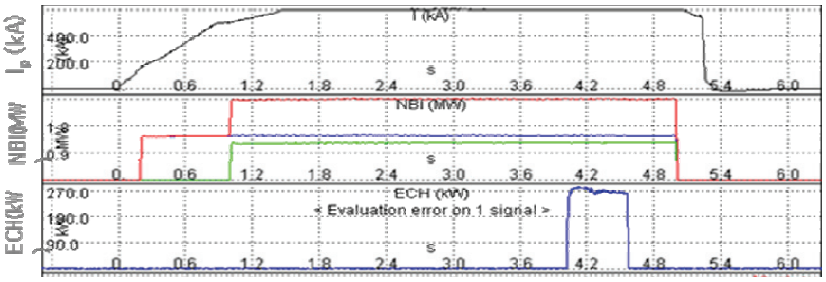

Fig2(a)

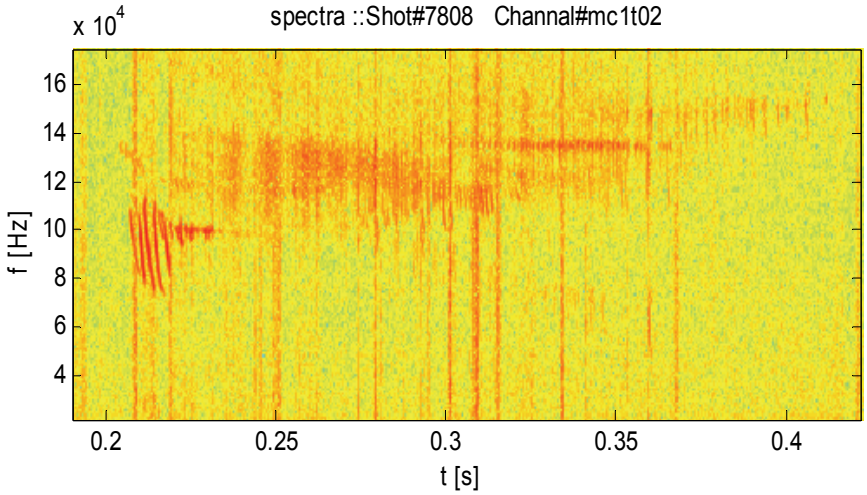

Fig2(b)

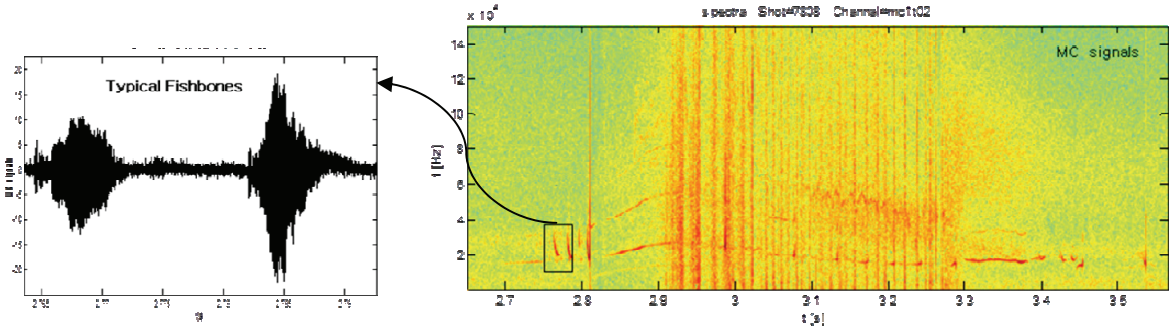

Fig2(c)

Fig2. EPM, fishbone mode and LLM observed during NBI in KSTR tokamak

(**Fig.(2a)** Experimental scenario, **Fig.(2b)** Observation if EPM at f=80~130 kHz when q(0)>1, **Fig.(2c)** Observation of typical fishbone mode and LLM **)**

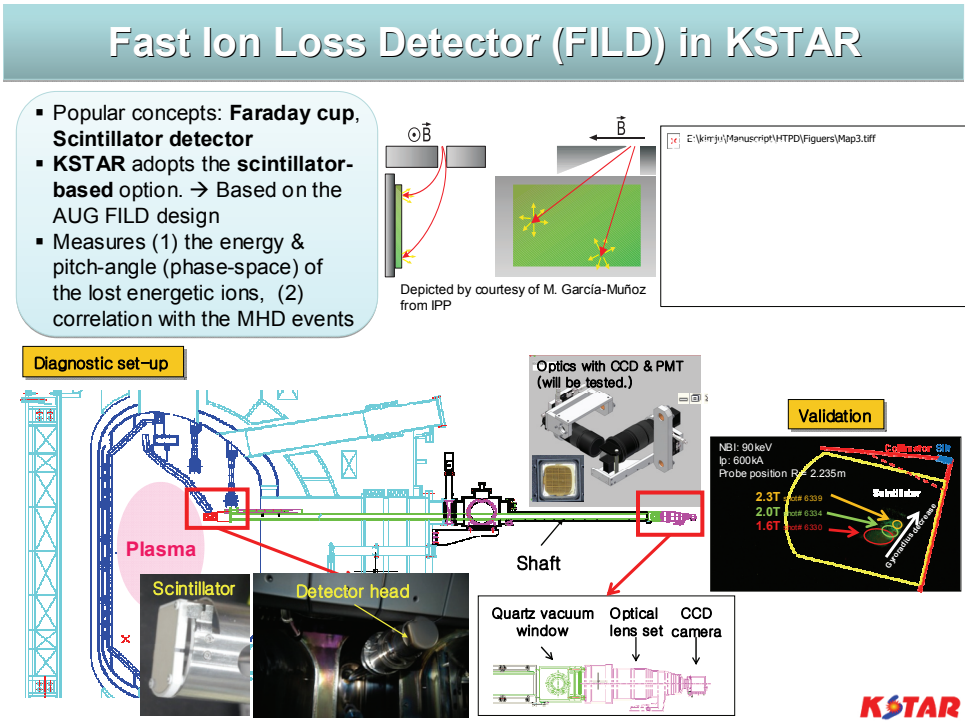

Fig3. Fast ion loss detector in KSTAR

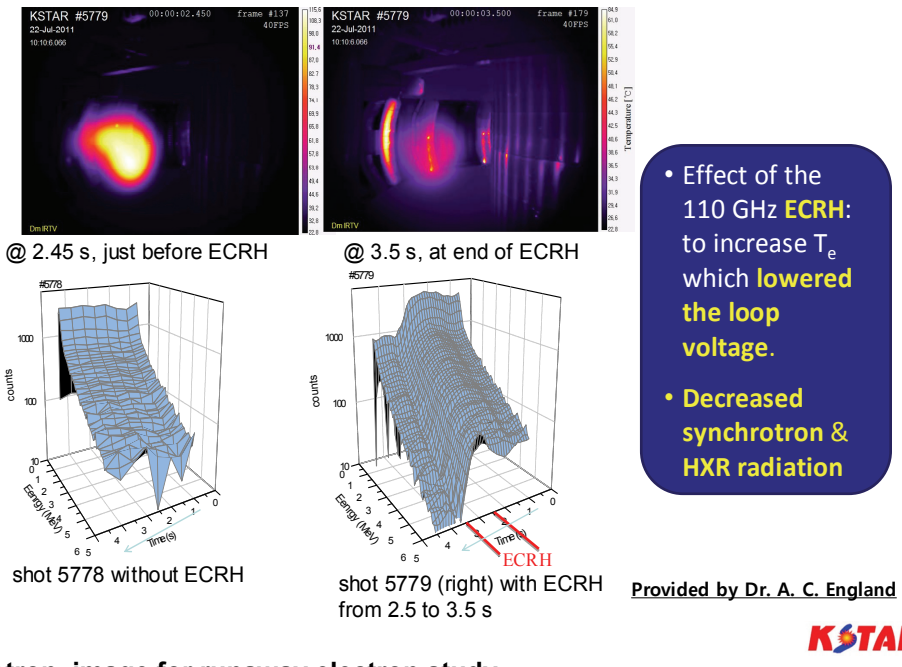

Fig4. Synchrotron image for runaway electron study

Category III

Development of MHD Spectroscopy Using Energetic-Particle-Driven Global Modes in 2D and 3D Toroidal Plasmas

K. Toi
National Institute for Fusion Science, Toki, Japan

Abstract

The development of MHD spectroscopy using energetic-particle-driven global modes is one of important issues toward realization of a fusion reactor. In the category III of the A3 foresight program, this project can be executed effectively through collaborations among 2D toroidal devices (KSTAR and EAST tokamaks) and a 3D device (LHD). In tokamaks, the reversed shear Alfvén eigenmodes (RSAEs) and beta-induced Alfvén eigenmodes (BAEs) are thought to be useful candidate instabilities for MHD spectroscopy. In LHD, global Alfvén eigenmodes (GAEs) in addition to RSAEs are listed as the candidates. This paper presents the present status of MHD spectroscopy using the RSAEs and GAEs in LHD. In the recent NBI heated plasmas of KSTAR, an interesting energetic ion driven mode has been observed for the first time and is thought to be GAE locates near the plasma central region. This GAE is thought to be a useful candidate mode for MHD spectroscopy in tokamak plasmas as well as LHD plasmas. This study is expanded to expand to EAST tokamak plasmas heated by intense RF heating.

1. Introduction

In a future fusion reactor, the installation of advanced and delicate plasma diagnostic systems will be considerably limited because of harsh environment caused by high neutron flux and high wall-temperature. It is of great importance to develop a simple and accurate method to be able to monitor plasma behaviors with high reliability. For this purpose, MHD spectroscopy was first proposed by using ELMs and Alfvén eigenmodes (AEs) excited by antennae for tokamak plasmas [1]. MHD spectroscopy is feasible and reliable because MHD theory is well-developed and provides good tools to interpret MHD behaviors in 2D and 3D toroidal plasmas. Energetic-particle-driven global modes can be used for MHD spectroscopy in 3D plasmas as well as 2D plasmas [2, 3]. This approach has a similarity to atomic spectroscopy and helioseismology. MHD spectroscopy is based on a unique relationship between mode frequencies of

Alfvén eigenmodes and various MHD equilibrium profiles such as the rotational transform $\iota/2\pi$ (or the safety factor q) and plasma pressure.

The *JSPS A3 foresight program* aims at clarifying and solving critical physics issues specific to steady state sustainment of high-performance plasmas through trilateral collaborations using three super conducting toroidal devices EAST, KSTAR and LHD. In the *Category III* of the A3 program, an objective is to develop MHD spectroscopy through collaborations among above three devices. The first step is to excite candidate modes for MHD spectroscopy by NBI and/or RF or energetic electrons. The second step is to clarify a unique relationship between the mode frequencies and radial locations of EP-driven modes and the $\iota/2\pi$ (=1/q) profiles on the condition that plasma temperature and density profiles are known. In the final application stage, the $\iota/2\pi$ (=1/q) profile in a certain toroidal plasma is determined through an iterative procedure so that all observed mode frequencies in the plasma and their radial locations should agree with the calculated results by MHD numerical codes such as NOVA-K or AE3D codes [4, 5] consistently. The procedure is shown in Fig.1. Note that in a fusion reactor these global modes should be controlled in acceptable levels without suffering from enhanced radial transport of energetic particles and bulk plasma. The development of MHD spectroscopy is also expected to give some insights for exploring an effective scenario to control these instabilities in benign levels.

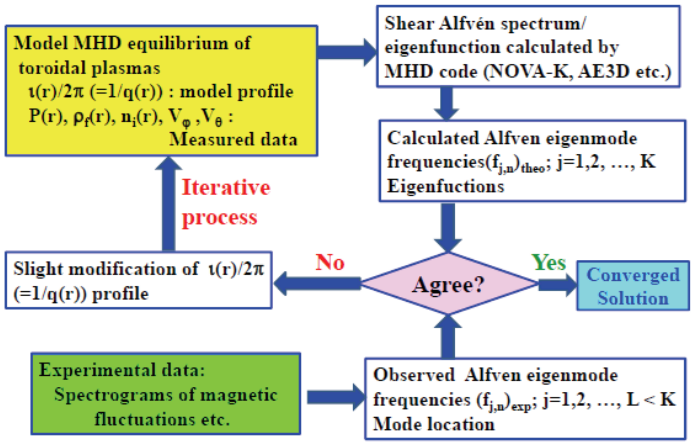

Fig.1 Procedure of MHD spectroscopy in a toroidal plasma.

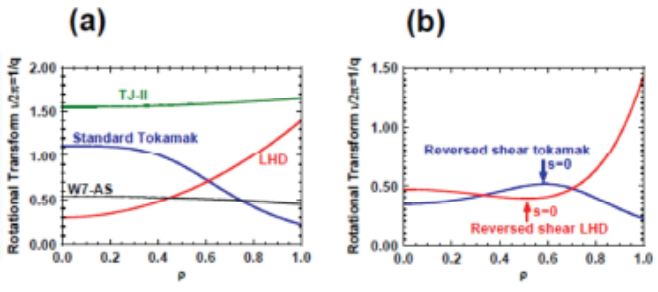

Fig.2 Typical $\iota/2\pi$ profiles in tokamaks and stellarator/helical devices. (a) monotonic profiles, (b) reversed magnetic shear profiles.

Tokamak and stellarator/helical plasmas have two types of $\iota/2\pi$ (=1/q) profiles. One is a monotonic profile and the other non-monotonic one which is called "reversed magnetic shear configuration". Figure 2 shows the monotonic $\iota/2\pi$ (=1/q) profiles in a standard tokamak , LHD and other low shear stellarators W7-AS and TJ-II. This figure also shows the reversed magnetic shear (RS-) configurations in a tokamak and LHD. In the tokamak RS-plasmas, reversed shear Alfven eigenmodes (RSAEs) are often excited by energetic passing ions and RF-generated energetic trapped ions. In most of cases the RSAE frequency evolves in time exhibiting a characteristic upward sweeping as the q-profile evolves in time, keeping the RS profile shape. A typical example is the accurate prediction of the time evolution of the q_{min} of the RS-plasma. The starting time of the RSAE frequency sweeping upward corresponds to the time when the q_{min} has passed the rational values such as 3.0, 2.5 and so on [6]. Figure 3 is cited from the paper [6] which describes the application of RSAE to q_{min} as an example of MHD spectroscopy. The results of MHD spectroscopy using RSAE agrees very well with the values measured by MSE diagnostic. In AUG, time evolution of q-profile was successfully predicted by using time evolutions of RSAE and beta-induced Alfven eigenmode (BAE) frequencies [7].

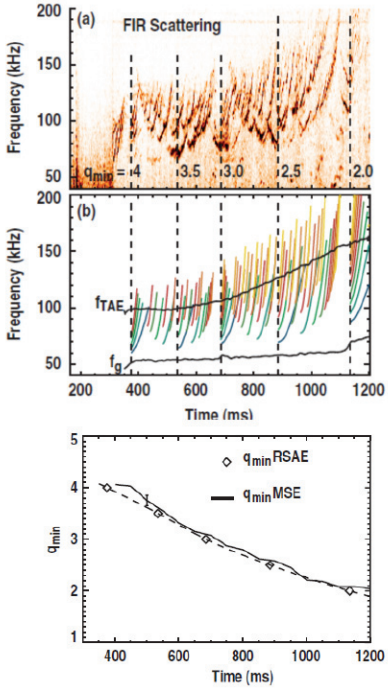

Fig.3 Spectrogram of the density fluctuations measured by FIR scattering (top) and calculated RSAE, TAE and GAM frequencies(middle). The lower graph shows time evolution of q_{min} measured by MSE and predicted by the RSAE frequency evolution [6].

2. RSAEs in a reversed shear plasma of LHD

In LHD, RS plasmas are generated by raising the toroidal beta or by counter neutral beam current drive where beam driven current is induced by counter tangential beams to decrease the external rotational transform generated by external helical coils [8, 9]. Figure 4 shows a typical example of the discharge waveforms and n=1 RSAE frequency evolution in the spectrograms of magnetic probe and microwave interferometer signals. When the frequency of RSAE has passed the minimum

indicated by two vertical lines in Fig.4(b), the minimum value of the $\iota/2\pi$ (=1/q) profile has reached the rational values, i.e., 1/2 and 1/3. At the two times, ECE electron temperature in the plasma central region exhibits a sharp drop. MSE diagnostic data are consistent with this prediction using the RSAE frequency evolution. In addition to the time of the minimum frequency of RSAE, the minimum frequency itself is determined by the geodesic acoustic mode (GAM) frequency and the frequency off-set due to the gradients of bulk plasma and energetic ion density [8, 9]. Accordingly, it also provides some important information of MHD equilibrium and contributes to one aspect of MHD spectroscopy. In the RS plasma of LHD, another interesting n=0 mode which is thought to be the GAM destabilized by energetic ions is also clearly excited. The mode frequency mainly depends on electron and ion temperatures, although the frequency is also dependent on energetic ion content and averaged energy [10]. In LHD plasmas, RSAE and GAM driven by energetic particles are good candidate modes for MHD spectroscopy[8].

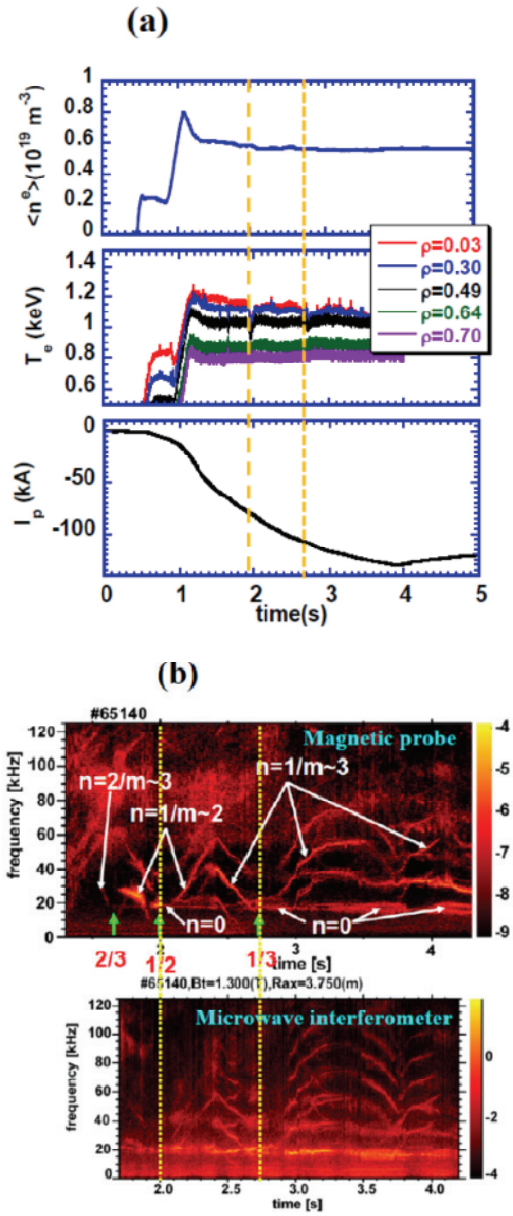

Fig.4 (a)Waveforms of line averaged electron density, electron temperature measured by ECE and plasma current induced by NBCD, (b) Spectrograms of magnetic probe and microwave interferometer signals. Two vertical lines indicate the time that the minimum of the rotational transform in the RS-plasma has passed 1/2 and 1/3 rational values, respectively.

3. Alfvenic modes in an NBI heated plasma on KSTAR

In the experimental campaigns of 2011 on KSTAR, we have detected an Alfvénic mode which does not show a simple Alfvén velocity scaling but indicates the *q*-profile evolution in time. The spectrogram of magnetic probe signal shows the time evolution of the mode frequency in Fig.5(b), together with the discharge waveforms of an NBI heated circular plasma (Fig.5(a)). The calculated *n*=2 TAE frequency is around 200 kHz. The frequency increases in time during the rising phase of both line averaged electron density and plasma current, and reaches the TAE frequency rage. This shot will not have a reversal of magnetic shear even in the current rise phase, because the ECE signal at plasma center has sawtooth activities already in the course of the current rise. The most likely interpretation is that the central value of the safety factor *q(0)* evolves above 1 and then decreases well below 1, i.e., 0.85-0.9. The *q(0)*~0.9 is inferred to be sustained in the current flat top phase. In the large sized plasma having high electron temperature,

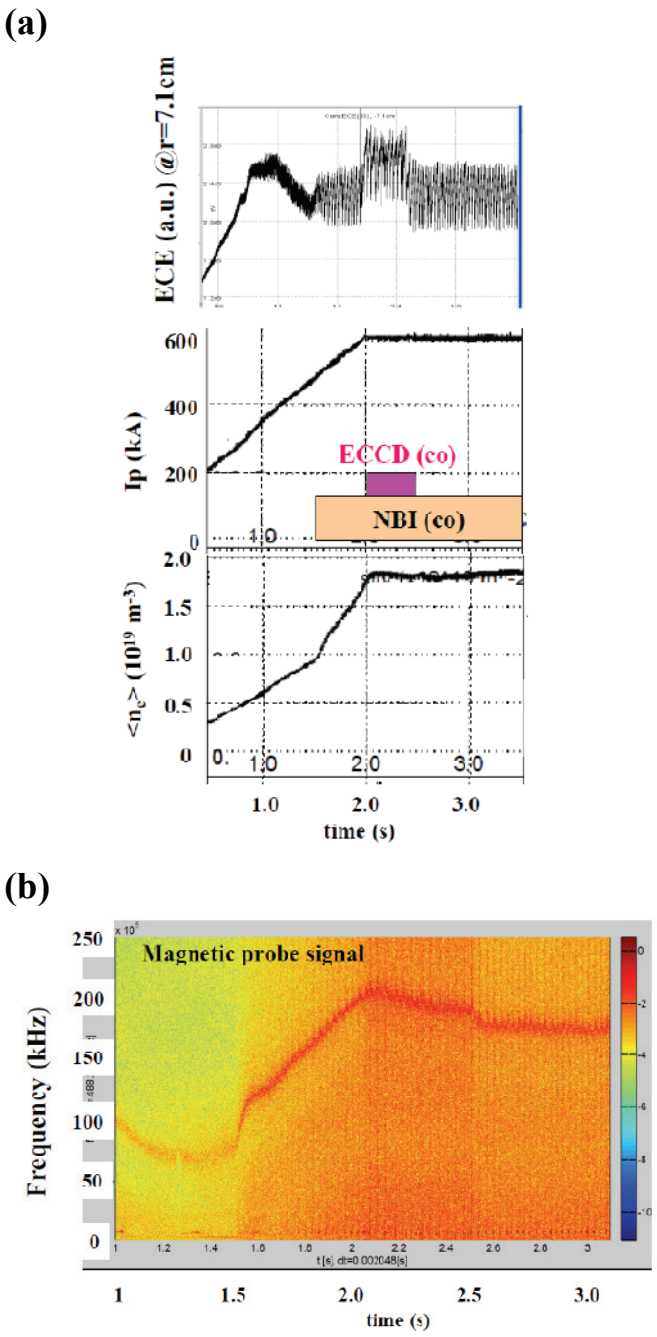

Fig.5 (a)Waveforms of ECE signal, plasma current and line averaged electron density in a circular cross-section plasma with sawtooth activities on KSTAR. (b) Spectrogram of magnetic probe signal. The coherent mode has an n=2 structure.

the *q(0)* well below 1 will be easily sustained even during sawtoothing phase, as discussed other large tokamaks [11,12]. To draw out a final conclusion more studies are necessary in KSTAR.

4. Plans in 2013

In the A3 program, we aims at establishing MHD spectroscopy using energetic-particle-driven coherent modes in two tokamaks (KSTAR and EAST) and one stellarator/helical device, LHD. In the next fiscal year, identifications of energetic ion and electron driven modes in LHD are conducted to establish MHD spectroscopy. In KSTAR, decisive identification of the above-mentioned Alfvénic mode is planned on elongated limiter and divertor plasmas heated by NBI in the range of ~3 MW. A preparatory study is planned to start in EAST plasmas heated by intense ICRF heating without or with high power lower hybrid current drive.

Acknowledgements

We acknowledge the KSTAR team for their support in the collaborative experiments in 2011 and 2012 for studies of energetic particle driven Alfvénic modes. In particular, we thank Jun Gyo Bak for analyzing magnetic probe data. We are also grateful to Jayhyun Kim and Junghee Kim for their excellent support to join the KSTAR experiment. This research is supported in part by the *Japan-Korean Collaboration Program and the the JSPS-NRF-NSFC A3 Foresight Program on Critical Physics Issues Specific to Steady State Sustainment of High-Performance Plasmas*.in the field of Plasma Physics (NSFC: No.11261140328)

References

[1] J.P. Goedbloed et al. Plasma Phys. Control. Fusion **35,** B277(1993).
[2] S.E. Sharapov et al., Phys. Lett. A **289**, 127 (2001).
[3] K. Toi et al., Plasma Phys. Control. Fusion **53**, 024008 (2011).
[4] C.Z. Cheng, Physcs Rep. **211**, 1(1992).
[5] D.A. Spong et al., Phys. Plasmas **17**, 022106 (2010).
[6] M. Van Zeeland et al., Nucl. Fusion 46, S880 (2006).
[7] Ph. Lauber et al., Plasma Phys. Control. Fusion **51**, 124009(2009).
[8] K. Toi et al., Plasma Phys. Control. Fusion **53**, 024008 (2011).
[9] K. Toi et al., Phys. Rev. Lett. **105**, 145003 (2010).
[10] G.Y. Fu, Phys. Rev. Lett. **101**, 185002 (2008).
[11] H. Soltwisch and H.R. Koslowski, Plasma Phys. Control. Fusion **37**, 667 (1995).
[12] M. Yamada et al., Phys. Plasmas **1**, 3269 (1994).

Recent Progress of Hybrid Simulation for Energetic Particles and MHD

Y. Todo
National Institute for Fusion Science, Japan

1. Introduction

Energetic particle driven instabilities (e.g. Alfvén eigenmodes) are one of the most important issues for burning plasmas because they lead to energetic alpha particle redistribution and losses. Several hybrid simulation models have been constructed to study the evolution of Alfvén eigenmodes destabilized by energetic particles. Recent hybrid simulation results of energetic particle driven instabilities are presented in this paper.

In the hybrid simulation models, the bulk plasma is described by the reduced or full MHD equations and the energetic particles are simulated with particle or Vlasov method. The coupling models between the MHD equations and the energetic particles can be classified into two types, pressure coupling model and current coupling model. In MEGA code [1-3], the following nonlinear MHD equations with the current coupling model are employed.

$$\frac{\partial \rho}{\partial t} = -\nabla\cdot(\rho\mathbf{v}) + \nu_n \Delta(\rho - \rho_{eq}), \tag{1}$$

$$\rho\frac{\partial}{\partial t}\mathbf{v} = -\rho\boldsymbol{\omega}\times\mathbf{v} - \rho\nabla(\frac{v^2}{2}) - \nabla p + (\mathbf{j}-\mathbf{j}_h')\times\mathbf{B} + \frac{4}{3}\nabla(\nu\rho\nabla\cdot\mathbf{v}) - \nabla\times(\nu\rho\boldsymbol{\omega}), \tag{2}$$

$$\frac{\partial \mathbf{B}}{\partial t} = -\nabla\times\mathbf{E}, \tag{3}$$

$$\frac{\partial p}{\partial t} = -\nabla\cdot(p\mathbf{v}) - (\gamma-1)p\nabla\cdot\mathbf{v} + (\gamma-1)[\nu\rho\omega^2 + \frac{4}{3}\nu\rho(\nabla\cdot\mathbf{v})^2 + \eta\mathbf{j}\cdot(\mathbf{j}-\mathbf{j}_{eq})] + \nu_n\Delta(p - p_{eq}), \tag{4}$$

$$\mathbf{E} = -\mathbf{v}\times\mathbf{B} + \eta(\mathbf{j}-\mathbf{j}_{eq}), \tag{5}$$

$$\mathbf{j} = \frac{1}{\mu_0}\nabla\times\mathbf{B}, \tag{6}$$

$$\boldsymbol{\omega} = \nabla\times\mathbf{v}, \tag{7}$$

where μ_0 is the vacuum magnetic permeability, γ is the adiabatic constant, ν and ν_n are artificial viscosity and diffusion coefficients chosen to maintain numerical stability and all the other quantities are conventional. The subscript "eq" represents the equilibrium variables. The energetic ion contribution is included in the MHD momentum equation [Eq. (2)] as the energetic particle current density $\mathbf{j}_h'$. The energetic particle current density $\mathbf{j}_h'$ in Eq. (2) includes the contributions from parallel velocity, magnetic curvature and gradient drifts, and magnetization current. The $\mathbf{E}\times\mathbf{B}$ drift disappears in $\mathbf{j}_h'$ due to the quasi-neutrality [1]. We see that electromagnetic field is given by the standard MHD description. This model is accurate under the condition that the energetic ion density is much less than the bulk plasma density. The MHD equations are solved using a fourth order (in both space and time) finite difference scheme.

2. Alfvén eigenmode stability and energetic particle transport in an ITER steady state operation scenario

Stability of Alfvén eigenmodes and the associated transport of energetic alpha particles and beam deuterium particles were investigated for an ITER steady state operation

scenario using MEGA code. The equilibrium data is provided on the ITER web site [4]. The specific parameters are major radius 6.2m, minor radius 2m, and total plasma current 9MA. The particle simulation method is applied to both alpha particles and beam deuterium particles. The finite Larmor radius effects are taken into account for both the species. The numbers of grid points are (256, 512, 256) for cylindrical coordinates (R, φ, z). The numbers of computational particles are 17 million for each alpha particles and beam deuterium ions. The computational resources used for one run are 40 hours using 8192 CPU cores of the IFERC-CSC Helios computer.

It was found that toroidal Alfvén eigenmodes (TAE modes) with toroidal mode number from 12 to 22 are unstable and the saturation level of the magnetic fluctuation is 0.2% normalized by the toroidal field. Figure 1 shows the spatial profiles of the TAE modes in the linearly growing phase and the saturation phase. Slight redistributions take place for alpha and beam deuterium particles with beta value perturbations 0.03% and 0.01%, respectively.

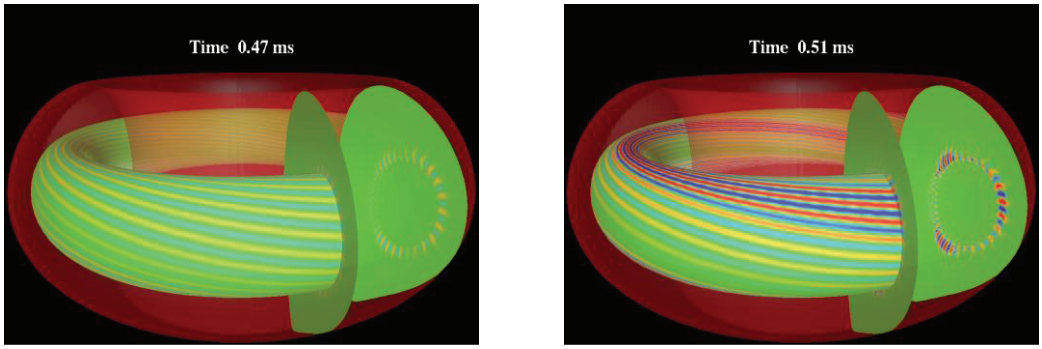

Fig. 1 Spatial profiles of TAE modes in the linearly growing phase (left) and in the saturation phase (right).

3. Linear properties and nonlinear frequency chirping of energetic particle driven geodesic acoustic mode in LHD

Linear properties of energetic particle driven geodesic acoustic mode (EGAM) in the Large Helical Device (LHD) plasmas were investigated using MEGA code [5]. It was found that the EGAM is a global mode with the spatially uniform oscillation frequency despite the spatial variation of the local geodesic acoustic mode frequency. Figure 2 shows the spatial profiles of EGAM. We see in the figure the poloidal mode numbers of poloidal velocity fluctuation, plasma density fluctuation, and magnetic fluctuation are *m=0, 1* and *2*, respectively. Oscillation frequency, linear growth rate, and spatial width of EGAM were compared for different physics conditions. The EGAM frequency is proportional to the square root of the plasma temperature. The frequency is lower for higher energetic particle beta value. The mode spatial width is larger for larger spatial width of the energetic particle distribution and for the reversed shear safety-factor profile than the normal shear profile. It was also found that the EGAM propagates radially outward in the linearly growing phase, and the propagation speed is slower for the spatially broadened modes.

Nonlinear frequency chirping of EGAM was also investigated using MEGA code [6]. Figure 3 shows the evolution of EGAM frequency spectrum and poloidal velocity. We see in the figure both frequency chirping up and chirping down take place in the nonlinear evolution of EGAM. It was found that two hole-clump pairs are formed in the energetic particle distribution function in 2-dimensional velocity space of pitch angle variable and

energy. One pair is formed in the phase space region that destabilizes the instability, while the other in the stabilizing region. The transit frequency of the hole (clump) in the destabilizing region chirps up (down), while in the stabilizing region the hole (clump) chirps down (up). We see in Fig. 3 that the transit frequencies of particles in the holes and clumps are in good agreement with the chirping EGAM frequency indicating that the particles are kept resonant with the EGAM during the nonlinear frequency chirping. Continuous energy transfer takes place from the destabilizing phase space region to the stabilizing region during the spontaneous frequency chirping of the wave.

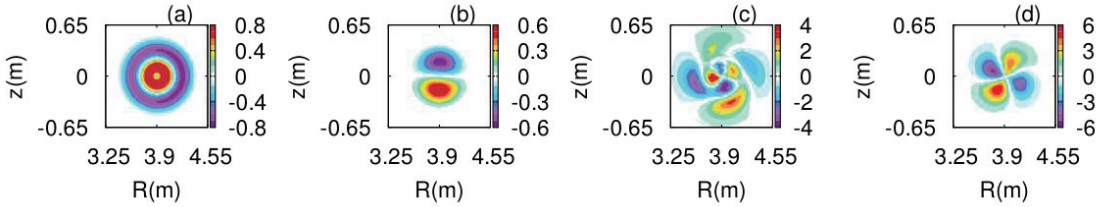

Fig. 2 EGAM perturbations on a poloidal cross section, (a) poloidal velocity, (b) plasma density, (c) poloidal magnetic field, and (d) radial magnetic field. The dominant poloidal mode numbers are (a) m=0, (b) m=1, (c) m=2, and (d) m=2. [5]

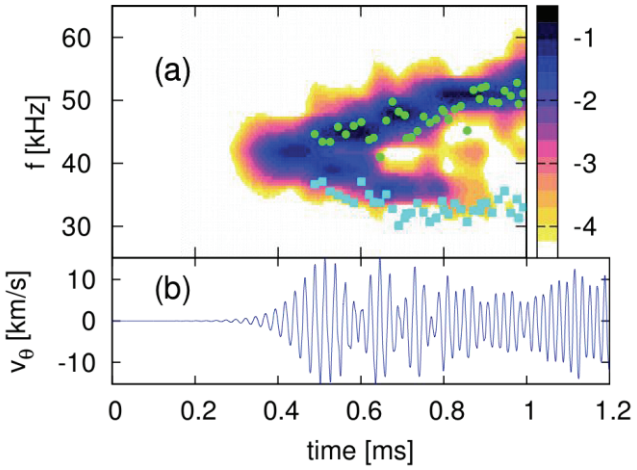

Fig. 3 Time evolution of (a) EGAM frequency spectrum and (b) poloidal velocity. Both the panels share the horizontal axis. Color bar indicates the magnitude in logarithmic scale. Green dots and cyan squares plotted in panel (a) represent transit frequencies of the hole and clump, respectively. [6]

4. Nonlinear MHD effects on Alfvén eigenmode bursts

The energetic-particle transport and losses enhanced by Alfvén eigenmodes are an important concern for burning plasmas. Computer simulation is a powerful tool to investigate the interaction between Alfvén eigenmodes and energetic particles. In our previous work [7], we performed the first numerical demonstration of toroidal Alfvén eigenmode (TAE) bursts with parameters similar to a TFTR experiment and reproduced many of the experimental characteristics. These include: a) the synchronization of multiple TAEs, b) the modulation depth of the drop in the stored beam energy, c) the stored beam energy. It was demonstrated by surface of section plots that both the resonance overlap of different eigenmodes and the disappearance of Kolmogorov-Arnold-Moser (KAM)

surfaces in phase space due to overlap of higher-order islands created by a single eigenmode lead to particle loss.

We have extended the MEGA code to simulate recurrent bursts of Alfvén eigenmodes by implementing the energetic-particle source, collisions, and losses [8]. The Alfvén eigenmode bursts with synchronization of multiple modes and beam ion losses at each burst were successfully simulated with nonlinear MHD effects for the physics condition similar to the previous reduced simulation for the TFTR experiment. It was demonstrated with a comparison between nonlinear MHD and linear MHD simulation results that the nonlinear MHD effects significantly reduce both the saturation amplitude of the Alfvén eigenmodes and the beam ion losses. Two types of time evolution were found depending on the MHD dissipation coefficients, namely, viscosity, resistivity, and diffusivity. The Alfvén eigenmode bursts take place for higher dissipation coefficients with roughly 10% drop in stored beam energy and the maximum amplitude of the dominant magnetic fluctuation harmonic $\delta B_{m/n} / B \sim 5 \times 10^{-3}$ at the mode peak location inside the plasma. For lower dissipation coefficients, the Alfvén eigenmodes amplitude is at steady levels $\delta B_{m/n} / B \sim 2 \times 10^{-3}$ and the beam ion losses take place continuously. The two types of evolution are compared in Fig. 4.

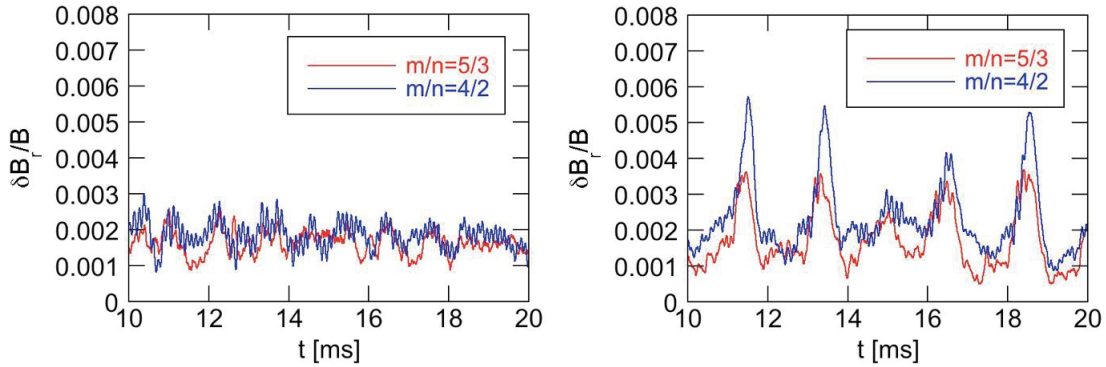

Fig. 4 Evolution of the dominant radial magnetic fluctuation harmonics with m/n=4/2 and m/n=5/3 at each peak location for nonlinear MHD run with $\nu = \nu_n = \eta / \mu_0 = 10^{-7} \mathrm{v}_A R_0$ *(left) and and* $5 \times 10^{-7} \mathrm{v}_A R_0$ *(right). [8]*

5.Acknowledgments

This work was supported partly by JSPS-NRF-NSFC A3 Foresight Program in the field of Plasma Physics (NSFC, No. 11261140328).

References

[1] Y. Todo and T. Sato, Phys. Plasmas **5**, 1321 (1998).
[2] Y. Todo *et al.*, Phys. Plasmas **12**, 012503 (2005).
[3] Y. Todo, Phys. Plasmas **13**, 082503 (2006).
[4] IDM DATA folder: Plant Breakdown Structure / TBD. Plasma / 10.1.1 Plasma Confinement/EnergeticParticles / ITER reference data for EP modeling/ Update2011/ 9MA plasma equilibrium
[5] H. Wang and Y. Todo, Phys. Plasmas **20**, 012506 (2013).
[6] H. Wang, Y. Todo, and C. C. Kim, *Hole-Clump Pairs Creation in the Evolution of Energetic Particle Driven Geodesic Acoustic Mode*, to appear in Phys. Rev. Lett. (2013).
[7] Y. Todo, H. L. Berk, and B. N. Breizman, Phys. Plasmas **10**, 2888 (2003).
[8] Y. Todo, H. L. Berk, and B. N. Breizman, Nucl. Fusion **52**, 033003 (2012).

Study on TAE-Induced Fast-Ion Loss Process in LHD

K. Ogawa, M. Isobe, K. Toi, A. Shimizu, D. A. Spong[1], M. Osakabe, S. Yamamoto[2] and LHD experiment group

National Institute for Fusion Science, Toki, 509-5292, Japan.
[1]Oak Ridge National Laboratory, Oak Ridge, Tennessee, 37831, USA.
[2]Institute for Advanced Energy, Kyoto University, Uji, 611-0011, Japan.

Characteristics of fast-ion losses induced by toroidal-Alfvén eigenmode (TAE) have been investigated over wide parameter ranges of the Large Helical Device (LHD) plasmas to reveal the fast-ion loss process. To study fast-ion losses, a scintillator-based lost-fast ion probe (SLIP) is used, and an increment of fast-ion loss flux due to the TAEs from the neoclassical orbit loss level ($\Delta\Gamma_{\text{fast ion}}$) is measured. It is newly found that the dependence of fast-ion loss flux on TAE magnetic fluctuation amplitudes changes at a certain fluctuation level. Experimental results show that in the small TAE magnetic fluctuation amplitude ($b_{\theta\text{TAE}}$) regime, $\Delta\Gamma_{\text{fast ion}}$ is proportional to $b_{\theta\text{TAE}}$ whereas $\Delta\Gamma_{\text{fast ion}}$ increases with the square of $b_{\theta\text{TAE}}$ in the larger $b_{\theta\text{TAE}}$ regime. Simulation by orbit following codes that incorporates magnetic fluctuations with frequency chirping down due to TAEs suggests the change of the fast-ion loss process from a convective ($\Delta\Gamma_{\text{fast ion}} \propto b_{\theta\text{TAE}}$) to a diffusive ($\Delta\Gamma_{\text{fast ion}} \propto b_{\theta\text{TAE}}^2$) character as $b_{\theta\text{TAE}}$ increases.

One of the critical issues in realizing self-sustained DT burning plasma is that how well alpha particles will be confined, since alpha particles are a primary heat source in the plasma. During the slowing down of alpha particles due to Coulomb collisions, the alpha particles can excite the fast-ion-driven magnetohydrodynamic (MHD) modes such as toroidal-Alfvén eigenmode (TAE) which are predicted to induce a localized damage on plasma facing components due to the impact of alpha particle losses. Better understanding of transport and loss processes of alpha particles is required to reduce the alpha particles losses for avoidance of the problem. In the Large Helical Device (LHD), radial transport and loss of fast ions due to TAEs and energetic-particle modes have been observed using a neutral particle analyzer and a scintillator-based lost-fast ion probe (SLIP) [1-3]. Experiments have shown that fast-ion loss rate increases as TAE magnetic fluctuation amplitude ($b_{\theta\text{TAE}}$) increases as expected. Experiments have indicated that the process of fast-ion loss caused by TAEs changes from convective type to diffusive type, and vice versa according to magnetic configurations. It is associated with the radial extent of the TAE eigenfunction and fast-ion orbit width [4]. Recently, we have found that in addition to magnetic configuration, the process of fast-ion loss also changes according to $b_{\theta\text{TAE}}$ even in fixed configuration. Previous theoretical modeling for axisymmetric tokamak predicts that the process of TAE-induced

fast-ion transport changes from a convective type to a diffusive type as $b_{\theta TAE}$ increases [5]. In this paper, we report experimentally observed characteristics of fast-ion loss caused by TAE in non-axisymmetric system. We also make a comparison between experiment and simulation with the aid of orbit-following particle calculation that incorporates TAE magnetic fluctuations.

LHD shown in Fig. 1 is the largest heliotron device in the world having a major radius of 3.90 m and an average plasma minor radius (a) of ~0.6 m. In experiments described in this paper, a direction of the toroidal magnetic field (Bt) is in the counter clock wise from the top view. In this case, one of neutral beam injector (NB2) injects neutral beams in the counter direction while NB1 and NB3 inject beams in the co-direction. Fast ions created by these beams with injection energy up to 180 keV are super Alfvénic in this experiment. Fast-ion loss is measured by a SLIP. This instrument is essentially a magnetic spectrometer using LHD magnetic field, consisting of a pair of apertures and a scintillator plate. Bright spots on the scintillator due to impact of fast ions give information of the energy (E) and pitch angle (χ=arccos($v_{//}/v$)) of those ions, simultaneously. Here, v and $v_{//}$ stand for the velocity of the ions and its parallel component to the magnetic field line, respectively. Structure and function of the SLIP are described in Refs. 6 and 7. The poloidal magnetic fluctuation amplitude of TAE ($b_{\theta TAE}$) is measured by a Mirnov coil placed on the vacuum vessel. Toroidal mode number (n) and poloidal mode number (m) of TAE are identified by Mirnov coils arrays.

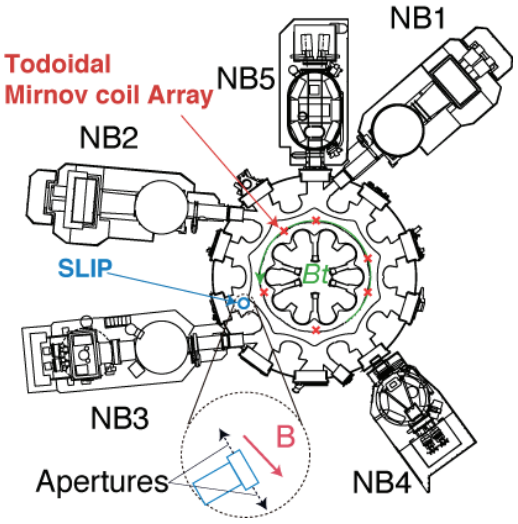

Fig. 1 Top view of the LHD, NB injectors, the SLIP, and the positions of Mirnov coils.

Measurements of fast-ion losses induced by TAE instabilities are performed in NB-heated LHD plasmas having three magnetic axis positions at finite beta, i.e. R_{mag}=3.75m (case A), 3.86 m (case B), and 4.00 m (case C). As R_{mag} becomes larger, fast-ion orbits tend to deviate largely from magnetic flux surfaces. Note that the TAE gap becomes wider with larger R_{mag} compared with smaller R_{mag} since

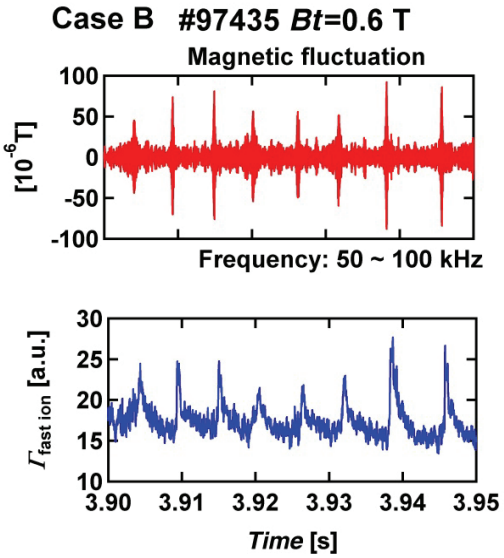

Fig. 2 Time traces of magnetic fluctuation for TAE range of frequency and $\Gamma_{fast\ ion}$ on the condition of Bt = 0.6 T. Small and large increases of $\Gamma_{fast\ ion}$ due to small and large TAEs are observed, respectively.

magnetic shear in LHD becomes weaker as R_{mag} becomes larger. Time traces of magnetic fluctuations on the TAE frequency range and the fast-ion loss flux ($\Gamma_{fast\ ion}$) in case B are shown in Fig. 2. Increases of $\Gamma_{fast\ ion}$ correlate with recurrent bursts of TAE are seen. Figure 3 shows the dependence of $\Delta\Gamma_{fast\ ion}$ normalized by fast-ion populations created by co-injected NB, i.e. $P_{NBco}\times\tau_s$ on $b_{\theta TAE}/Bt$ in cases A, B, and C. Here, $\Delta\Gamma_{fast\ ion}$, P_{NBco} and τ_s stand for increments of fast-ion loss flux due to TAEs from the neoclassical orbit loss level, the absorbed power of co-injected NBs and the Spitzer slowing down time, respectively. As shown in Fig. 3, the dependence of $\Delta\Gamma_{fast\ ion}/(P_{NBco}\times\tau_s)$ on $b_{\theta TAE}/Bt$ is changed at $b_{\theta TAE}/Bt$ ~7×10^{-5} in case B. In a small $b_{\theta TAE}$ regime, $\Delta\Gamma_{fast\ ion}/(P_{NBco}\times\tau_s)$ is proportional to $b_{\theta TAE}/Bt$ whereas in a large $b_{\theta TAE}$ regime, $\Delta\Gamma_{fast\ ion}/(P_{NBco}\times\tau_s)$ increases with the square of $b_{\theta TAE}/Bt$. In case A, $\Delta\Gamma_{fast\ ion}/(P_{NBco}\times\tau_s)$ is proportional to $b_{\theta TAE}/Bt$ in a small $b_{\theta TAE}/Bt$ region. In case C, $\Delta\Gamma_{fast\ ion}/(P_{NBco}\times\tau_s)$ is proportional to $(b_{\theta TAE}/Bt)^3$. The change of dependence of fast-ion loss flux on magnetic fluctuation amplitude has not been observed for these $b_{\theta TAE}/Bt$ ranges although the change may appear in unexplored regions in cases A and C.

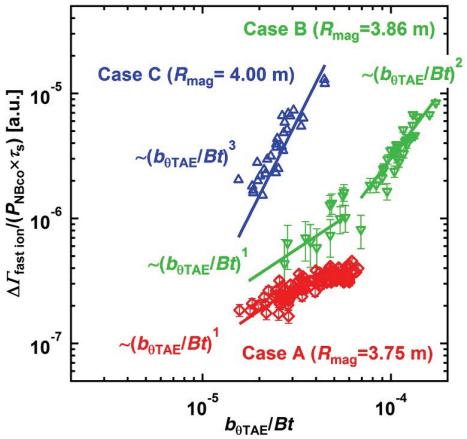

Fig 3 $\Delta\Gamma_{fast\ ion}/(P_{NBco}\times\tau_s)$ as a function of $b_{\theta TAE}/Bt$ in cases A, B and C. Dependence of fast-ion loss flux on $b_{\theta TAE}/Bt$ changes at $b_{\theta TAE}/Bt$~7×10^{-5} in case B.

A numerical simulation based on orbit following models including TAE fluctuation is performed to study the change of dependence of the fast-ion loss flux on TAE magnetic fluctuation amplitude observed in experiment. Calculation scheme is as follows. The three dimensional MHD equilibrium is reconstructed by VMEC2000 code [8] in the fixed-boundary condition. Next, the birth profile of fast ions created by NB injection is calculated by the HFREYA code [9]. Finally, the guiding-center orbit of each fast ion is followed using the DELTA5D code [10] that includes time-varying TAE fluctuation of which structure is given from the eigenfunction calculated by AE3D code [11]. Velocity distribution function of fast ion created by NB injection is formed by the method written in Ref. 4. The Coulomb collisions between fast ions and the bulk plasma are taken into account. This simulation is applicable to a confined plasma region inside of LCFS, because they are based on the VMEC equilibrium. Because DELTA5D is applicable only to the fast-ion orbit inside the LCFS, we use Lorentz orbit code to follow the orbit outside of the LCFS. It is also necessary to calculate fast-ion orbits reaching the SLIP since it works as a magnetic spectrometer.

Figure 4 shows calculated $\Delta\Gamma_{fast\ ion}/(P_{NBco}\times\tau_s)$ as a function of $b_{\theta TAE}/Bt$ for cases A and B. In case B, as observed in experiment (see Fig. 3), the change of fast-ion loss flux dependence on the magnetic fluctuation amplitude is obtained in the simulation. In the small

$b_{\theta TAE}$ regime, $\Delta\Gamma_{\text{fast ion}}/(P_{NBco}\times\tau_s)$ is proportional to $b_{\theta TAE}/Bt$ whereas $\Delta\Gamma_{\text{fast ion}}/(P_{NBco}\times\tau_s)$ increases with the square of $b_{\theta TAE}/Bt$ in a large $b_{\theta TAE}$ regime. The critical value of $b_{\theta TAE}/Bt$ is $\sim 3\times10^{-5}$ which is the same order of that in experiments $\sim 7\times10^{-5}$. According to theory by Sigmar [5], $\Delta\Gamma_{\text{fast ion}}$ proportional to $b_{\theta TAE}$ is suggested to be due to a convective type loss process whereas $\Delta\Gamma_{\text{fast ion}}$ scaling as the square of $b_{\theta TAE}$ is suggested to be due to a diffusive type loss process. The simulation and experimental results indicate that the fast-ion loss process changes from convective to diffusive in case B. Also in case A, as observed in experiment, $\Delta\Gamma_{\text{fast ion}}/(P_{NBco}\times\tau_s)$ increases linearly with $b_{\theta TAE}/Bt$ in small $b_{\theta TAE}/Bt$ regime and tends to saturate as $b_{\theta TAE}/Bt$ increases. It is interesting to note that saturation of $\Delta\Gamma_{\text{fast ion}}/(P_{NBco}\times\tau_s)$ is seen at $b_{\theta TAE}/Bt$ from $\sim 2\times10^{-5}$ to $\sim 1\times10^{-4}$. The change of the loss dependence appears when $b_{\theta TAE}/Bt$ goes up further. The loss dependence becomes a quadratic character at $b_{\theta TAE}/Bt$ of $\sim 10^{-4}$ that is in unexplored regions of experiments. Note that E and χ regions of fast ions reaching to the SLIP are 120-180 keV and of 30-40 degrees, respectively. These are similar to the experimentally measured E and χ.

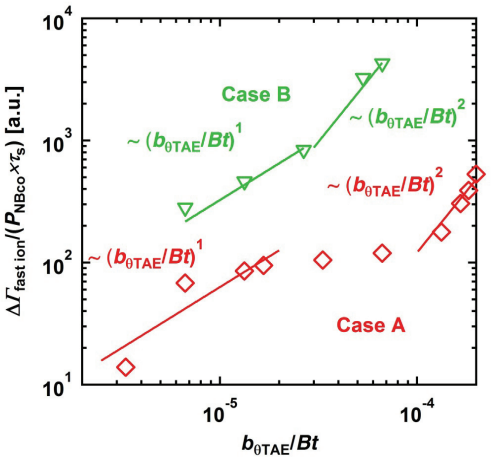

Fig 4 $\Delta\Gamma_{\text{fast ion}}/(P_{NBco}\times\tau_s)$ as a function of $b_{\theta TAE}/Bt$ in calculations for cases A and B. The dependence is similar to that obtained in experiments in case A in the small $b_{\theta TAE}$ regime. The change of the loss process from a convective type to a diffusive type is reproduced by simulation for case B.

To make the transport process visible, orbits of barely confined fast ions near the confinement/loss boundary and fast ions confined interior region are shown in Figs. 5 and 6, respectively. As seen in Fig. 5 (b), barely confined fast ions near the confinement/loss boundary escape from the plasma due to the radial excursion by TAE fluctuation immediately in small $b_{\theta TAE}$ case. Because the radial excursion increases lineally with $b_{\theta TAE}$, the fast ion into the loss region is proportional to $b_{\theta TAE}$, i.e. the fast-ion loss flux having this type of orbit is proportional to $b_{\theta TAE}$. As mentioned before, fast-ion loss having this dependence on $b_{\theta TAE}$ is referred as convective loss. It can be therefore reasonably concluded that experimentally observed fast-ion loss due to small $b_{\theta TAE}$ is caused

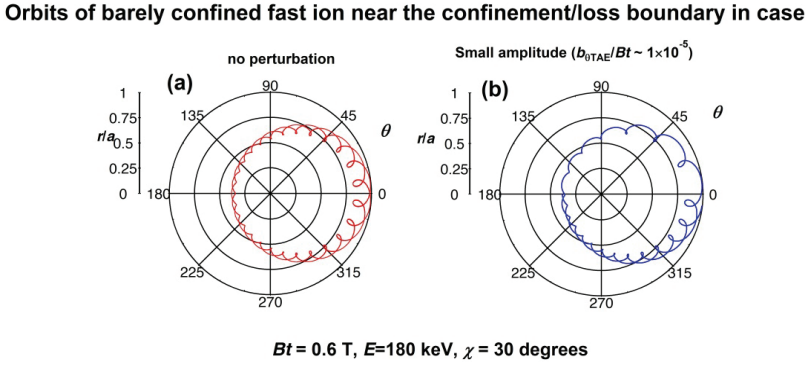

Fig. 5 Orbits of barely confined fast ions near the confinement/loss boundary without TAE (a) and with small TAE (b) in case A. The fast ion is lost with small TAE with convective process.

dominantly by a convective transport. Orbits of fast ions confined interior region tend to expand toward the outboard side of the torus as the TAE amplitude increase as seen in Fig. 6. As shown in Fig. 6 (b), as has been suggested, the fast ion does not escape from the plasma in small $b_{\theta TAE}$ case. In large $b_{\theta TAE}$ case, orbit of a fast ion expands gradually, then finally, the fast ion is lost from the confinement domain as shown in Fig. 6 (c). The displacement of fast-ion orbits due to mode overlapping leads to the transient growth of the broadening of the fast-ion spatial distribution. Because the growth of the broadening scales as $b_{\theta TAE}^2$, flux of fast ions escaping from the plasma is expected to be proportional to $b_{\theta TAE}^2$, and this is diffusive loss as mentioned before. It can be concluded, from what has mentioned above, that experimentally observed fast-ion loss due to large $b_{\theta TAE}$ is caused dominantly by a diffusive transport.

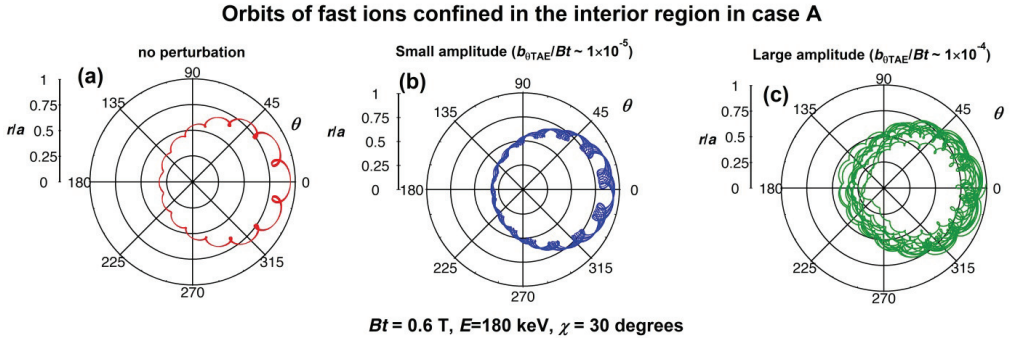

Fig. 6 Orbits of fast ions existing interior region without TAE (a), with small TAE (b), and with large TAE (c) in case A. The TAE fluctuation affects the fast-ion orbit repeatedly. The fast ion is lost with large TAE with diffusive process.

Characteristics of fast-ion loss process due to TAE are studied in LHD plasmas using the SLIP. It is found that in the smaller $b_{\theta TAE}$ regime, $\Delta\Gamma_{\text{fast ion}}$ is proportional to $b_{\theta TAE}$, whereas in large $b_{\theta TAE}$ regime, $\Delta\Gamma_{\text{fast ion}}$ increases with the square of $b_{\theta TAE}$. To understand the change of the dependence in three dimensional LHD plasma precisely, simulations based on an orbit following models that incorporates TAE magnetic fluctuations with frequency chirping down and radial profile of TAE are performed. The simulation reproduces the change of the loss process from convective ($\Delta\Gamma_{\text{fast ion}} \propto b_{\theta TAE}$) to diffusive ($\Delta\Gamma_{\text{fast ion}} \propto b_{\theta TAE}^2$) according to magnetic fluctuation amplitude. Orbit simulation shows that with a convective type loss process, the barely confined fast ion near the confinement/loss boundary is lost due to TAE with small amplitude whereas the fast ion confined in the interior region of the plasma is lost with a diffusive type loss process due to TAE with large amplitude. In small $b_{\theta TAE}$ region, convective type loss is thought to be dominant. As $b_{\theta TAE}$ increases, diffusive type loss increases and exceeds the convective type loss at a certain $b_{\theta TAE}$ level. The change of fast-ion loss process observed in experiments is explained by the change of the dominant loss process.

This work was supported in part by the Grant-in-Aid for Scientific Research from JSPS Nos.

21360457, 21340175 and 22-7912, from the LHD project budget (NIFS12ULHH003), and Japan/U.S. Cooperation in Fusion Research and Development. This work was also partially supported by the JSPS-NRF-NSFC A3. Foresight Program in the field of Plasma Physics (NSFC: No.11261140328). The authors are grateful to the LHD operation group for their excellent technical support.

[1] M. Osakabe, S. Yamamoto, K. Toi *et al*., 2006 Nucl. Fusion **46** S911.
[2] K. Ogawa, M. Isobe, K. Toi *et al*., 2010 Nucl. Fusion **50** 084005.
[3] M. Isobe, K. Ogawa, K. Toi, *et al*., 2010 Contrib. Plasma Phys. **50** 540.
[4] K. Ogawa, M. Isobe, K. Toi *et al*., 2012 Nucl Fusion **52** 094013.
[5] D. J. Sigmar, C. T. Hsu, R. B. White *et al*., 1992 Phys. Fluids B **4** 6.
[6] K. Ogawa, M. Isobe and K. Toi, 2009 J. Plasma Fusion Res. Series **8** 655.
[7] K. Ogawa, M. Isobe and K. Toi, 2008 Plasma Fusion Res. **3** S1082.
[8] S. P. Hirshman and O. Betancourt, 1991 J. Comput. Phys. **96** 99.
[9] S. Murakami, N. Nakajima, M. Okamoto *et al*., 1995 Trans. Fusion Technol. **27** 256.
[10] D. A. Spong , 2011 Phys. Plasmas **18**, 056109.
[11] D. A. Spong, E. D'azevedo and Y. Todo, 2010 Phys. Plasmas **17** 022106.

Quantitative analysis of carbon radiation in edge plasmas of LHD

C. F. Dong[1], S. Morita[1,2], T. Oishi[1,2], M. Goto[1,2], I, Murakami[1,2], E. R. Wang[2] and X. L. Huang[2]

[1]*National Institute for Fusion Science, Toki 509-5292, Gifu, Japan*
[2]*Department of Fusion Science, Graduate University for Advanced Studies, Toki 509-5292, Gifu, Japan*

Introduction

Heat load mitigation on divertor plates is one of critical issues in the next-generation magnetically confined fusion devices. A possible solution is to increase the radiation loss in the plasma edge, thereby reducing the heat flux to the divertor plates and spreading the exhaust power over the whole direction. The radiative divertor condition can be produced by injection of working gas or gaseous impurities into divertor region in tokamaks. This scenario has been demonstrated in previous results, which reveal a strong increase in radiation near the X-point region. In JT-60U [1], DIII-D [2] and JET [3], the detached plasma obtained by deuterium gas injection shows that the carbon is main radiating species near theX-point. Neon can contribute 60% of the total radiation in detached plasmas in JT-60U, when it is externally introduced.

Detached plasma in LHD can be produced using impurity gas puffing as well as the tokamaks. Recently, the detached plasma is achieved by use of externally supplied 1/1 magnetic island without impurity gas puffing. The connection length structure ($L_c \geq 10$m) in the ergodic layer consisting of stochastic magnetic field lines is shown in Fig. 1. In the general discharges, experimental result reveals that C^{3+} ion is located at the edge of ergodic layer [4], , while the previous results from JT-60U and DIII-D show that main radiator near the X-point region is C^{3+}. Therefore, it is of interest to compare the carbon radiation loss between LHD and tokamaks. Since the radiation from C^{3+} is much smaller than that from C^{5+}, it is also interesting to examine the difference in the detached plasma. In addition, it is important to study quantitatively the radiation from each ionization stage of carbon which is uniquely the dominant impurity in most tokamaks and LHD.

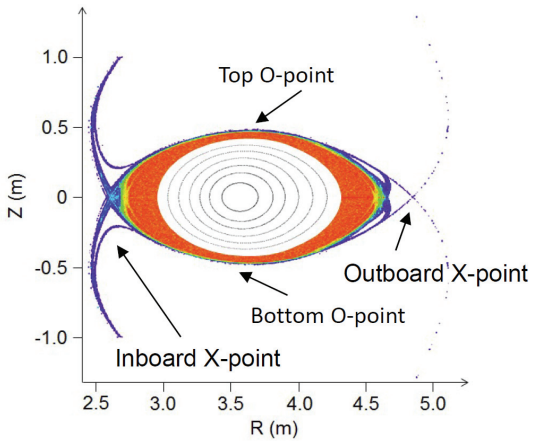

Fig. 1 Connection length ($L_c \geq 10$m) structure in ergodic layer in LHD at R_{ax}=3.90m.

Experimental arrangement

The result presented here is mainly obtained from EUV spectrometer [5], which works in wavelength range of 30- 650Å. In order to estimate the total radiation from C^{2+} - C^{5+} ions, use of the resonance transition is highly desired, i.e., CIII (977.02Å, $2s2p–2s^2$), CIV (1548.2Å, 2p–2s), CV (40.27Å, $1s2p–1s^2$) and CVI (33.73Å, 2p –1s). However, the wavelength range of EUV spectrometer is incapable of detecting the

line emission of such resonance transitions. Then, two VUV monochromators are adopted to monitor the resonance transitions of CIII and CIV. It is noted that both EUV and VUV spectrometers have the same line of sight. In order to obtain the total radiation power, the EUV spectrometer and the two VUV monochromators have to be absolutely calibrated. The absolute intensity calibration of EUV spectrometer is implemented using a newly developed method based on the measurement of EUV bremsstrahlung and visible bremsstrahlung. The detailed calibration process is presented in Ref. [6]. In EUV wavelength range, another line emission for CIII (386.2Å, $2s3p - s^2$) and CIV (312.4Å, 3p–2s) can be observed. The absolute intensity calibration on VUV monochromators is then performed by means of the intensity ratio of VUV to EUV carbon lines. The ratios for CIII (2p-2s/3p-2s) and CIV (2p-2s/3p-2s) obtained from ADAS are shown in Figs. 2 (a) and (b), respectively. Taking account of the electron temperature, the absolute intensity calibration factors for the two VUV monochromators are obtained. It is then possible to measure the radiation of C^{2+} - C^{5+} ions with absolute intensity simultaneously.

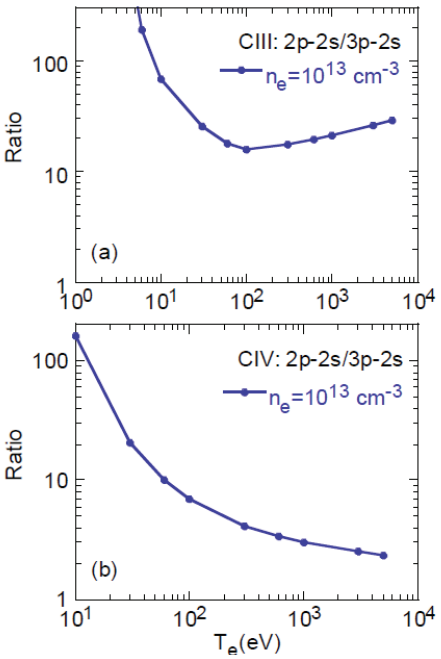

Fig. 2 Intensity ratios of (a) CIII (977.02Å/386.2Å, 2p-2s/3p-2s) and (b) CIV (1548.2Å/312.4Å, 2p-2s/3p-2s) analyzed from ADAS.

In order to divide the C^{3+} radiation from detached plasma into two parts of X- and O-points, a spatial measurement is required. A space-resolved EUV spectrometer [7] is installed in LHD perpendicular to the toroidal magnetic field at the horizontally elongated plasma cross section. This EUV spectrometer is also working in the wavelength range of 30- 650Å. Due to a limited CCD size (26.6mm), the vertical profile can be measured at upper half of LHD plasma.

Experimental results and discussion

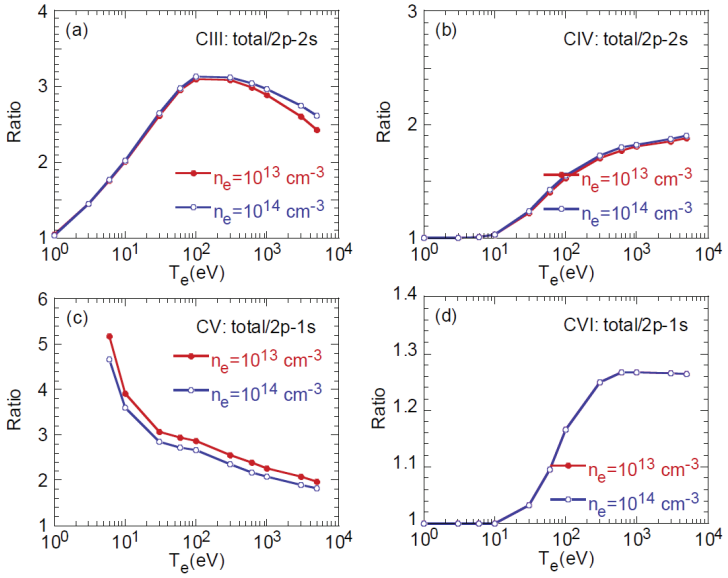

Fig. 3 Radiation power ratios of (a) CIII (total/2p-2s), (b) CIV (total/2p-2s), (c) CV (total/2p-1s) and (d) CVI (total/2p-1s) analyzed from ADAS.

Spectral lines of CIII ($2s2p– 2s^2$), CIV (2p–2s), CV ($1s2p –1s^2$) and CVI (2p –1s) emitted from general LHD discharges at magnetic axis of R_{ax}=3.60m are measured using EUV spectrometer and VUV monochromators. The total radiation power from each charge state in C^{2+} - C^{5+} can be estimated according to the radiation power ratio of CIII (total/2p-2s), CIV (total/2p-2s), CV (total/2p-1s) and CVI (total/2p-1s) analyzed with ADAS, as shown in Fig. 3. The radiation power ratios show that the resonance transition can occupy a sufficiently large fraction to the total radiation, i.e., CIII (2p–2s): 50%, CIV (2p–2s): 75%, CV (2p–1s): 40% and CVI (2p–1s): 85%. The total radiation power analyzed in general discharges is presented in Fig. 4. As seen from Fig. 4, the radiation from C^{2+} and C^{3+} ions are increased with electron density, whereas the radiation from C^{4+} and C^{5+} ions almost keep constant with electron density. This different density dependence indicates 'impurity screening' induced by the stochastic magnetic field layer. The radiation from C^{2+} and C^{3+} ions are relatively small, compared to C^{4+} and C^{5+} ions. It indicates that the C^{4+} and C^{5+} ions are the main radiator in general discharges of LHD. It is noted here that the exact value of C^{2+} - C^{5+} radiation has to be checked later due to a considerably large uncertainty appeared in the absolute calibration of spectrometers.

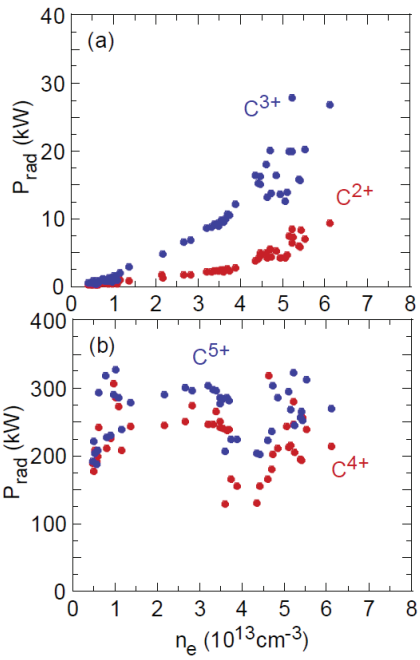

Fig. 4 Total radiation power from (a) C^{2+} and C^{3+} and (b) C^{4+} and C^{5+}.

The vertical profile of CIV (312.4Å, 3p–2s) is measured by the space-resolved EUV spectrometer to analyze the radiation power from detached plasma in X- and O-point regions separately. The detached plasma is produced by externally supplied 1/1 magnetic island instead of conventional method with gaseous impurities. The vertical profiles of CIV observed before detachment (t=4.6s) and during detached phase (t=5.6s) are shown in Fig. 5. The CIV vertical profile at t=4.6s shows a typical distribution pattern in general discharges, which has a sharp peak at plasma edge.

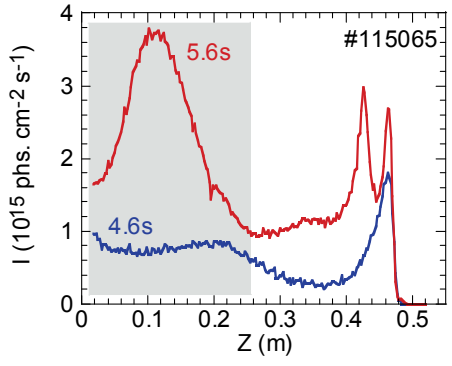

Fig. 5 Vertical profiles of CIV observed before detachment (t=4.6s) and during detached phase (t=5.6s).

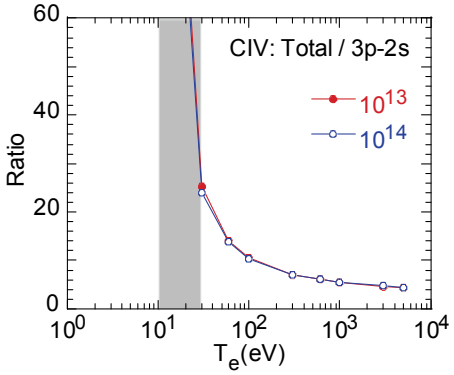

Fig. 6 Radiation power ratio of CIV (total/3p-2s) obtained from ADAS.

When the discharge enters the detached phase, two edge peaks are appeared. Since the inner peak position is very close to the position of last close flux surface in general discharges, it probably indicates a practical plasma edge in the detached plasma. The intensity of CIV near X-point is enhanced by a factor of 5 during the detached phase. Radiation power of CIV at 3p-2s transition (312.4Å) from X-point is estimated to be 7.5kW. The total radiation power of C^{3+} ion at X-point region can be then estimated using the same method introduced previously. The Radiation power ratio of CIV (total/3p-2s) analyzed from ADAS is shown in Fig. 6. It is found that this ratio is much sensitive to the electron temperature. The edge electron temperature profile at plasma edge at t=5.6s measured by Thomson scattering system is shown in Fig. 7. It is clear that T_e at $\rho \geq 1.0$ is less than 20eV. However, the temperature measurement at plasma edge relatively has a large uncertainty due to the too much low value. Therefore, the total radiation of C^{3+} ion is calculated at several different temperatures, i.e., 188kW (T_e=30eV), 525kW (T_e=25eV) and 1.23MW (T_e=10eV). The results show a large difference if T_e is changed among 10eV and30eV. In order to study exact radiation power for C^{3+} ions, further analysis is necessary.

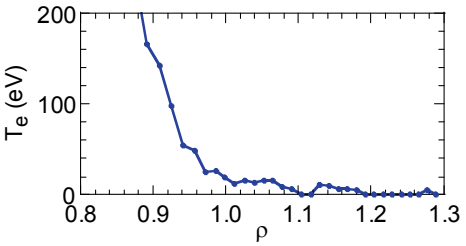

Fig. 7 Electron temperature profile at plasma edge at t=5.6s measured by Thomson scattering system.

Summary

Line emissions of CIII ($2s2p– 2s^2$), CIV (2p–2s), CV ($1s2p –1s^2$) and CVI (2p –1s) are measured with absolute value using EUV spectrometer and VUV monochromators to estimate the radiation power for C^{2+} - C^{5+} ions. The relevant atomic data for radiation power calculation are obtained from ADAS. The result shows that the radiation from C^{4+} and C^{5+} ions are much bigger than that from C^{2+} and C^{3+} ions, indicating C^{4+} and C^{5+} ions are the main radiator in general discharges of LHD. Different density dependence between C^{2+} and C^{5+} ions indicates the impurity screening. Vertical profile of CIV (3p–2s) observed in the detached plasma is remarkably different from that in the general discharge. Two edge peaks are appeared during the detachment phase instead of single edge peak before entering the detachment. The intensity of CIV emitted from X-point region is strongly enhanced by a factor of 5. The CIV radiation enhanced at the X-point is estimated to be 500kW, if T_e=25eV.

Acknowledgement

This work was partly supported by the JSPS-NRF-NSFC A3 Foresight Program in the field of Plasma Physics (NSFC: No.11261140328).

References

[1] T. Nakano, et al., J. Nucl. Mater. **390-391** (2009) 255.
[2] M. E. Fenstermacher, et al., Phys. Plasmas **4** (1997) 1761.
[3] C. F. Maggi, et al., J. Nucl. Mater**. 241–243** (1997) 414.
[4] C. F. Dong, et al., Phys. Plasmas **18** (2011) 082511.
[5] M. B. Chowdhuri, et al., Rev. Sci. Instrum. **78** (2007) 023501.
[6] C. F. Dong, et al., Rev. Sci. Instrum. **82** (2011) 113102.
[7] C. F. Dong, et al., Rev. Sci. Instrum. **81** (2010) 033107.

Numerical MHD Analysis of JET Edge Localised Modes with ITER-Like Wall

Ohjin Kwon[1], M Beurskens[2], I T Chapman[2], L Frassinetti[3], Hyunsun Han[4], S Saarelma[2] and EFDA-JET contributors[*]

[1]Department of Physics, Daegu University, Gyungbuk 712-714 Korea
[2]Euratom/CCFE Fusion Association, Culham Science Centre, OX14 3DB, Abingdon, UK
[3]Division of Fusion Plasma Physics, School of Electrical Engineering, Royal Institute of Technology, Association EURATOM-VR, Stockholm, Sweden
[4]National Fusion Research Institute, Daejeon 305-806 Korea

ABSTRACT

We have investigated ideal MHD stability of JET H-mode shots with the ITER-like wall. It has been found that the operational point of the baseline high-δ ILW shots just before the edge localized modes have less edge plasma current density and it is located closer to the ballooning-mode unstable region, compared with the baseline CFC wall plasma. Low-δ ILW operational points are located in the peeling-ballooning stability corner in the stability diagram. As the poloidal β increases with more peaked plasma pressure in the core and/or as plasma boundary shaping increases, the stability improves and higher pressure gradients can be allowed before destabilizing the modes.

INTRODUCTION

The ITER (International Thermonuclear Experimental Reactor) design comprises beryllium (Be) tiles on the first wall to avoid the tritium deposition problems in D-T operation and tungsten tiles on the divertor. Recently, through ITER-like wall (ILW) project [1], carbon fiber composite (CFC) tiles of plasma facing components of JET (Joint European Torus) have been replaced by Be tiles and tungsten divertor has also been installed. In the H-mode experiments following the installation, the JET ILW plasma has shown confinement degradation of ~25% from CFC plasma [2] in a conservative IPB98(y,2) energy confinement time (τ_E) scaling in the high-δ (upper $\delta = 0.4$) baseline (BL) H-mode operations. Both baseline H-mode operations show similar pedestal density while pedestal electron temperature is generally lower in ILW plasma. Therefore, the confinement degradation is due to the increased heat transport. When the nitrogen (N_2) impurity seeding was introduced in ILW plasma, the energy confinement recovers from τ_E in BL ILW operation, and it becomes slightly lower than τ_E in CFC plasma. The pedestal electron temperature also becomes comparable to CFC plasma values. As a result, the stored thermal energy increases from the baseline ILW plasma value to near CFC plasma value in the case of the N_2 seeded ILW plasma for the same total input power.

Edge electron temperature (T_e) evolution determined from electron cyclotron emission measurements in the high-δ baseline ILW operation without impurity seeding showed different edge localized mode (ELM) crash behavior, compare with CFC plasma.

[*] See the Appendix of F. Romanelli et al., Proceedings of the 24th IAEA Fusion Energy Conference 2012, San Diego, USA

Two different types of the ELM collapses have been observed in the ILW case. One is the fast T_e drop, followed by the recovery of T_e, while the other is followed by the additional T_e drop in the slow time scale. Typical time for the fast drop is 2~3ms and that for the slow drop is ~10ms. After the additional slow drop, time interval to the next ELM increases. In CFC plasma, each ELM behaves similarly with only fast drops with typical time of ~ 0.5ms. With N_2 impurity seeding in ILW plasma, the additional slow drop disappears, and similar behavior of each ELM as in CFC plasma may be recovered with only fast drops of T_e in ~ 1ms. It is the purpose of this study to understand these different behaviors of ELMs and confinement degradation in the ILW plasma compared with CFC plasma in terms of ideal edge MHD instability.

EDGE STABILITY OF ILW PLASMA

The edge pressure gradient profiles are obtained from high resolution Thomson scattering measurements just before the elm clashes over elmy period. The edge pressure is then fitted with tanh-function and the core $dP/d\psi$ is kept constant, where ψ is the poloidal flux function and P is the plasma pressure. These fitted pressure profiles are used for the equilibrium reconstruction in the fixed boundary HELENA equilibrium code [3]. The stability of the equilibria is determined using the MISHKA-1 code [4] for wide range of the toroidal mode number (n), $3 \leq n \leq 30$.

Figure 1 shows calculated stability diagram of the N_2 seeded high-δ elmy ILW discharge (shot 82814) in the no-wall limit. Here, $\langle j_\phi \rangle$ is the flux-surface averaged toroidal plasma current density at the flux surface where it has the maximum in the edge region, and α is the normalized pressure gradient,

$$\alpha = -\frac{1}{2\pi^2}\frac{dV}{d\psi}\left(\frac{V}{2\pi^2 R_0}\right)^{1/2}\mu_0\frac{dP}{d\psi} \simeq -\frac{2\mu_0 R_0 q^2}{B_0^2}\frac{dP}{dr},$$

at the same flux surface, where the approximation is in the cylindrical limit at the large aspect ratio, and V is the volume enclosed by the flux surface. The star in Figure 1 denotes the operational point and other points are obtained from perturbed equilibria around the star. The numbers represent the n-number of the most unstable mode in the range of n. In this scan, the current density profiles and the pressure gradient profiles are independently varied. Therefore, some currents in the stability diagram are not consistently determined from the bootstrap current calculation and are only for the purpose of determining the stability boundary in the $\langle j_\phi \rangle$-α space. This shot has $\beta_p \simeq 0.64$ and $\beta_N \simeq 1.65\%$, where β_p and β_N are poloidal and normalized beta respectively, and the plasma boundary has upper $\delta = 0.4$ in single null divertor geometry.

It is well established that ELMs are associated with pressure-gradient-driven ballooning mode [5], edge-current-(gradient)-driven peeling mode [6], or coupled peeling-ballooning mode [7]. Instability in the upper left corner of Figure 1 is due to the peeling mode which is more unstable for lower n. High n modes are stable in this region. The most dominant mode is the high n ballooning mode in the lower right corner where the $n \lesssim 10$ modes are stable. The upper right corner is where the intermediate-n peeling-ballooning mode becomes dominant. The operational point of shot 82814 lies where the ballooning mode is more dominant. At this point, $\langle j_\phi \rangle$ is lower than what the stability calculations results of BL CFC H-mode operation suggest [8], where the peeling-ballooning mode is most unstable. In Fig. 2, the stability diagram of shot 82819 shows that the operational point is further down the ballooning dominant region, inside the stability boundary compared with that of shot 82814. Global plasma parameters of shot 82819 are similar to those of shot 82814.

Beryllium has high electric conductivity (the electric resistivity of Be is $3.6 \times 10^{-8}\Omega$m at 20^{o}C), and the effect of the wall on the stabilization of MHD modes will be stronger for ILW wall. This stabilizing effect is shown in Fig. 3 as a function of n at the operational point of shot 82814. The wall is conformal and assumed to be perfectly conducting. Low n modes are more easily stabilized by the wall, while high n modes remain destabilized even with very tight wall position. The physical position of JET wall can be approximated to $r_{wall}/a \sim 1.07$, and considering finite resistivity of Be, the wall stabilization is not strong enough to influence high-n dominant instability of the operational point.

While BL high-δ discharges with ILW perform worse than those with CFC tiles, performance in hybrid ILW shots is found to improve. Therefore, we have investigated the effect of increased β_p due to the internal transport barrier. The plasma pressure profiles are modified in the core region to be more peaked with increasing β_p, while it remains the same outside the internal transport barrier in the edge region. Therefore the pressure gradient in the pedestal region does not increase with β_p in this modification. As it can be seen from the results shown in Fig. 4, shape of the stability boundaries does not change much, but they are shifted to higher values of α as β_p increases. The tip at the peeling-ballooning boundary also moves to higher $<j_{\phi}>$ and α considerably. As the stability boundaries widen, the operational point becomes stable when $\beta_p \gtrsim 0.8$ for this equilibrium. The Shafranov shift increases with β_p, which makes ψ more packed on the outboard side and flux surfaces become more shaped. This has stabilizing effect on the ideal MHD modes for the same $dP/d\psi$ profiles at the edge.

Stability analysis of JET shot 82636 (ILW, $\delta = 0.2$, $\beta_p \simeq 0.83$, $\beta_N \simeq 2.26\%$) in Fig. 5 shows different results from that for high-δ case of shot 82814. In this figure, the operational point of shot 82636 just before ELM lies in the peeling-ballooning corner in $<j_{\phi}>$-α space, allowing relatively higher plasma current. This result is similar to BL CFC H-mode results, and it may explain the experimental finding that performance in the low-δ discharges with ILW is comparable to that with the CFC tiles.

To find the effect of the plasma boundary shape on the stability boundary, single null diverted plasma boundary with upper $\delta = 0.2$ has been used for the same current density profile and for the same pressure profile modifications from shot 82814 to find stability boundaries of Fig. 4. The results are shown in Fig. 6. When only the boundary shape has been replaced from the experimental equilibrium of shot 82814, the shape of the stability boundary does not change much either, while the stable region shrinks from the original high-δ case. These results hold for wide range of β investigated in this study.

CONCLUSIONS

Experimental results have shown that ELM dynamics in the baseline high-δ shots with ILW at JET are different from those with plasma facing components of CFC tiles. The main difference is that two different types of the ELM collapses have been observed in the ILW case. One is the fast T_e drop followed by the recovery of T_e, while the other is followed by the additional T_e drop in the slow time scale. The fast drop in ILW plasma is slower than those of standard H-mode ELMs with CFC wall. Energy confinement degrades and the ELM interval increases in ILW plasma. The differences which appear in ILW operations are reduced in operations with impurity seeding, in low-δ boundaries, or in hybrid conditions.

From the MHD stability calculations of N_2 seeded high-δ elmy ILW discharge (shot 82814) just before the ELM, the operational point of shot 82814 is found to be located where the ballooning mode is more dominant. At this point, the peak current density at the edge is lower than one at the peeling-ballooning corner of the stability diagram, where the baseline high-δ CFC discharge operates. Low-δ ILW also operates near the peeling-ballooning stability boundary. To affect stability conditions considerably, tight fitting wall is needed. Wall stabilization is more effective for low-n instabilities and JET ILW is not expected to change stability of the operational point considerably. With the plasma pressure profiles modified in the core region to be more peaked with increasing β_p to study the effect of hybrid scenario, it has been shown that the shape of stability boundaries does not change but that stable region widens with increasing β_p, possibly due to increased Shafranov shift. When the shaping of the plasma boundary of single-null divertor increases as the upper δ changes from 0.4 to 0.2, the MHD stability is found to deteriorate.

Acknowledgements
This work was supported by EURATOM and carried out within the framework of the European Fusion Development Agreement. The views and opinions expressed herein do not necessarily reflect those of the European Commission. This work was supported partly by JSPS-NRF-NSFC A3 Foresight Program in the field of Plasma Physics (NSFC no. 11261140328).

References

[1] G F Matthews et al, 2009 Phys. Scr. **2009** 014030
[2] M Beurskens et al, 2013 Nuclear Fusion **53** 13001
[3] G. T. A. Huysmans, J. P. Goedbloed, and W. O. K. Kerner, Proceedings of CP90 Conference on Computational Physics (World Scientific, Singapore, 1991), p. 371
[4] A B Mihailovski et al, 1999 Plasma Phys. Rep. **23** 844
[5] J. W. Connor, R. J. Hastie, and J. B. Taylor, 1978 Phys. Rev. Lett. **40** 396
[6] J. W. Connor, R. J. Hastie, H. R. Wilson, and R. L. Miller, 1998 Phys. Plasmas **5** 2687
[7] P. B. Snyder et al, 2002 Phys. Plasma **9** 2037.
[8] S Saarelma et al, 2005 Plasma Phys. Control. Fusion **47** 713

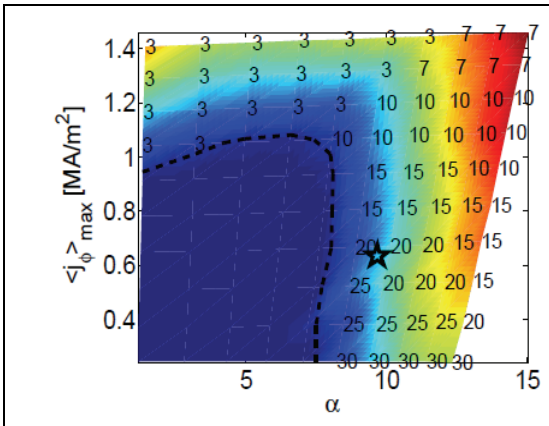

Figure 1. Stability diagram of JET elmy discharge (#82814) in $\langle j_\phi \rangle$-α space. The star denotes the operational point just before the elm crash. The numbers represent the n-number of the most unstable mode.

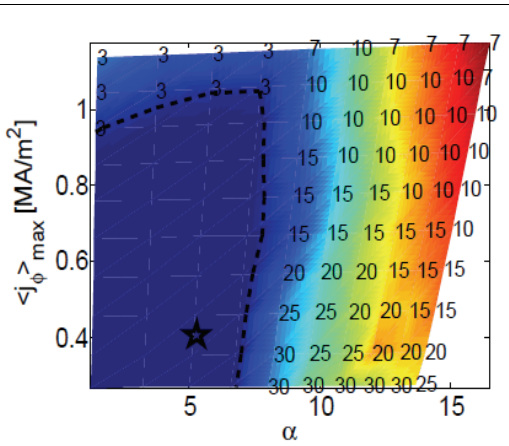

Figure 2. Stability diagram of JET elmy discharge (#82819) in $\langle j_\phi \rangle$-α space

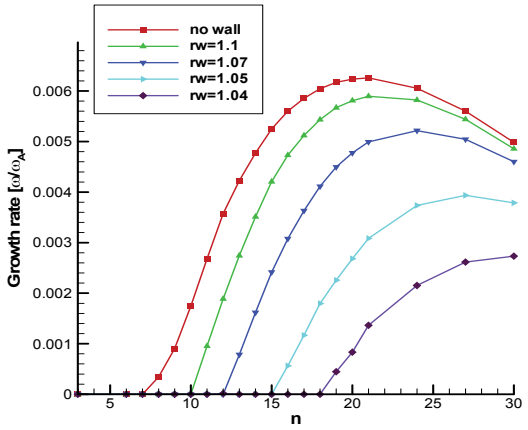

Figure 3. Effect of the perfectly conducting conformal wall on the mode stabilization as a function of n..

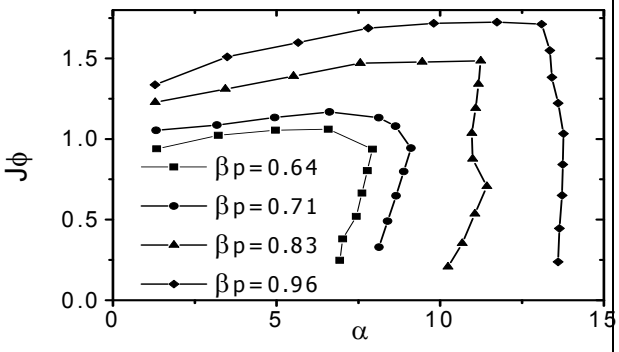

Figure 4. Stability boundaries in j_ϕ-α space for various β_p equilibria with modifications from the JET 82814 discharge.

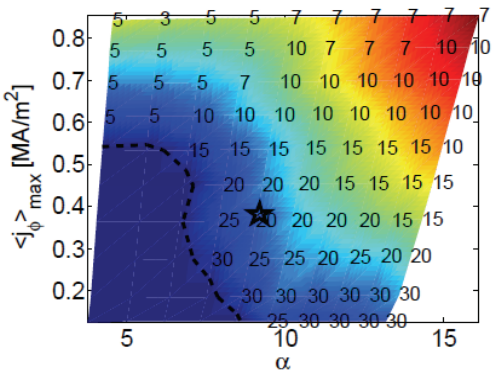

Figure 5. Stability diagram of JET elmy discharge (#82636) in $\langle j_\phi \rangle$-α space.

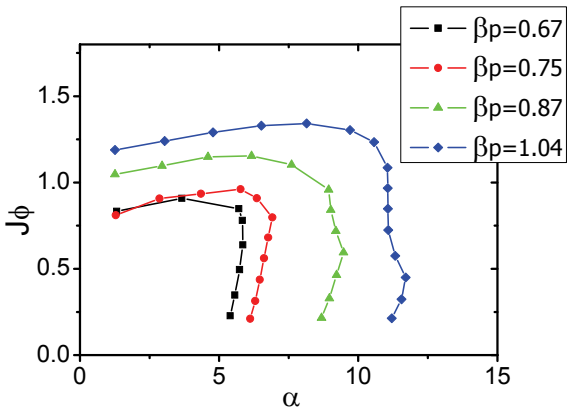

Figure 6. Stability boundaries in j_ϕ-α space for various β_p equilibria with pressure modifications from the JET 82814 discharge with low-δ boundary shape.

The Recent Research Progress on the J-TEXT Tokamak

Z.J. Wang[1], G. Zhuang[1], K.W. Gentle[2], X.W. Hu[1], Y.H. Ding[1], M. Zhang[1], Z.P. Chen[1], Z.J. Yang[1], L. Gao[1], X.Q. Zhang[1], Z.F. Cheng[1], Y. Pan[1], K.X. Yu[1], H. Huang[2], the J-TEXT team[1]
[1]College of Electrical and Electronic Engineering, Huazhong University of Science and Technology, Wuhan Hubei, 430074, China
[2]Institute for Fusion Studies, University of Texas at Austin, Austin, 78712, USA
E-mail contact of main author: wangzj@mail.hust.edu.cn

Abstract. The recent research progress on the J-TEXT tokamak is introduced. The interaction between resonant magnetic perturbations (RMPs) and plasma have been carried out on the J-TEXT tokamak and the results show that the m/n = 2/1 (m and n are the poloidal and toroidal mode numbers, respectively) mode locking is obtained with sufficiently large RMPs while suppression of the m/n = 2/1 tearing mode by moderate magnetic perturbation amplitude is also observed. With a model based on reduced magnetohydrodynamics (MHD) equations, both the mode locking and mode suppression by RMPs are simulated and the results are in good agreement with the experimental observations. To observe the current profile, a high resolution three-wave far infrared polarimeter/interferometer is set up and the first results indicate it works well.

1. Introduction

The J-TEXT tokamak [1] is a conventional iron core tokamak which is originally named as TEXT/TEXT-U tokamak and reconstructed for young student training and some physics research. The operation parameters of J-TEXT is summarized as: the major radius R = 105 cm, the minor radius r = 25-29 cm with a movable titanium-carbide coated graphite limiter, the maximum centrer-line toroidal field BT = 3 T, the maximum plasma current Ip = 400 kA lasting for 400 ms, plasma densities ne = 1-10×10^{19} m^{-3}, and electron temperature Te~1 keV. The main work on the J-TEXT tokamak in the recent years is emphasized on the observations and analysis of magnetohydrodynamic (MHD) activities, especially the influence of resonant magnetic perturbations (RMPs) on tearing mode[2,3]. Besides the three-wave far infrared laser polarimeter/Interferometer is set up and initial results is presented[4-6].

2. Influence of Resonant Magnetic Perturbations on the MHD Activities

2.1. Experimental Setup

In an attempt to investigate the influence of RMPs on the MHD instabilities, two sets of RMP field coils are installed on the J-TEXT tokamak. The layout of J-TEXT perturbation field coils is illustrated in Fig. 1. One set (namely static RMPs or SRMP) installed between the vacuum vessel and toroidal field coils can generate stochastic field perturbations at the plasma edge and was designed and installed on the TEXT-U

before[7]. The SRMP consists of three cosine coils arranged at toroidal angle intervals of 90 degrees, and two sine coils located at opposite positions. The other set, named dynamic RMP or DRMP [8] mounted inside the J-TEXT vacuum chamber consists of twelve saddle coils, which are assigned to four groups at equivalent locations toroidally. At present, Both SRMP and DRMP are operated in DC current mode. In future, the DRMP carrying AC current can generate rotating helical magnetic field perturbations with low mode numbers. A poloidal Mirnov array consisting of 24 2-D Mirnov pickup coils and a toroidal Mirnov array consisting of 8 pickup coils are used to analyze the poloidal and toroidal structures of the MHD modes. And the locked mode detector including a pair of saddle probes installed outside the vacuum vessel at opposite toroidal locations is used to detect stationary 2/1 magnetic island.

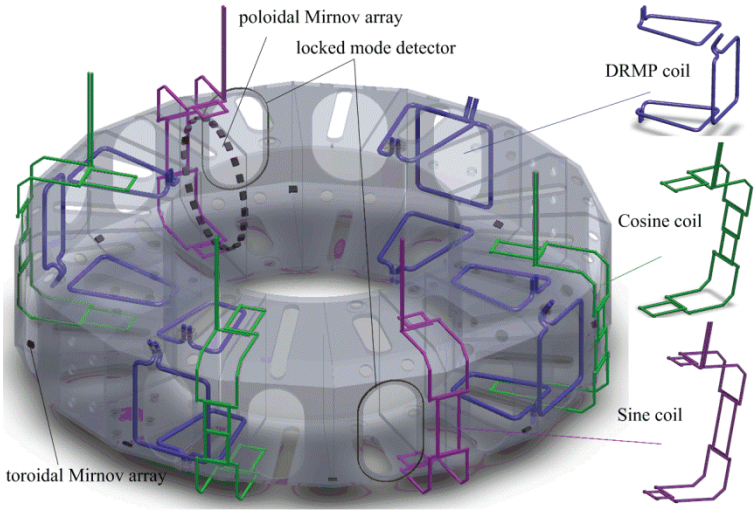

FIG. 1. The layout of SRMP coils (including Sine coils in violet and Cosine coils in green) and DRMP coils (in blue), poloidal Mirnov array, toroidal Mirnov array, and locked mode detector on the J-TEXT tokamak.

We have done mode structure analysis to the SRMP and DRMP field. About SRMP, because the coil width is a little small, it has many high toroidal modes., Under the typical ohmic discharging condition on J-TEXT, the edge safety factor is about 3.5 and the main resonant modes are just 2/1 and 3/1 mode. So the perturbed magnetic field with a dominant component of m/n = 2/1 (m and n are the poloidal and toroidal mode number, respectively) is primarily needed to study its effect on the m/n = 2/1 tearing mode. Fig. 2. displays the whole corresponding radial field spectra of modes produced by SRMP (a) and DRMP (b) at plasma edge (a = 27 cm), respectively. In the figure, the amplitude of other components of SRMP such as m/n = 3/1, 2/3 and 3/3 are also large, but slightly smaller than that of m/n = 2/1, while the DRMP produces the radial perturbation field dominated by m = 2. We can get the suitable field spectrum by changing the direction and adjusting the amplitude of each coil current (in SRMP/DRMP coils). By the way, it is should be noted that the perturbed magnetic field given here is calculated without taking the plasma responses into account.

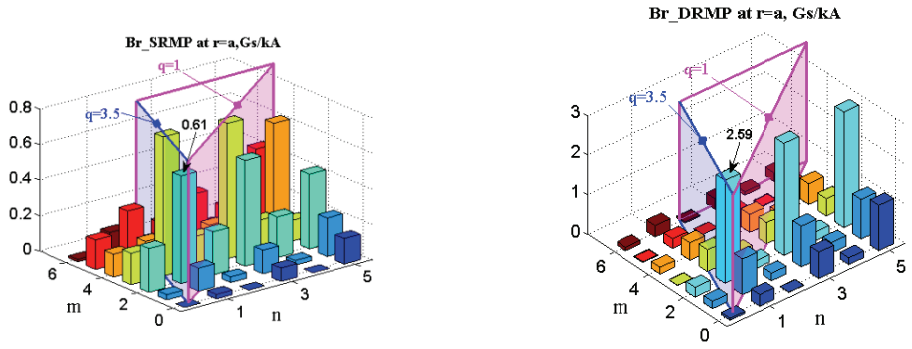

FIG. 2. the radial magnetic perturbation field spectra of modes produced by SRMP (a) and DRMP (b) at the plasma edge (a = 27 cm), respectively.

2.2. Observation and Simulation

When externally magnetic field perturbations are applied, the resulting electromagnetic force on the tearing mode can drive or drag the magnetic island and thereafter, change its rotation speed and affect the island width [9].Therefore, the mode locking and mode suppression phenomena are watched with different initial condition and RMP strength.

During mode locking, the mode frequency will decrease accordingly with the increase of the RMP strength and mode locking will occur when the RMP reaches the threshold. Then Br grows up quickly and there is a sudden decrease on soft X-ray and density and Fig 3a gives an example. On the other hand, RMP can suppress the tearing mode to very small or zero just in fig 3b, then we can usually see the appearance of saw tooth, which indicates a plasma confining improvement. However, if we maintain the RMP for long or increase the RMP amplitude, a locked mode may be stimulated. Then a large amount of energy loss or even disruption can be observed. The amplitudes of RMP in these two cases are respectively 3.7 G and 4.1 G, from which we can see that the result is very sensitive to the amplitude. when the initial mode frequency is low (typically smaller than 4 kHz), the mode can easily be locked. By statistics, we found RMP can suppress the tearing mode to a very small level under a high frequency (larger than 5.5 kHz), when the initial mode frequency is low (smaller than 4 kHz), the mode can easily be locked, just as showed in fig 3c .

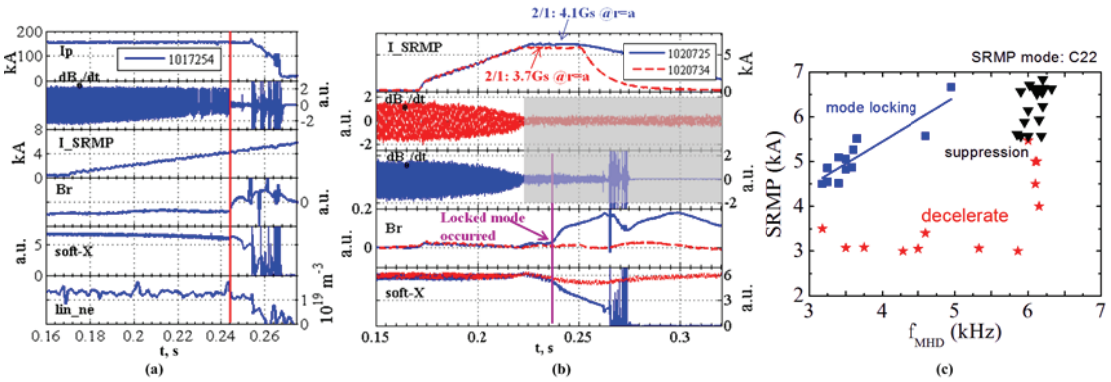

FIG. 3. Illustration of mode locking (3a), tearing mode suppression (J-TEXT shot

1020734, in red dash line) and locked mode (J-TEXT shot 1020725, in blue solid line) and the statistics between RMP intensity and tearing mode frequency respectively. Each signal indicates as plasma current (Ip), SRMP coil current (I_SRMP), Mirnov pickup coil signal (dBθ/dt), Locked mode signal (Br), loop voltage (Vloop), central line averaged plasma density (lin_ne), intensity of Soft X-rays (soft X) tearing mode frequency (f_{MHD}) .

To explain the mode locking and mode suppression by RMPs, a nonlinear numerical modeling based on reduced MHD equations has been carried out with the experimental parameters input[10]. The simulation results are shown in Fig 4. The normalized mode angular frequency, ω_p/ω_0, and island width at nonlinear saturation are shown as a function of the applied RMP amplitude ψ_a for $\omega_0=6.3\times10^3/\tau_R$ in figure 4(a) and $9.5\times10^3/\tau_R$ in figure 4(b), respectively, where ω_p (ω_0) is the mode angular frequency with (without) the RMP. The initial island width for these calculations is $w_0=0.04a$ at $t=0$, and the RMP is applied from $t=0$. For a lower original mode frequency ($\omega_0=6.3\times10^3/\tau_R$ in figure 4(a)), no mode stabilization by the RMP is observed. The mode frequency decreases with increasing ψ_a, while the island width slightly increases. The mode locking happens for sufficiently large RMP amplitude, $\psi_a > 4.1\times10^{-6}aB_t$, resulting in a sharp increase in the island width and drop in the mode frequency (to zero). The about 50% drop in mode frequency before mode locking has been predicted theoretically in [11] and observed experimentally in [12]. For a higher original mode frequency ($\omega_0=9.5\times10^3/\tau_R$ in figure 4(b)), however, the mode is stabilized by the RMP if the RMP amplitude is not too large. Three different regimes are observed from figure 4(b):

(i) *Mode suppression regime* ($\psi_a<4.46\times10^{-5}aB_t$), in which the island width decreases with increasing RMP amplitude. It is interesting to note that the mode frequency decreases with increasing ψ_a for $\psi_a\leq2.2\times10^{-5}aB_t$ but increases for $2.2\times10^{-5}aB_t<\psi_a<4.46\times10^{-5}aB_t$. Such a frequency increase is likely to be caused by a weaker electromagnetic force acting on the island with decreasing island width.

(ii) *Small locked island regime* ($4.46\times10^{-5}aB_t<\psi_a<5.6\times10^{-5}aB_t$), in which the mode is locked to the RMP as indicated by the zero mode frequency, while the island width is very small, different from the usual mode locking which corresponds to a large island.

(iii) *mode locking regime* ($\psi_a>5.6\times10^{-5}aB_t$), beginning from a large jump in the island width. The mode frequency is also zero in this regime, but the island width is significantly larger than the original one without RMP.

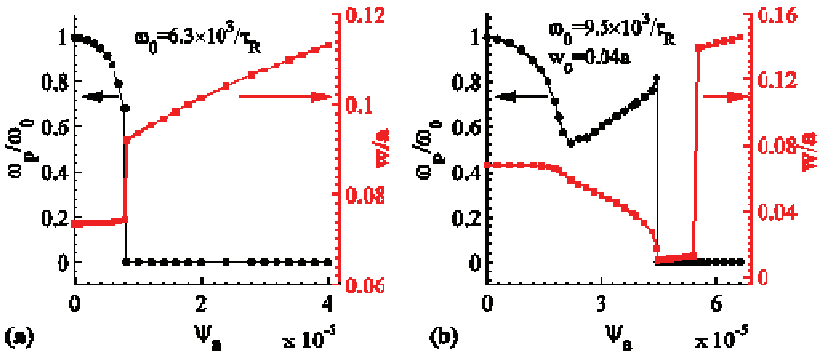

FIG. 4. Normalized mode angular frequency, ω_p/ω_0, and island width, w/a, at

nonlinear saturation versus ψ_a for $\omega_0=6.3\times10^3/\tau_R$ (a) and $9.5\times10^3/\tau_R$ (b), with the initial island width $w_0=0.04a$. For a lower value of ω_0 as shown in (a), only mode locking is seen with increasing ψ_a. For a higher value of ω_0 (b), however, three different regimes exist: (i) *Mode suppression regime* ($\psi_a<4.46\times10^{-5}aB_t$), in which the island width decreases with increasing RMP amplitude; (ii) *Small locked island regime* ($4.46\times10^{-5}aB_t<\psi_a<5.6\times10^{-5}aB_t$), in which the mode is locked to the RMP as indicated by the zero mode frequency, while the island width is quite small; (iii) *Mode locking regime* ($\psi_a>5.6\times10^{-5}aB_t$), beginning from a large jump in the island width.

3. First results from Three-Wave Far Infrared Laser Polarimeter/Interferometer

To increase the understanding of MHD evolutions, a three-wave far infrared polarimeter/interferometer is designed and set up for current profile change. While the simultaneous interferometric and polarimetric measurements can be achieved and the temporal resolution and phase resolution is 1μs and ~0.1 degree respectively. Eight chords with 5cm chord-spacing are installed in the latest campaign for the profile measurement, which could be increased to 30 mixers with 1.5cm spacing in the future. The typical results are shown in figure 5 in which waveform of plasma current is given in fig 5a, evolution of Faraday Angle is shown in fig 5b and the profile of Faraday Angle in three different time points is indicated in fig 5c. It is found that the zero-crossing point of Faraday Angle profile is slightly shifted outward ~2cm compared to center of the plasma (0 cm) and in consistence with Shafranov shift on J-TEXT tokamak. The plasma current is 180 kA and qa is ~4 in this charge and the chord positions of -10cm, -5cm, 0cm, 5cm, 10cm, 15cm, 20cm and 25cm.

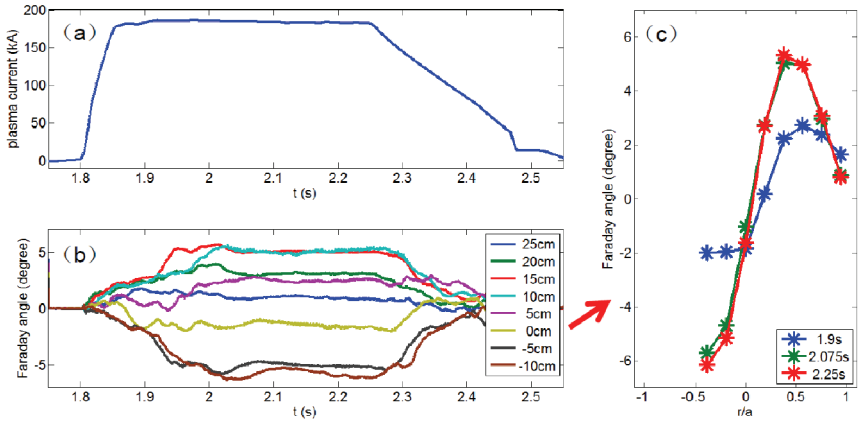

FIG. 5. the time trace of plasma current (a), Faraday Angle at eight different place (b) and the Faraday Angle profile at different time respectively.

4. Summary

The recent experimental campaign on the J-TEXT tokamak emphasizes the observation and analysis of MHD activity under different conditions. Firstly, the experimental investigation and simulation of the interaction between the RMPs and the Ohmic plasma are carried out by using the newly developed RMP coils. With sufficiently large RMPs, the m/n=2/1 (m and n are the poloidal and toroidal mode numbers) mode locking is easily obtained. In addition to normal mode locking events,

suppression of the m/n=2/1 tearing mode by moderate magnetic perturbation amplitude is observed. With experimental parameters as input, both the mode locking and mode suppression by RMPs are also obtained from nonlinear numerical modeling based on reduced MHD equations. It is found that the suppression of the tearing mode by RMPs of moderate amplitude is possible for a sufficiently high plasma rotation frequency and low Alfvén velocity. A high resolution three-wave far infrared polarimeter/interferometer is constructed with 1μs temporal resolution and about 0.1 degree phase resolution respectively, the initial results is consistent with calculation.

Acknowledgement We are grateful for the help from the Southwestern Institute of Physics and the Institute of Plasma Physics, Chinese Academy of Science. This work is supported by the Ministry of Science and Technology of China (Contract 2010GB107004, 2011GB109001) and National Natural Foundation of China (No. 10935004, 10990214) and the JSPS-NRF-NSFC A3 Foresight Program in the field of Plasma Physics (NSFC, No.11261140328).

References

[1] ZHUANG, G., et al., “The reconstruction and research progress of the TEXT-U tokamak in China”, Nucl. Fusion 51 (2011) 094020

[2] W. Jin, et al., “Dependence of plasma responses to an externally applied perturbation field on MHD oscillation frequency on the J-TEXT tokamak. Plasma”, Phys. Control. Fusion 55 (2013) 035010

[3] B. RAO, et al., “Tearing mode suppression by using resonant magnetic perturbation coils on J-TEXT tokamak”, Physics Letters A 377 (2013) 315–318

[4] CHEN, J., et al., “Design of far-infrared three-wave polarimeter-interferometer system for the J-TEXT tokamak”, Rev. Sci. Instrum. 81 (2010) 10D502

[5] CHEN, J., et al., “Progress of the in-building J-TEXT FIR three-wave polarimeter”, JINST. 7 (2012) C01064

[6] CHEN, J., et al., “First results from the J-TEXT high-resolution three-wave polarimeter-interferometer”, Rev. Sci. Instrum. 83 (2012) 10E306

[7] GENTLE, K.W., et al., The Texas Experimental Tokamak: A Plasma Research Facility, DOE/ER/542/41-151, FRCR #470, Univ. of Texas, Austin (1995)

[8] B. RAO, et al., Design of the in-vessel magnetic coils for generating a rotating resonant magnetic perturbation on the J-TEXT tokamak plasma. IEEE Trans. Appl. Supercond. 22 (2012) 4201804

[9] FITZPATRICK, R., “Interaction of tearing modes with external structures in cylindrical geometry”, Nucl. Fusion 33 (1993) 1055

[10] HU, Q.M., et al., “Effect of externally applied resonant magnetic perturbations on resistive tearing modes”, Nucl. Fusion 52 (2012) 083011

[11] Fitzpatrick R. "Bifurcated states of a rotating tokamak plasma in the presence of a static error-field", Phys. Plasmas 5(1998) 3325

[12] Hender T.C., Fitzpatrick R. et al "Effect of resonant magnetic perturbations on COMPASS-C tokamak discharges", Nucl. Fusion 32(1995) 2091

Physics of Energetic Electrons and Positrons in Tokamaks

Jian Liu[1], Hong Qin[1,2], Xiaoyin Guan[2], Qian Teng[3]

[1] University of Science and Technology of China
[2] Princeton Plasma Physics Lab
[3] Peking University

Positrons can be created when energetic runaway electrons, which usually carry up to tens of MeV energy, interact with background electrons and ions. A brief calculation gives an interesting result that Tokamaks may be the largest artificial positron factory in the world. This talk intends to introduce the persent understanding about the physics of energetic positrons in Tokamaks, including their pair-production, drift motion, radiation, and annihilation in Tokamaks. The possible experimental application and future work is also discussed.

Introduction to Runaway Electrons

Early in 1959, Dreicer discussed the runaway electron in a fully ionized gas immersed in constant field along the background magnetic field [5]. The collisional friction between an electron and background plasmas will first increase then decrease when the electron's energy rise, which means that there exists a peak value of the friction force. This is an unstable situation. When the external electric force is larger than the firction force, the electron can be accelerated faster and faster, neglecting radiation. This kind of electrons are named as runaway electrons. The external electric field which can balance the peak friction force is called Dreicer Field, written as

$$\mathrm{E_D} = \frac{\mathrm{n_e e^3 \ln \Lambda}}{4\pi\epsilon_0^2 \mathrm{T}}. \quad (1)$$

If external electric field exceeds $\mathrm{E_D}$, all the electrons can be accelerated to runaway ones. The external field which can balance the minimum friction force is called the critical field $\mathrm{E_C}$. The minimum friction force happens when the velocity of electron reaches the light velocity. So we have

$$\mathrm{E_C} = \frac{\mathrm{n_e e^3 \ln \Lambda}}{4\pi\epsilon_0^2 \mathrm{m_e c^2}}, \quad (2)$$

and

$$\frac{\mathrm{E_C}}{\mathrm{E_D}} = \frac{T_e}{m_e c^2} \ll 1. \quad (3)$$

Even though the electric field is not strong enough, because of the high velocity tail of Maxwellian distribution, there still exists runaway electrons. The typical loop electric

field lies between critical field and Dreicer filed

$$E_C \ll E \ll E_{D.} \quad (4)$$

It have been observed that a large amount of runaway electrons appear in large tokamak disruptions. There are many mechanism which produce runaway electrons in tokamaks, such as runaway avalanche, non-Ohmic current drive, and magnetic recnection.

Creation and Annihilation of Positrons

Pair production is the creation of an elementary particle and its anti-particle when a photon interacts with other particles. In pair production the photon's energy must exceed the total rest mass energy of the two particles. The energy conservation, momentum conservation, electric charge conservation, and many other conservation laws must hold in this procedure. The rest mass energy of electron is 0.51MeV, while in post-disruption plasmas in tokamaks the runaway electrons typically have energy between 10 and 20 MeV. It's sufficient for the pair production of electron and positron

$$\gamma + \gamma \rightarrow e^- + e^+. \quad (5)$$

At high energy, the cross-section of pair-production of electron and positron is approximately [2]

$$\sigma_p = \frac{28(Z_s \alpha r_e)^2}{27\pi} \ln^3 \gamma_e \qquad (\gamma_e \gg 1), \quad (6)$$

where $\alpha = e^2/4\pi\epsilon_0\hbar c = 1/137$ is the fine-structure constant, Z_s is the charge carried by particle species s, $r_e = e^2/4\pi\epsilon_0 m_e c^2$ is the classical electron radius, and $\gamma_e = E/m_e c^2$ is the Lorenz factor for the runaway electrons. Total pair-production cross-section over entire energy range up to 100MeV can be numerically fit as

$$\sigma_{tot} = aZ^2 \ln^3\left(\frac{\gamma_e + x_0}{3 + x_0}\right), \quad (7)$$

where $a = 5.22\mu b$, $x_0 = 3.6$. Thus given the runaway current is $I_r = 0.5MA$, the major radius $R = 1.75m$, the background electron density is $n_e = 3 \times 10^{19}/m^3$, we can estimate the positron production rate in a disruption as

$$S_p = \frac{4\pi R I_r \sigma_p n_e}{e} = 1.1 \times 10^{13}/s. \quad (8)$$

This value is actually an underestimate because the ions with higher Z_s are not considered here. Nevertheless, this value is still much higher than the production rate in accelerators where the dominating Coulomb repulsion hinders the increment of the beam density. Most of the positrons born in the pair-production have Lorentz factors satisfying $1 \ll \gamma_+ \ll \gamma_e$, which means the original positrons are also relativistic.

The annihilation cross-section can be written as

$$\sigma_a = \frac{\pi r_e^2}{1+\gamma_+}\left[\frac{\gamma_+^2 + 4\gamma_+ + 1}{\gamma_+^2 - 1}\ln\left(\gamma_+ + \sqrt{\gamma_+^2 - 1}\right) - \frac{\gamma_+ + 3}{\sqrt{\gamma_+^2 - 1}}\right], \quad (9)$$

where γ_+ is the Lorentz factor of positron. The total pair-production cross-section σ_{tot}, pair-production cross ultra-relativistic approximation $\sigma_{\gamma\gg1}$, near threshold total cross-section σ_{th}, and annihilation cross-section σ_{an} are numerically plotted in Fig.1[3] for $Z = 1$.

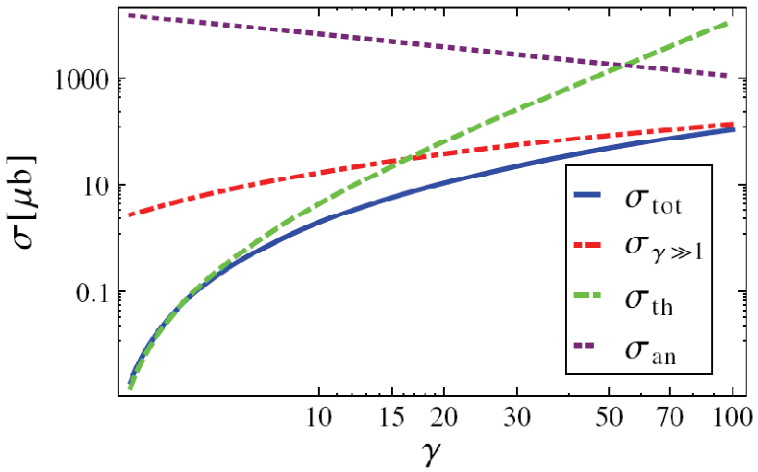

Fig.1

Dynamics of Runaway Particles in Tokamak

After high energy positrons are created in tokamaks, their behaviors are strongly affected by loop electric field, background magnetic field, and the background plasmas. Almost all positrons are runaway positrons. Since the only difference between runaway electrons and positrons is the sign of electric charge, their behaviors in tokamaks are similar. Runway particles mainly lose their energies in two different ways. One is radiation loss, the other is collision friction. Because of the gyromotion in magnetic field, runaway particles lose their energy through synchrotron radiation. The recoil experienced by positrons, namely Abraham–Lorentz force, slows them down at the rate

$$\left(\frac{dp_\perp}{dt}\right)_{rad} = -\frac{p_+\sqrt{1+p^{-2}}}{\tau_r}, \quad (10)$$

where $p = \gamma v/c$ is the relativistic momentum normalized to $m_e c$, $p_\perp$ is the perpendicular component of the momentum, and $\tau_r = 6\pi\epsilon_0 m_e^3 c^3/e^4 B^2$. On the other hand, collisional friction from the plasma electrons slows down a positron at the rate

$$\left(\frac{dp}{dt}\right)_{col} = -\frac{1+p^{-2}}{\tau}, \quad (11)$$

where $\tau = 1/4\pi r_e^2 n_e c \ln\Lambda$ is the collision time between relativistic positrons and electrons. Initially, at very high energy, the positrons mainly lose their energy through synchrotron radiation. Roughly speaking, for runaway particles with $p \geq 3$, radiation is the dominant energy loss mechanism. When positrons slow down to medium

relativistic velocity, collision effect begins to surpass radiation and thermalize them. Because cyclotron radiation and its recoil are strongly spatially anisotropic with respect to the background field, the change of runaway particles' momentum requires more detailed calculation.

To further study the dynamics of runaway particles, we can focus on their evolution in phase space. We start from the Lagrangian of gyrocenters

$$\mathrm{L} = (\mathrm{e}\mathbf{A_0} + \mathrm{e}\mathbf{A_1} + \mathrm{p}_\parallel \mathbf{b}) \cdot \dot{\mathbf{x}} - \gamma \mathrm{mc}^2, \quad (12)$$

where $\mathbf{A_0}$ corresponds to background magnetic field, $\mathbf{A_1}$ corresponds to the effective electric field as

$$\mathrm{E}_{\mathrm{eff}} = -\frac{\partial \mathrm{A}}{\partial \mathrm{t}} = \frac{\mathrm{F_S} + \mathrm{F_c} + \mathrm{F_B}}{\mathrm{e}}, \quad (13)$$

where

$$\mathrm{F_c} = \frac{\mathrm{n_e e^4} \ln \Lambda \, \mathrm{m}}{4\pi\epsilon_0^2} \frac{\gamma^2}{\mathrm{p}^2} \quad (14)$$

is the collisional drag force,

$$\mathrm{F_s} = \frac{2}{3} \mathrm{r_e mc^2} \gamma^4 \left(\frac{\sqrt{\gamma^2 - 1}}{\gamma} \right)^3 \left(\frac{1}{\mathrm{R}_0^2} + \frac{\sin^4 \theta}{\mathrm{r_g^2}} \right) \quad (15)$$

is the synchrotron radiation drag force, and

$$\mathrm{F_B} = \frac{4}{137} \mathrm{n_e mc^2} \gamma \mathrm{r_e^2} (\mathrm{Z_{eff}} + 1) \left(\ln 2\gamma - \frac{1}{3} \right) \quad (16)$$

is the bremsstralung drag force. According to this set of equations, we can obtain the behavior of runaway particles. Besides parallel acceleration, because of the toroidal geometry, positrons also process an outward drift velocity

$$\mathrm{v_{dr}} = \frac{\mathrm{q}}{\mathrm{B}_0} (E_\parallel + \mathrm{E_{eff\parallel}}), \quad (17)$$

where the effective electric field

$$\mathrm{E_{eff}} = \frac{\mathrm{F_s} + \mathrm{F_c} + \mathrm{F_B}}{\mathrm{e}}. \quad (18)$$

Fig.2 presents evolution of runaway particles in configuration and momentum spaces. The left two figures shows the drift of passing orbit projection in intersection surface perpendicular to toroidal direction in configuration space. The left up one is with collision, and the left down one is without collision. The left two figures compare the time revolution of parallel and perpendicular momentum. These figures show that collisions effect runaway particles in momentum space more than in configuration space.

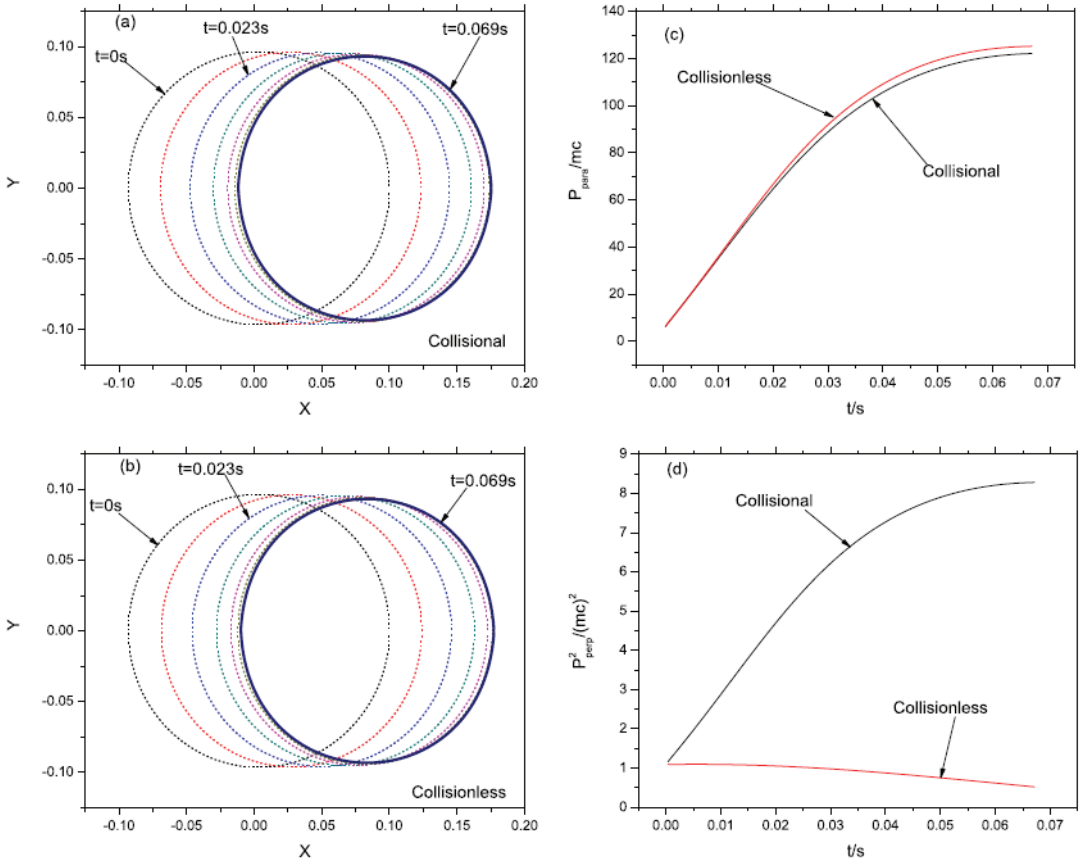
(a)
t=0.023s
t=0.069s
t=0s
Collisional
Y
X
(c)
Collisionless
Collisional
P_{para}/mc
t/s
(b)
t=0.023s
t=0.069s
t=0s
Collisionless
Y
X
(d)
Collisional
Collisionless
$P^2_{perp}/(mc)^2$
t/s

Fig. 2

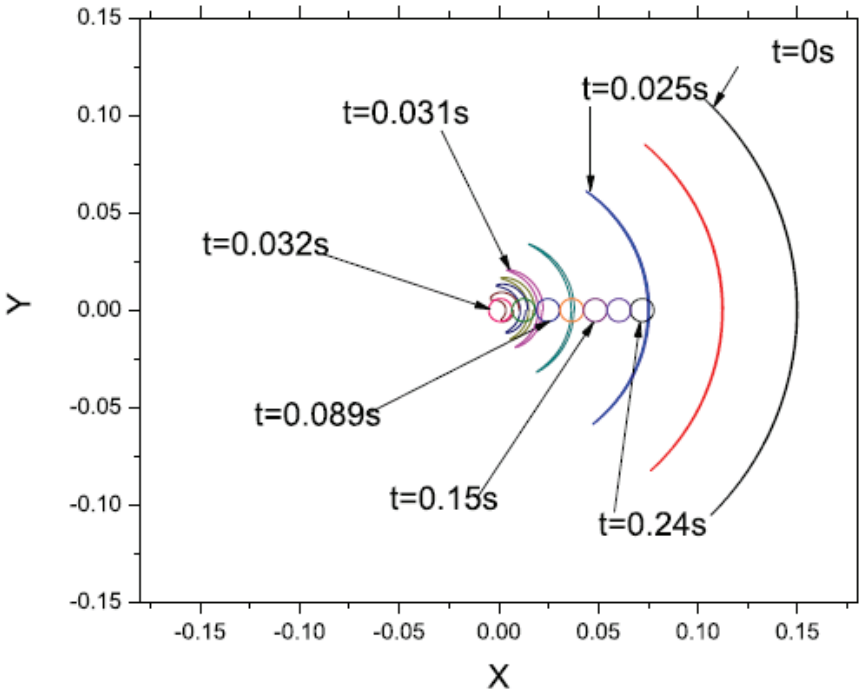
t=0s
t=0.025s
t=0.031s
t=0.032s
t=0.089s
t=0.15s
t=0.24s
Y
X

Fig. 3

Fig. 3 shows a case that a trapped particle transits to a runaway particle. The trapped orbit first drifts to the center due to Ware pinch. Then the particle becomes passing ones and being accelerated to runaway particles. The orbit begins to drift outwards. Numerical results show that for large loop electric field, runaway particles are more likely to drift out a long distance and collide the wall.

Prospect on Experimental Application

The portion of positrons is very small compare with runaway electrons since the small pair production cross-section. Hence the feedback phenomena from positrons can be neglected. On the other hand, the characteristic annihilation spectrum offers a good diagnostic method. Positron has been used as a probe tool in many fields, such as momentum distribution techniques, positron moderator, and positron lifetime spectroscopy. The positron emission tomography (PET), which is a medical imaging technique based on pair production to diagnose diseases in brain or heart, has been broadly used. In PET, tracer is first injected into body to create positrons. In 1986, Surko et al. proposed to use positrons to study transport in tokamak plasmas [7]. Their proposal based on the injection of positrons. According present understanding, the number of natural produced positrons in tokamak plasmas is much more than the injection dose. This active diagnostics is neither necessary nor valid.

The positrons from pair-production in plasmas will offer important information, such as the distribution of runaway electrons. Further study on mechanism of positrons in tokamak will give more precise knowledge of positrons' behavior and may offer more benefit in plasma science and technology.

Acknowledgements

This work was partly supported by the JSPS-NRF-NSFC A3 Foresight Program in the field of Plasma Physics (NSFC: No.11261140328).

References:

[1] M. Bakhiari, G. Kramer, and D. Whyte, Phys. Plasmas **12**, 102503 (2005)
[2] P.Helander, and D. Ward, Phys. Rev. Lett. **90**, 135004 (2003)
[3] T. Fulop, and G. Papp, Phys. Rev. Lett. **108**, 225003 (2012)
[4] X. Guan, H. Qin, and N. Fisch, Phys. Plasmas **17**, 092502 (2010)
[5] H. Dreicer, Phys. Rev. **115**, 238 (1959)
[5] R. Kulsrud, Y. Sun, N. Winsor, and H. Fallon, Phys. Rev. Lett. **31**, 690 (1973)
[6] J. Wesson, *Tokamaks*, Clarendon Press-Oxford, 2004
[7] C. Surko, et. al., Rev. Sci. Inst. **57**, 1862 (1986)

EAST ICRF System for Long Pulse Operation

Y.P. Zhao[1)],X.J. Zhang*[1)],Y.Z. Mao[1)], C.M. Qin[1)], S. Yuan[1)], D.Y. Xue[1)], L. Wang[1)], S.Q. Ju[1)],Y. Chen[1)], H.Wang[1)],Y. Lin[3)], J.G. Li[1)], B.N. Wan[1)], X.Z. Gong[1)],Y.T. Song[1)], G. Taylor[2)],S. Wukitch[3)],J.M. Noterdaeme[4,5)],F. Braun[4)], R. Magne[6)], X. Litaudon[6)], R. Kumazawa[7)], T. Seki[7)], H. Kasahara[7)]

[1)]Institute of Plasma Physics, Chinese Academy of Sciences, Hefei 230031, China
[2)]Princeton Plasma Physics Laboratory,USA
[3)]MIT Plasma Science and Fusion Center, Cambridge, MA 02139, USA
[4)]Max-Planck Institute for Plasma Physics, D-85748, Garching, Germany
[5)] University of Gent, Belgium
[6)]CEA, IRFM, F-13108 Saint-Paul Lez Durance, France
[7)]National Institute for Fusion Science, Toki, 509-5292 Japan
*Email：xjzhang@ipp.ac.cn

Abstract: Radio frequency (RF) power in the ion cyclotron range of frequencies (ICRF) is one of the primary auxiliary heating techniques for Experimental Advanced Superconducting Tokamak (EAST). A6.0MW ICRF systems in the range of 25-70 MHz has been put into operation during the EAST 2012 spring campaign. The ICRF systems consist of two port-mounted antennasand each antenna is driven by two independent 1.5MW RF power source.Another four 1.5MW ICRF system is under way of construction.The system will deliver more than 10MW of RF power to the plasma for 1000 sec pulse length.This paper gives brief introduction of the ICRF systems capabilityon EAST.

1. Introduction

The research objectives of EAST are to perform advanced tokamak research in high performance regime and to explore methods for achieving a steady-state operation for a tokamak fusion reactor.EAST is a fully superconducting tokamak (R = 1.75m, a = 0.4m, Bt = 3.5T, pulse length<= 1000 sec) being commissioned at ASIPP. Since the first plasma in 2006, much significant progress has been achieved [1, 2]. RF power in the ion cyclotron range of frequencies is one of the primary auxiliary heating techniques for EAST.

EAST tokamak is equipped with an ICRF system consisting of fourtransmitters, totaling 6.0 MW and two low field side antennas at two dedicated horizontal ports, B-port and I-port. The ICRF system has been designed to operate for long pulse length up to 1000 s. Each transmitter is connected by a nine inch transmission line, through a three stub matching system, and vacuum insulated transmission lines to an antenna.The performance of ICRF heating has progressed steadily on EAST [3-7].Up to 2.0 MW of RF power was injected into plasmas during the 2012 spring campaign andplasma performance was greatly improved [8].

2. The main technical feature of ICRF Systems on EAST

A 6.0MW ICRF system with long pulse operation at megawatt levels in a frequency range of 25 to 70 MHz has been designed as a part of the research and

development (R&D) for EAST. The RF transmitters were tested in a matched dummy load where a RF output power of 1.5 MW was achieved. Another6.0 MW ICRF system is under way of construction.The total heating power will be more than 10MW in the near future.

2.1 RF Power Amplifier

There are fourRF transmitterin the ICRF system. A block diagram of ICRF system is shown in Fig. 1. The RF transmitter units are shown in the section enclosed by the dotted red line. A transmitter setup includes the amplitude and frequency control and monitor unit, a RF power amplifier chain, direct current (DC) high voltage power supply (HVPS) and cooling system.

Each RF power amplifier chain consists of low power stage and high power stage. The low power part is composed of a phase and amplitude controller (PAC) which has four RF output ports each designed to produce a 20-mW (13dBm) RF signal with a adjustable phase shift from 0^{o} to 360^{o}, a computerized waveform generator producing a desired reference pulse waveform, and a RF switch which is used in each amplifier chain to cut off RF power immediately once the reflected power fraction exceeds the specified value. The high power part includes a three-stage RF power amplifier chain, i.e. 5 kW-stage broadband solid state amplifier (SSA), 100 kW-stage tetrode drive power amplifier (DPA) and 1.5 MW-stage tetrode final power amplifier (FPA), tunable from 25 MHz to 70 MHz. The gains of the SSA, the DPA and the FPA are about ~46 dB, ~14 dB and ~13 dB, respectively. In order to protect the components of the amplifier and to achieve a stable operation of the transmitter, the DC HVPSs based on pulse step modulation (PSM) technology were developed for tetrode tubes because of its great advantages, such as fast response, low short-circuited energy, flexibility, etc.

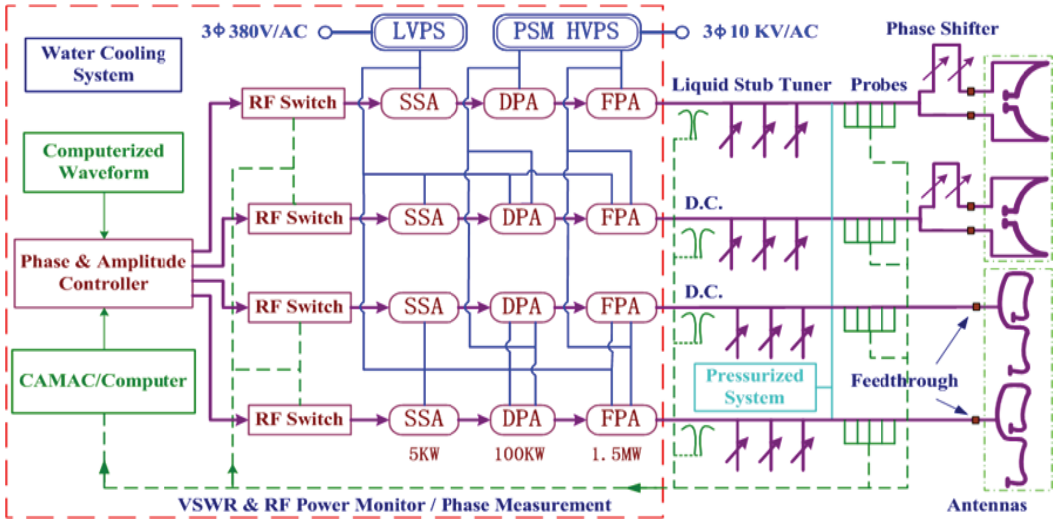

Fig.1 Block diagram of the ICRF system on EAST.

Transmitter tests were conducted with a matched dummy load over a frequency range from 25 MHz to 70 MHz in steps of 1 MHz. Figure 2 shows the test results of the transmitter. An averaged maximum RF output power of 1.5 MW was achieved in

a frequency range of 25 MHz - 65 MHz with an efficiency varying from 60 to 70 percent. The gains of about 14 dB and 13 dB were obtained for the DPA and the FPA, respectively. Unfortunately, both RF output power and efficiency of the transmitter decreased rapidly at frequencies higher than 65 MHz because of the limitation of operation frequency of tetrode tube.

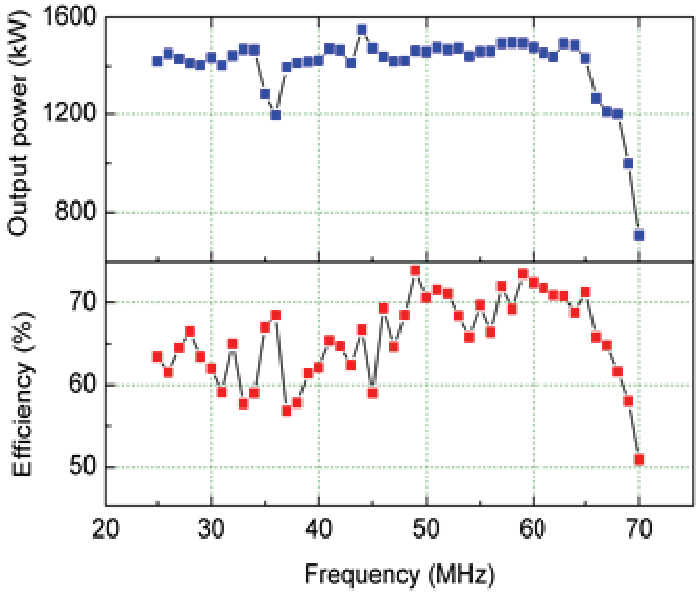

Figure 2 High power tests of the RF transmitter over thefrequency range from 24 MHz to 70 MHz. The averagedRF output power of 1.5 MW was achieved with an efficiency of about 60~70 percent in the frequency range of25~65 MHz

2.2 The RF matching system andICRF Antenna systems

The ICRF system consist of four triple liquid stub tunersand two port-mounted antenna, as shown in Figure 3. The RF matching system is shown in figure 3(left). It utilizes the difference of radio frequency wavelengths in gas and in liquid due tothe different relative dielectric constants. The liquid (i.e. oil silicon) is filled between innerconductor and outer conductor. By using a pump to control the liquid level, the parametersof this matching system can be changed. Due to the CW operation, the inner and outer conductor of the liquid stub tuner must be cooled by pure water.

There are two ports for ICRF antenna system on EAST. The phase between the current straps can be change in 0-360.For long pulse operation, the antennas have many cooling channels inside the current strap, cavity wall, the faraday screen and vacuum transmission line. In order to adjust the coupling of the antenna to plasma, the antenna can be moved a little in radial direction. The ICRF antenna at B port is grounded at the center, and have a coaxial feed line connected to each end of the current strap, as shown in Fig.3 (right). After going through two vacuum feedthrough, the top and bottom coax feed lines of each current strap are connected to each other in a resonant loop configuration. The length of the current strap that coupled power to plasma is 700mm. The antenna at I port are folded, end grounded with a central current feed, as shown in Fig.3 (middle). The length of the current strap is 750mm. Two 1.5MW RF transmitter is attached to the antenna through a matching system.

The matching system consists of three stub tuner. Phase between the straps is controlled in the low power parts of the RF system.

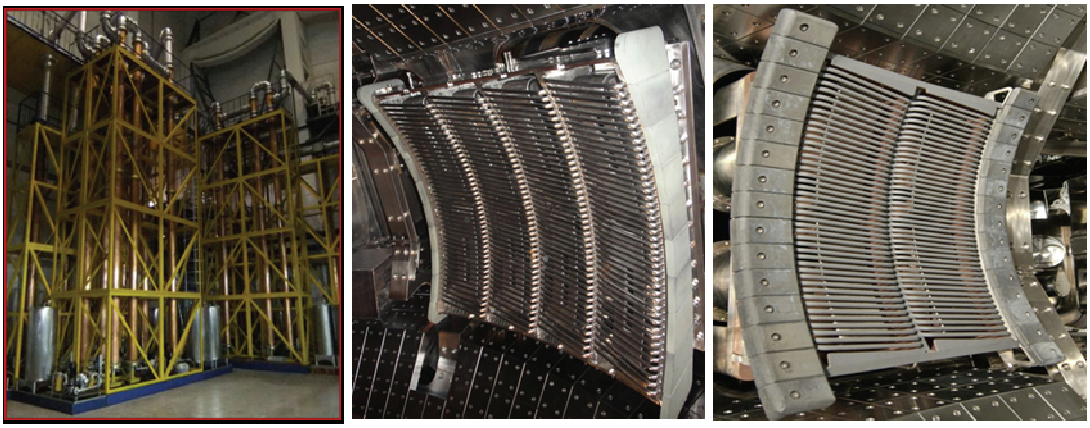

Figure 3 The ICRF matching system (left) and antenna systems: Four-strap antenna at I-port(middle),Two-strap antenna at B-port(right).

3. Summary

A 6.0 MW (1000 s) ICRF system has been put into operationon EAST.The transmission line, antenna, vacuum feedthrough and matching components for long pulse and high power operation have been developed.An averaged maximum RF output power of 1.5 MW was achieved in a frequency range of 25 MHz - 65 MHz with an efficiency varying from 60 to 70 percent. Another 6.0 MW ICRF system is under way of construction.

Acknowledgments

The authors would like to acknowledge the support of the EAST operation and diagnostics group. This work was supported partly by National Magnetic confinement Fusion Science Programme (grant no. 2010GB110000). This work was also supported partly by the National Natural Science Foundation of China under grant no.11105179, and 11175208. This work was supported partly by JSPS-NRF-NSFC A3 Foresight Program in the field of Plasma Physics (NSFC no. 11261140328).

References

[1] Wan B.N. et al., Fusion Eng. Des. 85(2010) 1048.
[2] Wan B.N. and International Collaborators Nucl. Fusion 49(2009) 104011.
[3] Jiangang Li et al., Nucl. Fusion 51 (2011) 094007
[4] X.J.Zhang, et al. Physics and Engineering Aspects of the ICRF Heating System on EAST，23rd IAEA，2010
[5] X.J. Zhang et al., Plasma Sci. Technol. 13 (2011) 172
[6] X.J. Zhang et al., Nucl. Fusion 52 (2012) 032002
[7] X.J Zhang et al., Nucl. Fusion 53 (2013) 023004
[8] X.J Zhang et al., Preliminary ICRF Heating Results on EAST,A3 Foresight Program Seminar, Kushiro, Japan, 201

Program of A3 Seminar

(22-25 January 2013)

21 January 2013 (Monday)
Registration: 17:00-21:00

22 January (Tuesday)			
Session 1 (Opening) Chair: Prof. S.Morita	09:00	**S. Morita** (NIFS)	**Welcome speech** (10 min)
	09:10	**W.P.Chen**	**Welcome speech** "Short comments on A3 collaboration" (10 min)
	09:20	**J.G.Li** (ASIPP)	**Welcome speech** "Chinese future MCF plan" (25 min)
	Registration & Coffee Break 9:45-10:15		
Session 2 (Category I-1) Chair: Prof. J. G. Li	10:15	**Y.K.Oh** (NFRI)	Progress of the KSTAR experiments and perspective for ITER scientific researches (25 min)
	10:40	**S.Sakakibara** (NIFS)	Present Status of MHD study in Helical Plasmas (25 min)
	11:05	**H. Y.Guo** (ASIPP)	Progress toward high performance steady-state operation in EAST (25 min)
	11:30	**Y.Kishimoto** (Kyoto U.)	Simulation of Turbulence in toroidal plasmas (tentative) (25 min)
	Lunch Break11:55-13:30		
Session 3 (Category I-2) Chair: Prof. Y.K.Oh	13:30	**N.Xiang** (ASIPP)	Sheath and boundary conditions in tokamak plasmas (25 min)
	13:55	**L.Q.Hu** (ASIPP)	Diagnostics upgrade and capabilty available for Physics study on EAST (25 min)
	14:20	**Y.S.Bae** (NFRI)	The operation of the heating system for the steady-state plasma achievement (25min)
	Coffee Break 14:45-15:15		
Session 4 (Category I-3, 4) Chair: Prof. H.K.Park	15:15	**S.Kubo** (NIFS)	Issues of high power/ long pulse ECRH experiments in LHD (25 min)
	15:40	**X.J.Zhang** (ASIPP)	Preliminary ICRF Heating Results on EAST (25 min)
	16:05	**Y.Liu** (ASIPP)	Recent progress of the microwave diagnostics and related physics study on EAST (25 min)
	16:30	**B.Lv** (ASIPP)	Plasma Rotation Behavior of RF heated H-mode discharges on EAST (25 min)

23 January (Wednesday)			
Session 5 (Category IIa-1) Chair: Prof. Y.S.Bae	08:30	**G.-N.Luo** (ASIPP)	R&D of PFMC and related PWI activities at ASIPP (25min)
	08:55	**N.Ashikawa** (NIFS)	Plasma wall interactions in fusion devices (25 min)
	09:20	**K.S.Chung** (Hanyang U.)	Korean Plasma-Material Researches (25 min)
	09:45	**S.Morita** (NIFS)	Impurity spectroscopy in fusion plasmas and plan for A3 collaboration (25 min)
	Coffee Break 10:10– 10:40		
Session 6 (Category IIb-1) Chair: Prof. H.Y.Guo	10:40	**D.Kato** (NIFS)	Atomic and Molecular processes in fusion plasmas (25 min)
	11:05	**H.K.Park** (POSTECH)	Validation and Verification of MHD Physics vis 2D/3D ECE Imaging system on KSTAR (25min)
	11:30	**S.Ohdachi** (NIFS)	Edge MHD instabilities and imaging diagnostics (25 min)
	11:55	**K.Toi** (NIFS)	Comprehensive understanding and control of edge localized modes in 2D and 3D toroidal plasmas (25 min)
	Lunch 12:20-14:00		
Session 7 Discussion on A3 program	Opening of web site for A3 collaboration Logo mark for A3 program Education of young scientists Discussions on next seminar and workshop plans Discussion on coordinator meeting Discussion on budget for networking Discussion on annual report of A3 collaboration		

24 January (Thursday)			
Session 8 (Category III-1) Chair: Prof.O.J.Kwon	08:30	**M.Isobe** (NIFS)	Energetic-particle diagnostics and physics in toroidal fusion plasmas (25 min)
	08:55	**C.M.Ryu** (POSTECH)	Current research efforts of the Energetic particle study in Korea (25 min)
	09:20	**K.Toi** (NIFS)	Development of MHD spectroscopy using energetic-particle-driven modes in 2D and 3D toroidal plasmas (25 min)
	09:45	**Y.Todo** (NIFS)	Recent progress of hybrid simulation for energetic particles and MHD (25 min)
	Group photo & Coffee Break 10:10 - 10:40		
Session 9 (Young scientists) Chair: Prof. J.G.Kwak	10:40	**K.Ogawa** (NIFS)	Study on fast ion loss in the large helical device (25 min)
	11:05	**C.F.Dong** (NIFS)	Quantitative analysis of carbon ions in edge plasmas of LHD (25min)
	Lunch Break 11:30 - 13:30		
Session 10 (Alternative) Chair: Prof. N.Xiang	13:30	**O.J.Kwon** (Daegu U.)	Numerical MHD Analysis of JET High Beta Experiments with ITER-like wall (25 min)
	13:55	**Z.J.Wang** (HUST)	The recent research work on the J-TEXT tokamak (25 min)
	14:20	**J.Liu** (USTC)	Physics of Energetic Electrons and Positrons in Tokamaks (25 min)
	Coffee Break 14:45-15:15		
Session 11 (Personal exchange and closing) Chair: Prof. L.Q.Hu	15:15	**S.H.Dong** (ASIPP)	Management and personnel exchange of A3 in ASIPP Discussion on personnel exchange (10 min)
	15:25	**N.Tonouchi** (NIFS)	Management and personnel exchange of A3 in NIFS Discussion on personnel exchange (10 min)
	15:35	**J.H.Han** (NFRI)	Management and personnel exchange of A3 in NFRI Discussion on personnel exchange (10 min)
	15:45	**S.Ohdachi** (NIFS)	Web site of A3 Collaboration
	16:15	**S.Morita** (NIFS) **Y.K.Oh** (NFRI) **L.Q.Hu** (ASIPP) **J.G.Kwak** (NFRI) **Y.P.Zhao** (ASIPP)	Summary reports "Comments on Future plan of KSTAR" (10 min) by J.G.Kwak "Comments on ICRF experiment of EAST" (10 min) by Y.P.Zhao
	17:05	**M.Kwon** (NFRI)	**Closing speech** "Comments on Korean fusion research" (10 min)

25 January (Friday)	
Session 12 Chair: Prof.S.Morita Prof.L.Hu Prof.Y.K.Oh	09:00-12:00 Plenary meeting on future collaboration at each category for A3 Foresight Program on Critical Physics Issues Specific to Steady State Sustainment of High-Performance Plasmas Category I: Steady state sustainment of magnetic configurations (Current drive and profile control) Category II: Edge and divertor plasma control Category IIa: Transport of edge and divertor plasmas Category IIb: Stability of edge plasma Category III: Confinement of alpha particles (Interaction of energetic particle and bulk plasma) 13:30-17:00 Individual discussions on plans for personnel exchange and preparation of hardware construction of diagnostics and heating devices Discussion with younger scientists on future study related to A3 collaboration

(END)

List of participants

ASHIKAWA Naoko
National Institute for Fusion Science
322-6 Oroshi-cho, Toki-shi, Gifu
509-5292, Japan
E-mail: ashikawa.naoko@LHD.nifs.ac.jp

BAE Young-soon
KSTAR Reseach Center,
National Fusion Research Institute
169-148 Gwahak-ro, Yuseong-gu, Daejeon
305-806, Korea
E-mail: ysbae@nfri.re.kr

CHUNG Kyu-Sun
Division of Electrical and Bio-engineering,
Center for Edge Plasma Science,
Hanyang University
222 Wangsimni-ro, Seongdong-gu, Seoul,
133-791, Korea
E-mail: kschung@hanyang.ac.kr

DON Chunfeng
National Institute for Fusion Science
322-6 Oroshi-cho, Toki-shi, Gifu
509-5292, Japan
E-mail: dong.chunfeng@nifs.ac.jp

GUO Houyang
Institute of Plasma Physics,
Chinese Academy of Science
P.O.Box 1126, Heifei, Anhui 230031,
P.R. China
E-mail: hyguo@ipp.ac.cn

HU Liqun
Institute of Plasma Physics,
Chinese Academy of Science
P.O.Box 1126, Heifei, Anhui 230031,
P.R. China
E-mail: lqhu@ipp.ac.cn

ISOBE Mitsutaka
National Institute for Fusion Science
322-6 Oroshi-cho, Toki-shi, Gifu
509-5292, Japan
E-mail: isobe.mitsutaka@LHD.nifs.ac.jp

KATO Daiji
National Institute for Fusion Science
322-6 Oroshi-cho, Toki-shi, Gifu
509-5292, Japan
E-mail: kato.daiji@nifs.ac.jp

KISHIMOTO Yasuaki
Graduate School of Energy Science,
Kyoto University
Gokasho, Uji-shi, Kyoto
611-0011, Japan
E-mail: kishimoto@energy.kyoto-u.ac.jp

KUBO Shin
National Institute for Fusion Science
322-6 Oroshi-cho, Toki-shi, Gifu
509-5292, Japan
E-mail: kubo.shin@LHD.nifs.ac.jp

KWON Oh-Jin
Department of Physics, Daegu University
Daegudaero 201, Jinryang Gyeongsan
Gyeongbuk 712-714 Korea
E-mail: ojkwon@daegu.ac.kr

LIU Jian
University of Science and Technology of China
Hefei Anhui, 230026, P.R. China
E-mail: jliuphy@ustc.edu.cn

LIU Young
Institute of Plasma Physics,
Chinese Academy of Science
P.O.Box 1126, Heifei, Anhui 230031,
P.R. China
E-mail: liuyong@ipp.ac.cn

LUO Guangnan
Institute of Plasma Physics,
Chinese Academy of Science
P.O.Box 1126, Heifei, Anhui 230031,
P.R. China
E-mail: gnluo@ipp.ac.cn

LU Bo
Institute of Plasma Physics,
Chinese Academy of Science
P.O.Box 1126, Heifei, Anhui 230031,
P.R. China
E-mail: blu@ipp.ac.cn

MORITA Shigeru
National Institute for Fusion Science
322-6 Oroshi-cho, Toki-shi, Gifu
509-5292, Japan
E-mail: morita.shigeru@LHD.nifs.ac.jp

OGAWA Kunihiro
National Institute for Fusion Science
322-6 Oroshi-cho, Toki-shi, Gifu
509-5292, Japan
E-mail: ogawa.kunihiro@lhd.nifs.ac.jp

OHDACHI Satoshi
National Institute for Fusion Science
322-6 Oroshi-cho, Toki-shi, Gifu
509-5292, Japan
E-mail: ohdachi.satoshi@LHD.nifs.ac.jp

OH Yeong-Kook
KSTAR Reseach Center,
National Fusion Research Institute
169-148 Gwahak-ro, Yuseong-gu, Daejeon
305-806, Korea
E-mail: ykoh@nfri.re.kr

PARK Hyeon K.
Physics Department, POSTECH
77 Cheongam-ro, Nam-gu, Pohang, Gyungbuk 790-784, Korea
E-mail: hyeonpark@postech.ac.kr

RYU Chang-Mo
Physics Department, POSTECH
77 Cheongam-ro, Nam-gu, Pohang, Gyungbuk 790-784, Korea
E-mail: ryu201@postech.ac.kr

SAKAKIBARA Satoru
National Institute for Fusion Science
322-6 Oroshi-cho, Toki-shi, Gifu
509-5292, Japan
E-mail: sakakibara.satoru@lhd.nifs.ac.jp

TODO Yasushi
National Institute for Fusion Science
322-6 Oroshi-cho, Toki-shi, Gifu
509-5292, Japan
E-mail: tohdo.yasushi@nifs.ac.jp

TOI Kazuo
National Institute for Fusion Science
322-6 Oroshi-cho, Toki-shi, Gifu
509-5292, Japan
E-mail: toi@nifs.ac.jp

WANG Zhijiang
Huazhong University of Science and Technology
J-TEXT Laboratory, Building 15, East campus, No.1037 Luoyu Road
Wuhan, Hubei, 430074, P.R. China
E-mail: wangzj@ mail.hust.edu.cn

XIANG Nong
Institute of Plasma Physics,
Chinese Academy of Science
P.O.Box 1126, Heifei, Anhui 230031,
P.R. China
E-mail: nxiang@ipp.ac.cn

ZHANG Xinjun
Institute of Plasma Physics,
Chinese Academy of Science
P.O.Box 1126, Heifei, Anhui 230031,
P.R. China
E-mail: xjzhang@ipp.ac.cn

ZHAO Yanping
Institute of Plasma Physics,
Chinese Academy of Science
P.O.Box 1126, Heifei, Anhui 230031,
P.R. China
E-mail: zhao_yp@ipp.ac.cn